Durham E-Theses

Experimental investigations of excited-state dynamics in conjugated polymers using time-resolved laser spectroscopy

SNEDDEN, EDWARD,WILLIAM

How to cite:

SNEDDEN, EDWARD,WILLIAM (2011) *Experimental investigations of excited-state dynamics in conjugated polymers using time-resolved laser spectroscopy*, Durham theses, Durham University. Available at Durham E-Theses Online: http://etheses.dur.ac.uk/888/

Use policy

EXPERIMENTAL INVESTIGATIONS OF EXCITED-STATE DYNAMICS IN CONJUGATED POLYMERS USING TIME-RESOLVED LASER SPECTROSCOPY

Edward William Snedden

_____

Abstract

In this thesis, time-resolved laser spectroscopy has been used to advance the understanding of the excited-state dynamics in a variety of conjugated polymers and related systems.

The properties of electron-phonon coupling in the conjugated polymer ladder-type methyl-substituted poly(para-phenylene) have been investigated using steady-state and picosecond fluorescence spectroscopy, with results demonstrating the thermal population of low energy stretching modes of the polymer backbone in the excited-state after thermalisation. Polarised measurements are used to demonstrate a fundamental relationship between the vibrational mode of the polymer through which fluorescence occurs and the corresponding fluorescence polarisation. Time-resolved measurements confirmed that the electron-phonon coupling in the polymer does not influence the fluorescence lifetime, with observations to the contrary attributed to the presence of an underlying defect state.

Picosecond fluorescence spectroscopy has also been used to investigate the properties of intramolecular energy transfer between different monomer subunits in the conjugated copolymer Super Yellow. The photoluminescence quantum yield of the copolymer was measured and its relatively high value was attributed to the effect of the aforementioned energy transfer.

Femtosecond pump-probe spectroscopy has been used to identify and characterise the properties of interchain exciton formation in ladder-type methyl-substituted poly(para-phenylene). This process was observed to occur with a time period of 1ps, which was attributed to the time required for a singlet exciton to become delocalised over adjacent polymer chains.

Finally, delocalised polaron generation in blends of the regio-regular polythiophene poly(3-dodecylthiophene-2,5-diyl) with the electron acceptor [6,6]-phenyl-C_{61}-butyric acid methyl ester was investigated using femtosecond pump-probe spectroscopy. Both the rate and yield of delocalised polaron formation were shown to be dependent on excitation energy, with the dissociation of geminate polaron-pairs making a substantial contribution to the yield. This latter observation is significant, as the geminate recombination of polaron-pairs constitutes a fundamental and inherent loss of potential delocalised polarons in this system.

EXPERIMENTAL INVESTIGATIONS OF EXCITED-STATE DYNAMICS IN CONJUGATED POLYMERS USING TIME-RESOLVED LASER SPECTROSCOPY

Edward William Snedden

_____

A thesis submitted to the Faculty of Science, Durham University, for the degree of Doctor of Philosophy

Organic Electroactive Materials Group
Department of Physics
University of Durham
January 2011

Contents

List of Figures

List of Tables

Index of Abbreviations

Declaration

I confirm that no part of the material offered herein has previously been submitted by myself for a degree in this or any other University. Where material has been generated through joint work, the work of others has been indicated.

Edward William Snedden

Durham

Acknowledgements

I am indebted to many people for their help, encouragement and support during the course of my research in Durham. First and foremost I would like to thank my supervisor Professor Andy Monkman for his leadership, guidance and invaluable advice which has directed and propelled my work forward. I would also like to thank my co-supervisor Dr. Fernando Dias for his many constructive comments and open support, particularly in relation to my work on polymer solar cells. My thanks also go to Dr. Dechang Dai, the University Laser Officer, for his expertise and immense help in keeping the femtosecond and picosecond laser systems running efficiently throughout the course of my studies, in addition to numerous helpful discussions on matters concerning ultrafast laser physics.

I have been most fortunate to collaborate with and work alongside an amazing group of people in the Department of Physics whose friendship will remain long into the future. My particular thanks go to Dr. Vygintas Jankus and soon-to-be-doctors Chien-Jung Chiang and Daniel Bright, for keeping our office a source of great fun over the past three years. My heartfelt thanks go to Dr. Helen Vaughan for her friendship and for her help on countless occasions.

Finally and most of all, I would like to thank both of my parents for a never-ending stream of love and support, and for giving me the tremendous opportunities that I have had to date.

For my parents,

thank you for everything and more.

Chapter 1   Introduction

1.1   Conjugated polymers

For the first half of the twentieth century it was generally understood that polymers did not conduct electricity. While inorganic solids were known to possess a wide range of different electrical properties, including conductivity, semi-conductivity and insulation, polymers were very much confined to being insulators. In 1977 however, Alan Heeger, Alan MacDiarmid and Hideki Shirakawa, who shared the Nobel Prize for Chemistry in 2000,[1] discovered that polyacetylene could display near-metallic levels of conductivity upon doping with sodium. This pioneering research was followed up by the discovery in 1990 by Richard Friend of electroluminescence – the emission of light as a result of an applied current - from poly(p-phenylene vinylene).[2] Both of these materials are examples of conjugated polymers, which are polymers characterised by a network of alternating single and double covalent bonds along their backbones. This bonding network allows for an excitation of the polymer to become delocalised over a large number of chain segments, imbuing these systems with conducting and semiconducting properties.

In the twenty years following on from Friend's work there has been a significant worldwide research effort made into the fundamental photophysical properties and optoelectronic applications of conjugated polymers. Much of this work has focussed on utilising conjugated polymers as the active emitting material in so-called organic light emitting diodes (OLEDs). OLED technology is expected to revolutionise the lighting and display industry, offering efficient, self-emitting display units featuring large viewing angles at low manufacturing costs. Indeed, OLED-based display units are already available commercially in mobile phone and monitor display units, with the first commercial white-light OLED flat panel units expected to

break into the open market in 2013.[3] Further research is required however to realise a 'plastic electronics' future in which the inherent mechanical flexibility of a conjugated polymer can be utilised in an OLED device. Some examples of early prototype OLED technology are shown in Fig. 1.1.

Figure 1.1: Examples of OLED display technology: Sony 27" OLED Television, and LGChem flat panel OLED lighting. Images from Refs. [4, 5], released into the public domain.

Recent years have also seen a surge in interest concerning the development of photovoltaic devices in which a conjugated polymer is used as the active optical material. With continuing developments allowing the power-conversion efficiency of such devices to pass 7% during 2010,[6] there is anticipation that organic photovoltaic technology may yet realise its promise as a practical and affordable solution in the photovoltaic market.[7, 8] Significant work still remains however in order to develop a sufficiently efficient organic photovoltaic device that can compete with the more established technology based on silicon that currently dominates the market. To this end, formulating a detailed description of the photophysical processes that occur in an organic photovoltaic system has become a subject of focus for many research groups worldwide, including as of 2010 the Organic Electroactive Materials Group at Durham University. An example of a prototype organic solar cell array is shown in Fig. 1.2.
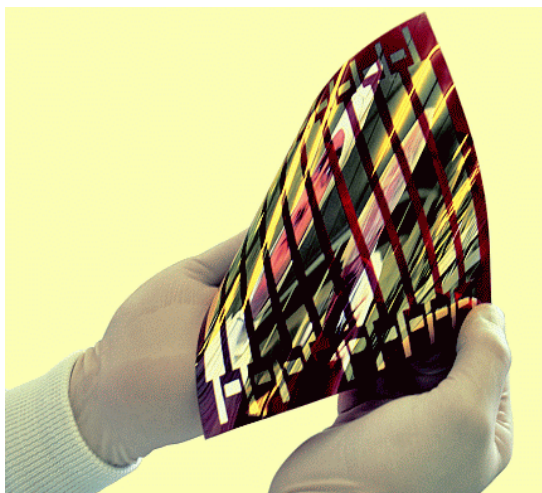
Figure 1.2: A conjugated polymer solar cell array, produced by Siemens. Image from Ref. [9], released into the public domain.

Aside from their application in numerous optoelectronic devices, conjugated polymers are innately fascinating systems in their own right and display a wealth of photophysical phenomena that can be attributed to the confinement of photoexcitations in the quasi-1D geometry of a polymer chain. As a result of this confinement both electron-electron and electron-phonon interactions are enhanced in conjugated polymers as compared to, for example, bulk inorganic semiconductors, with the primary excitation consisting of a bound electron-hole pair called an exciton, as compared to a free electron-hole pair. Initial models that attempted to describe the photophysical properties of conjugated polymers began as extensions of inorganic semiconductor theory that incorporated enhanced electron-phonon coupling into the theoretical framework.[10] These ideas were later succeeded by the work of Bässler *et al.* which demonstrated that it was necessary to include a contribution from the substantial electron-electron interactions that arose in such systems as a result of the disordered nature of the polymer microstructure.[11] It was with this research that the 'modern' and now commonly accepted theoretical treatment of conjugated polymers was born.

1.2 Conjugated polymers and time-resolved laser spectroscopy

The current research canvas of conjugated polymers is vast and includes many individual areas of focus, such as energy transfer and migration,[12] spintronics,[13] quantum-chemical modelling of chain dynamics[14] and charge generation[15] to name but a few. Interest has also built up around the study of conjugated copolymers; conjugated polymers consisting of multiple, chemically distinct monomer subunits.[16] These systems display an even richer variety of photophysical phenomena as opposed to their homopolymer counterparts by allowing for specific interactions between different subunits along the same polymer chain.[17]

Many of the fundamental photophysical processes of conjugated polymers are characterised by very short time scales. For example, the fluorescence lifetime of a conjugated polymer is typically of the order of 100 ps.[12, 18] Exciton energy transfer occurs with a time period between the order of 1 and 100 ps,[12, 19, 20] with the thermalisation of excess vibrational energy on a polymer chain occurring over an even shorter period of the order of 100 fs.[21] As a consequence time-resolved laser spectroscopy has emerged at the forefront of experimental investigations into the photophysical properties of conjugated polymers, with the ability to process timescales as short as 10 fs[22] proving an invaluable tool. At the heart of these investigations is the ultrafast laser itself, whose continuing development has now moved out of the academic community to become commercially available.[23] The Organic Electroactive Materials Group in Durham University has access to two Ti:Sapphire ultrafast laser oscillators, incorporating both picosecond and femtosecond operation. The femtosecond system, consisting of both a Ti:Sapphire laser oscillator and a regenerative amplifier, is shown in Fig. 1.3.

Figure 1.3: The femtosecond laser system of the Organic Electroactive Materials Group, Durham University. The Ti:Sapphire oscillator can just be seen at the left hand side of the image, with the regenerative amplifier in main view.

The field of ultrafast laser spectroscopy is broad, diverse and incorporates many different experimental techniques. Each of these methodologies has certain advantages and disadvantages and it is therefore often necessary to combine results from different experiments to build up a complete physical picture of a system. For example, picosecond fluorescence spectroscopy, which encompasses methodologies such as time-correlated single-photon counting and streak camera measurements, is able to measure the fluorescence lifetime of photoexcitations in conjugated polymers over periods of time ranging from 10 ps up to 10 ns.[18, 20] This method is limited however in its ability to only probe the population dynamics of excited states which emit with a sufficient intensity to be adequately detected and has a minimum time-resolution typically of the order of 1 ps. On the other hand, femtosecond pump-probe spectroscopy can be used to measure time-resolved absorption and is therefore able to probe the dynamics of both emitting and non-emitting excited states over time periods typically

ranging from 100 fs up to several nanoseconds.[24] Unfortunately the practical implementation of pump-probe spectroscopy is often non-trivial to perform, with the results from this method often complicated by a large number of different factors, both experimental and physical in origin. Furthermore the experimental limitations associated with this method means that it is typically only possible to accurately measure excited-state processes over femtosecond and picosecond timescales; to accurately measure longer processes, such as phosphorescence and charge recombination which are active on a microsecond timescale, another experimental method is required.

1.3 Thesis summary

This thesis outlines the details of several studies performed with the aim of advancing the current understanding of the excited-state dynamics in a variety of conjugated polymers through the application of time-resolved laser spectroscopy. A comprehensive review of the effects of electron-phonon coupling in the steady-state and time-resolved fluorescence spectra of the conjugated polymer ladder-type methyl-substituted poly(para-phenylene) (MeLPPP) has been performed, under the intention of addressing the nature of an unidentified long-lived state in the time-resolved fluorescence spectrum. Femtosecond pump-probe spectroscopy has also been applied to the study of MeLPPP in order to characterise an unidentified photoinduced absorption band in the transient transmission spectrum of the polymer.

In addition to investigating issues of a fundamental nature, time-resolved laser spectroscopy has also been applied to develop a description of the microscopic processes in conjugated polymers that have a direct bearing on macroscopic properties of certain optoelectronic devices. Picosecond fluorescence spectroscopy has been applied with the aim of investigating the relationship between the excited-state dynamics in the prototypical emitting conjugated copolymer Super Yellow and its high photoluminescence quantum yield, which characterises

the copolymer for use in an OLED. Femtosecond pump-probe spectroscopy is also applied to develop a description of the microscopic processes behind charge generation in a typical organic photovoltaic system, consisting of the regio-regular conjugated polymer poly(3-dodecylthiophene-2,5-diyl) (P3DDT) doped with the electron acceptor [6,6]-phenyl-C_{61}-butyric acid methyl ester (PCBM).

A detailed summary of the content of this thesis proceeds below. Following this chapter, the conceptual background behind the research presented in this thesis is given in chapters 2 and 3. Chapter 2 begins with an introduction to the basic theory of conjugated polymers and their photophysical properties, before developing towards more specific theoretical concepts that are considered in later chapters. Chapter 3 consists of a description of the theoretical and practical concepts behind the application of time-resolved laser spectroscopy to the study of conjugated polymers. A description of other supplemental experimental techniques is also included.

The remaining chapters of this thesis detail the results and analysis of experiments performed on different systems based on conjugated polymers. Both the work of chapters 5 and 6 are conceptually related to and follow on from the discussion of chapter 4. Although the order in which these chapters are presented could have easily been exchanged, the decision has been made to arrange the work of this thesis by the principle experimental method used in each chapter; the research of chapters 4 and 5 incorporates the use of picosecond fluorescence spectroscopy, while chapters 6 and 7 incorporate the use of femtosecond pump-probe spectroscopy.

In chapter 4 the properties of electron-phonon coupling in the conjugated polymer MeLPPP has been studied using steady-state fluorescence spectroscopy, polarised fluorescence spectroscopy and picosecond fluorescence spectroscopy. Temperature dependent measurements are used to demonstrate the thermal population of low energy stretching modes of the polymer backbone in

the excited-state after thermalisation. It is proposed that the depopulation of these modes at low temperatures initiates a structural change in the polymer which is observed to occur below 150 K. Polarised measurements are used to demonstrate a fundamental relationship between the polarisation of fluorescence and the vibrational mode through which radiative decay occurs. This behaviour is attributed to the presence of strong interchain interactions in the polymer. Finally, time-resolved studies are used to confirm that the electron-phonon coupling of the polymer does not influence the fluorescence lifetime, despite early measurements appearing to show otherwise. In those cases the observation of an energy dependent fluorescence lifetime is instead attributed to the presence of a photophysical defect of the polymer.

In chapter 5 the dynamics of intramolecular energy transfer in the prototypical emitting conjugated copolymer Super Yellow has been investigated using picosecond fluorescence spectroscopy. Energy transfer between adjacent but chemically distinct copolymer subunits is confirmed in the analysis of dynamic data obtained using a streak camera, with this energy transfer proposed to contribute to the high photoluminescence quantum yield of the copolymer. In a similar manner to that discussed in chapter 4, a study of the electron-phonon coupling in the copolymer is also performed, with the thermal population of low-energy ring-torsional modes of the polymer backbone shown to determine the form of the fluorescence spectrum as a function of temperature.

In chapter 6 femtosecond pump-probe spectroscopy has been used to identify and characterise the dynamics of interchain exciton formation in MeLPPP. Measurements of the photobleaching dynamics, performed as a function of probe energy, are used to identify the presence of an unidentified photoinduced absorption transition which overlaps with the photobleaching band of the polymer. Using results from polarised pump-probe spectroscopy, this photoinduced absorption is confirmed to have a transition dipole moment perpendicular to that of the intrachain singlet exciton population, with the photoinduced absorption consequently

attributed to the formation of interchain exciton states. This finding correlates with the presence of strong interchain interactions in regions of MeLPPP in the solid-state, as proposed in chapter 4.

Finally, in chapter 7 the dynamics of charge generation in a typical organic photovoltaic system, consisting of the regio-regular conjugated polymer P3DDT doped with the electron acceptor PCBM, has been studied using femtosecond pump-probe spectroscopy. This research marked the first step of a much larger research project concerning the photophysical processes in an organic solar cell system. By measuring and analysing the photoinduced absorption dynamics of key excitonic and charged states in the system, a model of charge generation in ordered regions of polymer is developed, focussing on the contribution of geminate-pair dissociation towards the charge yield.

Chapter 2   **Theoretical considerations**

This chapter provides a conceptual background to the electronic properties of conjugated polymers and their photophysical behaviour. It should be noted that such a discussion is not intended to be a comprehensive guide to all aspects of study within the field of conjugated polymers; some sections have been developed more at the expense of others according to their priority within the context of the research presented in this thesis.

The first three sections of this chapter consider the fundamental physics of conjugated polymers, beginning with a discussion of the molecular and electronic properties of conjugated polymers, before moving to describe the nature of the fundamental excitations of these materials and their photophysical properties. The remaining sections address more in-depth fields of study directly related to the research presented in chapters 4 through 7; electron-phonon coupling in conjugated polymers, exciton energy transfer and migration, and the photophysics of polymer/electron acceptor blends.

2.1   **The chemical structure of organic molecules**

Organic chemistry, the study of molecules and compounds based on the element carbon, is a vast field with a wide range of applications. The structural diversity of organic compounds arises from the chemical properties of carbon; in particular, the ability of carbon to form chemical bonds with up to four neighbours. Amongst many things, this property of carbon allows it to be connected in chains of varying length through the repetition of a single structural unit. A polymer is a large molecule consisting of many such repeat units. Indeed, some polymers can consist of more than a thousand repeat units and reach a total length of 1 μm[25] and as such are also referred to as macromolecules. If a chain consists of only a few (for example, up to ten) repeat units, then the structure is referred to as an oligomer. Given the

flexibility of the carbon-carbon bonds which make up the backbone of a polymer chain, these molecules can form complex shapes and can interact strongly with one another. This microscopic behaviour has a strong influence on the mechanical and electrical properties of polymers, which can be markedly different to inorganic materials.

The electronic properties of polymers are also strongly influenced by the type of chemical bonding that occurs between the carbon atoms along the chain. The carbon atoms in a polymer are bound together by covalent bonds, formed by the sharing of pairs of electrons between atoms. The concept of covalent bonding can be developed in more detail by calling upon some of the ideas of molecular orbital theory.[26] As a case study, consider the formation of diatomic hydrogen (H_2), shown in Fig. 2.1.
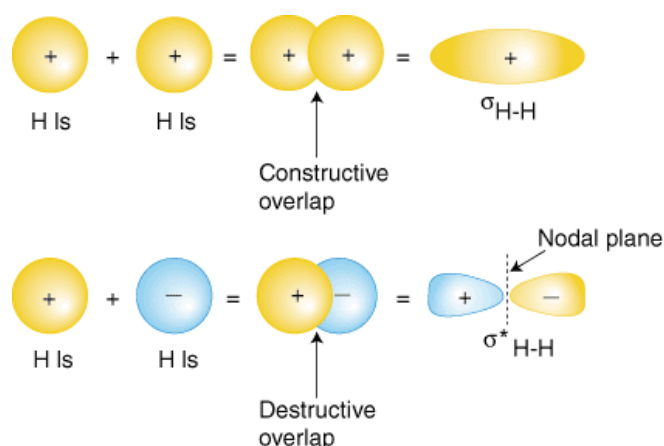
Figure 2.1: Molecular orbital formation in diatomic hydrogen. As two hydrogen atoms are brought together, the 1s atomic orbitals of each atom begin to overlap with each other. When this overlap is constructive a σ molecular orbital is formed; when the overlap is deconstructive a $\sigma*$ molecular orbital is formed. Figure adapted for use from Ref. [27].

As two hydrogen atoms are brought together, the 1s electrical orbitals of each atom begin to overlap, with the negatively charged electron in the 1s orbital of one atom feeling an increased electrostatic attraction towards the other positively charged nucleus, and vice-versa. Eventually

the two orbitals can no longer be considered distinct, resulting in the formation of two new molecular σ orbitals with different energies. When the 1s orbital overlap is constructive, a low energy bonding σ molecular orbital is formed; when the orbital overlap is deconstructive, a high energy anti-bonding σ* molecular orbital is formed.

The origin of the break in degeneracy between the molecular orbitals is a consequence of the probability distribution associated with each orbital. In the σ orbital electrons have a high probability of being found in the region between the two nuclei and thus experience a large electrostatic attraction. This reduces the total energy of the system with respect to the initial atomic orbital energies. In the σ* orbital a nodal plane of zero-probability instead lies between the two atoms and as a result the electrons are more tightly confined, which increases the energy of the σ* orbital with respect to the atomic orbital energies. The energy levels of the σ and σ* molecular orbitals in hydrogen are shown in Fig. 2.2.
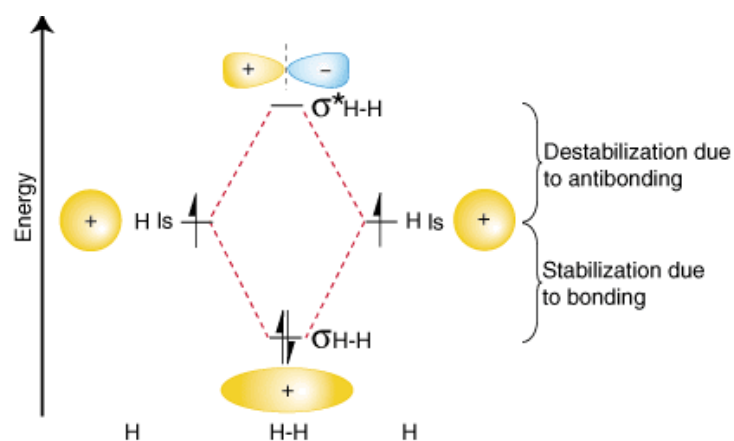
Figure 2.2: Molecular orbital energies in diatomic hydrogen. The electrons of each hydrogen atom are filled into the σ molecular orbital with equal and opposite spins as according to the Pauli exclusion principle. This results in the formation of a covalent bond. Figure adapted for use from Ref. [27].

In the case of diatomic hydrogen, the two electrons in the 1s atomic orbitals are filled into the lowest energy molecular orbital (σ molecular orbital, as discussed above), with equal but opposite spins according to Pauli's exclusion principle, which states that no two electrons in a single electronic system may possess the same set of quantum numbers. This lowers the overall energy of the system and results in the formation of a covalent bond, as shown in Fig. 2.2. The σ molecular orbital is completely filled and is referred to as the highest occupied molecular orbital (HOMO); the σ* is completely unoccupied and is referred to as the lowest unoccupied molecular orbital (LUMO).

In order to explain the molecular geometry of organic systems it is necessary to introduce the concept of hybridisation, in which the atomic orbitals of an atom are combined together to form a new set of orbitals with different energies and orientations. To help develop this point further, consider below the covalent bonding in methane and ethylene.

The carbon atom possesses four valence electrons in a $2s^2 2p^2$ electronic structure. In methane the 2s and the $2p_x$, $2p_y$, and $2p_z$ orbitals are combined together in a process referred to as sp^3 hybridisation to form a new set of four degenerate orbitals. As shown in Fig. 2.3, these orbitals are oriented at 109.5° with respect to one another,[28] with each one overlapping with the 1s orbital of a hydrogen atom in a tetrahedral structure. These highly directional orbitals have an improved degree of overlap with the 1s orbitals of the four surrounding hydrogen atoms, as compared with overlap involving partially filled 2p orbitals. This results in an increase in the electrostatic interactions in the bonds and a reduction to the total energy of the system.
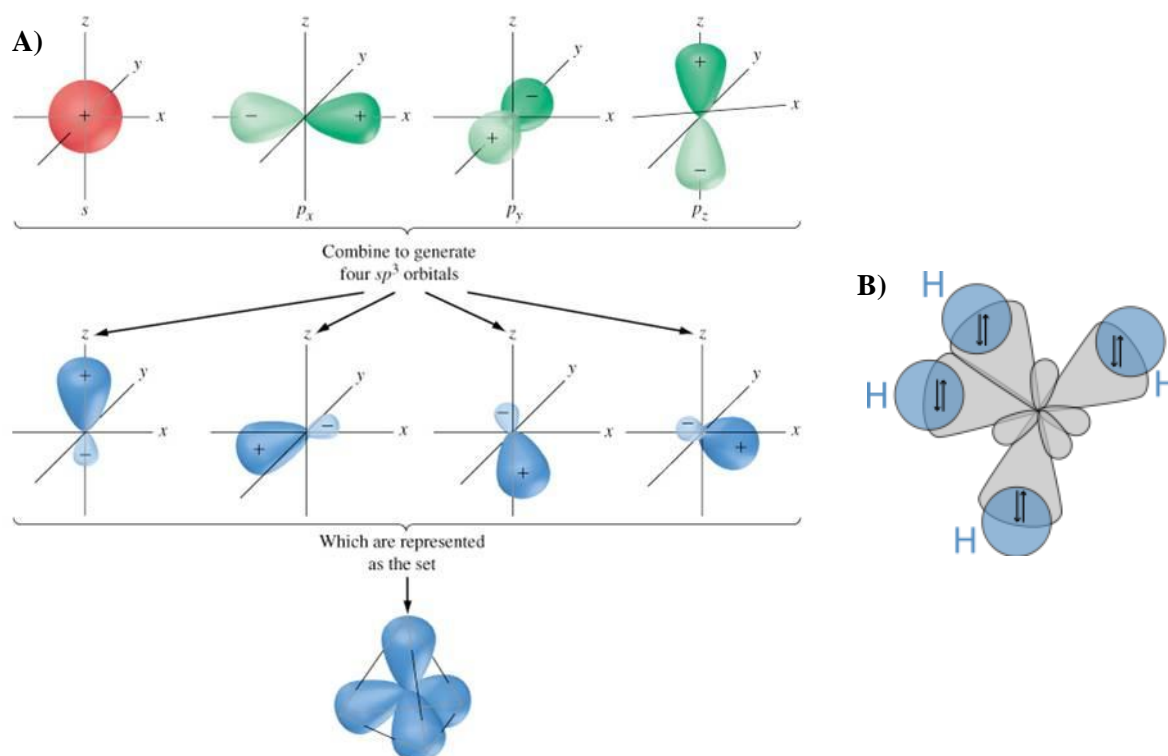
Figure 2.3: A) Formation of sp^3 hybridised orbitals. The 2s, 2p$_x$, 2p$_y$ and 2p$_z$ atomic orbitals of carbon are combined together to form a new set of so-called sp^3 hybrid orbitals. Figure adapted for use from Ref. [28]. B) Chemical structure of methane, highlighting the overlap of the sp^3 hybrid orbitals of a carbon atom with four surrounding hydrogen atoms. Image by K. Aainsqatsi, released into public domain.

A different hybridisation scheme is required to explain the geometry of the ethylene molecule, which is known to be planar. In this case, the 2s orbital of carbon is mixed with the 2p$_x$ and 2p$_y$ orbitals to form three sp^2 hybrid orbitals oriented at 120°; the 2p$_z$ orbital is left unchanged and lies perpendicular to the plane defined by the sp^2 orbitals. The shape and orientation of these orbitals is shown in Fig. 2.4. The sp^2 hybrid orbitals in ethylene form three σ bonds; two involving overlap with the 1s orbitals of hydrogen atoms, with the third overlapping with the sp^2 orbital of the other carbon atom. The remaining 2p$_z$ orbitals also overlap to form a π

molecular orbital between the two carbon atoms into which two electrons are filled, forming an additional bond. The combination of the σ and π bonds together is referred to as a double bond.
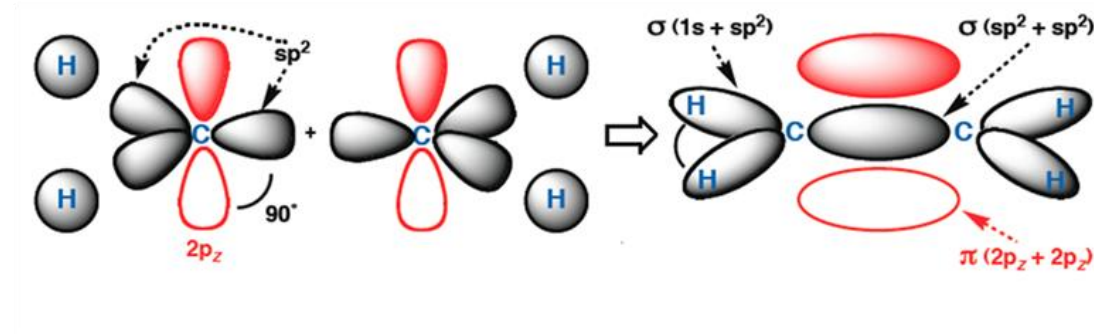
Figure 2.4: Molecular orbital formation in ethylene. Each carbon atom is sp^2 hybridised. Two hybrid orbitals of each atom form σ bonds with two hydrogen atoms, with the remaining hybrid orbitals overlapping together to form a σ bond between the two carbon atoms. The 2p$_z$ orbitals of each carbon atom which are not involved in the hybridisation process also overlap together, forming a π molecular orbital. The combination of both the σ and π orbitals that act between the two carbon atoms together is referred to as a double bond. Figure adapted for use from Ref. [27].

Given the geometry of the 2p$_z$ orbital overlap, the π molecular orbital is restricted to lie out of plane and consequently is not as effective at maximising electrostatic interactions as the σ molecular orbitals. This results in a smaller energy splitting between the π and π* orbitals, as compared with the σ and σ* orbitals, and consequently the HOMO in ethylene is the π orbital, with the π* forming the LUMO. The geometry of the π overlap also acts to restrict torsional motion about the carbon-carbon bond, as any significant rotation will decrease the 2p$_z$ orbital overlap and eventually destroy the π orbital, resulting in an increase to the total energy of the system.

2.2   Conjugated polymers

Benzene, shown in Fig. 2.5A, is an organic compound consisting of six sp^2 hybridised carbon atoms in a ring structure, connected by a series of alternating single and double bonds in what is referred to as a conjugated structure. As in the case of ethylene, the $2p_z$ orbitals of each atom overlap together to form a π orbital network that encompasses all six atoms, allowing for electrons in that orbital to become delocalised over the entire ring.
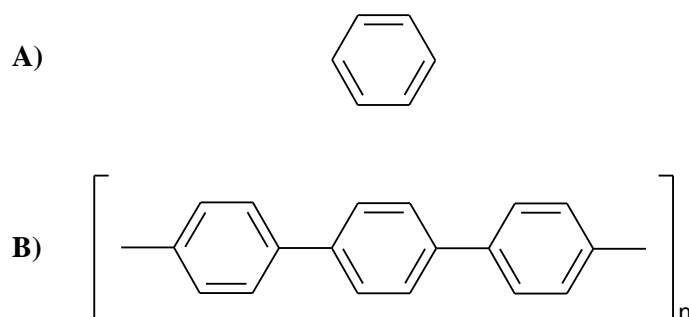
Figure 2.5: Chemical structures of A) benzene and B) poly(para-phenylene). Both molecules consist of an alternating pattern of single and double covalent bonds, referred to as a conjugated structure.

Imagine now connecting a large number of benzene molecules together to form the polymer poly(para-phenylene), which is shown in Fig. 2.5B. In this new structure the alternating series of single and double bonds is preserved between rings and extends across the entire macromolecule, making poly(para-phenylene) a simple example of a conjugated polymer. In a similar manner to that discussed in the context of benzene, the $2p_z$ orbitals of each carbon overlap to form a large π orbital network that allows electrons to be theoretically delocalised over the entire macromolecule, assuming there is no mechanism that breaks the conjugation at any point. Unlike more common bulk inorganic conductors and semiconductors, in which delocalisation can occur in all three dimensions, the orbital overlap present in a conjugated

polymer restricts the delocalisation of charge to lie solely along the chain direction in a quasi-1D geometry.

It is the delocalisation of electrons in such a π orbital network from which the fundamental electronic properties of conjugated polymers are derived. The primary electronic transition in a conjugated polymer is the $\pi-\pi*$ transition, corresponding to the excitation of an electron from the HOMO to the LUMO. The difference in energy between the HOMO and LUMO is governed by the number of electrons and nuclei that participate in bonding in the π orbital network and therefore is related to the extent of the conjugation along the polymer backbone. The number of monomer units over which the conjugation extends is referred to as the conjugation length. Longer conjugation lengths involve more electrons and nuclei; this stabilises the bonding in the polymer and reduces the HOMO-LUMO energy interval. This concept is analogous to the simple quantum mechanical treatment of a particle in a box, although a more quantitative description requires the use of molecular exciton theory[29] and quantum chemical simulations.[12]

The concept of unbroken conjugation along an entire polymer chain is rarely realised in practice and the chain length of a conjugated polymer is not the determining influence on the HOMO-LUMO energy interval. This is a consequence of the fact that conjugated polymers do not typically form well-ordered, periodic structures like most inorganic semiconductors, but possess a strong level of disorder at both intramolecular and intermolecular length scales.[11] For example, a conjugated polymer is subject to various conformational defects that can twist the polymer backbone out of place, such as chemical impurities and torsional distortions.[14, 30, 31] At these defect points π-orbital overlap between adjacent carbon atoms is no longer possible and the conjugation is said to be broken.
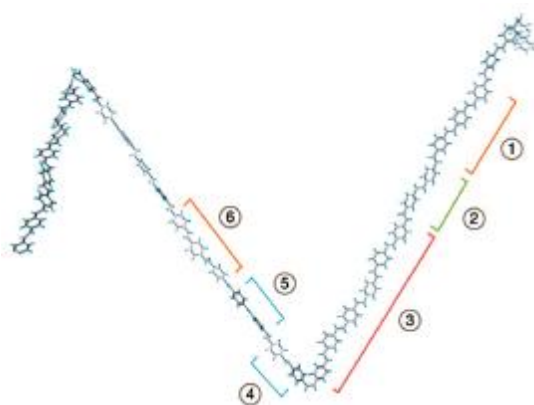
Figure 2.6: Example of how a conjugated polymer can be broken up into a series of chromophores of different conjugation lengths, labelled 1-6. Figure adapted for use from Ref. [12].

As a consequence of this structural disorder, a single polymer chain can be broken into segments of different conjugation lengths called chromophores[11] which are typically between two to five repeat units in length.[11, 12, 32] An example of how a single chain can be broken into different chromophores is shown in Fig. 2.6. Averaging over many different polymer chains leads to a distribution of chromophore conjugation lengths which in most cases is assumed to be Gaussian.[33]

2.3   The fundamental excitations of conjugated polymers

2.3.1 Excitons

In conjugated polymers electron-electron interactions are strong as a result of the electronic confinement and occur with relatively weak coulomb screening (polyacetylene: $\varepsilon_r \sim 2$).[34] As a consequence, following photoexcitation an electron promoted from the HOMO to the LUMO of the polymer will remain strongly correlated to the hole in the LUMO, forming a bound quasi-particle state called an exciton. Such a state is neutrally charged and does not contribute to the conductivity of the system. This situation can be compared with that of bulk inorganic

semiconductors (silicon: $\varepsilon_r = 11$)[35] in which the screening is moderate and the result of photoexcitation is an uncorrelated electron-hole pair. This difference between the basic results of photoexcitation is a fundamental distinction between the electronic properties of conjugated polymers and inorganic semiconductors.

Conjugated polymers are also characterised by strong electron-phonon coupling and upon photoexcitation a polymer chain will reconfigure about an exciton in the excited state.[36, 37] This process can be understood as the exciton lowering its energy by surrounding itself with a 'cloud' of phonons. Results from quantum chemical simulations have shown that this structural reorganisation involves the planarization[38, 39] of the polymer. As the electron-hole pair moves through the polymer system, so will the corresponding distortion of the polymer; the bound electron-hole pair and the corresponding distortion field together constitute a quasi-particle state.

There are two primary classes of exciton which refer to how tightly bound the electron and hole are to one another. Mott-Wannier excitons have lower binding energies and are delocalised over multiple polymer chains; in this respect they are often referred to as interchain or charge-transfer excitons. Frenkel excitons are tightly bound states in which the electron and hole are confined to the same molecular unit and are also referred to as intrachain excitons. On the basis that in most conjugated polymers electron-electron interactions between chains are mediated by a weak van-der-Waals type attraction, the primary photoexcitation of a conjugated polymer is typically a molecular Frenkel exciton with a binding energy of ~0.5 eV.[40]

Both the electron and hole that make up an exciton are spin ½ particles. As a consequence, the total spin (S) of an exciton is zero, referred to as a singlet exciton, or one, a triplet exciton. The corresponding wavefunctions of these states are shown in Eq. 2.1.

$$S = 0 \ (singlet) \quad \frac{1}{\sqrt{2}}(|\uparrow_1\downarrow_2\rangle - |\downarrow_1\uparrow_2\rangle) \ m_s = 0$$

$$S = 1 \ (triplet) \quad \begin{cases} |\uparrow_1\uparrow_2\rangle \ m_s = 1 \\ \frac{1}{\sqrt{2}}(|\uparrow_1\downarrow_2\rangle + |\downarrow_1\uparrow_2\rangle) \ m_s = 0 \\ |\downarrow_1\downarrow_2\rangle \ m_s = -1 \end{cases} \qquad (2.1)$$

In Eq. 2.1 m_s is z-component of the spin and 1 and 2 are particle labels. A diagrammatic representation of the different exciton spin states is shown in Fig. 2.7. It should be noted that, for simplicity, in this figure the electron has been placed in the LUMO of the conjugated polymer, with the exciton said to be in the S_1 state.
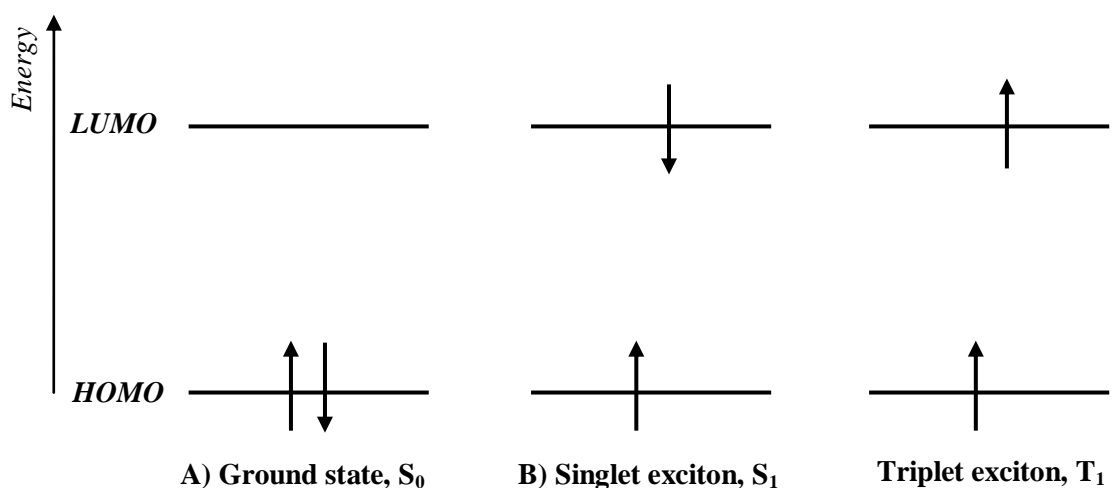
Figure 2.7: Relative spin orientations of the electron and hole for different electronic states in a conjugated polymer: A) polymer ground state (S_0); B) first singlet exciton state (S_1) and C) first triplet exciton state (T_1).

For most conjugated polymers the triplet energy is approximately 0.7 eV lower than the corresponding singlet energy.[41] This amount of energy is known as the exchange energy and is fundamentally related to the anti-symmetry of the quantum wavefunction required of any fermion state. This origin of this energy arises from the fact that in the spatial state of the

triplet wavefunction, which must be anti-symmetric, electron-electron repulsions are reduced as the electron density associated with the wavefunction vanishes as the two particles move to the same position.

2.3.2 The polymer density of states

As discussed in section 2.2, the length of a conjugated segment is the primary factor in determining the HOMO-LUMO separation of a chromophore and thus in turn the exciton energy. Having a distribution of chromophore lengths in a conjugated polymer thus results in an inhomogeneous distribution of exciton energies. The distribution of exciton energies is known as the density of states (DOS) of the conjugated polymer, with an example DOS shown in Fig. 2.8.
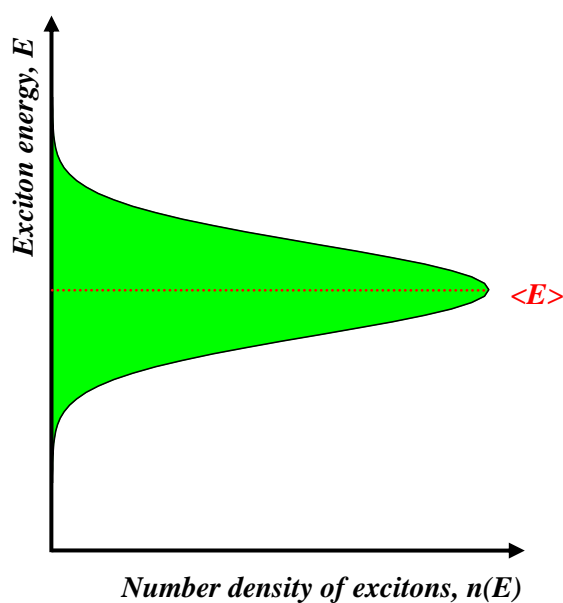
Figure 2.8: Example of a Gaussian DOS of a conjugated polymer. In this circumstance the DOS has been chosen to be completely filled (green fill), with the average exciton energy <E> lying directly in the middle of the DOS.

The DOS of a conjugated polymer is a dynamic quantity and is dependent on temperature. Thermal fluctuations can generate a brief reconfiguration of the DOS by changing the conformation of a polymer chain for a short period of time.[20, 30, 31] For example, a conjugation break generated by a torsional twist may be briefly overcome through a thermally assisted rotation of the chain, increasing the conjugation length and thus temporarily lowering the corresponding chromophore energy. At lower temperatures there is less thermal energy for such processes to occur, typically resulting in a decrease to the inhomogeneous broadening of the DOS.

2.3.3 Polarons

When a single charge is injected into a conjugated polymer, strong electron-phonon interactions result in the distortion and polarisation of the polymer around the charge. As the particle travels through the system, so will the associated distortion; this quasi-particle is called a polaron. Unlike excitons, which are neutrally charged and do not contribute to the conductivity of a conjugated polymer, polarons can move from chromophore to chromophore upon application of an electric field, forming the passage of an electrical current. This process is however complicated by the amorphous microstructure of a conjugated polymer,[42-44] with the conductivity of such systems measured to be between 1×10^{-6} and 1 $cm^2 \cdot V^{-1} \cdot s^{-1}$, as compared to $\sim 1\times10^{3}$ $cm^2 \cdot V^{-1} \cdot s^{-1}$ for inorganic semiconductors.[33]

The energy levels of the polaron state, shown in Fig. 2.9, differ from that of an exciton and lie within the HOMO-LUMO interval of the polymer. There are in general three different possible polaron states in a conjugated polymer; a free electron polaron, a free hole polaron and a geminate electron-hole pair. Direct polaron generation in a conjugated polymer can occur either through the injection of charge under the application of an electric field or through the

introduction of a chemical dopant which oxidises/reduces the chains. These processes result in the formation of free electron and hole polarons.
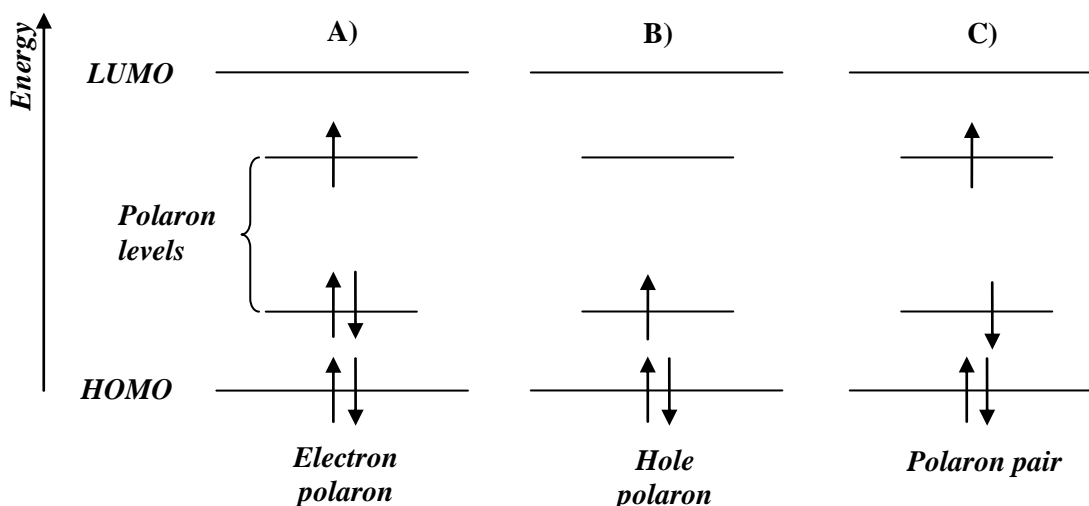
Figure 2.9: Polaron energy levels in a conjugated polymer. A) Electron polaron created by adding one electron into a polaron level; B) hole polaron created by removing one electron from the HOMO of the polymer; C) electron-hole pair as created when the binding energy of an exciton is overcome.

Direct optical generation of polarons in a conjugated polymer is complicated by the fact that upon absorption an electron and hole will remain correlated to one another, forming a neutral exciton. It is therefore clear that a direct path towards polaron generation involving optical excitation necessitates exceeding the binding energy (~0.5 eV) of the exciton state. This can be done in a number of different ways.

The most effective mechanism of polaron generation following photoexcitation is the application of a sufficiently strong electric field that can offset the coulomb binding energy between the electron and hole of an exciton.[45] Other mechanisms of polaron generation are based upon generating an exciton with a sufficient degree of excess energy that can be used to overcome the coulomb binding energy. This can be achieved either through one-step excitation

with a high energy source, known as an auto-ionization process, or two-step excitation involving a primary excitation followed by a second 'push' excitation.[46]

Two-step excitation leading to polaron generation has been extensively studied in conjugated polymers.[46-51] The general principle of such a process is that optical re-excitation of an exciton generates a highly excited singlet state (typically denoted as S_N) with a large exciton-hole separation.[52] In such states the correlation between electron and hole is significantly reduced, leading to the formation of polarons. Reported charge yields from this method are much lower as compared with electric-field assisted dissociation, with experiments showing that the polarons generated from excited singlet states rapidly recombine to reform S_1 excitons before they can be collected as a photocurrent.[46, 50] This has led to polarons being classified into two distinct types: if the electron and hole remain coulombically bound to each other, such that charge recombination will only occur between that pair and no other, then the polarons are said to form a geminate polaron-pair. If the electron and hole have no correlations of any kind then they are referred to as free polarons. It is possible to distinguish between free polarons and geminate polaron-pairs in terms of their recombination dynamics: the recombination of free polarons is dependent on the excitation density; the recombination of geminate pairs is not.[47] Geminate polaron-pairs are also thought to retain some degree of spin-correlation; both singlet and triplet geminate pairs can exist.[53]

2.4 The photophysics of conjugated polymers

In section 2.2 the role of electron delocalisation in stabilising the HOMO-LUMO energy gap of a conjugated polymer was discussed. This physical property has important ramifications for the interaction of conjugated polymers with light; for the conjugation lengths typical of these systems, the HOMO-LUMO energy gap approaches that accessible by the visible (450-800 nm) and near-ultraviolet (350-450 nm) regimes of the electromagnetic spectrum. As such

conjugated polymers have a high degree technological significance; they are examples of organic semiconductors which strongly interact with light and thus are materials which can be used in a wide range of optoelectronic devices.[54-57]

In such a context understanding the photophysical properties of conjugated polymers is a matter of great interest. In this section the basic photophysical processes that occur in a conjugated polymer are reviewed. These processes are neatly summarised in the so-called Jablonski diagram, shown in Fig. 2.10.
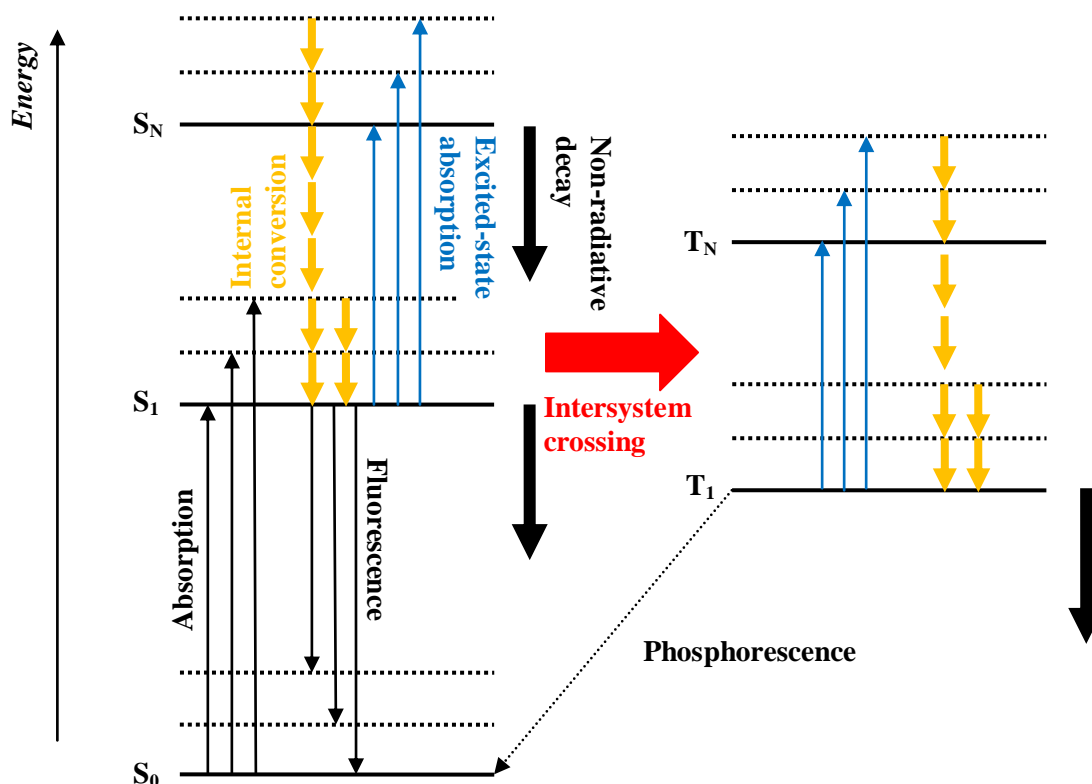
Figure 2.10: The Jablonski diagram, which summaries most of the significant photophysical processes that occur in a conjugated polymer. Electronic (black lines) and vibrational sub-levels (dotted lines) have both been included. Photophysical processes that occur include absorption and fluorescence, excited-state absorption, non-radiative decay and internal conversion. Intersystem crossing occurs between the singlet (S) and triplet (T) manifolds of state, with a spin-forbidden transition from the T_1 to the S_0 occurring as phosphorescence.

2.4.1 The selection rules for optical transitions

Starting from the S_0 ground state of a conjugated polymer, the absorption of a photon of visible light will lead to an optical transition and the generation of a S_1 exciton in the excited-state. Such a process is typically modelled using the electric dipole approximation.[58] This is a perturbation approach which treats the absorption of a photon as an interaction between the dipole moment of the electronic system with the electric field of the photon. The rate of transitions between energy levels are governed by Fermi's Golden Rule:

$$\Gamma_{i,j} = \frac{2\pi}{\hbar} \left| \langle \psi_j | \hat{H}' | \psi_i \rangle \right|^2 g(E_j), \ \ where \ \hat{H}' = -F_0 q \underline{r} e^{-i\omega t} \tag{2.2}$$

Γ: Transition rate, $g(E)$: Density of states

F_0: Magnitude of electric field, $\underline{r}$: Orientation of dipole

ω: Frequency of electric field, i,j: Energy level index

It should be noted that the energetic dependence of these transitions is contained within the overlap of the initial (ψ_i) and final (ψ_j) state wavefunctions and is not explicitly clear in Eq. 2.2. It can however be shown that the transition rate will be directly related to the difference in energy between the transition interval and the incoming photon energy, with the transition rate largest when $E_j - E_i = \hbar\omega$. This principle is at the heart of all optical spectroscopic methods; a photon of light will interact with a sample and generate an electronic transition if its energy is tuned to the interval between two energy levels. There are however many other factors which affect the probability of a transition occurring which are also contained within Eq. 2.2. These factors are summarised by a set of conditions known as the selection rules. The selection rules related to parity, spin, angular momentum and orbital symmetry are now discussed in turn.

Parity

If a quantum wavefunction retains its sign under an inversion of particle coordinates it is said to be of even or gerade symmetry (denoted by the subscript g); if it changes sign it is said to be odd or ungerade (subscript u). The parity selection rule states that transitions between states of the same parity are forbidden; for example, g → u is allowed, but g → g is not.

Electron correlation effects in conjugated polymers result in the ground state S_0 being of even symmetry ($1A_g$), with the S_1 being of odd symmetry ($1B_u$), the S_2 even again ($2A_g$) and so on.[49, 59] As a consequence one-photon transitions between the S_0 and S_2 levels are forbidden. Note that the Mulliken symbols A and B are used to denote even and odd orbital symmetry following a rotation about the C_2 axis (corresponding to 180^0) of the molecule in question.[60]

Spin

The spin selection rule forbids transitions in which there is a change in the total spin (S). For example, the transition $S_1 \rightarrow T_1$ requires $\Delta S = 1$ and consequently is spin-forbidden. Likewise the process T_1 to S_0 is also spin-forbidden. Sufficiently strong spin-orbit coupling in conjugated polymers can allow such processes to occur, but with a probability that is a factor of 10^5 smaller than spin-allowed processes.[40]

Angular Momentum

In order to conserve angular momentum in an electronic transition (in which a photon is either created or absorbed) the system must also change its angular momentum by one unit.

Orbital symmetry

In order for a transition to be allowed there must be sufficient spatial overlap between the relevant orbital wavefunctions. For example, a transition between orbitals that are perpendicular in space to one another is forbidden.

Outside of the selection rules, it is also important to note that the transition rate of optical transitions also depends on the orientation of the electric field with respect to the electric dipole moment; absorption will be strongest when the electric field is aligned parallel to the dipole moment. This is the basis of polarisation spectroscopy and is a topic that is covered in more detail in section 3.9.

2.4.2 Absorption and fluorescence

When light of the correct frequency corresponding to a transition between energy levels is incident upon a sample, photons passing through that sample will be absorbed and the intensity of the light will vary as a function of the distance transmitted. The exact relationship associated with this process is expressed by the Beer-Lambert law, which is given in Eq. 2.3:[23]

$$I = I_0 \cdot 10^{(-\alpha D)} \tag{2.3}$$

α: Absorption coefficient

D: Distance transmitted through sample

The Beer-Lambert law can be equivalently written using the definition of optic density ($O.D.$), given in Eq. 2.4:

$$O.D. \equiv \log_{10}(\frac{I_0}{I}) = \alpha D \tag{2.4}$$

In these expressions the energy dependence of the transmitted intensity of a sample is incorporated into the absorption coefficient, which becomes a function of the incoming photon energy; $\alpha(\hbar\omega)$.

The probability for a photon to be absorbed and generate an electronic transition in a sample is governed by Eq. 2.2 and the selection rules discussed in section 2.4.1 above. It should be noted that the same rules can be applied to govern the reverse process, in which an excitation loses energy in the form of a photon under presence of a perturbing field. This process is known as stimulated emission, because the transition occurs in the presence of an applied electric field; when this process occurs in the absence of an electric field it is referred to as spontaneous emission.[23]

The physical origin of spontaneous emission can only be rigorously explained using quantum field theory.[61] Einstein was however able to show that the processes of stimulated and spontaneous emission must be related to each other on thermodynamic principles. A key conclusion of this work was that both the rates of stimulated and spontaneous emission depend on the same squared matrix term expressed in Eq. 2.2 above.[23] Consequently the selection rules of section 2.4.1 above can be equally applied to spontaneous emission.

The process in which emission occurs from a sample that has been optically excited is more commonly referred to as photoluminescence; when this process is allowed, as according to the selection rules outlined above, it is specifically referred to as fluorescence. By measuring the absorption and fluorescence spectra of a conjugated polymer it is possible to gain a great deal of information about the energies of the different electronic states in that sample, assuming that those states can be accessed by allowed, one-photon optical transitions.

2.4.3 Excited-state absorption

In the same way that it is possible for the ground state of a conjugated polymer to absorb a photon of light, resulting in a transition to an excited state, it is also possible for an excited-state to absorb a photon and undergo a transition to an even higher-lying state. This process is known as excited-state absorption. For example, an S_1 exciton can absorb a photon of light to undergo a transition to a higher excited singlet state S_N:

$$S_1 + \hbar\omega \rightarrow S_N \tag{2.5}$$

If the excited state was generated through the initial absorption of a photon, as discussed in the context of ground-state absorption in section 2.4.2, then the excited-state absorption process is also referred to as photoinduced absorption (PA).[24] Given the requirements imposed upon photon-mediated transitions expressed by the selection rules (section 2.4.1), it is clear that PA processes can generate transitions to one-photon forbidden A_g states. This method also provides access to high energy S_N states that often cannot be accessed experimentally, for example due to wavelength constrictions on the excitation source.[50, 51, 62]
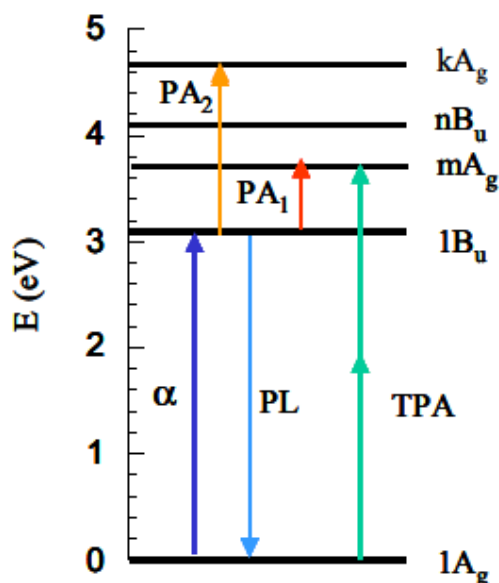
Figure 2.11: A summary of different optical transitions in the conjugated polymer polyfluorene. In addition to one-photon transitions to and from the ground state of the polymer (absorption: α, and photoluminescence: PL), two-photon transitions (photoinduced absorption: PA, and two-photon absorption: TPA) are also possible and access high-lying even-symmetry states. Figure adapted for use from Ref. [59].

The process of PA should be distinguished apart from two-photon absorption (TPA), which is specifically a non-linear optical process in which two photons of the same energy are simultaneously absorbed, leading to transitions to higher-lying excited states.[59, 63] TPA and PA are physically distinct in a number of ways; for example, whereas PA requires a transition to an intermediate state, for example the S_1 level, TPA does not involve any intermediate state. In addition, because TPA is a non-linear process it requires very high photon densities to be observed in a conjugated polymer and as such it can easily be prevented by selection of low power densities. A summary of these optical processes is given in Fig. 2.11.

It should be noted that the concept of excited-state absorption is equally applicable to transitions within the triplet manifold, although in such cases the initial T_1 state can only be generated optically through intersystem crossing from the singlet manifold of states. A T_1

exciton can absorb a photon to undergo a transition to a higher-lying excited triplet state T_N in a process more commonly referred to as triplet-triplet absorption.

Like the singlet state, polaron states have a manifold of different energy levels in which transitions can occur between. The most typical of these processes is the absorption of a photon of light, leading to the generation of an excited polaron state. It is typical to observe only two polaron absorption transitions;[46, 64] these are given in Fig. 2.12 for a hole polaron.
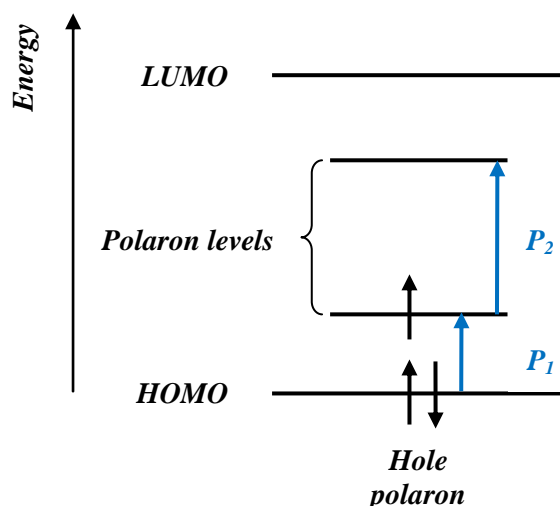
Figure 2.12: Doublet of polaron absorption transitions (denoted P_1 and P_2) in a conjugated polymer. For clarification, black arrows denote the spin states; blue arrows denote the polaron transitions.

2.4.4 Intersystem crossing and phosphorescence

The selection rules which govern the properties of electronic transitions in response to the electric field of a photon (section 2.4.1) state that spin must be conserved in any transition. As a consequence, transitions between the singlet and triplet manifold of states are spin-forbidden. Non-radiative transitions between these states are possible however in systems in which the spin-orbital coupling is sufficiently strong. Spin-orbital coupling is the interaction between the

orbital and spin degrees of freedom of an electron as mediated by the electromagnetic field of a nucleus.[65] This interaction can provide a sufficient perturbation as to allow singlet and triplet spin states to mix together, therefore permitting transitions between the two manifolds of state to occur. Such transitions are referred to as intersystem crossing.[66]

Intersystem crossing is an isoenergetic process and therefore requires the accepting energy level in any transition to be degenerate with that of the initial level. This accepting level can be a vibrational energy level; indeed, given that the S_1 and T_1 energy levels of a conjugated polymer are offset due to the exchange interaction, intersystem crossing originating from the S_1 energy level will typically only occur into one of the excited vibrational levels of T_1.

It is also possible for spin-orbit coupling to induce an emissive transition between the T_1 and S_0 energy levels of a conjugated polymer, which is a process that is also spin-forbidden. This transition is known as phosphorescence and occurs with a very low probability;[66] phosphorescence lifetimes, as compared to fluorescence lifetimes, are of the order of 10^3-10^5 times longer.[40] The low probability for phosphorescence has several important consequences for the photophysical properties of conjugated polymers. For example, because the lifetime of triplet exciton is so long, these states have ample opportunity to explore their surroundings and migrate through the polymer network.[67] In this regard triplet excitons also have a high probability to encounter and be quenched at non-emissive defect sites. This can pose an additional degree of difficulty in detecting phosphorescence from a conjugated polymer, which is already very weak. Experiments which measure the triplet population are typically done at very low temperatures as to minimise the rate of migration. They must also be purged of any defects; for example, solution samples must be degassed of oxygen, which is a very effective triplet quencher.

2.5 Electron-phonon coupling in conjugated polymers

Up to this point the role of strong electron-electron interactions in determining the photophysical properties of conjugated polymers has only been briefly discussed. This section proceeds to consider in more detail the influence of electron-phonon interactions on the photophysics of conjugated polymers.

2.5.1 The Born-Oppenheimer principle

The foundation of most theoretical treatments of electron-phonon coupling in a conjugated polymer and indeed most molecular systems, is the Born-Oppenheimer approximation.[40] This approximation is based on the fundamental idea that for a typical molecular system the nuclear masses far exceed the electronic masses, allowing the electronic distribution of the system to adjust instantaneously with respect to any change in the nuclear positions. This is an example of an adiabatic process; there is enough time for the eigenstate of the system to evolve to reflect the new nuclear coordinates, rather than being trapped in its initial eigenstate as would occur if the nuclear change was made rapidly.[68] Under these circumstances the wavefunction of a quantum state (ψ) is made up of the product of the electronic (Ψ_E) and nuclear (θ_N) wavefunctions:[40]

$$|\psi(\boldsymbol{R}, \boldsymbol{Q})\rangle = |\Psi_E(\boldsymbol{R}, \boldsymbol{Q})\rangle|\theta_N(\boldsymbol{Q})\rangle \tag{2.6}$$

In Eq. 2.6 $\boldsymbol{R}$ is the vector coordinate that represents the positions of the different electrons in the molecule; i.e. it has 3N dimensions, where N is the total number of electrons. Likewise $\boldsymbol{Q}$ is the vector coordinate that represents the different nuclear positions of the molecule and has 3K dimensions, where K is the number of nuclei.

The separation of variables in the Born-Oppenheimer principle dramatically simplifies the complex problem of solving the Schrödinger equation for the energy levels of a molecular system, which is a process made in two stages.[40] In the first stage the electronic energy of a molecule is calculated for a given *stationary* nuclear configuration, i.e. the kinetic energy of the nuclei is ignored. The electronic energy E_E for the particular nuclear arrangement $\boldsymbol{Q_i}$ can be calculated by solving the Schrödinger equation:

$$[\widehat{H}_E(\boldsymbol{R}) + \widehat{H}_{NE}(\boldsymbol{R}, \boldsymbol{Q_i})]|\Psi_E(\boldsymbol{R}, \boldsymbol{Q_i})\rangle = E_E|\Psi_E(\boldsymbol{R}, \boldsymbol{Q_i})\rangle \qquad (2.7)$$

In Eq. 2.7 $\widehat{H}_E$ and $\widehat{H}_{NE}$ are the energy operators for the kinetic energy of the electrons and the electron-nuclear interactions respectively. By making small changes to the nuclear coordinate and repeatedly solving the Schrödinger equation at each new position the total electronic energy can be solved as a continuous function of the nuclear positions, $E_E(\boldsymbol{Q})$, which is known as the potential energy surface (PES) of a molecule.

In the second stage the motion of the nuclei is considered to occur within a potential defined by the PES, with the nuclear energy calculated by solving the Schrödinger equation:

$$[\widehat{H}_N + E_E(\boldsymbol{Q})]|\theta_N(\boldsymbol{Q})\rangle = [E_N + E_E(\boldsymbol{Q})]|\theta_N(\boldsymbol{Q})\rangle = E|\theta_N(\boldsymbol{Q})\rangle \qquad (2.8)$$

In Eq. 2.8 $\widehat{H}_N$ is the kinetic energy operator of the nuclei, with the total energy (E_{Total}) of the system the linear sum of the nuclear and electronic energies:

$$E_{Total} = E_N + E_E(\boldsymbol{Q}) \qquad (2.9)$$

A conjugated polymer can support many different types of molecular vibration, including stretch modes of the polymer backbone and the rotation of repeat units about the axis defined

by the backbone.[14, 39, 69-71] Each of these different types of vibration can be represented by a different nuclear wavefunction θ_N. It then follows that the total energy of a quantum state in a conjugated polymer is the linear sum of the electronic and vibrational energies.

2.5.2 The Franck-Condon principle

Due to strong electron-phonon coupling, when a conjugated polymer interacts with a photon of light both the electronic and nuclear degrees of freedom are simultaneously excited. Such excitation of the nuclear manifold can be equivalently thought of as an excitation of the vibrational modes of the polymer chain. This has a profound influence on the optical spectra of conjugated polymers. Consider an electronic transition from the S_0 ground state of a polymer to the S_1 excited state following the absorption of a photon. Working within the Born-Oppenheimer approximation and following on from Eq. 2.9, the energy required for this transition (ΔE) will be equal to the sum of the electronic energy gap to be surmounted in addition to an integer number of vibrational quanta of energy $\hbar\omega$:

$$\Delta E = \left(E_{S_1} - E_{S_0}\right) + n\hbar\omega \tag{2.10}$$

As a consequence, instead of just observing one transition in the absorption spectrum, corresponding to the electronic transition between the ground and excited states, a series of transitions are observed in which a vibrational mode of the polymer is excited in addition to the electronic transition. This can be observed as a progression of peaks in which the electronic transition is essentially repeated at different vibrational energies. This is shown in Fig. 2.13.
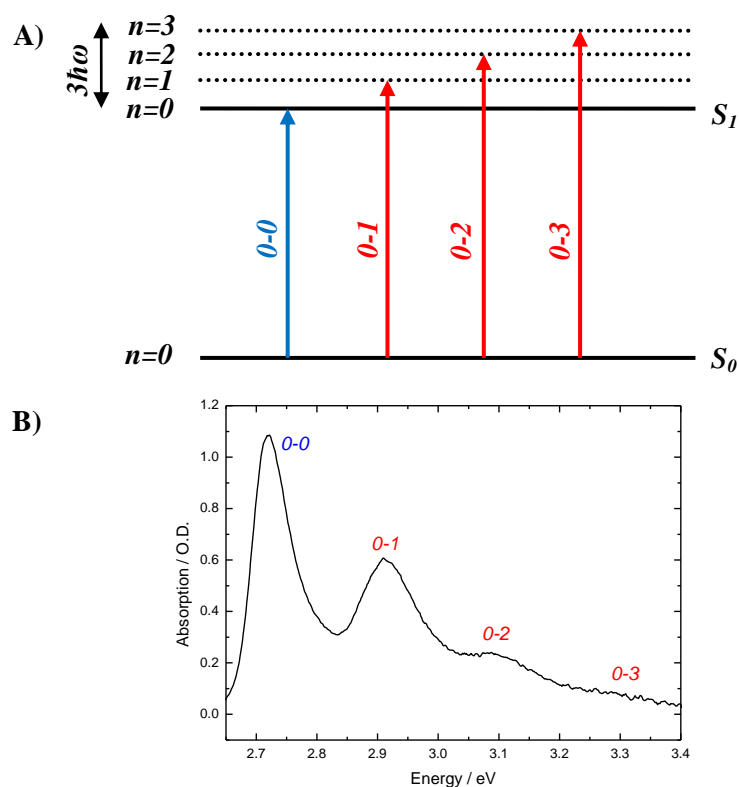
Figure 2.13: A) Simultaneous excitation of the electronic and vibrational degrees of freedom in a conjugated polymer. In addition to a single electronic transition from the S_0 to the S_1 state (blue line), three additional transitions involving one, two and three quanta of vibrations (red lines) are also possible. B) The absorption spectrum of ladder-type methyl-substituted poly(para-phenylene), in which the zero-phonon transition and three excited vibrational transitions of a carbon-carbon stretch mode[72] are observed.

It is clear from the absorption spectrum of the conjugated polymer shown in Fig 2.13B that the intensity of each vibronic replica is not constant. In order to understand the origin behind this behaviour it is necessary to return to the rate of optical transitions in a conjugated polymer as summarised in Eq. 2.2 and apply the Born-Oppenheimer separation of variables; the result is an expression involving two distinct terms:

$$\Gamma_{i,j} = \left[\frac{2\pi}{\hbar} \left|\left\langle \Psi_E^j(\boldsymbol{R},\boldsymbol{Q})\right|\widehat{H}'(\boldsymbol{R})\left|\Psi_E^i(\boldsymbol{R},\boldsymbol{Q})\right\rangle\right|^2 g(E_j)\right] \cdot \left|\left\langle \theta_N^j(\boldsymbol{Q})\right|\theta_N^i(\boldsymbol{Q})\right\rangle\right|^2 \qquad (2.11)$$

Note that the nuclear wavefunctions θ_N can be taken out of the perturbation matrix element as $\widehat{H}'$ is a function of the *electronic* distribution. As it can be clearly seen in Eq. 2.11, the probability of a transition occurring is determined not only by the overlap of the electronic wavefunctions of the initial (*i*) and final (*j*) states, but also by the overlap of the corresponding vibrational wavefunctions.

The vibrational wavefunctions $\theta_N(\boldsymbol{Q})$ of a molecular system can be calculated by solving Eq. 2.8. For both the ground and excited states of a conjugated polymer it is typical to expand the PES $E_E(\boldsymbol{Q})$ to the second order for small values of $\boldsymbol{Q}$, resulting in harmonic potential for which the nuclear wavefunctions can be easily solved for. It should be noted however that such an approximation is not always able to accurately reproduce experimental results. For example, it is necessary in polymers with torsional degrees of freedom to incorporate an additional anharmonic contribution into the PES. This is included in order to take into account the steric interaction between adjacent repeat units of a polymer when they are rotated with respect to one another.[39] This situation however will not be considered further.

The wavefunctions of a harmonic potential form a complete, orthonormal set. As a consequence one would initially expect to only observe the zero-phonon transition (0-0 as shown in Fig. 2.13) between the ground and excited states of a conjugated polymer, assuming of course all transitions in the ground state originated from the zero-phonon level. Any other transition would involve the overlap of orthogonal states, with the resulting overlap integral equal to zero.[73] This appears to directly contradict experimental observations (see Fig. 2.13B) in which multiple orders of a vibrational transition can be observed.

This observation can be reconciled with theory if the PES of the ground and excited states of a conjugated polymer are offset in conformational space. This difference would represent a reconfiguration of the chemical structure of the polymer chain in the excited state. As discussed briefly in section 2.3.1, the electron-phonon coupling in a conjugated polymer leads to the alteration of the polymer backbone around an excitation. This alteration results in an overall decrease in the energy of the system and typically involves the planarization of the polymer backbone and a stiffening of the chemical bonds.[38, 39, 71] An example of this process is shown in Fig. 2.14.

.

Ground state
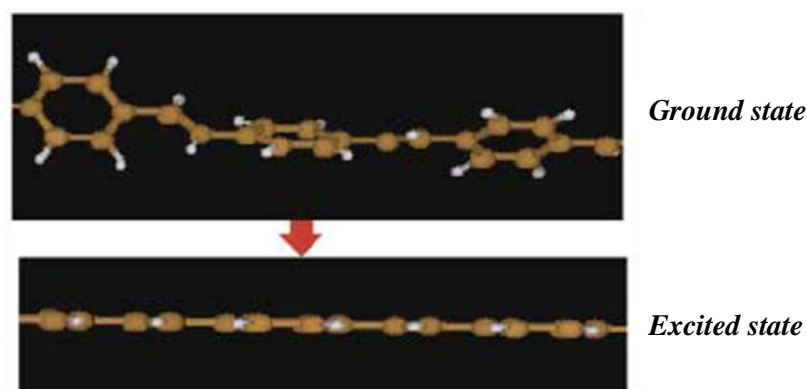
Excited state

Figure 2.14: Ground and excited state geometries of poly(p-phenylene-vinylene) oligomers, as simulated using quantum chemical methods. A planarization and stiffening of the chemical bonds is noted in the excited state. Figure adapted for use from Ref. [38].

It takes approximately 1 ps for the geometry of a molecule to change and adopt its new equilibrium configuration in the excited-state.[30, 58, 74] This time is much longer in comparison to the time required for the corresponding electronic transition, which occurs with a lifetime of the order of 10 fs.[58] Consequently any electronic transitions can be considered to occur instantaneously in comparison to the structural rearrangement. This is known as the Franck-Condon (FC) principle.

As a consequence of the offset in conformational space (formally defined by the vector $\Delta \boldsymbol{Q}$) between the ground and excited PESs, the vibrational wavefunctions of the ground and excited states no longer form one complete set together, but two independent complete sets. Vibrational wavefunction overlap is now possible for transitions originating from the zero-phonon level of the ground state to vibrational levels in the excited state, and vice versa. The weighting of these different transitions can be solved for quantitatively by calculating the squared integral overlap of the ground and excited state nuclear wavefunctions, as per the second term given in Eq. 2.11. The resulting series of transition intensities form a Poisson-like distribution:[69]

$$I_{0-n} = \frac{e^{-S} S^n}{n!} \quad with \quad S = \frac{\omega |\Delta \boldsymbol{Q}|^2}{2\hbar} \tag{2.12}$$

The intensity of a transition from the zero-phonon level to a vibrational level of energy $n\hbar\omega$ (where n is as before the number of excited vibrational quanta) is determined by the so-called Huang-Rhys (HR) factor (S); the series of transition intensities I_{0-n} are also referred to as the FC factors. The HR factor reveals important information regarding the restructure of the molecule in the excited state and can be measured by recording the ratio between the intensity of different vibronic transitions, as according to Eq. 2.13 below:

$$S = \sqrt[n]{\frac{n! \, I_{0-n}}{I_{0-0}}} \tag{2.13}$$

For $S > 1$ the FC intensity distribution has a maximum at an energy of $\hbar\omega S$ and a variance of $\hbar\omega S^{\frac{1}{2}}$. From this it can be shown that S is a measure of the number of quanta of vibrations (of energy $\hbar\omega$) lost in the excited state to chain relaxation, with accordingly $\hbar\omega S$ the lost energy.[69, 73] This lost energy is known as the Stokes Shift and is the reason behind the

characteristic offset in energy of the absorption and emission spectra of conjugated polymers. If a conjugated polymer supports more than one type of bond vibration, as is nearly always the case, then both the absorption and fluorescence spectra will consist of a superposition of contributions from different vibrational modes and the total Stokes Shift will be equal to the linear combination of the energy loss associated each mode, as according to the sum $\sum_i \hbar \omega_i S_i$.[73]

The FC principle as applied to the absorption and fluorescence spectrum of a conjugated polymer is illustrated in Fig. 2.15. Upon absorption of a photon an electronic transition occurs between the ground and excited states and is represented by a vertical line, as the time taken for the electronic transition to occur is much shorter than the required time for the nuclear rearrangement to finalise. In the excited state the exciton generated rapidly loses any excess energy, which is dissipated amongst the molecular vibrations of the polymer. This process is referred to as internal conversion[40] (see Fig. 2.10) and occurs on a timescale of 100 fs.[21, 75, 76] Given how quick this process is, it follows that all the excess vibrational energy will be lost before an exciton fluoresces with a lifetime of the order of 100 ps. It can thus be assumed that in the excited state all emissive transitions begin from the zero-phonon level, which is a concept known as Kasha's rule.[40] Under Kasha's rule there is now complete symmetry between the vibrational wavefunction overlap for absorption and fluorescence and the two appear as mirror images of one another. This is also demonstrated in Fig. 2.15.
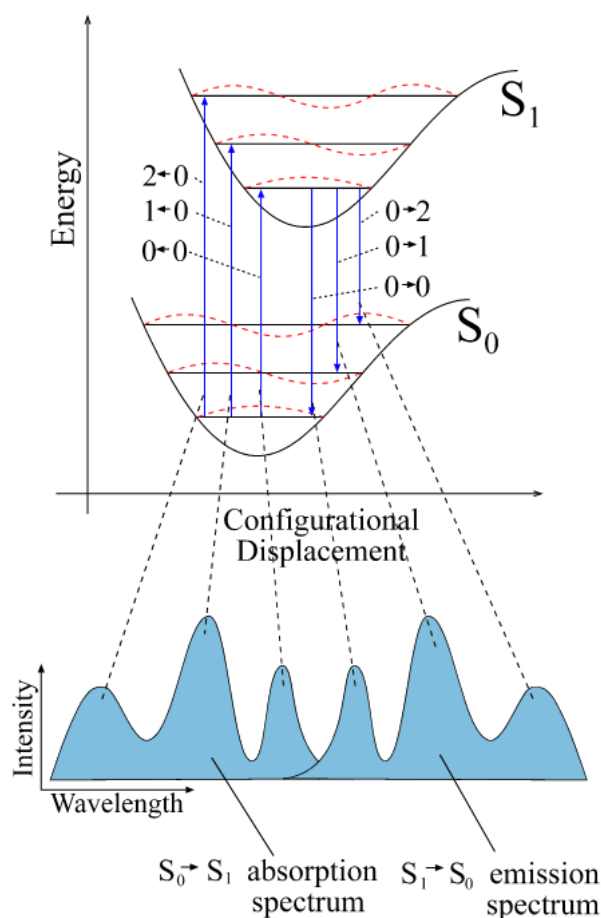
Figure 2.15: The FC principle applied to radiative transitions between the S_0 and S_1 energy levels of a conjugated polymer. Absorption transitions begin from the zero-phonon level of the ground state and occur to different vibrational levels in the excited state, with the intensity of each transition weighted by the wavefunction overlap of each level. Electronic transitions appear as vertical lines to reflect that the time required for a transition to occur is much shorter than the time for nuclear rearrangement in the excited state to be completed. After relaxing to the zero-phonon level of the excited state, emissive transitions occur to all levels in the ground state and the fluorescence spectrum of the polymer is the mirror image of the absorption spectrum. Image kindly provided by R. Thompson.

2.6   Excitation energy transfer and migration

Following the excitation of a chromophore, an exciton can move along the polymer chain on which it was created, or, if the polymer chains are packed sufficiently close to one another as in

the case of a film, between chains. This process is not limited to a single step; an exciton can continue to move between chromophores until it recombines and emits a photon of light, or until it encounters a 'trap' state such as a chemical defect or other charge-accepting moiety. This movement is known as exciton migration or diffusion. A single step in this process, in which an exciton transfers its energy from one chromophore to another, is known as excitation energy transfer (EET).[12] If EET occurs between chromophores on the same chain, then it is referred to as intrachain EET; if this process occurs between different polymer chains, then it is referred to as interchain EET. There are two primary mechanisms for EET in conjugated polymers which are reviewed below.

2.6.1 Förster resonant energy transfer

Förster resonant energy transfer (FRET) is a dipole-dipole interaction in which the excitation energy of an excited donor (D*) unit is transferred to an acceptor (A) unit through a resonance interaction:[58]

$$D^* + A \rightarrow D + A^* \tag{2.14}$$

While at a first glance this process may appear similar to the emission from the excited donor and the absorption of that energy by the acceptor, the mechanism behind FRET is completely different and does not involve an intermediate photon. FRET instead requires sufficient electronic coupling between the donor and acceptor, imparting a distance limitation to the energy transfer. Assuming that the donor-acceptor separation (R_{DA}) is much greater than the dipole moment of the respective states (referred to as the point-dipole approximation), then the rate (k_{ET}) of such a dipole-dipole process is expected to decrease inversely to the sixth power of the separation:

$$k_{ET} = \frac{1}{\tau_D}\left(\frac{R_0}{R_{DA}}\right)^6 \tag{2.15}$$

In Eq. 2.15 τ_D is the lifetime of the donor in the absence of energy transfer. R_0, the Förster radius, is the distance between donor and acceptor at which energy transfer to the acceptor and the natural decay of the donor occur with equal probabilities. It can be shown that R_0 is related to the spectral overlap between donor and acceptor and the relative orientation of their respective dipole moments, as according to Eq. 2.16 below:[58]

$$(R_0)^6 = \frac{9000\ln(10)\,\langle\kappa^2\rangle\Phi_D}{128\pi^5 n^4 N_A}\int_0^\infty f_d(\lambda)\epsilon_A(\lambda)\lambda^4 d\lambda \tag{2.16}$$

n: Refractive index of medium

Φ_D: Fluorescence quantum yield of donor

N_A: Avogadro's constant

There are two terms of note in Eq. 2.16. The first is the integral (often referred to as the 'J' factor), which quantifies the spectral overlap between the normalised (with respect to area) fluorescence spectrum of the donor $f_d(\lambda)$ and the molar absorption coefficient of the acceptor $\epsilon_A(\lambda)$. It should be stressed that $\epsilon_A(\lambda)$ is not normalised and thus the J factor is dependent on the magnitude of $\epsilon_A(\lambda)$. An example of how this quantity may be determined is shown in Fig. 2.16 for FRET between poly(9,9-diethylhexyl fluorine) (PF) and tetraphenyl porphyrin (TPP).

The second term of note in Eq. 2.16 is the orientation factor κ which is included to take into account the relative orientation of the dipoles of donor and acceptor with respect to one another. As the integral in Eq. 2.16 implicitly averages over all chromophores in a system it is

only possible to define an average orientation factor $<\kappa^2>$, which is equal to *2 / 3* for a random distribution of dipole moments.
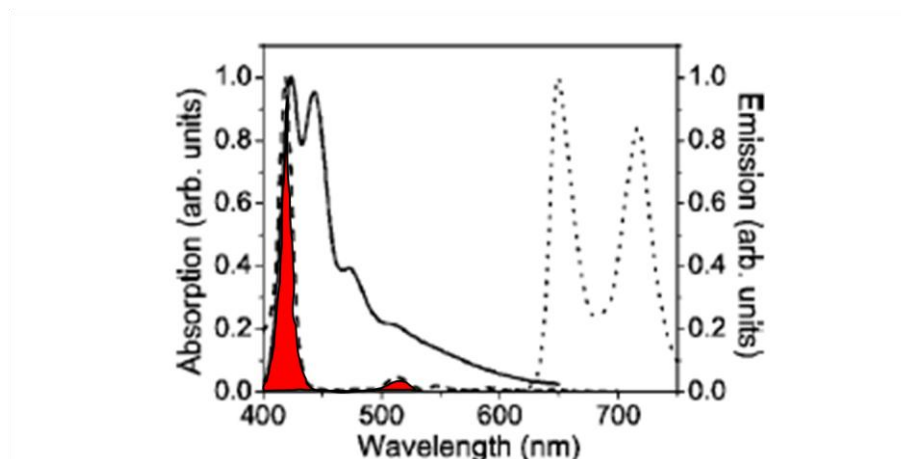
Figure 2.16: Spectral overlap (red area) between the normalised fluorescence spectrum of PF (solid line) and absorption spectrum of TPP (dotted line). This quantity can be used to calculate R_0, as according to Eq. 2.16. Figure adapted for use from Ref. [77].

As for a resonant process, the energy transfer in FRET must occur between degenerate donor and acceptor transitions. This does not however preclude FRET occurring from a high energy chromophore to a low energy chromophore. In these situations energy transfer will involve energy levels within the vibronic manifold of states. As demonstrated in Fig. 2.17, a transition to a low energy acceptor can be offset by excitation of the acceptor to an excited vibronic level.[78]

The framework of FRET is applied extensively to EET processes in conjugated polymers, as these systems possess strongly allowed optical transitions and a large spectral overlap between donor and acceptor. It should be noted however that in certain circumstances the application of FRET to EET in conjugated polymers has also been debated. The principal argument behind this, in certain systems, is that the size of the chromophores involved in the energy transfer are comparable to the inter-chromophore spacing, thus invalidating the point-dipole approximation

at the heart of the theory. Various approaches, such as the transition density approach and line-dipole approximation, have been developed to address this issue.[32] As an example, in recent work performed by Shaw *et al.* the rate of singlet-singlet annihilation in a β-phase polyfluorene film was measured and compared against the predictions of a model developed by the authors.[79] As will be discussed in section 2.6.6, the rate of annihilation is mediated by the properties of exciton migration and thus singlet-singlet annihilation can be used as a tool to study the properties of exciton migration.[80]
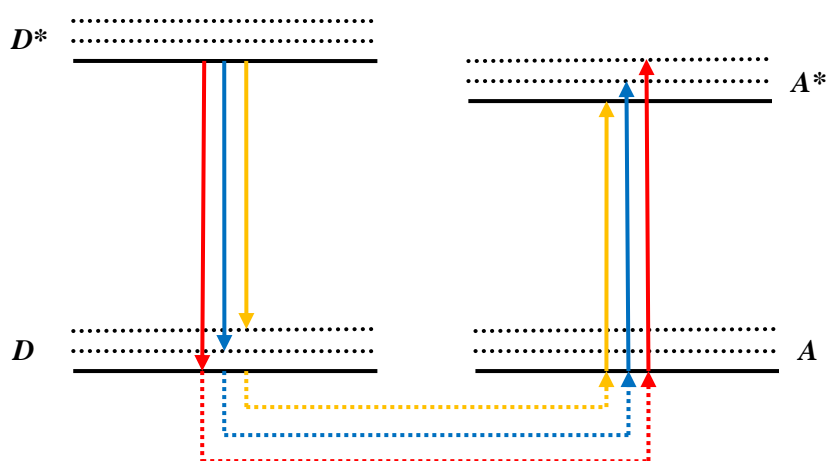
Figure 2.17: Förster resonant energy transfer between offset donor (D) and acceptor (A) states. Energy transfer between degenerate donor and acceptor states is made possible by using vibrational energy levels. Matching colour lines are indicative of the different possible coupled transitions that can occur. Figure adapted for use from Ref. [78].

Initial frameworks developed by Shaw *et al.* to describe singlet-singlet annihilation in β-phase polyfluorene incorporated FRET as the primary EET mechanism, but were however unable to accurately replicate experimental results. The β-phase of PFO is known to form a well-ordered structure in which the polymer chains are packed tightly together. Under these conditions the delocalisation of an exciton becomes comparable to the interchromophore spacing and the point-dipole approximation can no longer be applied to the system. In light of this fact, a

second model was instead developed in which exciton energy transfer was based on the line-dipole approximation. This model showed a marked improvement over the first and was able to accurately reproduce experimental data.

In cases in which optical transitions are forbidden, such as transitions involving triplet states and polaron hopping, FRET cannot under any approximation be applied to describe energy transfer, which must instead proceed through a separate mechanism.

2.6.2 Dexter energy transfer

Dexter energy transfer (DET) is a direct electron transfer process between donor and acceptor states mediated by the exchange interaction, in which the excited electron of the donor is exchanged for the ground-state electron of the acceptor.[81] This requires the electronic orbitals of the two species involved to be overlapping and as such is only active at very short distances; it thus can be thought of as a collision-type interaction. The transfer rate associated with this process follows an exponential dependence on the donor-acceptor separation (R_{DA}):[82]

$$k_{ET} = KJ\exp\left(-\frac{2R_{DA}}{L}\right) \tag{2.17}$$

In Eq. 2.17 L is the average van der Waals radius of the donor and acceptor orbitals and it is because of the size of this quantity that DET is only effective over very short distances. J retains its definition from section 2.6.1 above as the spectral overlap between the fluorescence of the donor and the absorption of the acceptor, but in DET the contribution of the donor absorption $\epsilon_A(\lambda)$ is normalised, i.e. J does not depend on the magnitude of $\epsilon_A(\lambda)$.

The K factor is included in Eq. 2.17 above to take into account the specific nature of the orbital interactions. For example, it is clear that the orbital overlap will not only depend on R but also

the relative orientation of the orbitals; orthogonal orbitals will not overlap and under these conditions $K = 0$. The role of orbital orientation has been studied in extended-chain systems, in which conjugated polymers have been dissolved in nematic liquid crystals.[83] In these systems it was found that the rate of intrachain EET, in which DET was assumed to be the dominant mechanism, was dependent on the chain conformation, with increased transfer rates occurring for the more extended systems, in which the orbital overlap between chromophores was greater.

2.6.3 Comparison of Förster and Dexter energy transfer
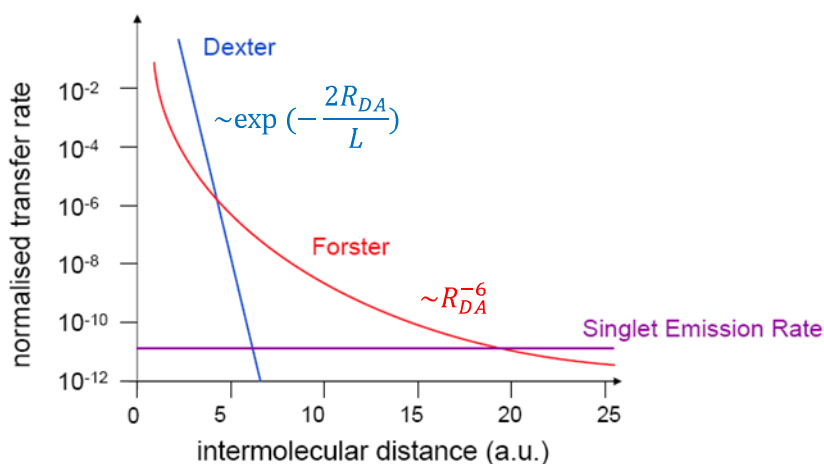
Figure 2.18: Comparison of FRET (red line) and DET (blue line) as a function of donor-acceptor distance. DET is found to be the dominant mechanism only at very short distances; FRET is dominant at longer distances. Image adapted for use from Ref. [27].

It is clear from the discussions of sections 2.6.1 and 2.6.2 that the mechanisms of DET and FRET differ in several key aspects. For example, each mechanism has a different dependence on the donor-acceptor separation R_{DA}. Whereas FRET is a long range interaction in which the

rate of EET decreases according to R_{DA}^{-6}, DET on the other hand is a short range interaction in which the rate of EET decreases according to $\exp{(-2R_{DA}/L)}$. A comparison of these different dependencies is made in Fig. 2.18. In a system in which both FRET and DET are possible, it is clear that at short distances DET is the more effective and wins out; at longer distances however FRET is the more dominant mechanism.

In addition FRET and DET both differ in terms of their dependence on the magnitude of the transition dipole moments of the donor and acceptor radiative transitions. Whereas FRET is based on a dipole-dipole interaction and can thus only occur in systems with large transition dipole moments, DET is mediated by the exchange interaction and is independent of the magnitude of the transition dipole moments. As a consequence FRET cannot be applied to describe EET in systems in which there is no allowed optical transitions, such as triplet EET, which instead proceeds through DET.[82] This should be distinguished from the fact that both FRET and DET depend on the spectral overlap between donor and acceptor, as quantified by the J factor.

There are other distinctions between FRET and DET. For example, as discussed in context of the J factor, FRET depends on the magnitude of the acceptor absorption coefficient, whereas DET does not. The rate of FRET can also be related to measurable quantities, such as the fluorescence quantum yield of the donor and the refractive index of the system at hand. The rate of DET on the other hand is instead mediated by the exchange interaction and cannot be directly related to an experimental quantity.

2.6.4 Dispersive and non-dispersive exciton migration

Having established the basic physical principles of EET, this section now considers how an exciton can move through a network of polymer chains using EET to 'hop' between

chromophores. The fundamental starting point in this discussion is the energetic distribution of available chromophores which an exciton can occupy, as expressed by the DOS of the polymer (section 2.3.2).

What migration pathways are open to an exciton will clearly depend on the number of nearby chromophores available to hop to and thus in turn the location of the exciton in the DOS. First consider a situation in which excitation is made well above the edge of the absorption band, corresponding to the excitation of the shortest chromophores in the system. As emission in a conjugated polymer is red-shifted with respect to the absorption, energy transfer via FRET is most favourable in a 'downhill' direction, i.e. in which there is a decrease in energy.[32] Some of these downhill chromophores will be sufficiently close to one another and have an orientation favourable for FRET, resulting in EET. At early times there are a large number of unoccupied sites to which an exciton can jump to and subsequently the downhill energy transfer is rapid, occurring within 1-10 ps. As the exciton moves to the lower energy chromophores in the DOS the number of possible hopping sites decreases and the rate of migration thus decreases in turn. This initial phase of migration, characterised by a time-dependent hopping rate, is referred to as dispersive migration.

After a short period of time an exciton will reach the lowest energy chromophores in the DOS. In this situation there is a very high probability that an adjacent chromophore will be occupied, and concordantly the rate of migration slows down dramatically as to that measured in the dispersive regime. Now migration between chromophores can still occur, but only because of thermal fluctuations and only to states very close in energy. In this regime the hopping rate is approximately constant and thus referred to as non-dispersive migration. Non-dispersive migration is heavily dependent on the polymer morphology and typically occurs on a timescale between 10 and 100 ps. In a ordered system, there will be a large number of polymer sites with a similar energy as the starting chromophore within the energy transfer radius, and thus the rate

of migration will be high. In a disordered system however these sites will be on average further away from the starting site and thus the rate of migration is reduced significantly.

Using these concepts it is now possible to address the observation that intrachain migration occurs on a longer timescale than interchain migration.[12, 32] Recent studies have shown that single step interchain and intrachain EET occur with similar rates.[32] The difference in the rates of migration can be attributed to the fact that there are a different number of available sites to transfer to in each mechanism. In a film the polymer chains can overlap with one another and a single polymer chain can be surrounded by many nearest neighbours.[84] As such there can be many more sites for an exciton to hop to that are on different chains, as compared to those on the same chain. Under these circumstances the probability for an exciton to move between chains is greater than the probability to move along the same chain and therefore the rate interchain migration is larger than that of intrachain migration.

2.6.5 Temperature dependence of exciton migration

It is clear from the discussion in section 2.6.4 that one of the primary factors that determines the rate of migration in a conjugated polymer is the total number of adjacent sites an exciton on a chromophore can hop to; an exciton has a greater probability to make a hop if there is more sites to which it can move to. The thermal energy in a conjugated polymer has a significant influence on this process by allowing an exciton to hop to a chromophore that is greater in energy than the site on which it begins. By allowing for these so-called 'uphill' hops in the polymer DOS an exciton has access to a larger number of potential hopping sites, resulting in an increase to the rate of migration. This concept is developed in greater detail below.

The rate $W_{i,f}$ at which an exciton can move between initial (i) and final (j) chromophore sites will be dependent on two terms.[85] The first term $\chi_{i,j}$ expresses the rate at which the

fundamental physical process of the hop occurs between chromophores and is determined by the relevant hopping mechanism; the second term reflects the Boltzmann probability for an uphill jump in energy to occur:

$$W_{i,j} = \chi_{i,j} P_{thermal}(E_i, E_j, T) \tag{2.18}$$

For singlet excitons hopping is typically thought to be mediated by the properties of FRET (section 2.6.1); hopping of triplet excitons proceeds using DET (section 2.6.2). It is also equally possible to incorporate a discussion of polaron hopping into this framework, which occurs through electron tunnelling.

$$\chi_{i,j} \propto \begin{cases} \left(\dfrac{R_0}{R_{i,j}}\right)^6 & singlet\ excitons \\ \exp\left(-\dfrac{2R_{i,j}}{L}\right) & triplet\ excitons \\ \exp\left(-2\gamma R_{i,j}\right) & polarons \end{cases} \tag{2.19}$$

For the rate of polaron hopping given in Eq. 2.19, γ is the so-called inverse localisation radius, which is related to the height of the energetic barrier through which tunnelling occurs.

The thermal probability of performing an uphill hop will be dependent on simple Boltzmann statistics; the probability of a downhill hop occurring is assumed to always be one:

$$P_{thermal}(E_i, E_j, T) = \begin{cases} 1\ if\ E_j < E_i \\ \exp\left(-\dfrac{(E_j - E_i)}{k_B T}\right)\ if\ E_j > E_i \end{cases} \tag{2.20}$$

As it can be seen in Eq. 2.20, at high temperatures there is a finite probability for an excitation of a conjugated polymer to hop to a chromophore that is higher in energy. This increases the total number of possible sites within a given radius to which an excitation can hop to.

Therefore after averaging over a large number of different states and hopping occurrences, the total rate of migration is found to increase at high temperatures. On the other hand at low temperature the probability of an uphill jump is negligible, reducing the number of hopping pathways and thus the total rate of migration.

The role of temperature is not limited to influencing the thermal probability of an uphill jump occurring through Boltzmann statistics. For example in the case of singlet exciton migration, it is clear that even if there is a finite thermal probability for an exciton to reach an adjacent chromophore of higher energy, the offset in energy between chromophores may be too great to facilitate sufficient spectral overlap between the absorption of the acceptor and the emission of the donor, as required for FRET. In this context the thermal properties of the distribution of chromophore energies, i.e. the polymer DOS, is equally important to the properties of migration. At high temperatures thermal fluctuations generate dynamic changes in the energetic landscape by changing the conformation of a polymer chain for short periods of time.[20, 30, 31] For example, the thermally activated torsional modes of a polymer chain may temporarily restore orbital overlap at a conjugation break, increasing the conjugation length and thus changing the corresponding chromophore energy. These modes may also equally destroy orbital overlap and generate new conjugation breaks. It can therefore be seen from the argument above that there will be a greater distribution of chromophore energies and therefore a greater probability for there to be an adjacent chromophore of the correct energy to which an exciton can hop to at high temperatures. Exciton migration under these circumstances is said to be thermally activated.[20]

Upon decreasing the temperature there will come a critical point at which there will be not enough thermal energy in the system to facilitate such dynamic changes within the polymer DOS. Consequently a turnover to a thermally non-activated migration regime can be noted for different polymers by changing the temperature.[18, 20] The temperature at which this occurs is

reflective of the amount of thermal energy required to infer changes within the polymer DOS and is dependent on the microstructure of the polymer at hand. In disordered systems such as polyfluorene, a large amount of energy is required to make the required changes and consequently a crossover to the non-activated regime is noted at high temperatures (200 K); for relatively well-ordered systems, such as ladder-type methyl-substituted poly(para-phenylene) (MeLPPP), this crossover occurs at a much lower temperature (80 K).[20]

It is clear from the discussion above that the concepts of conformational relaxation and non-dispersive migration are fundamentally related to one another, making it difficult to separate the two experimentally for most polymer systems.[86] Conformational relaxation involves a reduction in the energy of an exciton through the optimisation of the chain geometry in the excited state in response to the presence of the exciton. In order to distinguish between non-dispersive migration and conformational relaxation, a rigid polymer system, such as MeLPPP, can be used, in which double-bridging between adjacent phenyl groups along the polymer backbone prevents any significant degree of conformational relaxation.[87]

2.6.6 Singlet-singlet annihilation

Just in the same way it is possible for there to be a transfer of exciton energy between two chromophores, there can equally be a transfer of energy between two excitons. When this latter process involves two S_1 excitons, all of the energy of one exciton is given to the other which is excited into a higher energy level:[88-90]

$$S_1 + S_1 \rightarrow S_0 + S_N \qquad (2.21)$$

As one singlet exciton is essentially lost in this process, returning to the ground state, this energy transfer between excitons is referred to as singlet-singlet annihilation (SSA). The

physics of SSA are fundamentally no different from that of singlet EET; in this case both the donor and acceptor states are S_1 excitons.

Following on from the discussion of section 2.6.1, the rate of energy transfer between excitons will only be significant when two excitons come sufficiently close to one another as to interact. If after photoexcitation two excitons are not generated within the required distance for SSA, they must first migrate sufficiently close to one another. As such the properties of SSA are heavily dependent upon the excitation density. For example, after increasing the excitation density there will come a point when the average distance between excitons is small enough for them to interact immediately, allowing for a significant fraction of the S_1 population to undergo SSA. Measurements performed by King *et al.* have shown that this threshold density is of the order of $\sim 2 \times 10^{12}$ photons·cm^{-2} in the conjugated polymer polyfluorene.[88]

The S_N singlet state generated as a result of SSA has two possible pathways through which it can decay. The first is for the state to undergo rapid non-radiative decay and return to the S_1 level.[46, 50] The other possibility is for the S_N state to dissociate into a pair of polarons (P^+ and P^-):[52, 88, 90-92]

$$S_N \rightarrow (1 - \eta)(S_1 + heat) + \eta(P^+ + P^-)$$
(2.22)
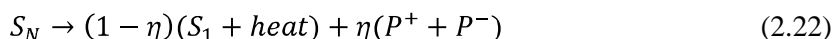
In Eq. 2.22 η is included as the branching ratio of polaron formation to non-radiative decay. SSA can therefore be used as a pathway to generate polarons in a conjugated polymer *without* the need of an electric field.

2.7   The photophysics of polymer/electron acceptor blends

Following photoexcitation in a conjugated polymer, the primary excitation that is formed is a neutral exciton in which an electron and hole are bound together. Thus in order to generate free charges in a conjugated polymer it is necessary to provide a mechanism which allows for the binding energy of the exciton to be overcome.   This concept was considered briefly in section 2.3.3. One example of such a mechanism is autoionization, whereby an excess thermal energy is used to separate the exciton. Two-photon processes are also capable of generating polarons, in which a photoexcited exciton interacts with and uses the energy of a second photon to dissociate. These mechanisms however are not efficient; for example, the branching ratio of polarons to excitons under direct one-photon photoexcitation is around 10% in film, although such a value depends strongly on the film nanomorphology.[64]

In order to make a photovoltaic device based on a conjugated polymer that can compete with the more established devices based on silicon, much higher yields of charge are required under one-photon photoexcitation conditions. To date, the most successful method used to achieve this is to introduce an electron-accepting moiety into the polymer network.[93-95]   The basic concept behind this method is that an exciton that reaches an interface between polymer and acceptor can dissociate as a result of electron transfer to the acceptor.   Internal charge generation efficiencies of up to 50% have been measured for blends of the polymer regio-regular   poly(3-hexylthiophene)   (RR-P3HT)   with   the   electron   acceptor [6,6]-phenyl-C_{61}-butyric acid methyl ester (PCBM), with corresponding photovoltaic devices based on this blend reaching external power-conversion efficiencies of just over 5%.[96]

Recent years have seen a significant research effort made into understanding the fundamental photophysics of charge generation in polymer/acceptor blends. New ideas are being generated at a rapid rate and even the most basic principles of charge generation in these systems have

come under scrutiny.[97, 98]   In this section a summary of the current and most commonly accepted photophysical model of charge generation in a polymer/electron acceptor blend is presented, following step-by-step the various processes that occur between the photoexcitation of a polymer up until the generation of free charges.

2.7.1 Electron transfer and charge-transfer states in polymer/acceptor blends

The basic principle behind charge generation in an organic photovoltaic system is the introduction of an electron-accepting element into the polymer which facilitates exciton dissociation. An exciton at an interface between polymer and acceptor can lose an electron, which undergoes electron transfer from the polymer to the acceptor. Rather than directly leading to the formation of a free polaron pair, the electron in the acceptor and the hole in the polymer remain partially correlated to one another at the interface as according to the coulomb attraction between the two. This lightly-bound state that exists across the interface is referred to as a charge-transfer (CT) state and is believed to be a key intermediate as part of the process of free charge generation.[93-95, 99]

The electron transfer which precedes the formation of the CT state is a quantum tunnelling process in which the electron of an exciton is able to reach the acceptor by overcoming the energetic barrier between the polymer and acceptor at the interface. Such a process, shown in Fig. 2.19, is driven by the energetic difference between the LUMO of the polymer and the LUMO of the acceptor. In order for electron transfer to occur with a high probability, the LUMO of the acceptor must be lower than that of the polymer. This generates a driving force which is sufficient to overcome the coulomb binding energy of the exciton.[100] As the binding energy of an exciton is typically ~0.5 eV, there is a minimum separation of 0.5 eV imposed on the LUMO separation for efficient charge transfer.[93] This does not imply however that

increasing the LUMO separation past this point increases the probability of electron-transfer further; indeed, studies have shown that intervals greater than the minimum value of 0.5 eV do not lead to an appreciable increase in the number of CT states formed.[93]
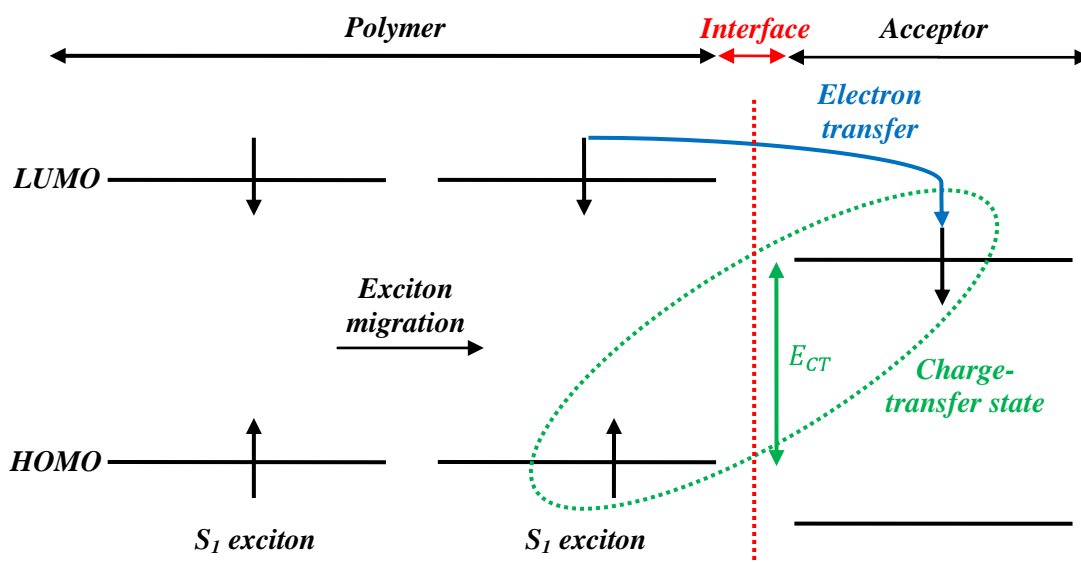
Figure 2.19: CT formation through electron-transfer: an exciton must reach a polymer/acceptor interface (by migration or otherwise) before it can undergo electron transfer between donor and acceptor. This results in the formation of a weakly bound CT state that exists at the interface.

On the basis that the CT state is only very weakly bound, the energy of the CT state is typically approximated to be the difference in energy between the LUMO of the acceptor and the HOMO of the polymer:

$$E_{CT} = E_{LUMO}^{Acceptor} - E_{HOMO}^{Polymer} \qquad (2.23)$$

The energy of the CT state is thought to be a critical parameter in determining the efficiency of polymer solar cells. Studies have shown that the open circuit voltage (V_{OC}) of a polymer solar cell, which in turn determines the power conversion efficiency of the cell,[93] is proportional to the energy difference between the HOMO of the donor and the LUMO of the acceptor, and

therefore E_{CT}.[93, 100, 101] It is therefore important when designing such a device not to choose materials in which the LUMO interval between donor and acceptor is too large, as this will reduce the efficiency of that device.

To develop as efficient a polymer solar cell as possible it is important for as many of the excitons that are generated in the polymer to reach an interface and form a CT state. As such it is crucial to maximise the interfacial area between polymer and acceptor. This can be achieved by mixing the two together to form a so-called bulk-heterojunction (BHJ) structure, which consists of a bi-continuous network of overlapping phases of polymer and acceptor (see Fig. 2.21).[93]

Recent studies of BHJ structures based on the conjugated polymer RR-P3HT and the electron acceptor PCBM have demonstrated a doping ratio of 50% by weight (wt%) to be the most efficient at generating a photocurrent in the blend.[102] Under such high doping regimes nearly all excitons are generated within range of an interface, leading to the rapid generation of CT states with near unity efficiency.[103] Interestingly this value was found to be less than the eutectic composition of the blend (65%) at which the interfacial area was maximised, indicating that the interfacial area alone, and therefore by extension the number of CT states formed in the blend, is not the sole determining influence on the photocurrent that can be obtained from such a system. This point will be discussed in more detail in the following section.

The rate-limiting step in CT generation is the migration of excitons to the polymer/acceptor interface; if an exciton is not generated sufficiently close to an interface it must migrate through the polymer until it reaches one.[104, 105] Exciton migration has been discussed at length in section 2.6 and typically occurs with a time period between the orders of 10 and 100 ps in a pristine film.[12] The time taken for an exciton to migrate to an interface in a blend of polymer and acceptor will depend on other factors; for example, in a BHJ device the concentration of

dopant and the respective size of the polymer/acceptor domains has been shown to have a significant influence.[106] For a 50% wt% doping ratio in a BHJ device the migration lifetime is typically of the order of 10 ps; the electron-transfer step is quicker than this by several orders of magnitude, occurring within 50 fs.[107]

The mechanism outlined above, in which exciton generation is considered a prerequisite of CT generation, was commonly accepted until recently, following research by Z.V. Vardeny *et al.* in which the quantum nature of the CT state was called into question.[97, 108] This work demonstrated that in a polymer/electron acceptor blend, CT states could be formed using photoexcitation below the energy gap of the polymer, i.e. without the need of S_1 excitons. In addition, absorption and electroabsorption measurements revealed the presence of a weakly absorbing state within the energy gap of the polymer, confirming a ground state transition associated with the CT state. This is a highly significant result, as it suggests that in such a system the electron acceptor interacts with the polymer to form a ground state charge-transfer complex, which has a separate set of orbitals and transitions.

2.7.2 Charge-transfer dissociation and charge generation

The fate of the CT state has a significant influence on the efficiency of charge generation in an organic photovoltaic system. There are three primary decay mechanisms of the CT state that have been identified in the literature to date. The first of these is for the CT state to recombine geminately; that is for the electron on the acceptor to recombine with its original hole in the polymer. This process has been measured to occur over a wide range of lifetimes, ranging from 300 ps in MeLPPP/PCBM blends[104] to 1ns in P3HT/PCBM blends.[99] The variance in the recombination lifetime has been attributed to the relative LUMO energies of the polymer and acceptor. If the separation between the LUMO levels is small, then the reverse transfer of the electron from the acceptor to the polymer can occur as part of a thermally assisted process (see

section 2.6.5). If however there is a large difference in energy then there will only be a small probability for the electron to make the required uphill step in energy, resulting in a longer CT lifetime. CT recombination contributes as a loss mechanism towards charge generation; clearly if there are fewer CT states at any given time then the possible number of free charges that can be formed will also be smaller. In order to prevent such a loss the energy levels of the polymer and acceptor must be chosen as to reduce the probability of back-transfer of electrons from the acceptor to the polymer.

Another potential loss mechanism of the CT is intersystem crossing within the CT manifold of states. CT states retain some degree of spin correlation and thus are classified as either singlet or triplet CT states according to the relevant spin orientations of the electron and hole, as in the case of excitons.[53] The exchange interaction also affects CT states in the same way as excitons; the triplet CT level is lower in energy than the singlet CT level. If the triplet level of the polymer is lower in energy than that of the triplet CT level, intersystem crossing within the CT manifold will result in triplet CT states which are then able to recombine geminately as triplet excitons.[93] This process is outlined in Fig. 2.20. The loss of CT states to triplet excitons presents another key design consideration for developing efficient charge generation in an organic solar cell; a polymer with a triplet level higher than the corresponding CT triplet level must be chosen.

The final and most important process which the CT state can undergo is dissociation, leading to the formation of free polarons in the polymer and acceptor. The fundamental principle of CT dissociation remains the same as exciton dissociation; in order for the electron and hole to be fully separated and become uncorrelated free polarons, the coulomb binding energy of the CT state must be overcome. As the binding energy of the CT state is less than that of an exciton, CT dissociation occurs with a higher probability than exciton dissociation. This is the basis for

using polymer/acceptor blends in polymer solar cells; it is much easier to generate charges in a conjugated polymer by using the CT state as an intermediate.

Separation of the CT state occurs through a process in which the electron hops away from the interface in the acceptor domain, with the hole moving away from the interface into the polymer.[94] As the electron and hole separation increases the small correlation that remains between the two decreases until a point is reached whereupon they can be considered to free polarons. The states that are formed as the electron and hole have moved apart from each other and the interface are referred to as charge-separated (CS) states.

The hopping mechanism by which the electron and hole move away from the interface is based on the same fundamental principle as outlined for polaron hopping in section 2.6.5 above, in which polarons move between transport sites through electron tunnelling. Unlike that discussion however in which the hopping of free polarons was considered, it is necessary when considering the dissociation of the CT state to include a contribution that takes into account any change in the coulomb energy of the electron-hole pair as they move apart from each other.[21]

The starting energy of the CT state will have a significant impact on the dissociation probability: a CT state with a large amount of excess energy will be able to use this energy to undergo rapid dissociation via local heating at the interface,[21, 94, 100] in a process similar in nature to autoionization as mentioned in the context of exciton dissociation. It is possible to generate CT states with varying degrees of excess energy by controlling the excess *exciton* energy. As the time taken for electron transfer to occur (45 fs)[107] is shorter than the time over which excess energy is dissipated as heat into the polymer (~100 fs),[21] any excess exciton energy is carried through into the CT manifold before it is lost. Recent studies have shown that CT states generated with excess energy can undergo near-instantaneous dissociation, leading to the rapid build up of polarons; on the other hand,[94] CT states with no excess energy have a very

small probability to dissociate and correspondingly a much longer lifetime.[97] A diagrammatic

summary of both these processes is given in Fig. 2.20.
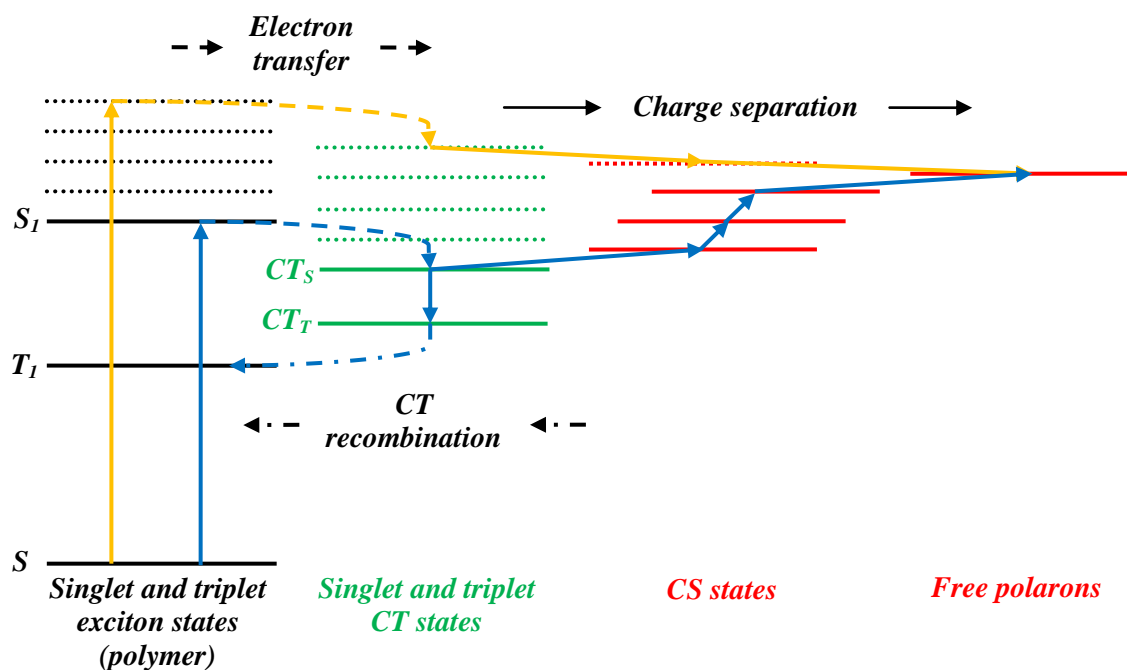
Figure 2.20: Pathways towards free polaron formation in a polymer/electron acceptor blend. 1) For excitation at the polymer energy gap (blue arrows), electron transfer to the acceptor results in a CT state being formed with no excess energy. Charge dissociation occurs relatively slowly through a series of thermally activated hopping steps in which the binding energy of the CT state is gradually overcome, eventually resulting in the formation of a free polaron pair. In addition, if the CT triplet level is higher in energy than the triplet level of the polymer, then intersystem crossing within the CT manifold of states followed by CT recombination and can lead to a loss of CT states. 2) For excitation above the polymer energy gap (orange arrows), electron transfer to the acceptor results in the formation of a highly excited CT state. The excess energy of this state can be used to facilitate rapid charge dissociation, resulting in the formation of free polarons.

The rate of CT dissociation can be aided by the presence of an external electric field. Although

such a concept does not exist naturally in polymer/acceptor blends, in photovoltaic device

architecture an internal electric field is setup by the potential difference between the electrodes

through which photocurrent collection occurs. The device architecture also has a significant

influence on the efficiency at which charges can be collected at the electrodes. In a BHJ device a percolating network of donor and acceptor phases, in which phase segregation occurs on a similar length scale to the diffusion length, facilities efficient charge extraction.[93, 102] Phase separation into large domains should be avoided, as the number of paths through which a charge can migrate to the electrodes is significantly reduced. By controlling the doping ratio of polymer to acceptor it is possible to generate different blend microstructures and thereby influence the charge generation efficiency.[102] As discussed however in section 2.7.1, any changes to the doping ratio may influence the formation dynamics of the CT state. It is therefore necessary to seek a balance between an efficient microstructure for charge transport and the yield of CT states that can be formed. It should be noted that similar alterations to the microstructure can also be made by thermally annealing samples, which has the effect of increasing the polymer and acceptor domain sizes.[93, 109]

The issue of charge transport can be dramatically simplified by using a bi-layer device architecture (shown in Fig. 2.21). In such a structure a layer of the electron acceptor is either spun or thermally evaporated on top of a polymer film, leading to effectively one interface between polymer and acceptor. Charge transport to the electrodes proceeds entirely in one continuous domain and therefore occurs with a higher mobility than that of charge transport in the more disordered BHJ structures.[95] This proceeds however at the expense of the number of CT states formed, as many excitons that are generated in the polymer will be too far away from the interface to form CT states and will recombine before they are able to undergo electron transfer. For this reason there has been a growing interest in designing bi-layer devices which utilise triplet excitons,[110, 111] on the basis that such states have a much longer lifetime and can thus migrate over a much longer length scale as compared to singlet excitons.[67]
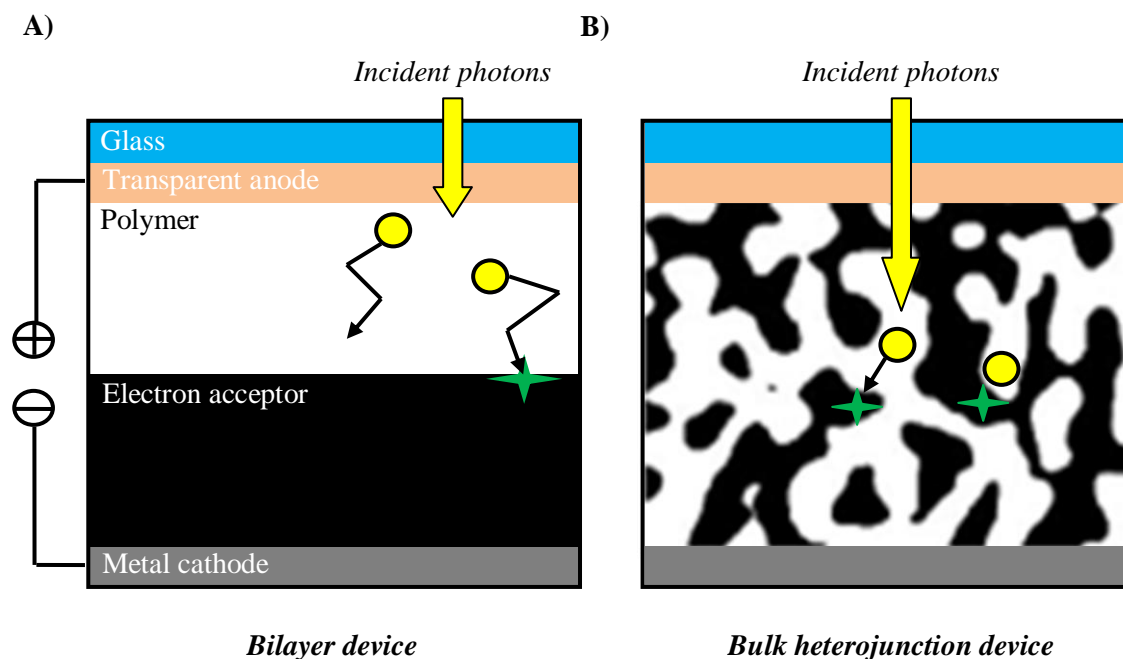
Figure 2.21: Comparison of (A) bi-layer and (B) BHJ organic solar cell structures. A) In a bi-layer structure excitons photogenerated in the polymer (white domains) must on average migrate a large distance to reach the interface with the electron acceptor (black domains) and form a CT state, with some excitons recombining before they are able to reach the interface. Following CT dissociation, charges migrate in continuous domains of polymer and acceptor and are collected at the electrodes. B) In a BHJ structure the polymer and acceptor are mixed together on a small length scale and consequently an exciton only has a small distance to migrate to reach an acceptor site. Following CT dissociation, charges migrate in a more disordered network of percolating domains of polymer and acceptor before being collected at the electrodes. Image of BHJ morphology adapted for use from Ref. [112].

Chapter 3   **Experimental methods**
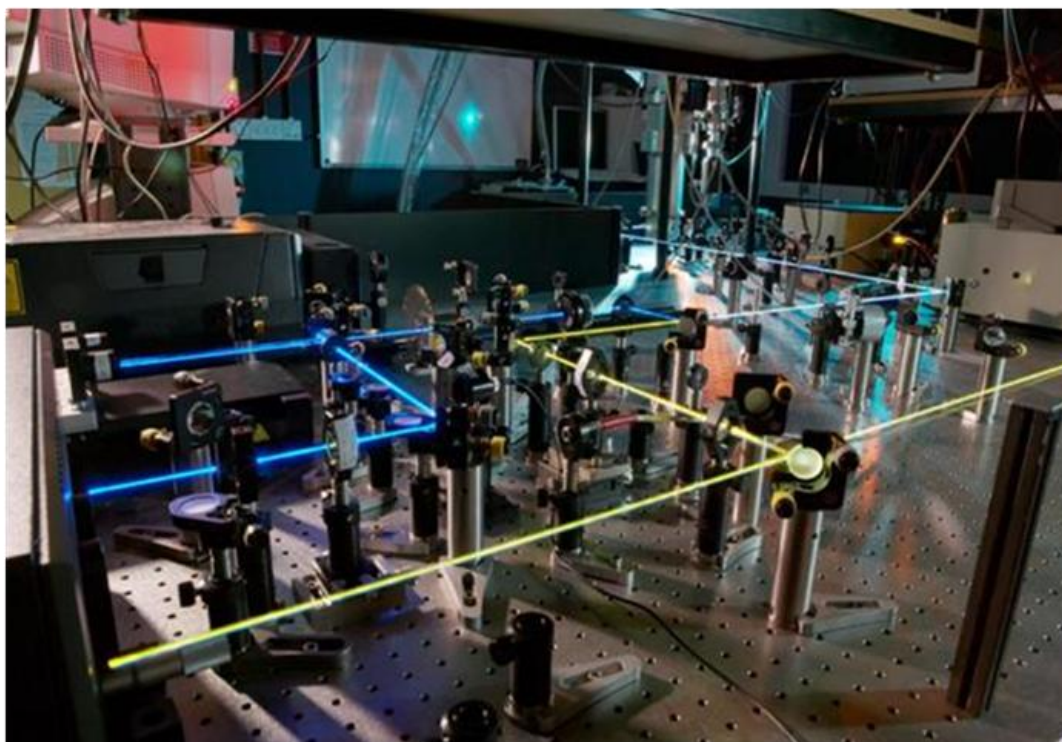
Figure 3.1: Photograph of the optical table for pump-probe spectroscopy measurements, including the ultraviolet and white light laser outputs of the opto-parametric amplifier (far left). Please note that this picture is no longer reflective of the current optical setup.

This chapter reviews the experimental methods used as part of the research described within this thesis. A significant fraction of this chapter dedicated to the principals and practical realisation of time-resolved laser spectroscopy in the femtosecond and picosecond regimes. A large amount of laboratory time has been devoted towards understanding and developing a high degree of competency with such systems and time-resolved laser spectroscopy forms a unifying link between all aspects of research outlined herein.

This chapter begins with a discussion of ultrafast laser systems, culminating in a description of the Ti:Sapphire laser oscillator. A discussion of the theory and practical realisation of both

femtosecond pump-probe spectroscopy and picosecond fluorescence spectroscopy follow. This chapter then concludes with a series of brief descriptions of other spectroscopic techniques and equipment used, followed by a discussion of polarised spectroscopy and details of sample preparation.

3.1 Conjugated polymers: the need for time-resolved spectroscopy

The principal excitations of conjugated polymers, singlet excitons, take part in dynamical processes which occur on very short time scales. These include thermalisation (~100 fs),[21, 75, 76] migration (1-100 ps)[18, 20, 32] and recombination (100-1000 ps).[20, 58] The extremely short duration of these processes is beyond the capability of ordinary gated electronic forms of detection. In order to measure a process occurring on the order of picoseconds, or indeed femtoseconds, it is necessary to seek other experimental methodologies. The most commonly utilised of these is time-resolved ultrafast laser spectroscopy, in which very short pulses of light can be used to probe the excitation dynamics of conjugated polymers.

Ultrafast laser spectroscopy is a broad field that encompasses various individual techniques. A unifying link between these techniques however is the nature of the laser system which generates the ultrafast pulses of light utilised in measurements. It is therefore of significant interest, before reviewing any of the specific details concerning the experimental methods performed in this study, to consider the theory and operation of a typical ultrafast laser system.

3.2 Generation of ultrafast laser pulses

From the basic theory of a laser source, it is known that the length of a laser cavity will place stringent restrictions on the frequency domain of its operation. Oscillation will only be

permitted on a discrete number of evenly spaced frequencies which constitute the longitudinal modes of the cavity:

$$\nu_q = \frac{qc}{2L} \equiv q.\Delta\nu \qquad (3.1)$$

q: An integer

c: Speed of light in the cavity

L: Cavity length

$\Delta\nu$: Mode spacing

When a laser operates, only those longitudinal modes for which the total cavity gain exceeds the total cavity losses will simultaneously oscillate. A standard continuous wave (CW) laser is therefore in the strictest sense of the word not a monochromatic source, nor is its output continuous with time; the output instead depends on the superposition of a number of different oscillating modes; this is considered with the use of Fourier transforms in Fig. 3.2.
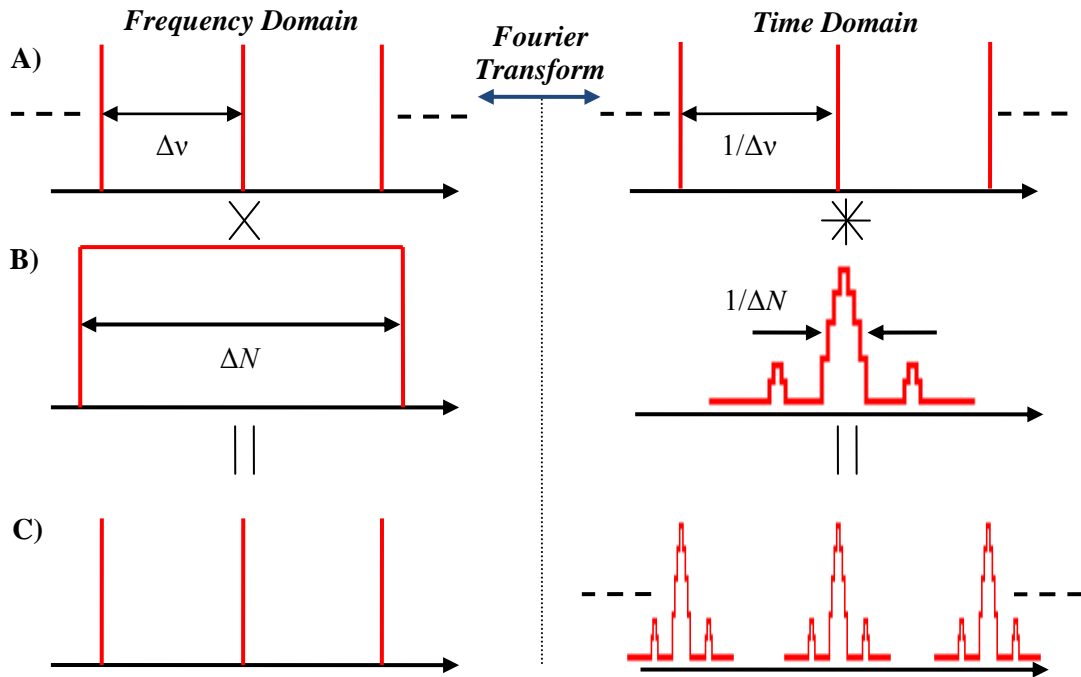
Figure 3.2: Fourier analysis of pulsed laser operation. A): The longitudinal modes of a laser cavity are represented by an infinite series of delta functions. The Fourier transform of this set is also an infinite series of delta functions, but with a temporal spacing that is the reciprocal of the frequency spacing. B): A finite number of the longitudinal modes for the cavity to oscillate on is selected by multiplying the delta functions with a hat function, whose width ΔN is equal to the number of selected modes (m) times the mode spacing (c/2L). The Fourier transform of a hat function is a *sinc* function, whose width is again the reciprocal of that in frequency space. C): The result in the time domain is the convolution of an infinite set of delta functions with a *sinc* function, resulting in a repeating train of pulses.

As it can be seen from Fig. 3.2, the resulting output from the superposition of a finite number of longitudinal modes in a laser cavity is a well established train of pulses. The width of a single pulse ($\Delta\tau$) is determined by the number of longitudinal modes (m) on which the cavity oscillates; the exact relationship between the pulse width and number of modes is stated here for use later on:

$$\Delta\tau = \frac{2L}{mc} \cdot K = \frac{K}{m\Delta v} \tag{3.2}$$

The nature of the numerical constant K is addressed below. Eq. 3.2 is an expression of the Fourier duality between time and frequency, in which the two are inversely proportional. The generalised relationship between the two is stated below in Eq. 3.3 and will be referred to again in this chapter. If the equality given in Eq. 3.3 applies then the relevant optical properties are said to be in the transform limit.

$$\Delta\tau\Delta\upsilon = K \tag{3.3}$$

For simplicity in the analysis of Fig. 3.2 a top-hat function has been used to select the longitudinal modes on which the cavity lazes on. Evaluation of the Fourier transform is readily performed and it can be shown that in this case $K = 1$. The choice of a top-hat function is clearly an approximation however, as in a real laser cavity not all longitudinal modes are selected to laze with the same intensity. The shape of the inhomogeneous gain curve of the gain medium instead determines the weighting at which the modes are selected, with typically a Gaussian or Lorentzian envelope chosen for this purpose. This leads to a different value of K (0.441 and 0.142 for the Gaussian and Lorentzian profiles respectively) in Eqs. 3.2 and 3.3.[23]

The time period (T) between pulses is determined by the reciprocal of the frequency spacing and is equal to the time taken for the pulse to make a single round trip in the cavity:

$$T = \frac{1}{\Delta\upsilon} = \frac{2L}{c} \tag{3.4}$$

Given this analysis above, a question remains to be asked: why don't all lasers operate in a pulsed regime? The answer to this arises in the nature of the phase relationship between the longitudinal modes of the cavity. In a CW laser, the modes have no fixed phase relationship to one another and as a result competition between the modes for amplification by the atoms of the gain medium results in large fluctuations and a noisy output. Using Fourier analysis, the

transform of a finite series of *randomly* phased delta functions is a CW level and noise. If there is a *fixed* phase relationship between the modes, the Fourier analysis proceeds as in Fig. 3.2 and the result is a train of pulses. It is therefore apparent that in order to move a laser into a pulsed regime, it is necessary for the phase relationship between the longitudinal modes of the cavity to be fixed. This process is known as mode-locking.

3.3   Mode-locking and the Ti:Sapphire laser oscillator

There are many possible ways to implement mode-locking in a laser cavity. Two of the most most commonly used methods are passive and active mode-locking.[23] Active mode-locking is based on the introduction of an actively controlled element into the laser cavity which modulates the amplitude of each longitudinal mode. Such a process is typically achieved by using an acousto-optical modulator to control the cavity losses by scattering light on and off of the optical path of the laser. This modulation introduces side-bands to every longitudinal mode. By tuning the frequency of the modulation to the mode spacing the side-bands are forced to overlap with the modes, resulting in a global locking of phases.

Passive mode-locking is based on using a saturable absorbing element in conjunction with the amplifying medium of the laser cavity.[23] Both the absorbing and amplifying elements are saturable in the sense that, at high intensities, their absorption and gain characteristics drop off hyperbolically to zero (no absorption) and one (no gain) respectively. This has important consequences for the passage of a short laser pulse. In each element only the front edge of the pulse is significantly modified; almost immediately after a pulse enters each medium, saturation will occur and the remainder of the pulse profile will be unaffected. Thus in the saturable absorber the leading edge of the pulse will be strongly absorbed, narrowing the pulse profile, and in the gain medium what remains of the leading edge will be strongly amplified. Consequently after many round trips through the cavity a single pulse will find itself narrowed

and amplified to a very strong maximum. This is the basis of passive mode-locking; one intense, short pulse profile will quickly rise to be dominant in the cavity and take all of the energy in the gain medium.

One of the most common applications of passive mode locking in an ultrafast laser system is the so-called colliding-pulse mode-locked dye laser.[23] In this system a ring cavity is used to support pulses which can travel in a clockwise or anti-clockwise direction. The saturable absorber in the cavity is chosen to saturate only when pulses travelling in opposite directions simultaneously enter the medium. As a consequence, these two pulses will be favoured at the expense of all others in the cavity, which will experience moderate losses due to the absorbing element; this corresponds to the onset of mode-locking in the cavity. In addition, a stationary wave is set up in the cavity as a consequence of the superposition of the clockwise and anti-clockwise pulses. This acts to transfer energy from one pulse into the other and vice versa, improving the mode-locking further.

The 1990s saw a dramatic advance in the field of ultrafast laser physics with the development of titanium-doped aluminium oxide ($Ti:Al_2O_3$/Ti:Sapphire) as a gain medium.[23] The Ti:Sapphire crystal is stable, possesses a wide absorption band in the blue-green part of the visible spectrum and lazes over a wide emission band between 650 and 1100 nm.[113] This broad absorption band allows the gain medium to be pumped by a wide range of sources, including solid-state diode lasers. Most importantly, the Ti:Sapphire crystal also exhibits the feature of self-mode-locking.

Self mode-locking, the ability of a cavity to mode-lock without any external intervention, is based around the Kerr lens effect and consequently is also sometimes referred to as Kerr lens mode-locking. The Kerr effect is a non-linear optical phenomenon accessed at high intensities in which the refractive index (n) of a medium is affected by the light passing through it:[23, 113]

$$n = n_0 + n_2 I \tag{3.5}$$

As a consequence of the Kerr effect, the response of the medium to the passage of a Gaussian transverse electromagnetic mode (TEM) will be effectively to act as a converging lens; this is known as the Kerr lens effect. In conjunction with a narrow slit placed at one end of the cavity, it is possible to accept the passage of high intensity states, as these can be focussed through the narrow slit, while at the same time reject the lower intensity ones. By introducing a series of pulses of different intensities into the cavity (usually achieved by rapidly vibrating a mirror or prism), the Kerr lens effect will allow the highest intensity pulse train to be singled out at the expense of all others; this is shown in Fig. 3.3. The effect of isolating a single pulse train in the cavity is the complete equivalent of mode-locking; high intensity pulses are favoured over the low intensity continuous regime.
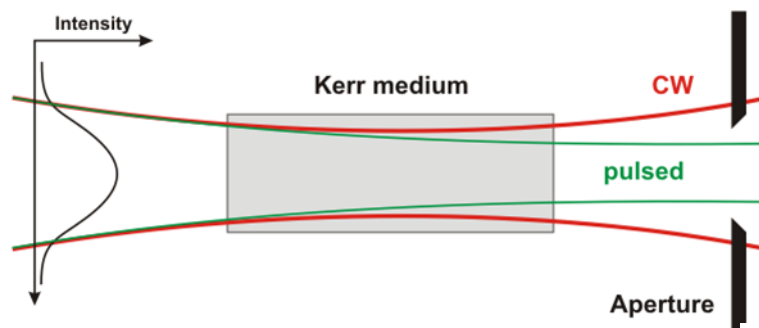
Figure 3.3: Kerr Lens effect and self mode locking in a Ti:Sapphire oscillator cavity. Whereas high intensity pulses are focussed by the gain medium through an aperture placed at one end of the laser cavity, low energy pulses are only weakly focussed and thus encounter large losses. Image released into the public domain by BoP.

As a consequence of the broad gain of the Ti:Sapphire crystal, a Ti:Sapphire oscillator is able to laze over a very large number of longitudinal modes. In conjunction with the self-mode locking feature of the cavity, such a system can produce optical pulses of the order of

picoseconds in duration.[113] These pulses are not transform limited however; in order to reduce the pulse duration to this limit, optics which compensate for the group velocity dispersion (GVD) of the pulse in the cavity must be incorporated.

GVD is an optical process which acts to temporally broaden a pulse of light during its passage through a transparent medium.[23, 113, 114] This arises from the fundamental fact that, for most common materials, the refractive index of a medium has a non-linear dependency on the frequency of light passing through it. As a consequence, different frequencies of light will travel with different speeds, leading to what is referred to as a 'chirped' pulse.[23] An example of a chirped pulse is shown in Fig. 3.4; for the pulse shown, red frequencies travel in the leading edge of the pulse, with blue frequencies in the tailing edge. Such a process disturbs the precise phase relationship between the different spectral components in an optical pulse and consequently increases the pulse duration away from the ideal transform-limited case.

In order to correct for GVD it is necessary to incorporate an optical setup which results in an effective negative GVD.[23] This can be achieved using a simple optical setup involving a pair of prisms, or equivalently a pair of diffraction gratings. By accurately controlling the optical path lengths of the different frequency components in a pulse, it is possible to bring these components back into phase and return the pulse to the transform limit; red frequencies are made to travel over a larger distance than blue ones, thus bringing these spectral components from the leading and tailing edges respectively back towards the pulse centre.
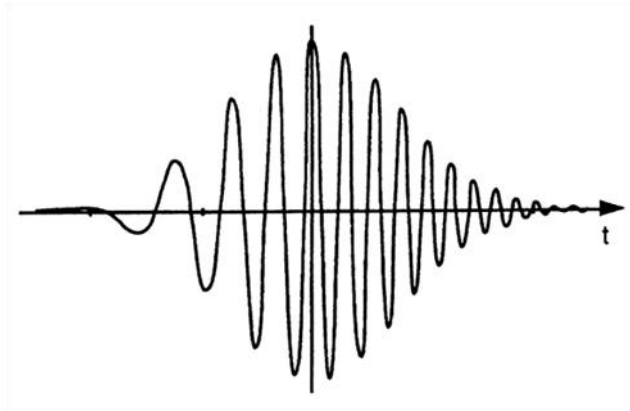
Figure 3.4: A chirped laser pulse, with red frequencies in the leading edge (t<0) and blue frequencies in the tailing edge (t>0). Figure adapted for use from Ref. [23].

The general model of laser oscillator used as part of this work for studies in both the femtosecond and picosecond regimes is a Coherent Mira 900 Laser. A schematic of the cavity is shown in Fig. 3.5. For operation in the femtosecond regime the cavity utilises mirrors M6 and M7, and prisms BP1 and BP2; operation in the picosecond regime excludes these optics, utilising the mirror M8 and a Gires Tournois etalon at position M9.[113] The Mira is pumped by a 5W Coherent Verdi V-5 laser. For femtosecond operation, the pair of prisms BP1 and BP2 are used to correct for GVD in the cavity, resulting in near-transform limited pulses of 150 fs in duration. A birefringent filter (BRF) allows for tuning of the lasing frequency across the Ti:Sapphire emission band from 700 to 1000 nm, although practical operation at the extremes of this range is complicated by low output intensities. In order to begin the mode-locking process an oscillating glass butterfly assembly is used to rapidly modulate the cavity length and introduce a series of pulses into the cavity; further oscillation of this assembly is no longer required after mode-locking has been achieved.

BP : Brewster prism
BRF : Birefringent filter
BS : Beamsplitter

L : Focusing lens
M : Mirror
TiAl$_2$O$_3$: Titanium:sapphire crystal
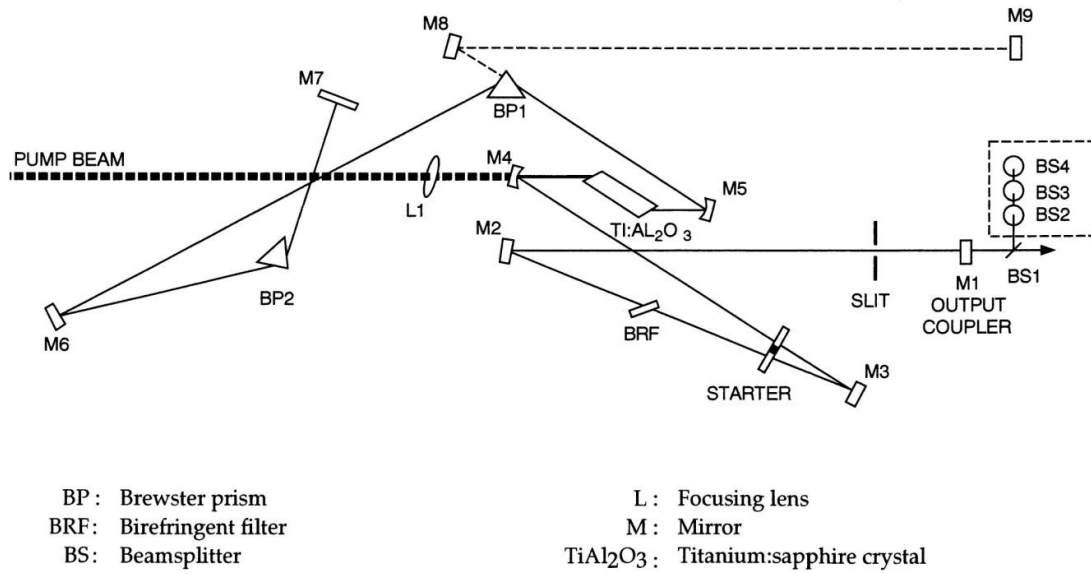
Figure 3.5: Schematic of the Coherent Mira 900-F cavity. Figure adapted for use from Ref. [113].

3.4   The laser amplifier

The Mira 900 running as a femtosecond oscillator (specifically classed as a Mira 900-F)
produces pulses of energy 6 nJ at a repetition rate of 76 MHz. This pulse energy is not
sufficient for most spectroscopic purposes and thus amplification is required. In these studies
this was achieved by the use of a Coherent RegA 9000 laser amplifier.[115] While maintaining
the pulse duration at ~180 fs, the amplifier increases the pulse energy to 5 µJ while reducing
the repetition rate to 100 kHz. A schematic of the amplifier cavity is shown in Fig. 3.6.

The amplifier consists of a second Ti:Sapphire cavity, pumped by a 10W Coherent Verdi V-10
laser, into which a single pulse from the femtosecond oscillator is fed using an acousto-optic
cavity dumper. This pulse is then allowed to pass up to 22 times through the excited
Ti:Sapphire crystal and build up energy before being ejected by the cavity dumper. The phase
and delay time of the injected and output pulses determines the output pulse energy and is
adjusted using a separate electronic control box. The initial seed pulse of 150 fs will undergo

significant temporal broadening in the cavity as a result of the GVD experienced over the course of ~20 round trips in the amplifier cavity. Therefore in order to reduce the pulse width back to the near-transform limit, four passes off of a simple grating compressor are employed.

IB:	Ion Beamsplitter	WX:	White-Light Crystal
IPD:	Injection Photodiode	M0 - M8:	Cavity Optics
EPD:	Ejection Photodiode	IM1-IM5:	Injection Optics
QS:	Q-Switch	CM1-CM3:	Compressor Optics
CD:	Cavity Dumper	WM1 - WM2:	Whitelight Optics
FI:	Faraday Isolator	L0 - L5:	Lenses
CP:	Cube Polarizer	P0 - P4:	Pump Optics
DG:	Diffraction Grating	TS:	Ti:Sapphire Crystal
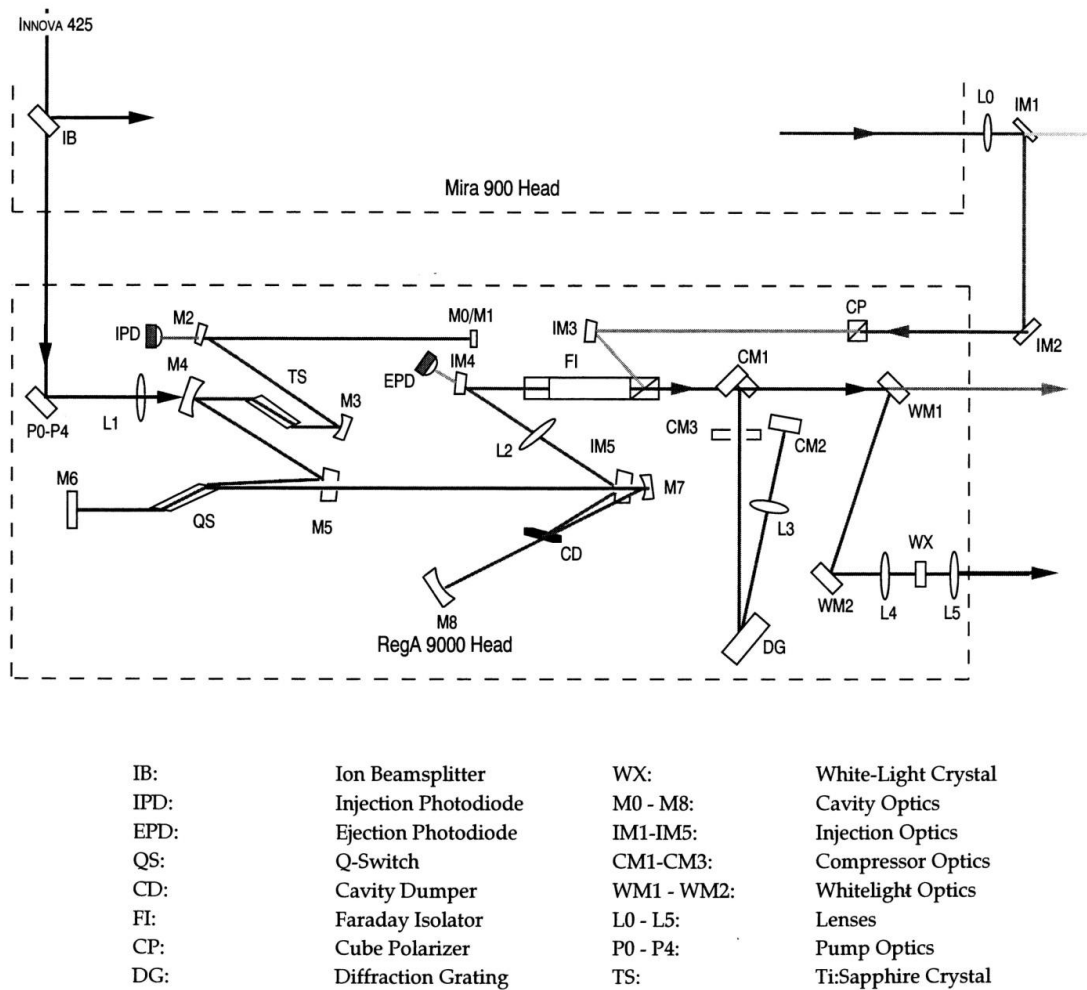
Figure 3.6: Schematic of the Coherent RegA amplifier cavity. Note that this schematic from the manufacturer includes one small error: the path M6-M7 does not travel through QS. Figure adapted for use from Ref. [115].

3.5   The opto-parametric amplifier

The output wavelength of the femtosecond oscillator can be tuned between 700 and 1000 nm; the laser amplifier works efficiently at a seed wavelength of ~780 nm. This is unsuitable for laser spectroscopy involving conjugated polymers, which typically peak in their absorption between 400 and 600 nm. As a consequence, an additional process is required to convert the 780 nm output from the amplifier to more convenient wavelengths. This can be achieved by the use of an Opto-Parametric Amplifier (OPA).
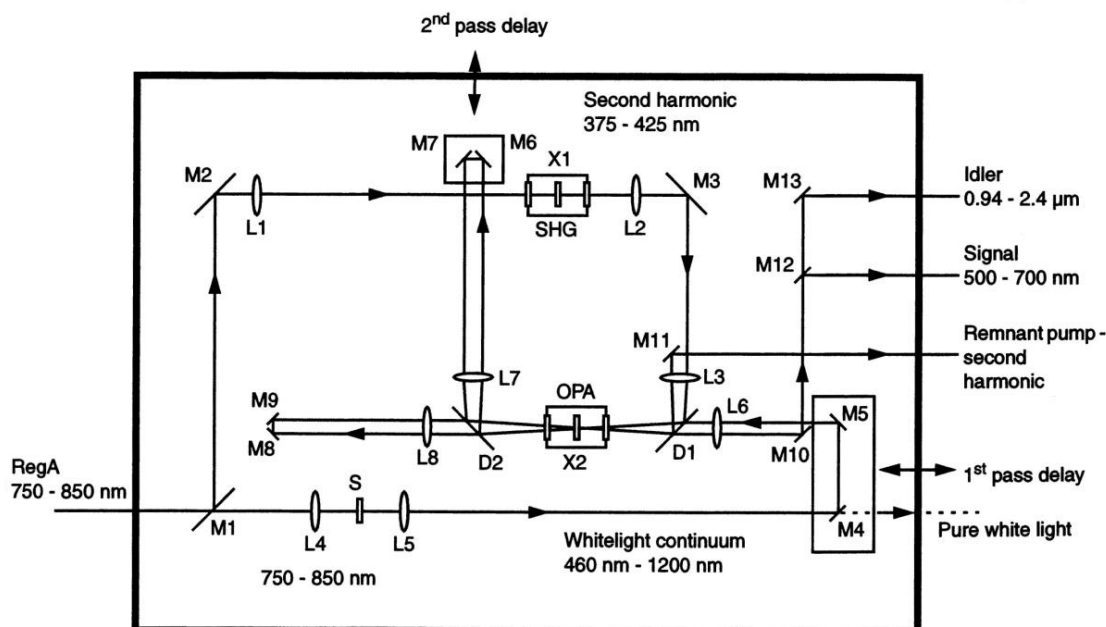
Figure 3.7: Schematic of the Coherent OPA-9400. Figure adapted for use from Ref. [116].

A Coherent OPA-9400 was used in these experiments, with the schematic of the OPA given in Fig. 3.7. The OPA utilises the high intensity of the femtosecond pulses produced by the laser amplifier in a variety of non-linear optical processes. The input from the oscillator is initially split, with 75% of the light undergoing frequency doubling to the ultraviolet (UV) in a second harmonic generator (SHG).[116] The remaining 25% is focussed into a Sapphire crystal (S, in

Fig. 3.7), which through the non-linear optical processes of self-phase-modulation (SPM) and GVD produces a white-light supercontinuum (WLSC) that ranges from approximately 440 to 970 nm. A sample spectrum of the WLSC is shown in Fig. 3.8.
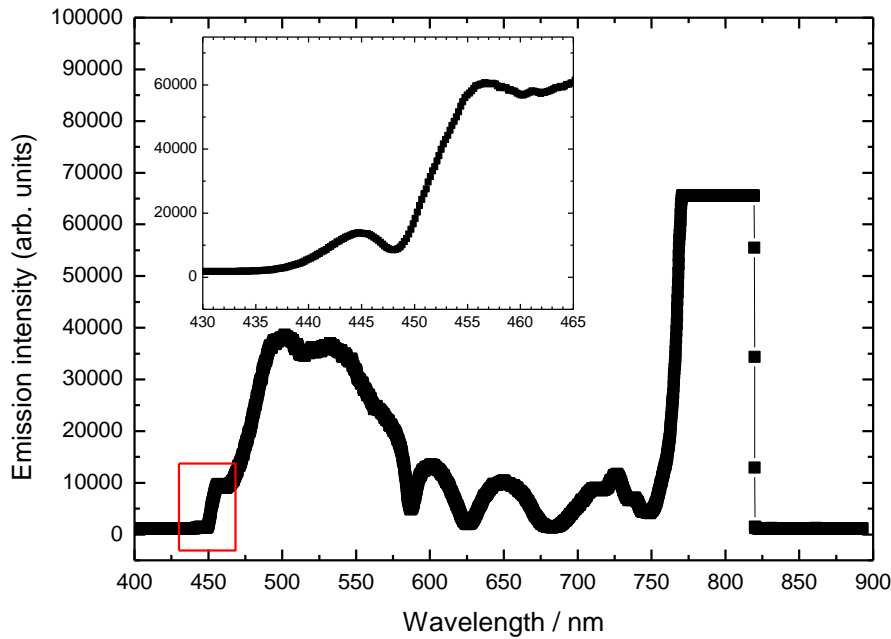
Figure 3.8: White-light supercontinuum output of the OPA, recorded using an Ocean Optics USB4000 spectrometer. The WLSC is very strong in the green (~525 nm) but weak in the red (700 nm) and deep blue (450 nm). It can also be seen that some output energies are unavailable (dips at ~626 and 689 nm). The spectrum also contains a significant fraction of remnant light from the laser amplifier which has saturated the detector response at ~780 nm. Inset: expansion of the low intensity region between 430 and 460 nm (red boxed region).

In order to understand the complete operation of the OPA it is first necessary to consider the process of SPM in more detail. SPM is an optical process which broadens an ultrafast pulse in the spectral regime.[116] Such a phenomenon arises as a result of the Kerr effect (Eq. 3.5) accessed at the high instantaneous intensities produced by the ultrafast pulses. In section 3.3 this effect was considered in the spatial domain, however the Kerr effect also has a significant

impact on the temporal profile of a pulse. Different parts of an ultrafast pulse will be subject to different refractive indexes; the peak of the pulse will experience the largest change, with the leading and trailing edges only experiencing a small change. This temporal modulation of the phase of the pulse leads to new frequencies being generated and the spectral profile of the pulse being broadened. It can be shown that, for a positive non-linear index of refraction, this process will result in a chirped pulse in a similar fashion to that discussed in context of GVD; red frequencies are generated in the leading edge of the pulse, with blue frequencies in the tailing edge. At a first consideration one might expect the spectral broadening associated with this process to lead to a shorter pulse, as according to the generalised Fourier relationship given in Eq. 3.3. SPM does not however result in a transform limited pulse and thus additional optics are required to reduce the pulse duration back to the transform limit.

The spectral chirp of the WLSC can be utilized in order to produce an amplified single-frequency output. This is achieved by mixing the WLSC and UV pulses together in a beta-barium-borate (BBO) crystal. A non-linear optical process, called opto-parametric amplification, occurs as the beams overlap. In this process a photon of UV light is lost in order to generate another photon of the same frequency as the WLSC output, thus amplifying that frequency component. In order to conserve energy, a second photon of much lower frequency is also generated. The amplified WLSC component is referred to as the 'signal' beam (SB), with the low energy remnant referred to as the 'idler' beam (IB). Energy conservation fixes a constraint on the frequency relationship between the UV, SB and IB photons:

$$\hbar\omega_{UV} = \hbar\omega_{SB} + \hbar\omega_{IB} \qquad (3.6)$$

Momentum must also be conserved throughout the process:

$$\hbar k_{UV} = \hbar k_{SB} + \hbar k_{IB} \qquad\qquad (3.7)$$

Frequency selectivity of the SB is possible by utilizing the chirp inherent in the WLSC and controlling the delay times between the UV and WLSC beams. By using micrometers which allow for very accurate control of the delay times, the UV pulse can be made to overlap with different temporal regions of the WLSC pulse. The conditions of energy and momentum conservation together also require for a global matching of phases between the different photons. This is achieved by rotating the BBO crystal to control the optical path of the photons.

In the OPA-9400 the UV and WLSC are made to overlap twice in the BBO crystal, resulting in the double amplification of the SB and a stronger output. The SB output can theoretically cover a significant portion of the visible WLSC spectrum (500-700 nm as specified by the manufacturer), with in turn the IB output covering a large range in the infrared (IR) (950-2400 nm). It is important to note that all of the processes described above are not 100% efficient; for example, some remnant 780 nm fundamental remains in the UV and SB and some UV is mixed into the SB.

It is clear that, in order to generate a strong SB output, there must be an adequate amount of light already present in the WLSC seed. As can be seen in Fig. 3.8 however, the WLSC has a non-uniform spectrum. As a consequence the SB output intensity varies as a function of wavelength, with operation at the extremities of this range complicated by very low light levels. By carefully aligning the optics of the OPA and with a stable and broad WLSC seed, it is possible with OPA used in these studies to extend the SB output down to 445 nm.

This section concludes the discussion of the theory and practical application of an ultrafast laser system. The following two sections consider how such a system can be applied in order to

perform time-resolved ultrafast spectroscopic measurements on femtosecond and picosecond timescales.

3.6   Pump-probe spectroscopy

3.6.1 Theory

Pump-probe spectroscopy is based around the use of two laser pulses to interact with a sample.[24] The first pulse, named pump, interacts with the ground state population of a sample to generate photoexcitations; the second pulse, named probe, interrogates those excitations. By controlling the delay between the pump and probe pulses it is possible to investigate how the excited-state population in a sample changes as a function of time. In this regard pump-probe spectroscopy is an excellent tool for investigating the excited-state dynamics of a conjugated polymer, as it not only provides the ability to measure population changes on femtosecond and picosecond timescales, but it also allows any excited state with an absorption transition to be probed, independent of whether such a state has a radiative decay or not.

The key concept on which pump-probe spectroscopy is based is that the amount of probe light transmitted through a sample (T) will change given the preceding interaction of the sample with the pump pulse. In typical experiments, the normalised differential transmission of the probe pulse is measured, which is defined in Eq. 3.8:

$$\frac{\Delta T}{T} \equiv \frac{T_{with\ pump} - T_{without\ pump}}{T_{without\ pump}} \tag{3.8}$$

The simplest interpretation of the physical significance of this quantity is based around population dynamics.[24] Consider a simple electronic system of M electronic levels; the

absorption coefficient ($\alpha(\omega)$) of the system is related to all of the possible transitions between

these levels:

$$\alpha(\omega) = \sum_{i,j}^{M} \sigma_{i,j}(\omega)[N_i - N_j] \tag{3.9}$$

$\sigma_{i,j}(\omega)$: Absorption cross-section for the transition between levels i and j

N_i: Population of level i

Within this formalism, the effect of the pump pulse is to change the population of the different

levels by instigating a transition from the ground state of the system to an excited state

($N \rightarrow N + \Delta N$), resulting in a change to the absorption coefficient ($\Delta\alpha$). Using the small signal

approximation of the Beer-Lambert law (Eq. 2.3), which relates the transmitted intensity to the

absorption coefficient:

$$\frac{\Delta T}{T} = -d\Delta\alpha \tag{3.10}$$

d: Sample thickness

the change in the measured quantity $\Delta T/T$ is:

$$\frac{\Delta T}{T} = -\sum_{i,j}^{M} \sigma_{i,j}(\omega)\Delta N_j d \tag{3.11}$$

By controlling the time delay between pump and probe pulses, it is possible to measure $\Delta T/T$

and hence the changing electronic populations ΔN_j as a function of time after excitation. An

example of the transient differential transmission dynamics of a conjugated polymer is shown in Fig. 3.9.
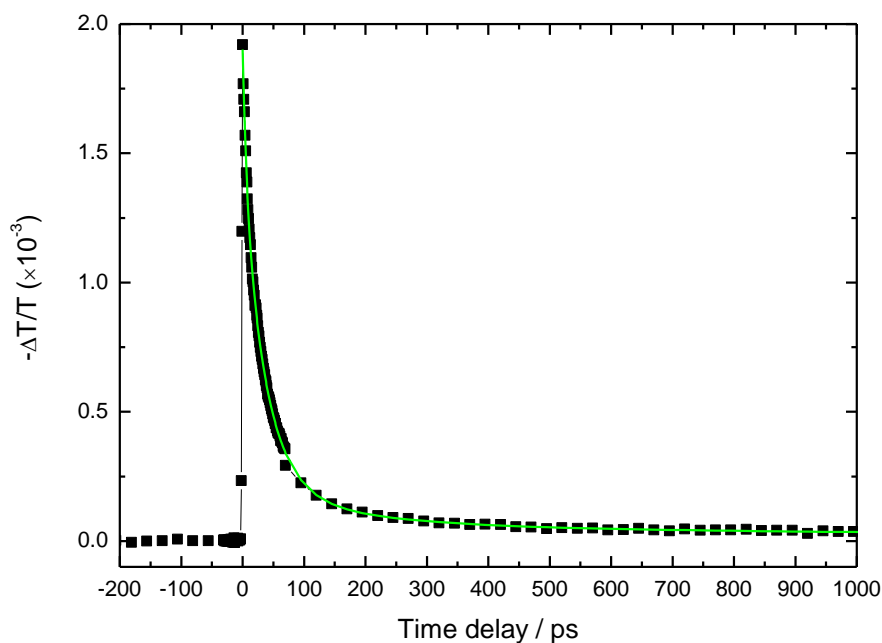
Figure 3.9: Transient differential transmission dynamics of methyl-substituted poly(para-phenylene), 390 nm excitation, 750 nm probe. In this situation the singlet excitons of the polymer are probed. As typical for the analysis of exciton dynamics, a tri-exponential decay fit (green line) has been applied to the data in order to measure the decay time constants.

There are in general three possible processes in pump-probe spectroscopy which are determined by the nature of the electronic population which the probe pulse interacts with; these are shown in Fig. 3.10. If the probe is absorbed by an excited state generated by the pump, then the process is referred to as photoinduced absorption (PA, see section 2.4.3 also) and $\Delta T/T$ is negative, as there is less transmission of the probe when the pump is active. It is possible to observe PA transitions corresponding to most of the primary excited states in a conjugated polymer. Indeed, one of the primary methods of characterising the population

dynamics of different excited states in a conjugated polymer is to measure the transient properties of the corresponding PA band, although this process can be complicated by the overlap of adjacent PA bands which are typically very broad.[106, 117]

If the probe pulse interacts with the ground state the process is referred to as photobleaching (PB). In this case the probe pulse has a smaller number of states to interact with, as most have been excited to a higher level due to the interaction of the sample with the pump. As a consequence the transmission of the probe is higher in the presence of the pump and $\Delta T/T$ is positive. The PB decay of a conjugated polymer simultaneously measures the recombination and subsequent return to the ground state of different excited states and is thus also often referred to as the PB recovery. By utilising the fact that the total number of states in the ground and excited levels is conserved, the PB can be thought of as an effective measure of the number of 'holes' in the ground state; as the ground-state recovers, due to exciton recombination or otherwise, the PB recovers. As a hole in the ground state may be equally associated with an exciton (singlet or triplet) or polaron, the PB recovery will contain dynamic contributions from multiple states. As such an analysis of the PB recovery can often prove complicated but can be used to obtain a significant amount of information concerning the excited-state dynamics of a conjugated polymer in a single experiment.[99, 118]

The probe pulse is also capable of generating stimulated emission (SE) from the excited state population; in this case the emitted photons count towards an effective increase in the probe transmission in the presence of the pump and $\Delta T/T$ is positive. Given that in such a process the probe pulse selectively interacts with the S_1 singlet exciton population, the SE decay is representative of the decay of the singlet exciton population.

S_N ————————   ————————   ————————

S_1 ————————   ————————   ————————

Photon out

S_0 ————————   ————————   ————————

Photoinduced absorption   **Photobleaching**   **Stimulated emission**
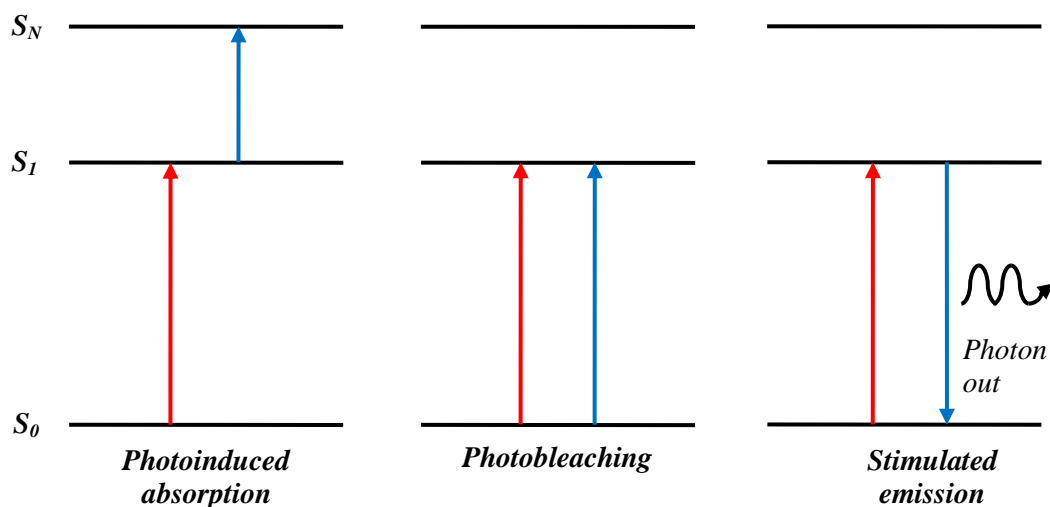
Figure 3.10: Possible processes in pump-probe spectroscopy. The red and blue arrows indicate the interaction of the pump and probe pulses respectively.

3.6.2 Practical implementation

Femtosecond pump-probe measurements were made using a conventional setup shown in Fig. 3.11. The optics can be conceptually separated into three sections; the generation of the pump and probe pulses, guiding optics that introduce a controllable delay between these pulses before focussing them onto a sample and finally the collection and detection of the probe pulse. These points are now considered separately in turn.

In sections 3.3 through 3.5 the three key components of the femtosecond laser system used in these experiments were discussed and as such they will not be considered in any further detail here. Pump and probe pulses were generated using the various outputs of the OPA, with many different combinations utilised. In the experiments detailed within this work only the UV and SB sources were used as a pump. Use of the UV as a pump was highly desirable, as the UV output is intense (~80mW at the OPA output) and free from significant power fluctuations. As

discussed above in section 3.5, the SB output has a non-linear response with frequency and requires a stable output from the amplifier and a good WLSC seed to operate efficiently.

The WLSC, SB and IB were all used individually as probes. By using the WLSC output the transient transmission spectrum (see below) of a conjugated polymer could be investigated in a single experiment for a range of pump-probe delays. For measurements of the differential transmission dynamics at a single frequency use of the SB (or IB when applicable) was desirable, as the sample is probed at one specific wavelength, rather than a range of wavelengths as in the case of the WLSC. Detection of one wavelength component in the WLSC was made possible by using a monochromator to filter out the selected component; the SB was however in most cases a more intense probe source, thus providing a larger signal-to-noise ratio (SNR) in the detected probe signal.

Femtosecond two colour pump probe spectrometer

A)

Mechanical chopper

Translation stage with retroreflector

RegA 9000

Mira 900

OPA 9400

Mira OPO

Monochromator with photodetector mounted at exit

Sample mounted in cryostat

Figure 3.11: A) Schematic of the optical table for two colour pump-probe spectroscopy, with UV (blue lines) pump and SB (green lines) or IB (red lines) probe. The probe beam is sent along a mechanical delay stage mounted with a retro-reflector. Both pump and probe beams are directed towards the sample, mounted in a cryostat, shown at the bottom left. After passing through the sample the probe beam is directed through a monochromator, with the intensity of the probe measured at the exit slit using a photodiode. Note that some of the equipment on the table (such as the Mira OPO) is used for other experiments.

Femtosecond white light pump probe spectrometer

B)

Mechanical chopper

Translation stage with retroreflector

RegA 9000

Verdi

Verdi

Mira 900

OPA 9400

Mira OPO

Sample mounted in cryostat

Monochromator with photodetector mounted at exit
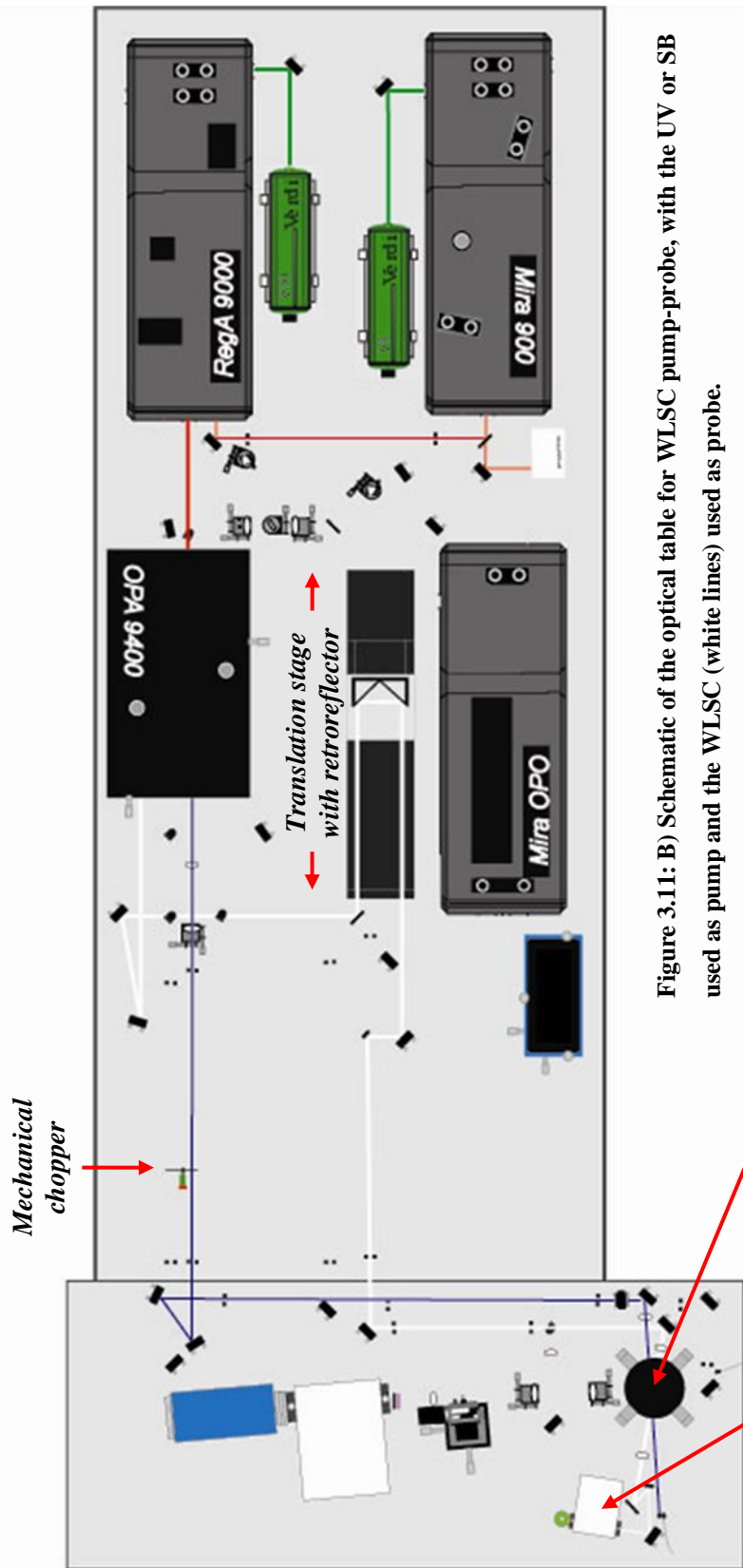
Figure 3.11: B) Schematic of the optical table for WLSC pump-probe, with the UV or SB used as pump and the WLSC (white lines) used as probe.

A schematic of the optical setup for pump-probe measurements, including the optical path of the pump and probe pulses, is given in Fig. 3.11. Pump pulses were directed towards the sample using a setup involving as few mirrors (UV-Visible, 95% reflectivity) as possible in order to maximise the available intensity at the sample position. The probe pulses were sent along optics that directed the beams off of a retro-reflector mounted on a motorised translation stage (Newport IMS-600). By adjusting the position of the retro-reflector on the translation stage it was possible to control the temporal delay between the pump and probe pulses. The translation stage had an effective temporal resolution of 3 fs[119] (the smallest possible step size supported by the stage was 1 µm) which was well below the pulse width of the system. It was important to ensure that the beams travelled exactly parallel to the stage alignment, as any other geometry would result in a spatial displacement of the beam while the stage was moving. This 'beam walking' was checked by viewing the beam in the far-field and moving the stage manually. Repeated corrections were then made until no movement was observed. To avoid the need to repeat this process in future experiments, the correct beam path was accurately marked with irises, with the orientation of the mirror directly before the translation stage fixed in place.

When applicable, polarisation optics were placed between the sample and translation stage. A variable $\lambda/4$ waveplate was fixed on the pump path, with individual linear polarisers applied to both pump and probe paths. With this equipment it was possible to orientate the pump and probe beams to be parallel and perpendicular to each other and thus measure the anisotropy of $\Delta T/T$ (see section 3.9).

Pump and probe beams were brought to a focus on the sample in a narrow-angle geometry ($\sim 20^0$). In order to ensure that the probe only interrogated the region of the sample under excitation by the pump, the probe spot was focussed to approximately one-third the size of the pump spot. Neutral density filters were mounted in both paths to allow for accurate control of

the power illuminating the sample. In situations when an increase to the maximum power density was required, the relevant lens position was translated to change the spot size directly.

Solid-state samples were mounted in a Cryomech closed-cycle Helium cryostat, allowing access to temperatures down to ~10 K. For all measurements samples were held under a dynamic vacuum (~10^{-3} mbar) in order to reduce the rate of sample degradation. The sample holder in the cryostat could be translated up and down, allowing access to a new region of a sample without having to significantly realign the pump-probe overlap. Solution samples were mounted in a custom-built sample holder placed directly beneath the cryostat.

After passing through the sample, the probe beam was collected using a lens and focussed on to the slit of a monochromator (Bentham M300). A tri-grating turret provided access to UV, visible and IR spectral regimes. After passing through the monochromator the probe was focussed on to an amplified silicon photodiode. The spectral resolution of the detection was determined by the entrance and exit slit widths on the monochromator. For a slit width of ~1mm a spectral resolution of ~5 nm could be achieved at the expense of low output intensity. For situations in which the transmitted light was below the threshold for detection, the exit slit of the monochromator was opened to ~7mm, resulting in a spectral resolution of ~15 nm.

In order to measure the differential transmission of the probe, the signal from the silicon photodiode was sent to a dual-phase lock-in amplifier (EG&G 7260) referenced to the frequency of an optical chopper placed along the pump path. This was designed such that the modulated (AC output) signal detected by the lock-in would be equal to the difference between the transmitted intensity of the probe with and without the pump ($T_{with\ pump} - T_{without\ pump}$). The total transmitted signal (DC output) could be approximated to be the transmission in the absence of the pump ($T_{without\ pump}$), assuming that the condition $T_{with\ pump} - T_{without\ pump} \ll T_{without\ pump}$ ($\Delta T/T \ll 1$) was met. This was indeed the case

for nearly all measurements made with this system, with $\Delta T/T$ typically of the order of 1×10^{-4} and maximum values never exceeding 1×10^{-2}. Most importantly, by using lock-in based detection in conjunction with a high pulse repetition rate, detection of values $\Delta T/T$ as small as 6×10^{-5} was possible, based on a noise level of $\pm 2 \times 10^{-5}$. By increasing the transmitted light intensity it was possible to decrease the noise level to $\pm 1 \times 10^{-5}$, although under these circumstances it was important not to saturate the detector response. It should be noted at this point that the silicon photodiode used in these experiments had a non-uniform spectral response, which is discussed in more detail in section 3.8.1. By measuring the normalised differential transmission this response could be ignored.

The temporal resolution of a pump-probe system is governed by the pulse width at the point of overlap between the pump and probe pulses. As described above (section 3.4), the laser amplifier produced ~180 fs pulses as measured at the exit of the amplifier. These pulses would undergo various broadening mechanisms, activated in turn by the non-linear optics associated with the OPA (section 3.5) and the alignment and focussing optics of the pump and probe paths. The final time resolution, as measured at the point of overlap, was measured by the previous operator of the system using cross-correlation methods and found to be ~500 fs.[120]

In order to accurately overlap the pump and probes spots on the sample and thus maximise the measured differential transmission, the translation stage was sent to the known zero pump-probe delay time of the setup being used. Fine adjustments were then made to the pump alignment on the sample while simultaneously measuring and attempting to maximise the AC output of the lock-in. In situations where the zero-delay time was not accurately known, a standard sample was used (one in which it was known that a strong signal could be detected) and the beams aligned by eye. The translation stage could then be scanned and the signal response from the lock-in monitored in order to find the zero-delay time. The alignment procedure to maximise the lock-in signal was required frequently, as any slight change made in

the optics of the experiment, for example changing sample position or beam polarisation, resulted in a change, often substantial, to the maximum differential transmission.

In order to make comparative measurements of the output it was necessary to ensure that the differential transmission was maximised before every experiment. Sample degradation was a frequently encountered problem in this regard, as exposure to a high-intensity pump source over a prolonged period of time, even that associated with the course of a single measurement, would remove some of the polymer from the film. This would change the intensity of signal measured. To minimise the cumulative effect of this process the excitation position was changed between measurements by translating the sample position up and down. With such a process it was necessary to excite a new sample region equivalent to that used previously and as such it was important to ensure that any films measured were completely homogeneous.

There are some key issues which arise concerning the detection system detailed above. For example, with such a setup it is important to ensure that the probe intensity is always much less than the pump intensity. If the excitation density generated by the probe is larger than that of the pump then not all of the probe photons can interact with the excited states generated by the pump. Those photons that do not interact cannot contribute to ΔT, which becomes saturated, but do however contribute to T and $\Delta T/T$ begins to approach zero. These conditions were avoided by controlling the probe intensity with a neutral density filter. This however was often not possible when using the WLSC as a probe, as reducing the intensity of the probe would result in the intensity at some wavelengths becoming too low as to be detected. Under such circumstances it was often necessary to reject large sections of data obtained, particularly around 780 nm due to residual light from the fundamental of the laser amplifier.

There are two primary types of measurement which were performed with the system detailed above. The first was to fix the detection wavelength by moving the monochromator to a

desired point and then monitor $\Delta T/T$ from the lock-in amplifier as the translation stage was moved. This allowed for the population dynamics at a single wavelength to be measured as a function of time (see Fig. 3.9). By utilising the full length of the translation stage a maximum pump-probe delay period of ~4 ns was achievable; the minimum time period was typically chosen to be 250 fs.

The second primary type of measurement performed was to fix the delay time and scan the monochromator, thus producing $\Delta T/T$ as a function of wavelength. By changing the delay time and repeating this process it was possible to produce the so-called transient transmission spectrum of a sample. It should be noted that as part of this process it was necessary to correct for the spectral chirp in the WLSC; such calculations were performed by the previous operator of the system.[120]

To perform both sets of measurements, custom-build Labview programs were employed to control the monochromator and translation stage while simultaneously measuring the output from the lock-in amplifier. Analysis of lifetime components present in the transient pump-probe data was performed by fitting the data to a multi-exponential model using in-built non-linear least squares fitting routines (based on the Levenberg-Marquardt algorithm) included as part of the data analysis and graphing software package OriginLab Origin 8.0.

3.6.3 Context

There are two areas of research described in this thesis in which pump-probe spectroscopy has been extensively used. Chapter 6 details a study in which interchain exciton formation has been recorded in films of ladder-type methyl-substituted poly(para-phenylene) (MeLPPP). In this study pump-probe spectroscopy proved an ideal tool to both identify the nature of an unidentified excited-state in a conjugated polymer and characterise its dynamics. Furthermore,

using the addition of polarisers a significant amount of information regarding the orientation of the aforementioned excitation could also be gained from the measurement process.

Chapter 7 details an extensive study of the PA dynamics of excitons and polarons in a typical solar cell blend. Pump-probe spectroscopy is based on absorption, rather than emission, and is therefore not as limited in what states it can probe as compared to fluorescence spectroscopy. This is vital in a solar cell system in which understanding the properties of the polaron state, which does not have an emissive transition, is key. Furthermore many of the dynamical processes in such a system occur on a sub-picosecond timescale, which can only be accurately accessed by pump-probe spectroscopy.

3.7 Picosecond time-resolved fluorescence spectroscopy

3.7.1 Theory

The study of fluorescence from conjugated polymers provides a significant amount of information concerning the properties of the singlet exciton state, which is the principal excitation of such systems. The radiative recombination of the exciton occurs with a lifetime typically of the order of 100 ps[18, 20] and as such specialised techniques are required to directly monitor this process as a function of time. Despite the many advantages of pump-probe spectroscopy outlined in section 3.6 above, it is often not possible in such experiments to accurately isolate the fluorescence lifetime of the singlet excitons. For example, the PA dynamics of the S_1 excitons in a conjugated polymer will not only be determined by the fluorescence lifetime, but may also involve components from bi-excitonic processes such as singlet-singlet annihilation which can often dominate the decay of the singlet population and obscure the fluorescence dynamics. The PA bands of a conjugated polymer are also broad and overlap with one another, meaning that it is possible to have multiple contributions from

different excited states at a single probe wavelength, making it difficult to accurately identify the fluorescence lifetime from amongst other components. Under such circumstances other ultrafast spectroscopic measurements are required to measure the fluorescence directly as a function of time.

Two principal methods exist for measuring time-resolved fluorescence on a picosecond timescale; time-correlated single-photon counting and streak camera detection. Both methods have their respective advantages and disadvantages concerning their use; these studies have focussed on the use of the latter method. A streak camera detector is a specialised piece of laboratory equipment that allows for direct measurement of fluorescence simultaneously as a function of both wavelength and time. As such it is of particular use when wishing to measure processes such as energy transfer and exciton migration (section 2.6).

In a streak camera detector, a basic schematic of which is given in Fig. 3.12, incident photons are focussed on to a photocathode array, which converts the photons into electrons.[121] These electrons are accelerated by a pair of electrodes towards a microchannel plate (MCP). Before they reach this array however they are subjected to the influence of a dynamic electric field which acts vertically. This field rapidly increases in magnitude with time and is used to deflect the electrons according to the time at which they are created at the photocathode array, as two electrons which arrive at different times will experience dramatically different fields. In order to calibrate the timing of this sweeping field with the arrival of the photons and the subsequent generation of electrons at the photocathode array, a small fraction of the excitation source is focussed on to a high-speed photodiode in order to generate a trigger pulse. This pulse is fed into a separate control unit, which in turn controls the timing of the sweep voltage.
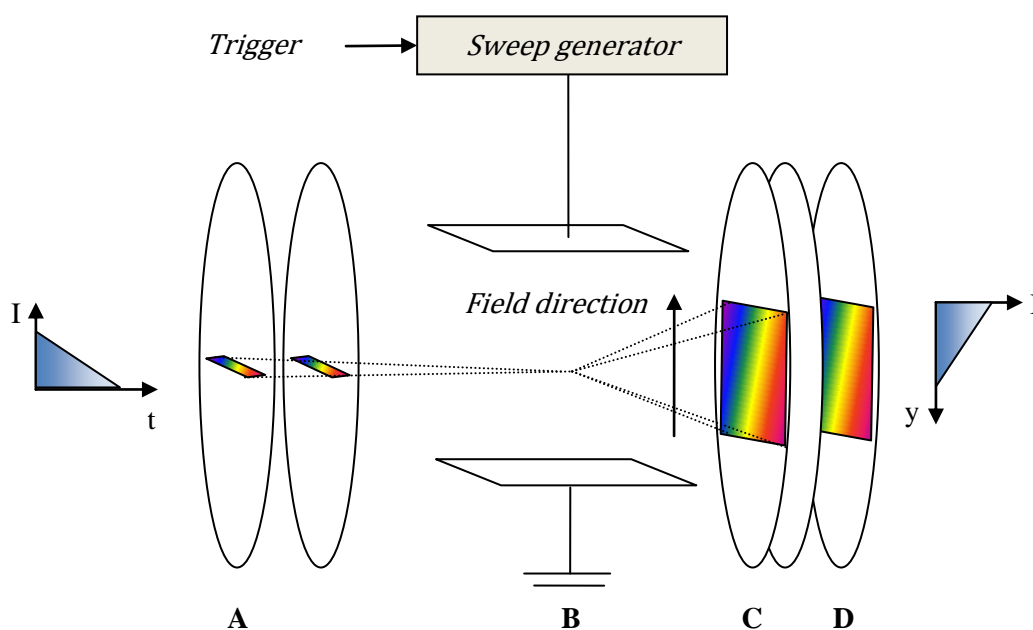
Figure 3.12: Basic schematic of a streak camera. Incoming light is focussed on to a photocathode array (A) and converted into an electron image, which is accelerated towards a MCP array (C). Before reaching the array, the electrons are subjected to a sweeping electric field (B) which disperses the electrons in a vertical direction according to the time at which they enter the field. The electron image is then amplified at the MCP array, before being converted back to a photon image at a phosphor screen (D). This image is then read by a CCD camera to produce the final streak camera image.

At the MCP array the electrical signal is amplified and the electrons are converted back to photons using a phosphor screen. These photons are then measured using a charge-coupled device (CCD) array to produce an image which is 1280×1024 pixels in size. Whereas the vertical axis of the image is equivalent to a time axis, the image is left unchanged in the horizontal direction. Thus by first dispersing the light horizontally according to wavelength, for example by using a diffraction grating, an image can be produced in which the fluorescence from a sample can be measured simultaneously as both a function of time and wavelength. This data is then averaged to produce a final image with dimensions of 640×512 pixels; an

example of an image from the streak camera detector used in this study (Hamamatsu C5680) is

shown in Fig. 3.13.
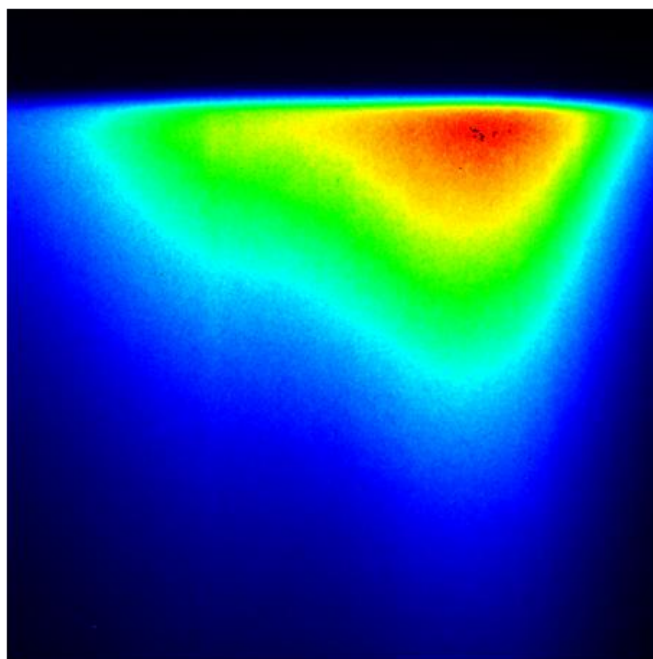
Figure 3.13: Streak camera image of the emission from Super Yellow in solution (p-xylene); 425 nm excitation at 295K. The horizontal direction corresponds to wavelength (increasing from right to left) and the vertical direction corresponds to time (increasing from top to bottom). The colour of the image is a measure of intensity, with dark blue showing regions of low intensity and red showing regions of high intensity.

The x-y image in Fig. 3.13 displays the number of photons detected by the streak camera as

both a function of wavelength (x direction) and the time of their arrival (y direction). The

number of photons obtained at a single pixel is indicated by the colour of the plot; red

represents regions of high intensity, while deep blue represents regions of low intensity. To

convert between the pixel number observed and the corresponding wavelength/time,

pre-calculated calibration data is used. When used in conjunction with picosecond pulsed

excitation source (~2 ps pulse width, as detailed in section 3.3), such a system can be used to

measure the spectral dynamics of conjugated polymer fluorescence with a minimum time

resolution of ~4 ps (the subject of the time resolution will be addressed in more detail in section

3.7.2).[122] In Fig. 3.13, a spectral region of 60 nm is measured over a time period of 2.2 ns.

3.7.2 Practical implementation
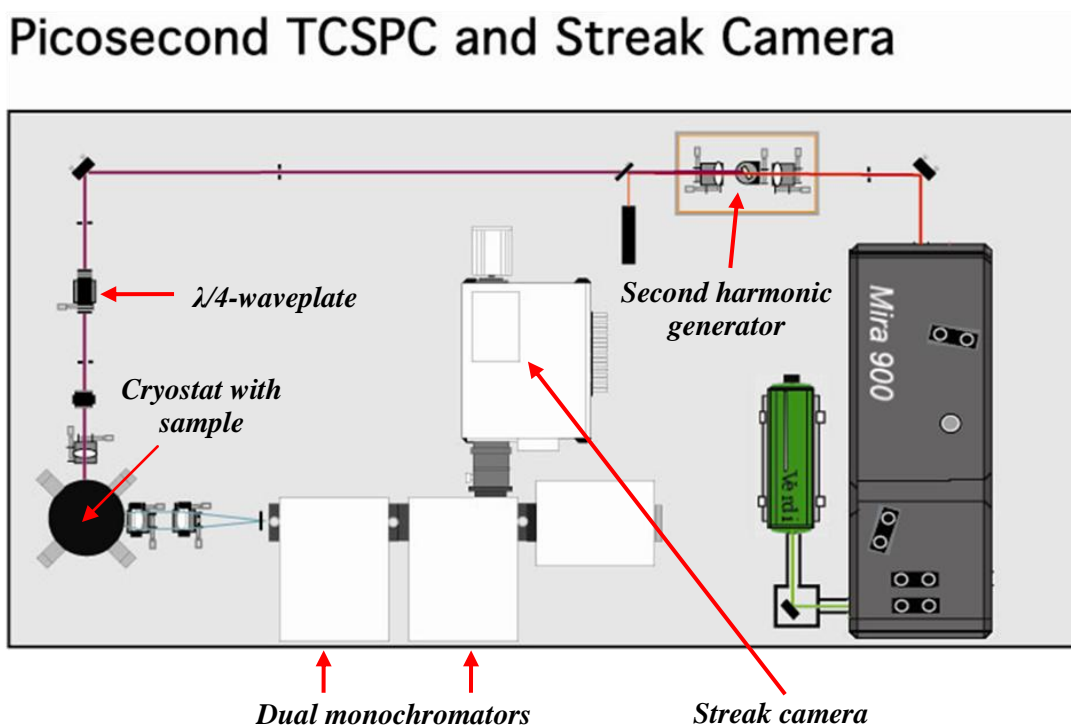
Figure 3.14: Schematic of the picosecond fluorescence detection equipment. Sample excitation is provided using the second harmonic of a Mira 900 Ti:Sapphire picosecond oscillator. Emission from the sample, typically mounted in a cryostat (bottom left), is collected and focussed on to a dual monochromator. The spectrally filtered image is then sent to the entrance slit of the streak camera (middle). Note that the streak camera setup on the optic table also runs in conjunction with a time-correlated single-photon counting setup, with the corresponding detector for that setup included at the bottom-right of the streak camera.

A schematic of the apparatus used as part of the operation of the streak camera is shown in

Fig. 3.14. Photoexcitation was achieved using the output of a Coherent Mira 900 Ti:Sapphire

laser oscillator, pumped by a Coherent Verdi 10 laser, which provides 2 ps pulses at a repetition

rate of 76 MHz. The wavelength of these pulses could be tuned over a spectral region from 700 to 1000 nm, with a maximum output power of ~2.1 mW possible for operation around 800 nm. In order to be able to photoexcite the conjugated polymers investigated in this study, the laser output was focussed into a BBO crystal in which second harmonic generation occurred, providing access to excitation wavelengths from 350 to 500 nm.

Before reaching the sample, a beam splitter was used to collect a small fraction of the excitation source at a trigger diode. The output of this diode was sent to a delay unit control box (Hamamatsu C6878) which controlled the sweep voltage of the camera.

Solid thin film samples were mounted in a Janis Research company VNF-100 liquid nitrogen cryostat, allowing access to dynamic vacuums of the order of 10^{-3} mbar and temperatures down to 100 K. Solution samples were mounted in 100 mm quartz cuvettes and placed in a custom-built sample holder. The excitation source was directed on to the sample using a mirror placed directly next to the cryostat window, with the excitation density controlled using a neutral density filter. When applicable, the polarisation of the excitation source could be controlled using a variable $\lambda/4$-waveplate in conjunction with a linear polariser.

In order to collect the emission for detection, a lens was placed near the sample position. The collected light was then focussed on to the entrance slit of a double subtractive monochromator (Acton Spectra Pro 2300i). To prevent scattered excitation light reaching and potentially damaging the detector, a suitable glass filter was placed before the entrance slit. For streak camera operation a mirror was placed in the housing of the first monochromator, with a 150 g·mm^{-1} grating housed in the second monochromator, resulting in images covering a spectral region ~100 nm wide. Emission was focussed into the streak camera at the 90^{0} exit of the second monochromator. The monochromator slit width was the primary factor in determining the spectral resolution; a typical resolution of 5 nm could be achieved using a slit

width of 250 μm. This was monitored by collecting and measuring the spectral profile of low intensity laser scatter by one of the previous operators of the system.[122]

The streak camera was controlled in two operating modes using a software package (HPD-TA 32) developed by the manufacturer of the camera. The first of these, 'focus mode', did not incorporate use of the sweeping field. The resulting images formed using this mode thus had no time resolution and only displayed the fluorescence spectrum of the sample under investigation. By not dispersing the spectrum vertically, detection of small light levels was made possible; as a consequence focus mode was used to maximise the alignment of emission into the streak camera and achieve as high a SNR as possible. Such alignment procedures typically consisted of controlling the size and position of the collected emission on the monochromator entrance slit by adjusting the collection lens position. For very low light levels, the integration time of data acquisition and the gain of the MCP array could be adjusted. At all times it was important to ensure that the intensity of light reaching the detector was not capable of causing any damage to the streak camera. This could be checked by reading the output image of the streak camera while simultaneously adjusting the optics; high light intensities capable of causing such damage appeared white on the output image.

Time resolution of the streak camera operation could be achieved by switching the camera to 'operate mode', which activated the sweeping field. The time per pixel of the final image could be controlled by selecting the rate at which the deflection field of the camera was swept. Four different operating modes of the camera could be accessed (time ranges 1 through 4) to allow increasingly greater time periods to be covered in a single camera image, at the expense of the average time resolution of the system. The shortest window covered by the camera (time range 1) was approximately 160 ps, corresponding to a time resolution of <7 ps (~4 ps under ideal conditions); the longest window (time range 4) covered a ~2200 ps period at the expense of a larger time resolution of <23 ps.[122]

In addition to the limitations posed by the deflection rate of the camera, other experimental factors also contribute towards the overall time resolution of the system. The ideal time-resolution of the camera can be expressed as a product of three factors:[121]

$$\Delta\tau = \Delta\tau_1 \times \Delta\tau_2 \times \Delta\tau_3 \tag{3.12}$$

$\Delta\tau_1$ is determined by the spatial spread of the input into the streak camera, which in turn is determined by the size of the collected emission focussed into the monochromator. $\Delta\tau_2$ is related to the sweep rate of the deflection field and the resulting impact it has on the time-per-pixel of the final CCD image, as discussed above. Note that for all experiments performed in this thesis the camera was run in time range 4. Finally, $\Delta\tau_3$ is an intrinsic component associated with the streak tube and the deflection field, and unlike the first two components, cannot be controlled through choice of experimental setup.

Data acquisition was performed using analogue integration, in which a pre-selected number of spectra were recorded and then averaged. Before these images could be analysed, different degrees of correction were first applied. A background image, corresponding to the streak camera image in the absence of sample excitation, was recorded before each measurement and subtracted. As part of such a process it was important to ensure that the same experimental conditions were maintained for the dark image (such as the ambient light level), in addition to use of the same integration time and gain.

Images were also subject to curvature correction. In operate mode, imperfections in the homogeneity of the sweeping field result in an elliptical deflection of the electron beam at a single delay time.[122] This curvature could be corrected by defining a parabolic curve corresponding to the zero-delay line and performing a matrix operation on the image using an inbuilt routine of the operation software.

Image analysis was conducted using the camera's software package (HPD-TA 32). Rectangular boxed regions of the image could be selected with the data saved as an ASCII file. Pixel-to-time/wavelength conversions were performed using the aforementioned calibration data to produce either a plot of the emission at a single wavelength as a function of time, or a plot of the fluorescence spectrum at a single time. Averaging over the width of the boxed regions selected (either in time or wavelength) was performed manually.

Analysis of lifetime components present in single-wavelength decay data was performed by fitting to a multi-exponential model using in-built non-linear least-squares fitting routines in OriginLab Origin 8.0.

3.7.3 Context

By being able to spectrally resolve the singlet exciton dynamics of conjugated polymers, streak camera measurements have proven an invaluable tool for investigating features such as exciton migration and energy transfer. This has been used in Chapter 5 of this thesis which outlines a study into energy transfer between adjacent monomer subunits in the conjugated copolymer Super Yellow. Correlating build-in and decay dynamics were measured simultaneously at two different energies in the copolymer using the streak camera, with the energy transfer occurring over a timescale of the order of 10 ps.

Streak camera results have also been used in chapter 4 of this thesis to investigate the fluorescence lifetime of MeLPPP as a function of emission wavelength. These studies were performed to investigate the potential role of vibrational motion in determining the fluorescence lifetime of a conjugated polymer. Streak camera measurements proved an ideal experimental method in this regard as they allowed for a simultaneous measurement of the

fluorescence dynamics across a wide energy range that simultaneously encompassed all of the key vibrational modes of the polymer.

3.8   Basic characterisation apparatus

3.8.1 Absorption and fluorescence spectroscopy

Steady-state ground-state absorption spectra were recorded using a Shimadzu UV-3600 spectrometer.[123] This system utilizes three separate detectors to cover a spectral region from 175 to 3650 nm, consisting of a photomultiplier tube (PMT) for the UV and visible, and InGaAs and PbS detectors for the near-infrared (NIR) and infrared (IR) respectively. Halogen (IR-visible) and Deuterium (UV) lamps are incorporated with a double monochromator to provide excitation with a high resolution (0.1 nm maximum). To record the absorption spectrum of a sample, the excitation source is split into two: the transmitted intensity of one beam which passes through the sample is subtracted from the transmitted intensity of a second parallel beam which passes through a reference. For measurement in solution, an identical cuvette containing the solvent is used as a reference; for a film, an identical substrate.

Steady-state fluorescence spectra were recorded using a Jobin-Yvon Fluorolog-3.[124] The Fluorolog-3 incorporates an L-shaped geometry in which excitation and the collection of emission from a sample are made perpendicularly. Excitation is provided through a Xenon lamp in conjunction with a double monochromator, covering a spectral region from 250 to 600 nm; emission is detected using a PMT tube, again in conjunction with a double monochromator, which covers a spectral region from 250 to 1000 nm. The use of dual monochromators allows for data collection at a spectral resolution of 1 nm.

The Fluorolog-3 can conduct two primary types of measurement. The first is to fix the excitation wavelength and scan the emission monochromator, thus measuring the fluorescence

spectrum of a sample. It is also possible to perform the reverse of this process, in which the emission energy is fixed and the excitation monochromator scanned. This is referred to as an excitation scan and can be used to provide information concerning the absorption characteristics of a sample.
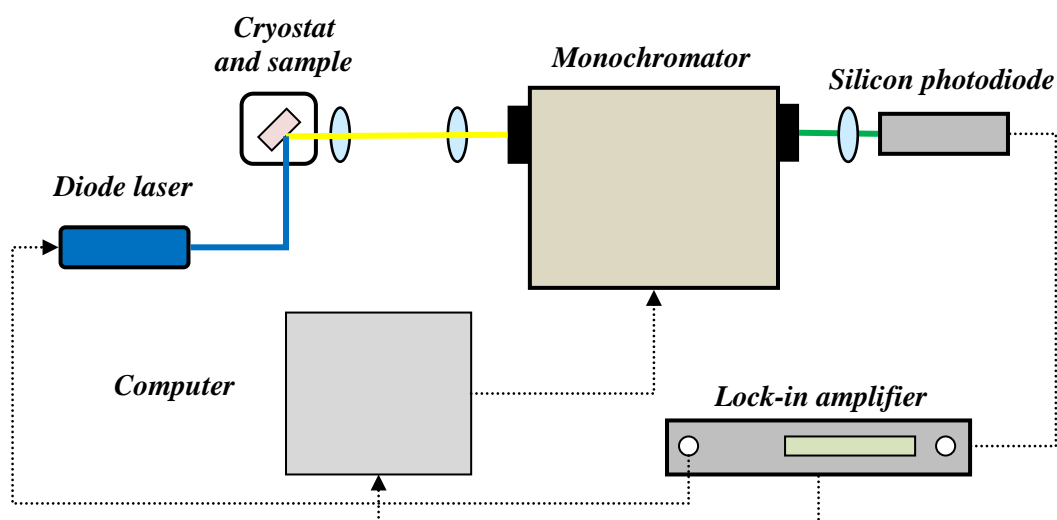
Figure 3.15: Schematic of lock-in based fluorescence detection apparatus. Sample excitation is provided by a diode laser modulated by the internal oscillator of a lock-in amplifier. Emission is collected at 90^0 with respect to excitation and is focussed on to the entrance slit of a monochromator. The filtered light is focussed on to a silicon photodiode, with the intensity of light modulated at the same frequency as the excitation source recorded using the AC output of the lock-in amplifier.

In order to measure very weak emission, for example emission from polymer/electron acceptor blends as performed in chapter 7, a new system was built from scratch which utilised lock-in based detection. A schematic of the system is shown in Fig. 3.15. Excitation was provided using a 355 nm steady-state diode laser, modulated by a 5V square wave from the reference output of a lock-in amplifier (EG&G 7220). Solid-state samples were mounted in a closed-cycle helium cryostat under a dynamic vacuum of 10^{-4} mbar, placed at an angle of 45^0 with respect to the excitation line. Emission was collected perpendicular to the excitation at the

exit window of the cryostat using a short focal length lens and focussed on to the slit of a monochromator (Bentham M300). The intensity of light at the exit slit of the monochromator was measured using a silicon photodiode, with the output of the photodiode sent to the lock-in amplifier. The lock-in amplifier in turn was internally referenced to the frequency of the square wave, in order to measure the fluorescence intensity.

Custom-built Labview programs were used to measure the fluorescence intensity as a function of wavelength by scanning the monochromator grating and measuring the AC component (corresponding to the fluorescence intensity) of the lock-in amplifier. With this system it was possible to measure differential transmissions as small as 10^{-5} mV, at the expense of a spectral resolution of ~15 nm; in order to detect a measurable signal with the silicon photodiode over a large wavelength range, it was necessary to fully open the exit slit of the monochromator.

A comparison of results obtained using both the Fluorolog-3 and the lock-in technique is shown in Fig. 3.16 for the quenched emission from the polythiophene derivative poly(3-dodecylthiophene-2,5-diyl) (P3DDT) doped with the electron acceptor [6,6]-phenyl-C_{61}-butyric acid methyl ester (PCBM). The lock-in based technique offers an increase in the SNR by nearly a factor of 3, allowing for individual vibronic modes to be observed in the fluorescence spectra. There are however several problems that arise when using the lock-in based technique. The first is that the system response at 710 nm shows a drop in intensity. This is due to saturation of the silicon photodiode due to the second order reflection of scattered excitation light through the monochromator. The second feature is that, as the intensity direct from the photodiode is measured, it is necessary to divide the data by the spectral response of the photodiode in order to reproduce the accurate line-shape of the fluorescence spectrum.
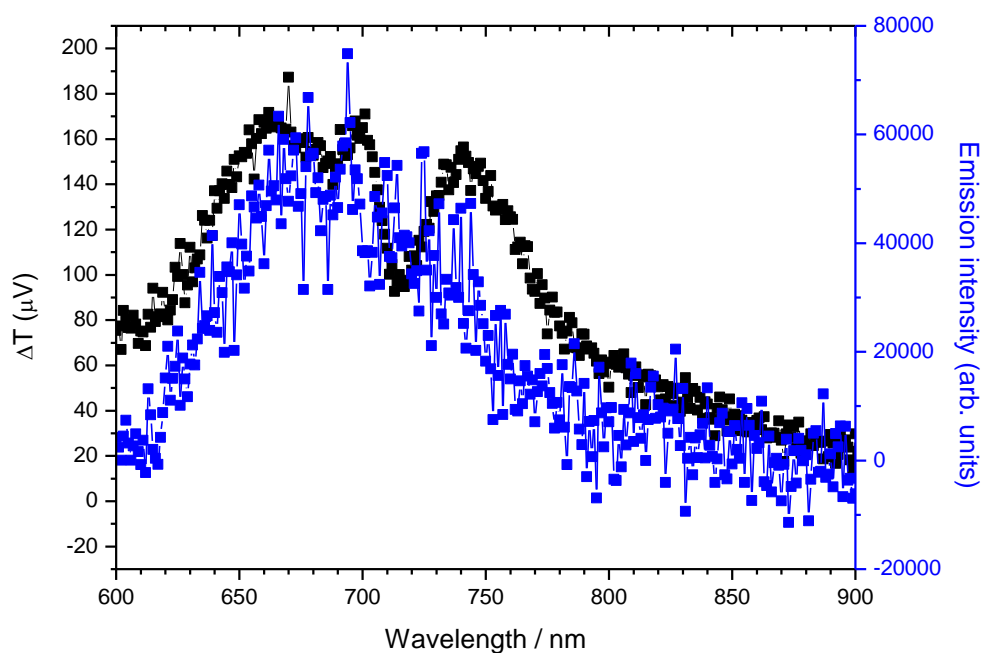
Figure 3.16: Comparison of the fluorescence spectrum from a P3DDT/PCBM (1:1 wt %) blend, obtained using the Fluorolog-3 (blue) and the custom-built system (black). A dip in the output of the custom system is observed at ~710 nm is attributed to detector saturation from the second order reflection of the excitation source through the monochromator. The black curve has been corrected for the detector response with wavelength.

Measuring the absorption and fluorescence spectra of a conjugated polymer was always taken as the first step as part of any study and as such examples of such data are included in all four results chapters of this thesis. These results provided vital information concerning the singlet exciton energies of different polymers, with the absorption spectrum used in pump-probe studies to control excitation density as a function of the pump wavelength. Absorption and fluorescence data were also used in the interpretation of pump-probe data to help identify the location of the PB and SE bands in transient transmission spectra. Chapter 4 of this thesis includes a comprehensive review of the fluorescence spectrum of MeLPPP in which individual vibrational modes could be identified in the data using a simple fitting procedure; a similar

procedure was also repeated in chapter 5 for the conjugated copolymer Super Yellow. Fluorescence data has also been used in chapter 7 to monitor exciton quenching in the conjugated polymer P3DDT when doped with the electron acceptor PCBM; in this circumstance, due to the low intensity of emission from the polymer both with and without the electron acceptor, the custom-built setup as outlined above was used to obtain a good SNR.

Site-specific fluorescence spectroscopy

Under typical excitation conditions the fluorescence spectra of conjugated polymers are subject to inhomogeneous broadening. In some polymers the spectral degree of broadening can become comparable to the spacing between adjacent vibrational modes in the fluorescence spectrum and as such distinguishing between those modes becomes impossible. It is therefore of interest, particularly in studies of vibronic coupling in conjugated polymers, to use experimental techniques in which the inhomogeneous broadening in the fluorescence spectra can be reduced, if not eliminated.

The fundamental basis of observing inhomogeneous broadening in the optical spectra of any system of chromophores is for there to be a difference in energy between those chromophores which are initially excited and those chromophores from which emission finally occurs.[73] For example, in a conjugated polymer this can occur as the result of conformational relaxation of the polymer chains,[31, 38, 125] in which a polymer in the excited state is able to relax into a more stable, lower energy structural arrangement. Exciton migration also contributes as a significant source of spectral relaxation. As discussed in section 2.3.2, a conjugated polymer has distribution of chromophore energies which makes up the polymer density of states (DOS). If an exciton is able to move between chromophores (see section 2.6) the respective absorption and emission chromophores of that exciton will be on average different and non-degenerate.[20, 77, 126]

It is clear that in order to reduce the inhomogeneous broadening in the fluorescence spectrum of a conjugated polymer it is necessary to minimise the effect of spectral relaxation mechanisms such as exciton migration. One method by which this can be achieved is to reduce the temperature at which the fluorescence spectrum is measured, which as discussed in section 2.6.5, will reduce the rate of exciton migration. In addition, by exciting directly in the tail of the DOS there is on average only a very small number of adjacent sites of the correct energy to which an exciton can move to (see section 2.6.4). This also reduces the rate of migration.[20, 77, 126] Under these circumstances it is possible for an exciton to remain trapped on the chromophore on which it was generated throughout its entire lifetime.[73] In such cases exciton recombination will occur on the same chromophore that was initially excited and the resulting emission is only homogeneously broadened.

The principal of exciting into the very bottom of the DOS to achieve only homogeneous broadening is referred to as site-selective fluorescence (SSF) spectroscopy.[73, 127] This is achieved experimentally by using a tuneable laser source to excite progressively deeper into the DOS of a sample, until homogeneous broadening conditions are met. To facilitate the likelihood of this process occurring, such measurements are performed at very low temperatures. In chapter 4 of this thesis SSF has been used to investigate the nature of vibronic coupling in MeLPPP. These measurements were performed using the Fluorolog-3 as detailed above in which the sample was cooled to 13.5 K using a Cryomech closed-cycle Helium cryostat, with the fluorescence spectrum of the sample monitored as a function of excitation energy.

3.8.2 Raman spectroscopy

Raman spectroscopy is an excellent tool with which to study the nature of the active bond vibrations in a wide range of different molecular systems, including conjugated polymers. The

basic physical principle behind this experimental method is the so-called Raman effect, in which light scattered from a substance gains or loses energy by interacting with the vibrational modes of that substance.[128, 129] This is considered in more detail below.

When a beam of light is incident upon a substance, the photons (of energy $\hbar\omega$) can interact with that medium in a number of ways. One of these processes is for the photons to be scattered by the sample.[128, 129] Most of this scattering is elastic (referred to as Rayleigh scattering); that is the energy of the incident and scattered photons remains constant. A fraction of incident photons also take place in inelastic scattering events, in which the energy of scattered photons is different to the incident photons. This latter phenomenon is referred to as the Raman Effect.[128, 129]
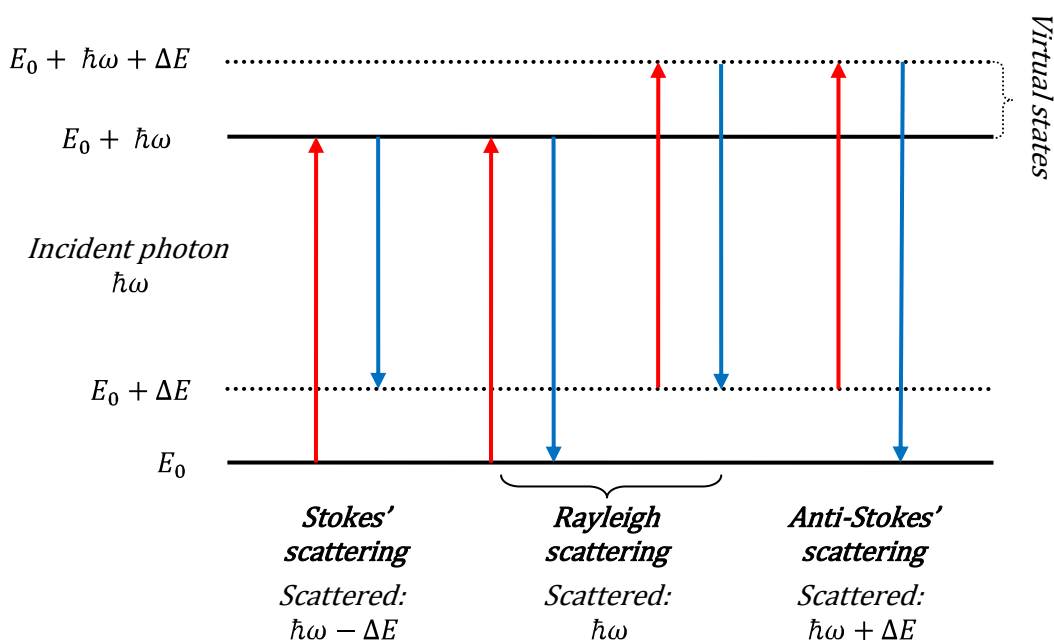
Figure 3.17: Schematic of Rayleigh, Stokes' and anti-Stokes' scattering processes in a molecular system involving a vibrational mode of energy ΔE. A photon of incident energy $\hbar\omega$ is able to interact (red lines) with virtual states of a molecular system. In addition to elastic Rayleigh scattering, the scattered photon (blue lines) can either lose one unit of vibrational energy (Stokes' scattering) or gain one unit (anti-Stokes' scattering).

The Raman Effect specifically involves the interaction of an incident photon of light with the virtual states of a sample. As an example, consider in Fig. 3.17 a molecule with a ground state E_0 and vibrational energy level $E_0 + \Delta E$ (where ΔE is the energy of a vibrational mode). After absorption to a virtual state, emission can occur to either the ground or vibrational energy level. Proceeding through the different transitions involving virtual states indicated in Fig. 3.17, it is possible for a photon to lose one unit of vibrational energy (corresponding to a scattered photon energy of $\hbar\omega - \Delta E$), or gain one unit of energy (corresponding to a scattered photon energy of $\hbar\omega + \Delta E$). These scattering processes are referred to as Stokes' and anti-Stokes' scattering respectively and together compromise the so-called Raman spectrum of a sample.

The type of molecular motion associated with a vibrational mode also has a strong influence on the intensity of the Raman scattering from a sample. This can be understood using a classical argument:[129] when a photon of light is incident upon a sample, the electric field of the light induces an electronic dipole moment in the sample. The magnitude and orientation of this dipole moment ($\boldsymbol{d}$) is related to the electric field ($\boldsymbol{\epsilon}$) by the polarisability tensor ($\underline{\alpha}$) of the system, as according to Eq. 3.13 below:

$$\boldsymbol{d} = \underline{\alpha}\boldsymbol{\epsilon} \tag{3.13}$$

In an isotropic medium the polarisability is a constant and the dipole moment is parallel to the applied electric field. In anisotropic media this is no longer the case and as given above, the true relationship is governed by the properties of the polarisability tensor. This quantity is critical, as it can be shown that Raman scattering from a vibrational mode will only occur if the molecular motion associated with that mode instigates a change to the polarisation tensor.[129]

By measuring the scattered light from a sample utilising a suitably sensitive method of detection, it is possible to measure the shift of the Stokes and anti-Stokes lines with respect to

the elastic scattering line and thus gain a great deal of information concerning the energy of the vibrational modes of a molecule. In chapter 4 of this thesis, a comprehensive analysis of the vibrational modes in the fluorescence spectrum of the conjugated polymer MeLPPP is detailed. As part of this work Raman spectroscopy was used to determine the energy of the different modes, which served as an important starting point for the rest of the analysis process.

3.8.3 Photoluminescence quantum yield measurements

The photoluminescence quantum yield (PLQY, Φ_{PLQY}) is one of the most important material characteristics of a conjugated polymer and is defined as the number of photons emitted from a sample relative to the number of exciting photons, as expressed below in Eq. 3.14:

$$\Phi_{PLQY} = \frac{Number\ of\ photons\ emitted}{Number\ of\ photons\ absorbed} \tag{3.14}$$

Although this definition of the PLQY seems simple at first, a significant amount of time has been spent refining various methods to measure it experimentally. This has been in no small part due to the significance of this quantity in characterising a conjugated polymer for potential use in an OLED device. As only limited PLQY studies have been performed in this work (see chapter 5), no more time will be spent discussing the development history of these methods. The remainder of this section will instead proceed to outline the two methodologies that were used in chapter 5 for calculating the PLQY in film and solution.

PLQY: Film

The PLQY of thin films were measured using the method outlined by de Mello *et al.* in which luminescence from both direct and secondary excitation – that is excitation from first order scatter off of an integrating sphere wall - is considered.[130, 131] Samples were mounted in a PTFE

coated integrating sphere (Lab Sphere), with the emission collected from the sphere measured

using a Jobin-Yvon Horiba Fluoromax-3 fluorimeter. The calculation of the PLQY (φ_{PLQY})

proceeds as follows:

$$\Phi_{PLQY} = \frac{\varepsilon_i(E) - (1-A)\varepsilon_0(E)}{A.l_e(E)} \; where \; A = \frac{l_0(E) - l_i(E)}{l_0(E)} \qquad (3.15)$$

In Eq. 3.15 ε_i and ε_0 are the integrated emission spectra as a result of direct and secondary

excitation respectively; likewise l_i and l_0 are the integrated excitation spectra under the same

conditions, with l_e the integrated emission from the sphere alone. In order to measure the

sample response (for both the emission and excitation spectra) under secondary excitation

conditions, the film inside the integrating sphere was oriented to be perpendicular to the

incoming excitation source. *A* is the absorption of the thin film, calculated in Eq. 3.15 from

the excitation spectra. It should be noted that a correction file that took into account the

spectral response of the fluorimeter and sphere together was applied to all recorded data.

PLQY: Solution

The PLQY of solutions was recorded using a Jobin-Yvon Horiba Fluoromax-3 fluorimeter and

performing the standard comparative method,[132] the details of which are outlined below in

Eq. 3.16:

$$\Phi_{PLQY} = \Phi_{standard}.\frac{\eta_{sample}^2 grad_{sample}}{\eta_{standard}^2 grad_{standard}} \qquad (3.16)$$

In Eq. 3.16 η is the refractive index and $grad$ is the gradient of a straight line plot of integrated

(with respect to energy) emission intensity versus the absorption at the excitation energy for

different concentrations of solution. As suggested by the name of the technique, this method

relies on use of a standard compound for which the PLQY is accurately known ($\Phi_{standard}$), with typically 9,10-diphenyl anthracene chosen for this purpose.

3.9 Polarised spectroscopy

3.9.1 Fluorescence anisotropy

In order for a photon of light to interact with a molecule and cause an electronic transition, the electric dipole moment corresponding to that transition must have a non-vanishing projection on to the polarisation orientation of the incoming photon; no transition will occur if the two are completely perpendicular. Consequently, when a polarised beam of light is incident upon a distribution of randomly oriented polymer chains, only those chains that fit the aforementioned condition will interact with the light and lead to an electronic transition; this process is referred to as photoselection. Polarised spectroscopy can thus be used to provide information concerning the orientation of the electric dipole moments present in a molecular system.[87, 125]

One of the most typical applications of polarised spectroscopy towards the study of conjugated polymers is the measurement of the fluorescence anisotropy.[58] In such an experiment, the excitation source is polarised, with the polarised emission both parallel ($I_\parallel$) and perpendicular ($I_\perp$) to the excitation polarisation recorded. These measurements are used to define the fluorescence anisotropy (r) of a sample, which is given below in Eq. 3.17.

$$r = \frac{I_\parallel - I_\perp}{I_\parallel + 2I_\perp} \qquad (3.17)$$

Eq. 3.17 holds as the strict definition of the fluorescence anisotropy. In order to measure both $I_\parallel$ and $I_\perp$ accurately one must typically take into account the polarisation response of the experimental equipment at hand. For example, a photodetector may be more sensitive to one

polarisation than the other, therefore skewing the measured experimental values from the true system response. In order to take this into account a polarisation instrument correction factor (G) is introduced into Eq. 3.17, leading to the practical definition of the fluorescence anisotropy given in Eq. 3.18.

$$\langle r \rangle = \frac{I_{vv} - GI_{vh}}{I_{vv} + 2GI_{vh}}, where \; G \equiv \frac{I_{hv}}{I_{hh}} \tag{3.18}$$

In Eq. 3.18 above $I_{i,j}$ is the intensity of the emission with excitation and emission polarisers set to the alignments i and j, with these alignments either being vertical (*v*) or horizontal (*h*) with respect to the relevant spectrometer channel.

For an isotropic distribution of chromophores, as typically encountered in a spun film or solution of a conjugated polymer, it can be shown that the fluorescence anisotropy can be directly related to the difference in angle (θ) between the absorption and emission electric dipole moments,[58] as according to Eq. 3.19:

$$r = \frac{3\langle cos^2\theta \rangle - 1}{5} \tag{3.19}$$

It should be noted that at this point it is only possible to measure an average value of the angle θ across all chromophores. From Eq. 3.19 the maximum anisotropy that can be obtained is 0.4, and occurs when the absorption and emission dipole moments lie parallel to one another. In conjugated polymers there are many processes which can result in a deviation from the maximum anisotropy and thus can be monitored by measuring the anisotropy as a function of time. For example, it is possible for a molecule on which an excitation is generated to undergo conformational relaxation, in which the chain, and thus the emission dipole moment, adopts a

new geometry.[125] This leads to a reduction in the fluorescence anisotropy with time and occurs on a timescale of the order of 10 ps.

Fluorescence anisotropy decay can also be used to measure exciton migration in conjugated polymers (section 2.6).[32, 133, 134] As an exciton migrates through the DOS of a conjugated polymer it will move between chromophores of different orientations. On average as an exciton moves away from the chromophore in which it was generated, there will be a decrease in $\langle cos^2\theta \rangle$, and thus as according to Eq. 3.19, a decrease in the fluorescence anisotropy. As such a process is independent of the chromophore energy, fluorescence anisotropy can be used to measure the dynamics of both downhill and iso-energetic migration, as opposed to experiments using for example a streak camera (section 3.7), which can only measure the dynamics of downhill migration.

3.9.2 Anisotropy in pump-probe spectroscopy

In a similar manner to fluorescence anisotropy, polarised pump-probe spectroscopy can be used to measure exciton migration between chromophores in conjugated polymers.[80, 135, 136] In this case, rather than measuring the polarised emission from a sample parallel and perpendicular to the excitation orientation, the polarised absorption of the probe pulse parallel and perpendicular to the polarisation of the pump is measured. This leads to the definition of anisotropy in pump-probe spectroscopy below in Eq. 3.20:

$$r = \frac{\dfrac{\Delta T}{T}_\parallel - \dfrac{\Delta T}{T}_\perp}{\dfrac{\Delta T}{T}_\parallel + 2\dfrac{\Delta T}{T}_\perp} \tag{3.20}$$

The concept of anisotropy decay in pump-probe spectroscopy is very similar to that of fluorescence anisotropy; the former is based on excited-state absorption, whereas the latter is

based on emission. As an exciton migrates away from the chromophore on which it was photogenerated by the pump pulse, it will on average move to a site with a different orientation of excited-state transition dipole moment, leading to a reduction in the anisotropy with time. By using pump-probe spectroscopy one can measure such a decay process on a scale of hundreds of femtoseconds. This is in contrast to measurements of the time-resolved fluorescence anisotropy, which have a typical time resolution of the order of picoseconds.

3.9.3 Magic-angle spectroscopy

Consider a typical pump-probe experiment in which both the pump and the probe are parallel. As an exciton moves off the chromophore it was generated on, the photoselection inferred by the polarisation of the pump will result in an ultrafast decay component in the probe response. This has the potential to lead to complications in the analysis of other photophysical processes which occur on similar timescales, such as energy transfer. It is thus often desirable to produce a result which is independent of polarisation. This can be achieved by performing polarised spectroscopy at the so-called magic-angle, corresponding to an angle between excitation and emission, or equivalently pump and probe, of 54.7^0. The derivation of this value proceeds below.

In order to measure a quantity free of polarisation, i.e. one that is not proportional to $I_\parallel$ or $I_\perp$, one seeks to measure the total intensity I_T.[58] Consider an arbitrary distribution of N chromophores: the total intensity from those emitting chromophores is given by the sum:

$$I_T = \sum_i^N I_i \tag{3.21}$$

If a linear polariser is introduced into the measurement, the resulting intensity measured through the polariser (I_p) will depend on the projection of the emitted light with respect to the angle of the polariser:

$$I_p = \sum_i^N I_i \cos^2 \alpha_{pi} \tag{3.22}$$

In Eq. 3.22 α_{pi} is the angle between the emission from unit i and the orientation of the linear polariser. Such a measurement can be repeated along three orthogonal directions(*x*, *y* and *z*) as shown in Fig. 3.18:
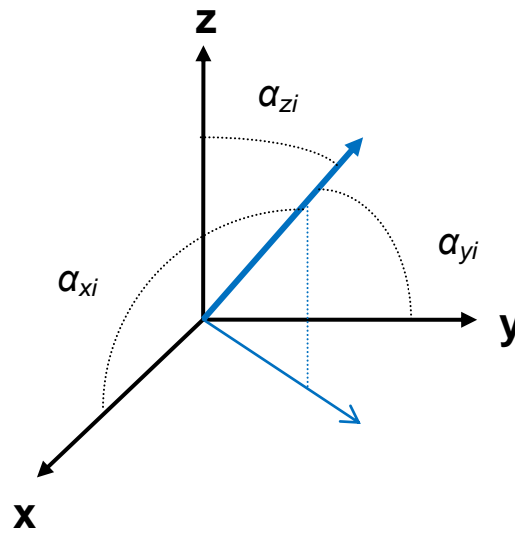
Figure 3.18: Orientation of emission dipole moment in a cartesian coordinate system.

$$I_x = \sum_i^N I_i \cos^2 \alpha_{xi} \quad I_y = \sum_i^N I_i \cos^2 \alpha_{yi} \quad I_z = \sum_i^N I_i \cos^2 \alpha_{zi} \tag{3.23}$$

Given the identity:

$$cos^2\alpha_{xi} + cos^2\alpha_{yi} + cos^2\alpha_{zi} = 1 \qquad (3.24)$$

The linear combination of the three projections is equal to the total intensity:

$$I_x + I_y + I_z = \sum_i^N I_i.(1) = I_T \qquad (3.25)$$

If excitation is chosen to lie along the z direction, then $I_x = I_y$, resulting in the following identity for the total intensity, which is *independent* of polarisation, shown in Eq. 3.26:

$$I_T = I_\parallel + 2I_\perp \qquad (3.26)$$

There are two ways to measure the I_T. The first is to measure $I_\parallel$ and $I_\perp$ independently and use Eq. 3.26, although this can be time consuming. A more effective method is to perform a single measurement with the emission (or probe) polariser set to an angle of 54.7^0. At this angle the vertical projection through the polariser $I_\parallel cos^2\alpha = 0.333I_\parallel$, with the horizontal projection $I_\perp sin^2\alpha = 0.667I_\perp$; under this circumstance the condition $I_\parallel + 2I_\perp$ is met and the measurement becomes independent of polarisation.

3.10 Polymer characterisation and sample preparation

The chemical properties of the conjugated polymers used in these studies were characterised by the average number of monomer repeat units on one chain and their polydispersity index (PDI). The PDI is a measure of the distribution of chain masses, or equivalently the distribution of chain lengths;[84] it is thus related to the distribution of conjugation lengths and therefore by extension the polymer DOS. The PDI is defined as the ratio of the weight averaged molecular weight (M_W) to the number average molecular weight (M_N), as detailed below in Eq. 3.27:

$$PDI \equiv \frac{M_W}{M_N} \quad where \quad \begin{cases} M_W = \dfrac{\sum_i M_i^2 N_i}{\sum_i M_i N_i} \\ M_N = \dfrac{\sum_i M_i N_i}{\sum_i N_i} \end{cases} \tag{3.27}$$

In Eq. 3.27 i is taken as the number of monomers along a polymer chain, with M_i the mass of the chain containing i monomers and N_i the number of chains with i monomers. The sum is taken over all possible values of i. If a polymer sample has a PDI of 1 then all chain lengths are the same and the sample is said to be monodisperse; this is however rarely achieved in synthetic polymers.[84] All the polymers used in this study had a PDI > 1; the exact value for a particular polymer used is stated in the relevant section.

The conjugated polymers used in these studies were obtained from a variety of different sources (as indicated in the relevant section) and were used without any further modification. Relevant chemical details (such as the PDI) were also obtained from the manufacturer.

Solutions of conjugated polymers were prepared in a variety of spectroscopic grade organic solvents with typical concentrations of <0.01 mg·ml^{-1} (O.D~0.003 in a 10mm quartz cuvette). By using such low concentrations, complications such as self-absorption and aggregation of the polymers in solution could be avoided.

Solid thin films of conjugated polymers were prepared by spin casting from solution (10 mg·ml^{-1}) on to 10 mm sapphire substrates. By spinning at a rate of 1500 rpm for 45 seconds, films approximately 80 nm thick, corresponding to an optical density of the order of 0.1, could be produced. When possible, these samples were then promptly mounted in vacuum as part of the appropriate experimental apparatus in order to minimise any photo-oxidisation between preparation and measurement. To ensure that all solvent had been

removed from the substrate, films were typically left for 30 minutes under vacuum before measurements commenced.

Chapter 4   Fluorescence vibronic analysis in a ladder-type conjugated polymer

Sections of this work have been submitted for publication:

4.1   Introduction

Ladder-type conjugated polymers, such as methyl-substituted ladder-type poly(para-phenylene) (MeLPPP) and poly(naphthylene-phenylene) (2,6-NLP), are of interest to the organic electroactive materials community for their application in optoelectronic devices such as organic light emitting diodes.[43, 137-139] These materials are characteristically defined as 'ladder' polymers on the basis that adjacent phenyl groups along the polymer backbone are bridged together in two places. This results in a rigid-rod chain structure in which rotational modes of the polymer backbone are thought to be prohibited.[140, 141] Removing the action of these rotational modes imbues ladder-type polymers with a high degree of intramolecular order and a narrow distribution of conjugation lengths. As a consequence these materials have also attracted interest as model systems in which to investigate the significant electron-phonon coupling that exists in conjugated polymers[36, 37, 69, 142] due to the relatively small degrees of inhomogeneous broadening observed in their optical spectra.[140, 141]

To briefly recap the discussion of section 2.5, within the Born-Oppenheimer approximation, the properties of electron-phonon coupling in a conjugated polymer are governed by the Franck-Condon (FC) principle, which states that changes within the nuclear manifold of states occur on a much longer timescale than any electronic transitions. A consequence of this

principle is that the intensity of vibrational transitions in optical spectra of a conjugated polymer are determined by the overlap between the relevant excited and ground state vibrational wavefunctions, with the results expressed as the so-called FC factors:

$$I_{0-n} = \frac{e^{-S}S^n}{n!} \; where \; S = \frac{\omega|\Delta \boldsymbol{Q}|^2}{2\hbar} \tag{4.1}$$

In Eq. 4.1 n is the order of the particular vibronic mode under question and ω is the frequency of vibration. S is the so-called Huang-Rhys (HR) parameter, with $\Delta \boldsymbol{Q}$ a vector representing the change in conformation of the polymer between the ground and excited states. The HR parameter of a particular vibrational mode can be measured experimentally using Eq. 4.2 below:

$$S = \frac{I_{0-1}}{I_{0-0}} \tag{4.2}$$

In Eq. 4.2 I_{0-0} and I_{0-1} are respectively the intensity of transitions originating from the zero-phonon vibrational level of the excited state to the zero and one-phonon vibrational levels of the ground state.

FC analysis has been successfully applied to describe the vibrational progressions observed in both flexible and planar oligomers.[14, 69-71, 142, 143] The last decade has also seen a significant research effort led by Spano *et al.* to develop theories that go beyond the Born-Oppenheimer approximation and consider situations in which the interactions between adjacent polymer chains are comparable in strength to the electron-phonon coupling of a single chain.[144-149] One of the primary consequences of such theories is that the electron-phonon coupling in a conjugated polymer can influence the polarisation of fluorescence, which is not possible solely within the Born-Oppenheimer approximation.

This chapter outlines the results of a comprehensive experimental review of the effects of electron-phonon coupling in the steady-state and time-resolved fluorescence spectra of the conjugated polymer MeLPPP. This work originated from a study of the time-resolved fluorescence from MeLPPP, which was made in order to characterise the singlet exciton dynamics of the polymer. As part of these experiments, a long-lived state was identified in the fluorescence spectrum of the polymer. As this state was found to be concurrent with the presence of a small peak, an additional study was performed with aim of modelling the contribution of vibronic modes in the steady-state fluorescence spectrum of MeLPPP. This would confirm whether there was any correlation between the aforementioned long-lived state with one of the vibrational modes of the polymer. The results of this study, while successful in assigning the origin of the long-lived state, also demonstrated new phenomena in the properties of the electron-phonon coupling in MeLPPP which merited discussion in their own right. This chapter therefore presents the results and analysis of both steady-state and time-resolved measurements, culminating in a discussion concerning the origin of the long-lived state.

In summary, this chapter begins with a review of results obtained using Raman and site-specific fluorescence (SSF) spectroscopy to identify the principal vibrational modes in MeLPPP. This data is also used to demonstrate a crossover between SSF and Raman emission at low excitation energies and temperatures. The contribution of vibrational modes in the steady-state fluorescence spectrum of MeLPPP in film is then investigated by applying a multi-gaussian model to the data, developed primarily from the results of the Raman and SSF measurements in addition to related theoretical predictions made by Karabunarliev *et al.*.[69] The results of temperature dependent studies are used develop a detailed understanding of how the low energy skeletal stretching mode of the polymer backbone influences the form of the fluorescence spectrum as a function of temperature. In particular, it is shown that thermal population of the skeletal stretch mode occurs in the excited-state after the thermalisation of excess energy, with

a new set of transitions originating from these so-called 'hot' levels appearing in the fluorescence spectrum as a function of increasing temperature.

Significantly, a distinct change in the behaviour of the vibrational mode amplitudes with temperature is identified at a critical point between 125 and 150 K. This is attributed to a change in conformation of the polymer with temperature and it is proposed that the aforementioned thermal population of the skeletal stretch mode in the excited-state plays a role in stabilising the polymer conformation.

Having identified and characterised the contribution of vibrational modes in the fluorescence spectrum of MeLPPP, an investigation into more specific points concerning the fundamental nature of electron-phonon coupling in conjugated polymers is then considered. Polarised fluorescence spectroscopy on stretched films of MeLPPP is used to demonstrate a fundamental relationship between the polarisation of fluorescence and the vibrational mode through which fluorescence decay occurs. This is highly significant as it demonstrates a failure of the Born-Oppenheimer approximation in MeLPPP, with this result readdressed in context of the theoretical approach of Spano. From this it is proposed that interchain interactions play an important role in determining the properties of fluorescence in MeLPPP. The role of interchain interactions in MeLPPP is also considered in chapter 6 of this thesis.

Picosecond fluorescence spectroscopy is also used to address the issue of whether the electron-phonon coupling in MeLPPP influences the fluorescence lifetime. Whereas in solution the fluorescence lifetime is shown to be independent of energy and therefore by extension the vibrational mode through which emission occurs, measurements of MeLPPP in film demonstrate an unexpected dependence of the longest decay component on excitation energy, with a long fluorescence lifetime measured at the spectral location of the transverse ring stretch mode of the polymer. Rather than addressing these results in context of electron-phonon

coupling, it is instead demonstrated that this long lifetime arises as a result of a broad, underlying defect state in films of MeLPPP. The role of such a defect in determining the excited-state dynamics of MeLPPP could impact the interpretation of fluorescence lifetime studies if not properly taken into consideration, with the results of previous studies readdressed in light of this conclusion.

4.2 Experiment

4.2.1 Materials

Unaligned solid thin films of the polymer MeLPPP (chain length of ~60 repeat units; polydispersity index = 1.3) were deposited onto sapphire substrates by spin casting at 1500 rpm for 45 seconds from a toluene (Romil) solution (10 mg·ml^{-1}, 30 mg·ml^{-1} for SSF measurements). Stretched films (×28 original length) of MeLPPP were prepared from a polyethylene solution as described in previous work.[87] Highly dilute solutions of MeLPPP (toluene, 0.001 mg·ml^{-1}) were prepared for picosecond fluorescence measurements. In addition to reducing self-absorption (absorption of photons emitted by the sample) effects in the fluorescence spectra, using such low concentrations ensured that the polymer chains were completely isolated, with no aggregation occurring.

4.2.2 Spectroscopic measurements

Room temperature absorption spectra were measured using a Shimadzu UV-3600 spectrometer. Temperature dependent absorption spectra were recorded using a USB4000 Ocean Optics spectrometer, with a broadband xenon lamp used as the excitation source. Fluorescence spectra were recorded using a Jobin-Yvon Fluorolog-3 which incorporates double excitation and emission monochromators in a right-angle geometry with automatic polarisers. For both temperature dependent absorption and fluorescence measurements solid-state samples were

mounted in a closed-cycle Cryomech helium pulse tube cryostat under a dynamic vacuum of 10^{-5} mbar, allowing access to temperatures down to 10 K. Dilute solution samples were held in a custom-made 10 mm quartz cuvette suitable for housing in a Janis Research company VNF-100 liquid nitrogen cryostat. SSF measurements were conducted at 13.5 K by setting the excitation monochromator slit width to 0.5 mm (corresponding to a spectral resolution of 0.5 nm) and varying the excitation energy. Raman spectra were recorded using a Horiba Jobin-Yvon LabRamHR Raman Microscope used in conjunction with a 2.31 eV laser excitation source, as described elsewhere.[150]

To develop a qualitative measure of the polarisation of fluorescence from stretched films of MeLPPP, the Jobin-Yvon Fluorolog-3 was programmed to record two full fluorescence spectra: I_{vv} and I_{vh}, with I_{ij} the intensity of emission with excitation (i) and emission (j) polarisers set vertically (v) and horizontally (h) with respect to the spectrometer channel. The sample stretch direction was placed vertically with respect to the spectrometer channel, with the ratio of I_{vv} to I_{vh} recorded, as defined below in Eq. 4.3:

$$Ratio = \frac{I_{vv}}{GI_{vh}} \tag{4.3}$$

In Eq. 4.3, $G \equiv I_{hv}/I_{hh}$ is the instrument correction factor included to take into account any anisotropic response of the measuring apparatus; a pre-recorded instrument correction factor, calculated as part of measurements on the laser-dye Coumarin-6,[150] was used in these experiments.

The choice of making measurements in stretched films, rather than isotropic films, was made in order to minimise the effect of exciton migration on the polarisation of fluorescence from the sample. Migration has been well documented as an anisotropy loss mechanism in isotropic

systems.[32, 133, 134]   As an exciton migrates through the DOS of a polymer it will by necessity move between chromophores of different orientation.   Therefore the orientation of the chromophore segment from which an exciton has migrated to and subsequently emitted from will on average be different from that of the chromophore on which it was generated. Consequently the steady-state fluorescence anisotropy of an isotropic film displays a non-uniform dependence with emission energy.[87]   This is no longer the case in an aligned system; if the degree of alignment is 100% accurate, by definition all chromophores are orientated along the same direction and therefore migration has no determining role on the anisotropic response.   Although the degree of chain alignment in stretched films of MeLPPP has been demonstrated not to be 100% efficient,[150] the influence of exciton migration on determining the anisotropic response of such samples is still expected to much less prominent than in an isotropic film.   Note that exciton migration can be similarly minimised by performing measurements in dilute solution; the signal-to-noise ratio of such experiments is however by necessity much lower and the range of temperatures for which a sample can be measured over is restricted by the freezing point of the solution.

Picosecond time-resolved fluorescence measurements were made using a Hamamatsu C5860 Streak Camera.   2 ps, 76 MHz pulses at 1.46 eV generated from a Coherent Mira 900 Ti:Sapphire picosecond laser, coupled to a second harmonic generator, were used to produce the excitation source at 2.92 eV. A vertical polariser was placed before the sample, which was mounted in a JANIS liquid nitrogen cryostat, with emission detected by a second polariser set at the magic angle (~55^0, see section 3.9.3) with respect to the vertical and focussed into a double subtractive monochromator (Acton Spectra Pro 2300i). A high resolution 300 g·mm^{-1} grating was used to spectrally disperse the emission before focussing into the streak camera. Fluorescence decays were obtained by averaging over a ~0.01 eV (2 nm) boxed section of the camera image.

4.3 Results

4.3.1 Raman and SSF spectroscopy

As a starting point in identifying the vibrational modes of MeLPPP, a review of results obtained previously using Raman and SSF spectroscopy was made. The Raman spectrum of MeLPPP in the solid-state is shown in Fig. 4.1A. The details of this spectrum are in excellent agreement with previous results,[72, 151] with the double peak at ~0.195 eV assigned to an aromatic CC stretch mode of the polymer backbone and a third peak at 0.164 eV identified as an interring CC stretch mode.

The SSF spectrum of MeLPPP at 13.5 K in the solid-state is shown for a range of excitation energies in Fig. 4.1B. As expected (section 3.8.1) a reduction to the inhomogeneous broadening is observed as excitation is made progressively into the low energy tail of the DOS. For excitation at 2.67 eV three vibrational modes are identified at 2.461, 2.494 and 2.570 eV, in good agreement with the results of previous studies.[73, 152] The associated vibrational energy of these modes was determined according to Eq. 4.4 below:

$$\hbar\omega_i = E^{0-0} - E_i^{0-1} \tag{4.4}$$

In Eq. 4.4 i denotes the mode under investigation, with 0-0 and 0-1 representing transitions originating from the zero-phonon level of the excited state to the zero-phonon and first order vibrational levels of the ground state respectively. By utilizing the simple approach of Ref. [152] and taking the position of the zero-phonon transition to be the centre of the first (high energy) peak in the fluorescence spectrum, (E^{0-0} = 2.637 eV), vibronic energies of 0.176, 0.143 and 0.067 eV are subsequently calculated. The first of these values is not in agreement with any of those obtained using Raman spectroscopy; no comparison of the latter

two values can be made, as Raman data was only measured down to 0.149 eV. The nature of

this discrepancy will be addressed in a later section.
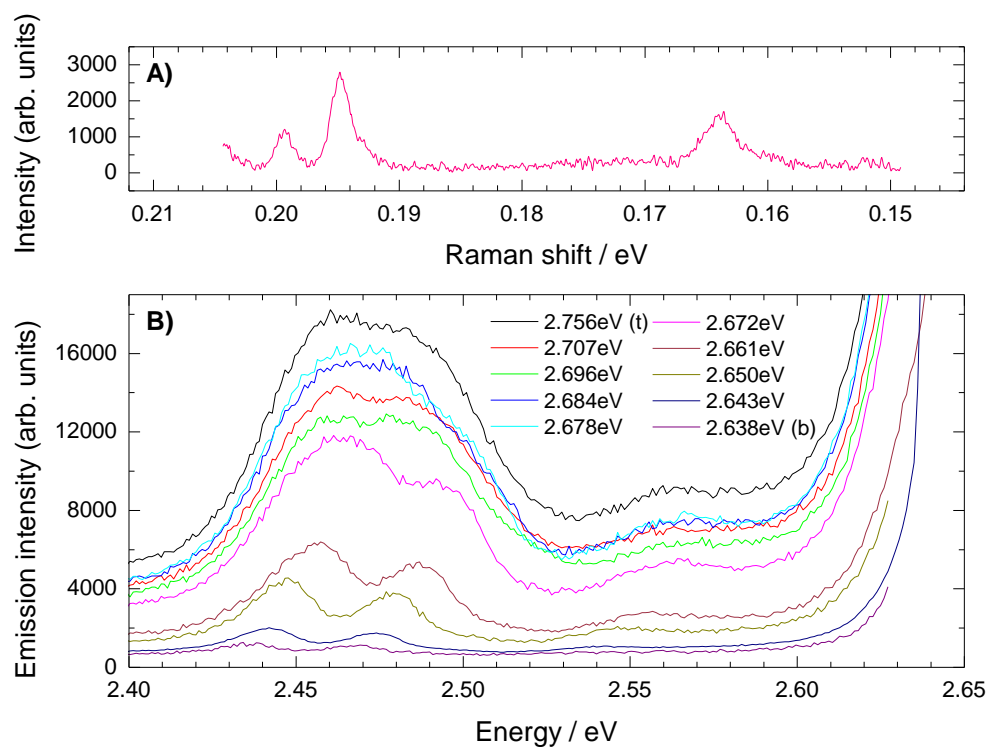
Figure 4.1: A) Raman spectrum of a MeLPPP film (recorded by Dr Helen Vaughan of the Organic Electroactive Materials Group, Department of Physics, Durham University). In accordance with the results of Ref. [72], two closely spaced peaks at 0.199 and 0.194 eV are identified as aromatic CC stretch modes, with a third peak at 0.164 eV identified as a CC interring stretch mode. B) SSF from a MeLPPP film at 13.5 K for various excitation energies (recorded by Dr Susanne Hintschich of the Organic Electroactive Materials Group, Department of Physics, Durham University). Individual vibrational modes can be observed in the fluorescence spectra at low excitation energies. A systematic shift of the spectrum with the laser line is observed for excitation energies below 2.672 eV.

For excitation energies equal to and below 2.661 eV the three vibronic features become well-resolved and are found to shift exactly with the excitation line. This behaviour is not consistent with SSF, but is however consistent with the onset of Raman emission (section 3.8.2). This

was confirmed by measuring the energetic separation of the observed vibronic features in the spectra with respect to the excitation energy: the values obtained (0.202, 0.170 and 0.104eV respectively for excitation at 2.650 eV) are in good agreement with the vibrational energies obtained from the Raman spectrum shown in Fig. 4.1A.

4.3.2　Review of theoretical studies

To consolidate the results of section 4.3.1 above, the vibrational energies obtained were compared against the results of a theoretical study performed by Karabunarliev *et al.* in which quantum chemical modelling, incorporating a rigorous treatment of electron-phonon coupling, was performed to reproduce the optical spectra of the oligomer ladder-type para-pentaphenyl (OLPPP$_5$).[69] Although it should be acknowledged that such a comparison between polymer and oligomer is by no means ideal, this theoretical work serves as a good starting position in which to gain further information concerning the physical nature of the vibrational modes in MeLPPP.

The results of Ref. [69] demonstrate that the optical spectra of OLPPP$_5$ include dominant contributions from four different vibrational modes: a C=C stretch mode ($\hbar\omega = 0.225$ eV), an aromatic CC stretch mode (0.196 eV), a transverse stretch (TS) of the phenyl groups (0.11 7eV) and a low energy skeletal stretch (SS) of the oligomer backbone (0.014 eV). A schematic of the molecular motion associated with each of these modes is shown in Fig. 4.2. While both the aromatic CC stretch and TS modes are also observed in the experimental data recorded from MeLPPP (see 0.202 and 0.104 eV measured using SSF spectroscopy), the theoretical considerations do not include a discussion of CC interring mode, identified in both the Raman and SSF data, at 0.17 eV. In addition, the C=C mode predicted from theoretical studies is not observed in the SSF data shown in Fig. 4.1B, nor has been recorded or discussed in previous Raman-based studies of MeLPPP which encompass the required spectral range.[72, 151, 153, 154] Note that the small rise observed at 0.204 eV in the Raman data shown in Fig. 4.1A is not of

the correct energy to be attributed to the C=C mode. The discrepancies between theoretical predictions and experiment may arise as a result of differences between the molecular dynamics of the polymer and oligomer, although no succinct conclusions can be made without a detailed understanding of the theoretical process involved in Ref. [69] which goes beyond the scope of this thesis.

C=C stretch

Aromatic CC stretch

Transverse ring stretch
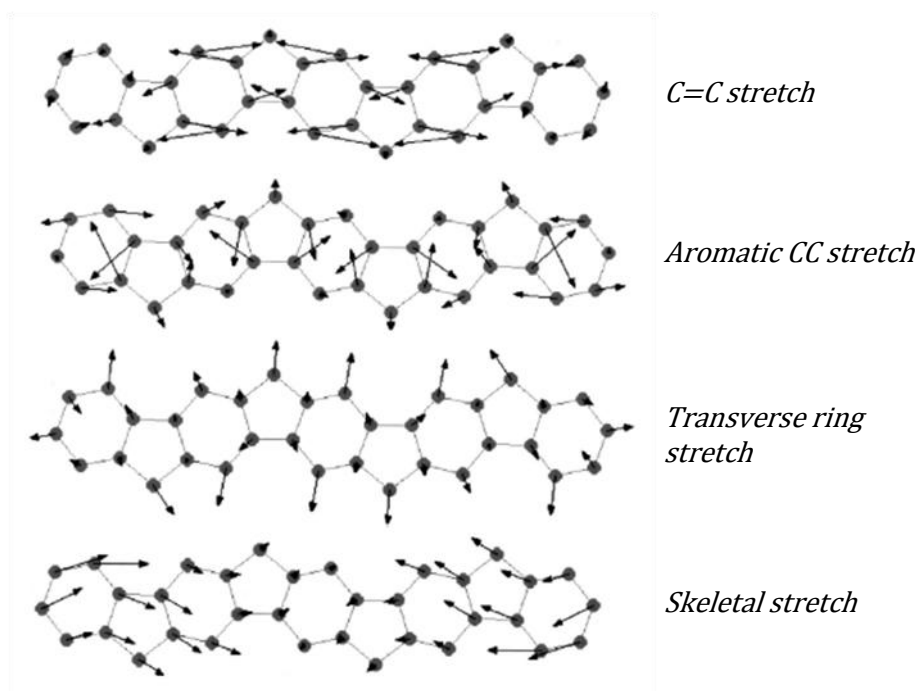
Skeletal stretch

Figure 4.2: Dominant vibrational modes in the optical spectra of the ladder-type oligomer OLPPP$_5$. From top to bottom: C=C stretch ($\hbar\omega$ = 0.226eV), aromatic CC stretch (0.196eV), transverse ring stretch (0.117eV) and skeletal stretch (0.014eV). Results and figure (adapted) from Ref. [69].

4.3.3 Temperature dependent fluorescence vibronic analysis

A quantitative study of the vibrational modes in MeLPPP was performed using steady-state fluorescence spectroscopy. Unlike the results obtained using Raman and SSF spectroscopy shown above, a direct and accurate identification of all of the vibrational modes in the

fluorescence spectra is hindered by a relative increase to the inhomogeneous broadening which results in the spectral overlap of adjacent modes. Aside from the need to measure the fluorescence spectrum at high temperatures, the increased broadening was a consequence of the relatively high excitation energy chosen in these experiments. In order to measure the complete fluorescence spectrum of MeLPPP and thus identify all of the contributing vibrational modes, it was necessary to excite the polymer far away from the spectral region of emission to avoid the presence of excitation scatter in the spectrum. The absorption and fluorescence spectra of MeLPPP in the solid-state at 295 K are shown in Fig. 4.3. The small Stokes shift (39 meV) recorded is consistent with that of a rigid ladder-type polymer,[58, 140] with three general vibronic features observed in the optical spectra. As a consequence of the small Stokes shift it was necessary to place the excitation line high up into the polymer DOS at 2.92 eV, imbuing the fluorescence spectrum with an increased degree of inhomogeneous broadening as compared to excitation at the absorption edge.

In order to extract the details of the underlying vibrational modes in the fluorescence spectrum, the data was modelled with a multi-gaussian model (using an in-built non-linear least squares minimisation routine of Microsoft Excel), with each peak representing the emissive transition of a different mode. This model is expressed below in Eq. 4.5:

$$F(E) = \sqrt{\frac{2}{\pi}} \frac{A_{0-0}}{w_{0-0}} \exp\left(-\frac{2(E - E_{0-0})^2}{w_{0-0}^2}\right) + \sum_i \sqrt{\frac{2}{\pi}} \frac{A_i}{w_i} \exp\left(-\frac{2(E - E_i)^2}{w_i^2}\right) \qquad (4.5)$$
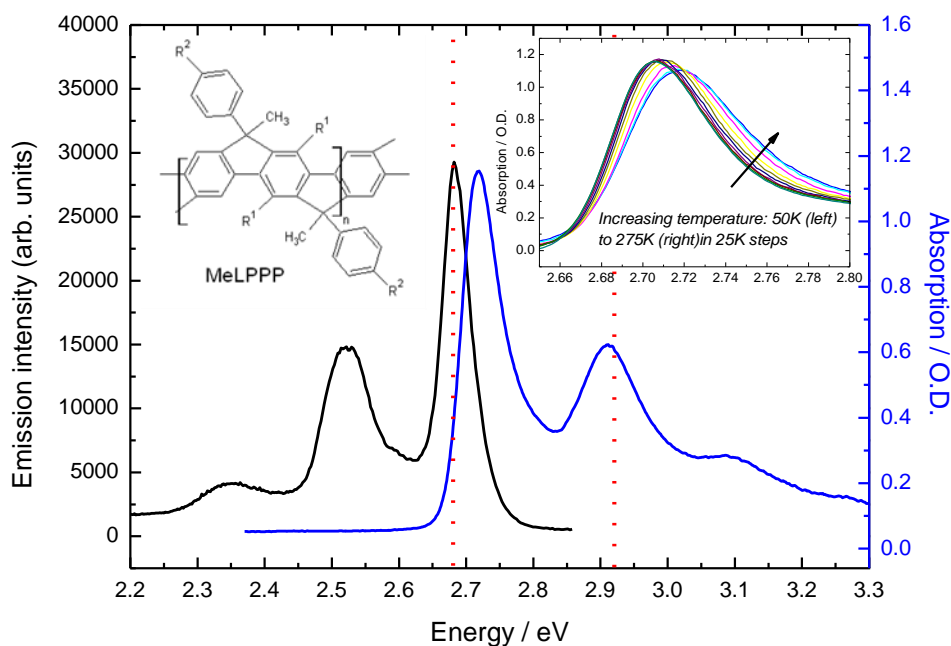
Figure 4.3: Absorption and fluorescence spectra (2.92 eV excitation) of MeLPPP in the solid state at 295 K. Excitation energies for fluorescence measurements (2.67 and 2.92 eV) are indicated (dotted red lines). Inset left: the chemical structure of MeLPPP; R^1 and R^2 are alkyl groups. Double-bridging between adjacent phenyl groups results in a rigid polymer backbone, of which the small Stokes shift observed (39 meV) is a consequence. Inset right: absorption spectrum of MeLPPP, recorded as a function of temeprature between 50 (left) and 275 K (right) in 25 K intervals. A blueshift of ~20 meV is recorded with increasing temperature between 50 and 275 K.

In the equation above $F(E)$ represents the fit to the fluorescence spectrum as a function of energy, A, E and w are the peak amplitudes, positions and widths respectively, with the sum i made over all possible contributing vibronic modes. Clearly the free application of a large number of peaks to a continuous dataset can be used to produce many possible fitting results. Therefore to ensure that the results produced by this fitting procedure remained physically consistent, several steps were taken which are listed below:

134

1. Peaks corresponding to the 0-0, aromatic CC, interring CC and TS modes were first incorporated into the model, with the positions of the 0-1 bond vibrational energies set to those energies as measured using Raman and SSF spectroscopy ($\hbar\omega_i = 0.2, 0.17$ and 0.104 eV for the aromatic CC^{0-1}, interring CC^{0-1} and TS^{0-1} transitions respectively). The positions of these peaks were fixed with respect to the position of the 0-0 peak, which was in turn left as a free parameter.

2. In accordance with the findings of the theoretical studies of Karabunaliev *et al.,* multiple repetitions of a low energy SS mode were also incorporated into the model. As the energy of this mode could not be confirmed in either Raman or SSF measurements (as described above), the corresponding vibrational energy was left as a free parameter.

3. All peak amplitudes were left as free parameters.

In early models all peak widths were linked to a single free parameter. The justification for this arose from the consideration that the width of each peak would be principally determined by the inhomogeneous broadening associated with the electronic polymer DOS and therefore would be independent of the particular mode in question. Using this condition in conjunction with points 1-3 above, the resulting model was however unable to successfully fit to the data at 50 K, primarily in three regions; in the vicinity of the broad feature at 2.45 eV, in the low intensity region around 2.55 eV and in the vicinity of the high intensity region at 2.64 eV. These issues were addressed as follows:

4. In order for the model to adequately fit to the data at 2.45 and 2.55 eV it was necessary to introduce additional peaks at 2.43eV and 2.51 eV. The physical justification for these peaks will be discussed in a later section.

5. In order to successfully fit to the data at 2.6 4eV it was necessary to allow the width of the 0-0 transition to vary as a separate free parameter. The physical origin of a

different broadening mechanism associated with the 0-0 is clearly a matter requiring further investigation, although it should be noted that single molecule studies performed on MeLPPP have demonstrated the homogeneous broadening of the 0-0 transition to be different from that of adjacent modes.[155]

The implementation of points 1 through 5 to the model produced a successful fit to the fluorescence spectrum of MeLPPP at 50 K which is shown in Fig. 4.4A. The errors included on the plot were estimated during the fitting process, in which it was noted that convergence to alternative positions/amplitudes was possible. As it can be clearly seen the SS mode identified from theory makes a significant contribution to the fluorescence spectrum, with multiple replicas as indicated measured at a vibrational energy of 0.026 eV. This value is of the same order of magnitude as the SS mode derived by Karabunaliev.[69]

In contrast with the classification of a previous study,[152] in order to correctly replicate the positions of both the aromatic and interring CC stretch modes, the 0-0 peak was not the largest observable peak in the spectrum, instead lying on the high energy shoulder of the SS^{0-1} peak at 2.663 eV. This observation resolves the discrepancy originally noted in the analysis of the SSF peaks, in which it was found that the measured vibronic energies were not in agreement with those obtained using Raman spectroscopy. It can now be seen that taking the 0-0 position to be the largest intensity peak in the fluorescence spectrum, as per the results of Ref. [152] is incorrect; if instead the vibrational energies in the SSF spectrum are calculated using the new 0-0 peak position at 2.663 eV, then the values obtained (0.202, 0.169 and 0.093 eV) become in much better agreement with the results of Raman measurements and theoretical predictions.
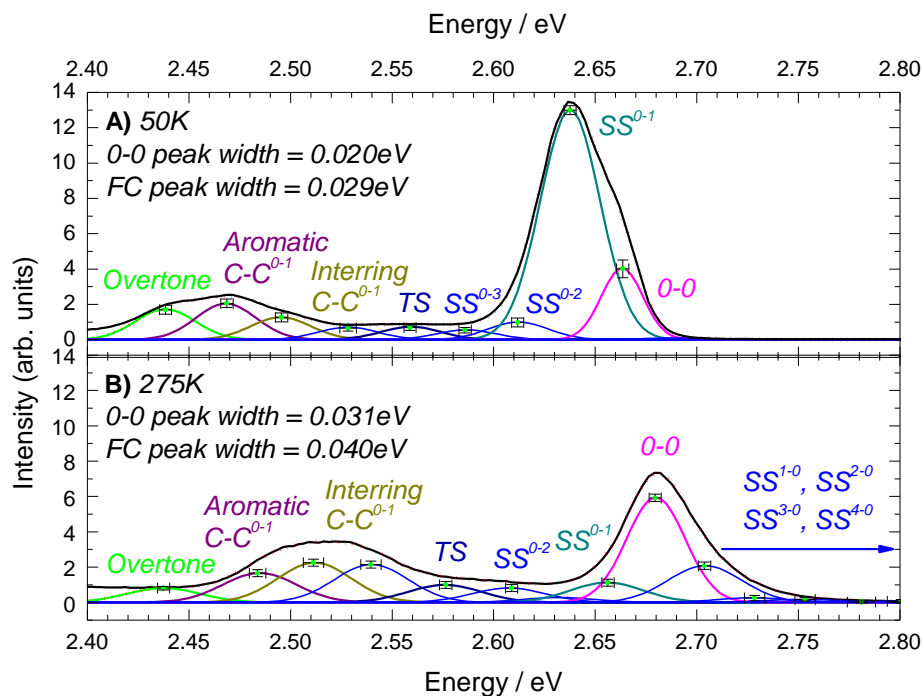
Figure 4.4: Normalised fluorescence spectra (2.92 eV excitation, black line) and multi-gaussian fit (red dotted line) of MeLPPP in the solid state at A) 50 K and B) 275 K. The individual gaussian components that make up the fit are shown, with key contributing peaks labelled. Note that the vertical scale of both plots has been fixed to allow comparison of the peak amplitudes at high and low temperatures.

Having successfully established the fitting procedure at 50 K, the fitting process was then repeated for the fluorescence spectra obtained at different temperatures. In order to measure relative changes in intensity of different vibronic modes, all fluorescence spectra were normalised to their area in order to take into account both the increasing quantum yield[20, 156] and the red-shift of the absorption spectrum away from the excitation line observed to occur with decreasing temperature. At temperatures of 100 K and above it was noted that the fitting procedure that was performed for 50 K was unable to successfully fit to the high energy shoulder of the fluorescence spectrum at ~2.75 eV. The temperature dependence of the

fluorescence spectrum in this region is shown in Fig. 4.5. As can be seen, a non-uniform increase in intensity in this region is noted with increasing temperature.

The temperature dependence of the emission intensity observed in Fig. 4.5 is indicative of a thermally activated contribution to the fluorescence spectrum. The possible role of an underlying defect state in this region can be ruled out on the basis that the increase in intensity observed is not reflective of a contribution from a single underlying state, which would emerge as a well defined peak. The behaviour in this region is instead attributed to the build-in of an increasing number of low energy thermally activated vibrational modes. On the basis that the only low energy mode identified in the spectrum at 50 K was the SS stretch mode, the high energy region was fitted by a fixed progression of SS modes with increasing peak energy with respect to the 0-0 transition. Each of these transitions would represent a transition from a vibrational sublevel in the excited state to the zero-phonon level in the ground state, i.e. a SS^{n-0} transition, where n represents the order of the excited vibronic state. These so-called 'hot' vibronic transitions have been discussed in context of conjugated polymers with torsional degrees of freedom, in which the thermal population of low energy rotational modes occurs instead.[39, 70, 71, 157]
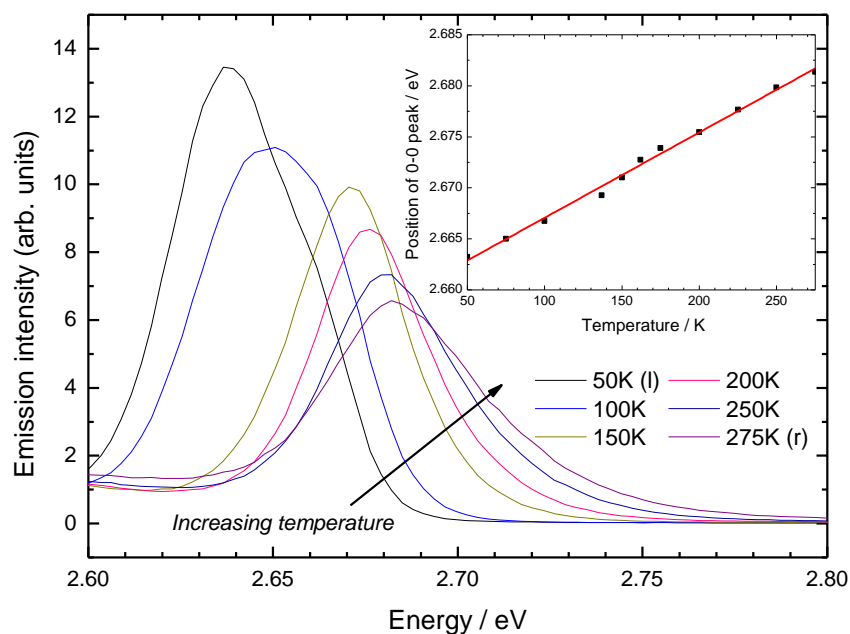
Figure 4.5: Normalised fluorescence spectra of a MeLPPP film (2.92 eV excitation) for a range of temperatures, highlighting the behaviour in the high energy region at 2.75 eV. For an increase in temperature from 50 K to 295 K a non-uniform increase in the intensity of the high energy shoulder of the main peak is observed, in addition to a blue-shift of the spectrum. Inset: 0-0 peak position plotted as a function of temperature, in which a near-linear blue-shift of the peak position is observed with increasing temperature.

Incorporating this progression produced a successful fit to the data at all temperatures; the result of the fitting procedure at 275K, including the extended progression of SS modes at energies both greater (SS^{n-0}) and smaller (SS^{0-n}) than the 0-0 energy, is shown in Fig. 4.4B. An approximate linear blueshift common to all peak positions (20 meV from 50 K to 275 K) is observed with increasing temperature; this is shown in the inset of Fig. 4.5. Note that an identical blueshift (~20 meV) was measured in the absorption spectrum of MeLPPP over the same temperature range (see inset of Fig. 4.3). These results are consistent with work of List *et al.*, in which the fluorescence spectrum of MeLPPP was measured as a function of temperature.[158] In that study the shift of the fluorescence spectrum with temperature was only

briefly attributed to the activation of vibrational modes in the polymer backbone, leading to a decrease in the average conjugation length of the polymer.   It has been well established in the literature that, in conjugated polymers displaying torsional degrees of freedom, rotational modes are able to generate breaks in the conjugation along the polymer backbone by twisting adjacent chain segments and preventing orbital overlap between them.[157, 159]   As discussed in section 4.1 above however, MeLPPP forms a rigid-rod structure in which such rotational modes are prohibited. The structural properties of MeLPPP as a function of temperature are discussed in a later section.

It is important to emphasise at this point that the plot of changing peak position shown in the inset of Fig. 4.5 was produced by taking the position of the 0-0 transition as obtained using the fitting procedure outlined above, as opposed to measuring the position of the high energy peak (shown in Fig. 4.5) directly from the plot without fitting, which appears to shift by ~50 meV. This apparent contradiction is also addressed in a later section.

In addition to the blue-shift with increasing temperature of the peak positions, a simultaneous increase in the peak widths (a change of 0.011 eV from 50 to 275 K) is also noted for all transitions.   This is reflective of an increase of the inhomogeneous broadening with temperature.[73] Note that a direct comparison of the peak widths obtained (~0.02 eV at 50 K) to those in the literature is not possible, as there are very few studies in which the vibrational modes in MeLPPP have been investigated. Comparison to the peak widths obtained in other conjugated polymers and oligomers is of limited use, primarily on the basis such widths are determined by the inhomogeneous broadening of the system which will vary from polymer to polymer. It should however be noted that peak widths obtained in this study were of the same order of magnitude as similar studies performed on poly(phenylenevinylene) (0.028 meV at 50 K)[157] and oligophenylenevinylene (0.015 eV at 15 K)[71] derivatives.

The temperature dependence of the peak amplitudes of key vibronic modes, as identified in the fluorescence spectra as part of the fitting process, are shown in Fig. 4.6. The amplitude of the first hot transition of the SS mode (SS^{1-0}) is shown in Fig. 4.6A. Although a general increase in peak amplitude is observed with increasing temperature, a marked change in behaviour is observed at a critical temperature of ~150 K. The thermal population of an excited vibronic mode is expected to follow a simple exponential dependence, according to Boltzmann (or equivalently Bose-Einstein) statistics. Although exponential-type behaviour is indeed noted either side of 150 K, the prominent change observed at that temperature is not consistent with simple thermal occupation and therefore requires another explanation.

The temperature dependence of the 0-0 and SS^{0-1} modes, in addition to that of the mode introduced at 2.43 eV at 50 K (as per the discussion of point 4 above) is shown in Fig. 4.6B. A distinct change in behaviour is observed in the data at ~137 K. The normalised temperature dependences of the SS^{0-1} and the hereto unidentified mode at ~2.43 eV were noted to be identical. On the basis of this observation and the fact that the unidentified mode at 2.43 eV is approximately offset by one quantum of the SS stretch mode energy from the aromatic CC^{0-1} mode, the mode at 2.43 eV is assigned to an overtone/combination[71] mode of the aromatic CC^{0-1} mode coupled to the SS^{0-1} mode. This overtone mode corresponds to a transition from the zero-phonon level of the excited state which results in the simultaneous excitation of two modes in the ground state.[71]
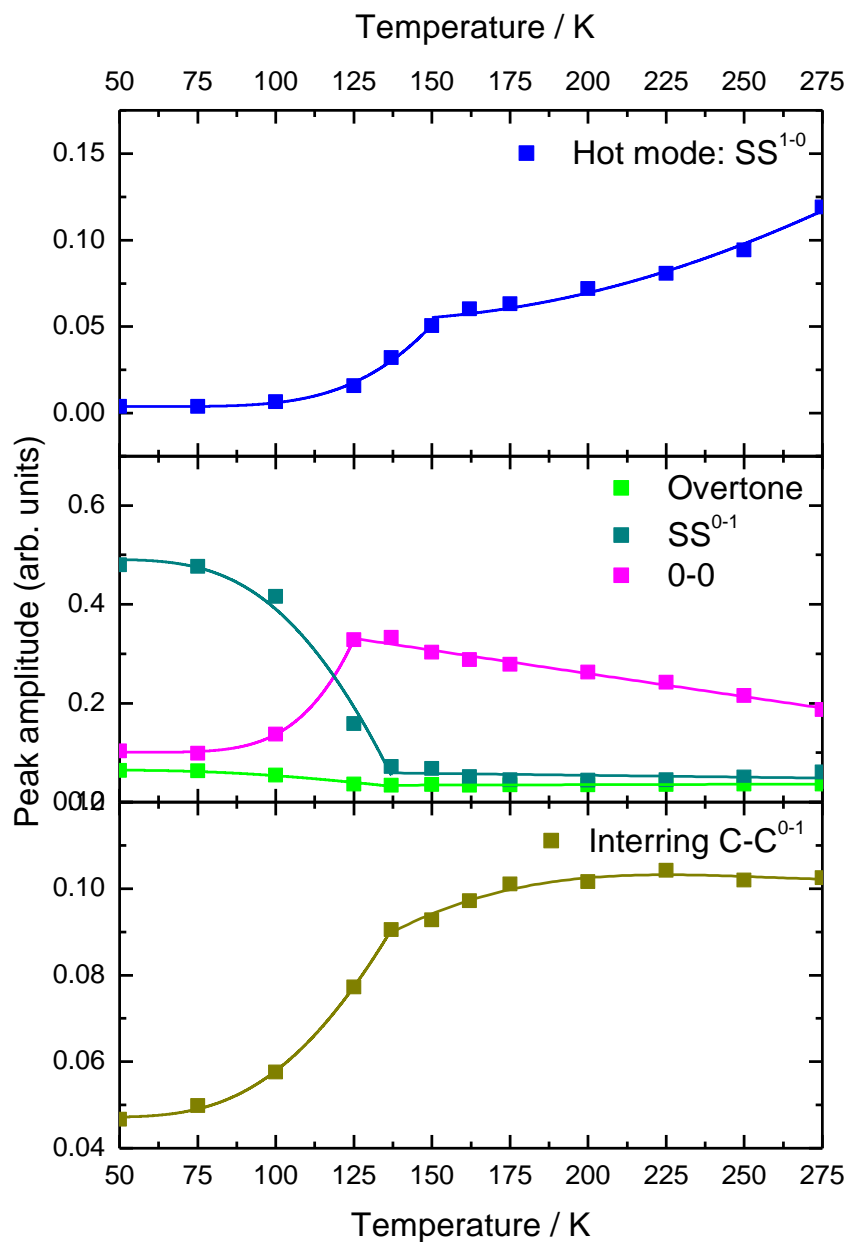
Figure 4.6: Temperature dependence of key vibrational modes in MeLPPP, as identified by fitting Eq. 4.6 to fluorescence data: A) thermally excited ('hot') SS^{1-0} mode (blue); B) 0-0 (magenta), SS^{0-1} (dark green) and overtone (green) modes; C) CC^{0-1} (brown) interring mode. Lines have been drawn as a guide to the eye. In all plots a distinct change in behaviour is noted between 125 and 150 K.

Between 275 and ~125-150 K a general increase in amplitude is observed for the modes with decreasing temperature. At 137 K however a large decrease in amplitude of the 0-0 mode is noted, with a concurrent increase in intensity observed in the SS^{0-1} mode. The similarity of the build-in and decay of the plots observed is indicative of a transfer of oscillator strength between the 0-0 and SS^{0-1} transitions. Indeed, a consequence of this transfer is that while at 50 K the SS^{0-1} is larger in amplitude than that of the 0-0 transition, at 295 K this order is reversed, with the 0-0 transition becoming the largest peak in the fluorescence spectrum. This crossover resolves the contradiction noted above concerning the apparent blue-shift measured directly from the fluorescence spectra (50 meV) and the true blue-shift (20 meV), as measured using the results of the fitting procedure; the redistribution of intensity between the 0-0 and SS^{0-1} modes gives the appearance of a much larger blue-shift than really exists.

The temperature dependence of the CC^{0-1} interring stretch mode is shown in Fig. 4.6C. A general increase in peak amplitude is recorded with rising temperature between 50 and 137 K. A change in behaviour is noted at 137 K, with only a small increase in amplitude recorded between 137 and 275 K. It should however be noted that this behaviour does not match that of the confirmed thermally activated SS^{1-0} mode shown in Fig. 4.6A, nor the 0-0 mode shown in Fig. 4.6B.

At this point it is important to take into consideration the potential role of self-absorption processes in the fluorescence spectra. Such an effect occurs when there is a large degree of spectral overlap between the absorption and fluorescence spectra. Upon inspection of Fig. 4.3 it can be seen that self-absorption effects in the fluorescence spectrum of MeLPPP at room temperature should be considered for energies greater that 2.725eV, thereby having a potential effect on the analysis of the 0-0 and hot SS^{n-0} peaks identified in the spectra. While such an effect would lead to an effective reduction of the peak amplitudes in this vicinity from their true values, the role of self-absorption in determining the change in behaviour observed at 137 K

can be eliminated on the basis that the temperature dependence of the overtone (Fig. 4.6B) and C-C$^{0-1}$ interring (Fig. 4.6C) modes were also observed to undergo a change in behaviour at temperatures around 150K; these modes however lie well beyond the region of spectral overlap between absorption and fluorescence where self-absorption effects cannot take place.

Following on from the observation of non-trivial behaviour in the temperature dependence of the mode amplitudes shown in Fig. 4.6, it was of interest to measure the temperature dependence of other key photophysical parameters in MeLPPP. An effective measure of the photoluminescence quantum yield (PLQY) was recorded by measuring the area under the (not normalised) fluorescence spectrum divided by the absorption measured at 2.92 eV at the same temperature; a plot of the temperature dependence of this quantity is shown in Fig. 4.7. A general increase of the PLQY with decreasing temperature is observed. Such behaviour is to be expected, as exciton loss mechanisms such as migration to trap states are hindered at lower temperatures.[20, 156, 158] The temperature dependence of the PLQY however undergoes a clear change in behaviour, again at ~150 K. To gain a better understanding behind the origin of this critical point, the temperature dependence of the PLQY was compared against the summed contribution of the 0-0 and SS$^{0-1}$ modes, which having been identified as the two largest modes in the fluorescence spectrum were expected to make the most significant contribution to the total PLQY; this is also shown in Fig. 4.7. As it can be seen the summed contribution largely replicates the behaviour of the PLQY with temperature, including the change in behaviour at 150 K. This observation confirms that the physical phenomenon behind the critical point observed in the PLQY at ~150 K is the same as that responsible for the critical points observed in the temperature dependence of the individual modes, shown in Fig. 4.6.
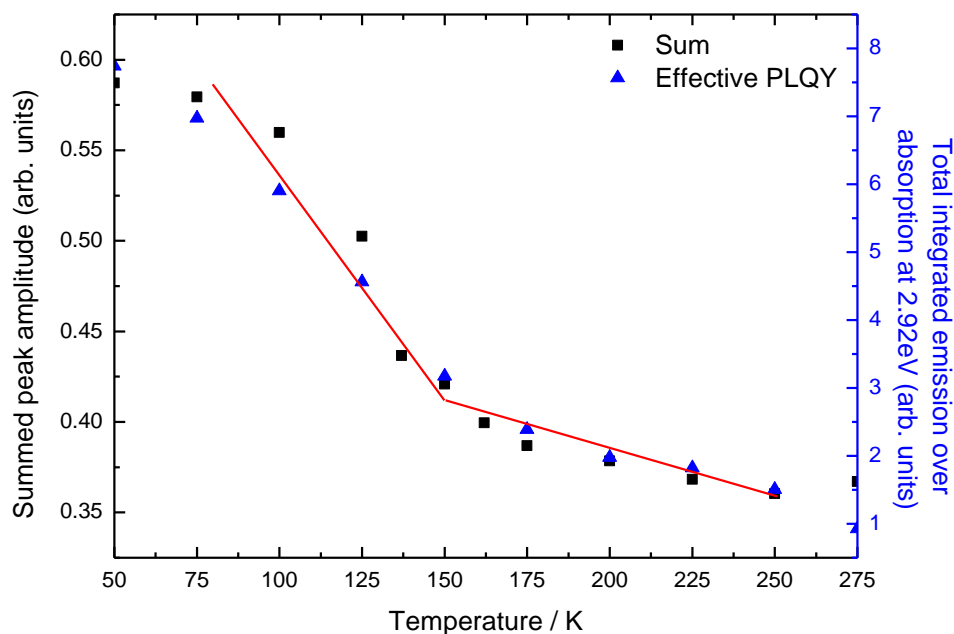
Figure 4.7: Temperature dependence of the area under the emission spectrum, divided by the absorption at 2.92 eV (blue triangles), taken as an effective measure of the PLQY. The temperature dependence of the summed contribution of the 0-0 and SS^{0-1} peak amplitudes (black squares) has also been included for comparison. Lines have been drawn as a guide to the eye. As for other measurements, a distinct change in behaviour of the temperature dependence of the PLQY is noted at ~150 K and is replicated in the temperature dependence of the summed contribution.

4.3.4 Polarised fluorescence studies

Polarised fluorescence studies were undertaken in aligned films of MeLPPP in polyethylene in order to reveal information concerning the orientation of the transition dipole moments associated with each vibrational mode. A quantitative analysis of the fluorescence anisotropy from stretched systems is complicated by the introduction of an systematic anisotropic property of the sample at hand (namely the stretch direction) and does not proceed simply.[160] In the context of this study however only a demonstration of an anisotropic sample response was

required; consequently the ratio of emission parallel and perpendicular to the excitation direction (as described in Eq. 4.3) could be used as a sufficient qualitative measure. This ratio is shown for a stretched MeLPPP film at 50 K for two different excitation energies in Fig. 4.8.

As can be observed at both excitation energies, distinct features emerge in the ratio of polarised emission, appearing as dips in the ratio of polarised emission recorded. These features become more resolved at lower excitation energies due to the reduction in the inhomogeneous broadening. An inspection of the features obtained at low excitation energy in Fig. 4.8 reveals a progression of dips similar to those obtained in SSF and standard low temperature fluorescence spectroscopy, indicating that the features in the ratio are directly related to the vibrational modes previously identified. A direct comparison can also be made in Fig. 4.8B for low energy excitation, where there is a clear correlation between the vibronic modes in the fluorescence spectrum and the polarised ratio. A systematic offset between the fluorescence peaks and dip positions is observed and attributed to inaccuracies in the pre-recorded instrument correction factor with energy.
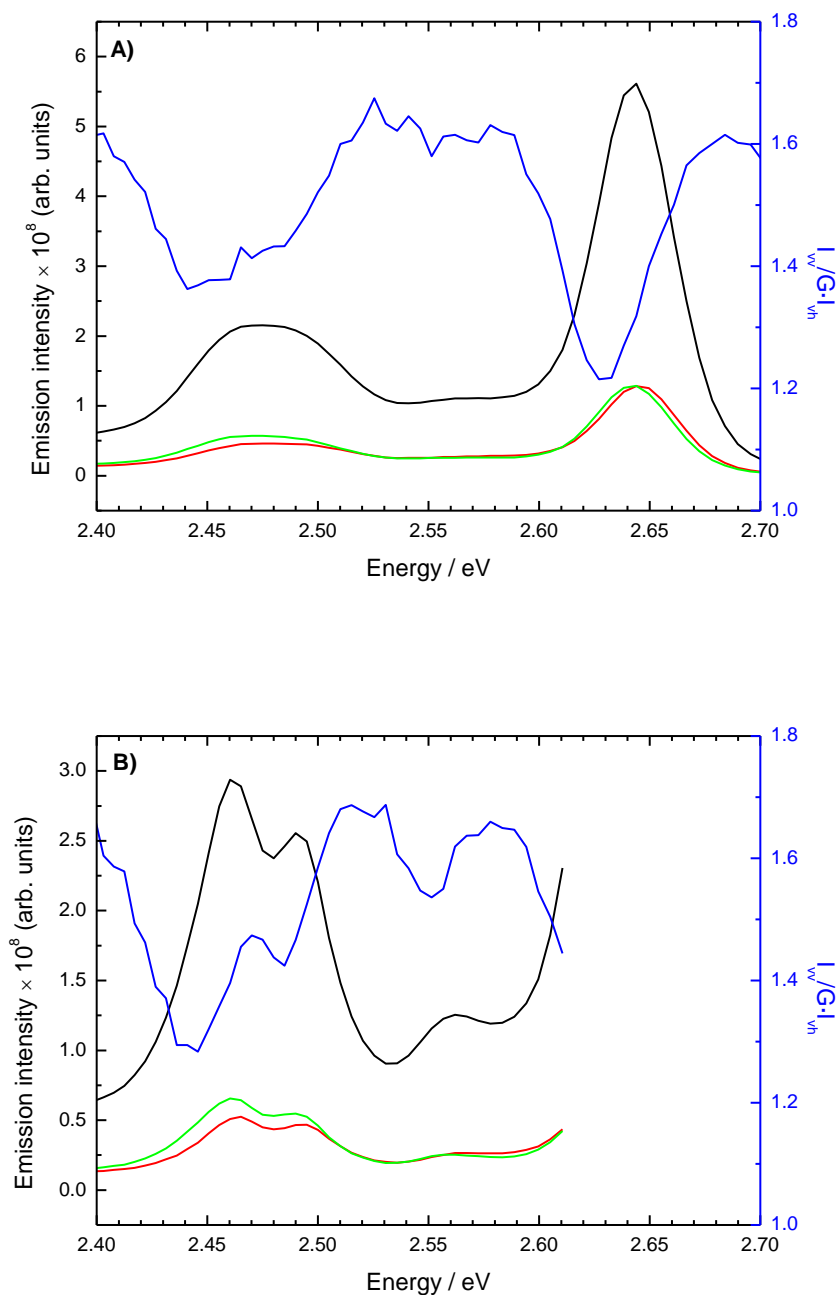
Figure 4.8: Polarised fluorescence of a stretched MeLPPP film at 50 K, A) 2.92 eV and B) 2.67 eV excitation. The ratio of polarised emission, calculated according to Eq. 4.3, is also shown (blue lines). Clear features at the position of the vibrational modes previously identified, are resolved at both excitation energies. Polarised (I_{vv}; red lines and I_{vh}; green lines) and un-polarised (black lines) fluorescence spectra have been included for reference.

To confirm the correlation between the observed dips in the polarised ratio and the previously identified vibrational modes in MeLPPP, the energetic separation between the dip positions and the 0-0 transition was calculated. To identify the 0-0 energy of the stretched spectrum for excitation at 2.92 eV, the fitting procedure outlined in section 4.3.3 above was repeated for the fluorescence spectra of the stretched film. Using the 0-0 energy extracted as a result of this process (2.669 eV), separations of 0.218, 0.184, 0.119 and 0.039 eV were obtained from Fig. 4.8A, with similar values of 0.223, 0.184 and 0.118eV obtained at 2.6 7eV excitation (using the same 0-0 position). Taking into account the aforementioned potential systematic error of ~0.01eV between the measured spectra and the polarised ratio, these values are in good agreement with the vibrational energies of the $C-C^{0-1}$ intra-ring, $C-C^{0-1}$ interring, TS and SS modes of the polymer. As a confirmation of the systematic error, it was also noted that the relative separation of the polarised features with respect to one another (as opposed to the position of the 0-0 transition) were in excellent agreement with the relative separation of the peak positions obtained using both fluorescence and SSF spectroscopy.

4.3.5 Time-resolved fluorescence spectroscopy

Having shown in section 4.3.3 that the mode structure of MeLPPP influences the fluorescence anisotropy, it becomes pertinent to ask whether the vibrational mode through which fluorescence occurs also has any influence on the fluorescence lifetime. To this end time-resolved fluorescence studies of both film and dilute solution samples of MeLPPP were performed using a streak camera.

Time-resolved fluorescence measurements of MeLPPP in dilute solution are shown in Fig. 4.9. Single energy decays, recorded at the vibronic positions identified in the analysis of section 4.3.3, were extracted from the streak camera image (Fig. 4.9A) by selecting and averaging over a 0.01 eV window; the results of this process are shown in Fig. 4.9B. As it can be seen the

fluorescence decay dynamics are identical for the different vibronic modes measured. Indeed, further measurements at other emission energies confirmed that the decay dynamics were completely independent of energy. In light of this a global mono-exponential fit to these datasets was performed to measure the fluorescence lifetime, with a value of 395 ps obtained.

A similar analysis of the fluorescence dynamics was repeated for MeLPPP in film. Multi-exponential dynamics were noted across the complete spectrum,[18, 20] with in particular a long-lived component, concurrent with a small peak centred at ~2.57 eV in the fluorescence spectrum observed in the streak camera image. Interestingly, this peak and the corresponding lifetime component were observed to become more pronounced at lower temperatures; the streak camera image of MeLPPP in film at 100 K is shown in Fig 4.10. Independent multi-exponential analysis of the fluorescence dynamics of single-energy decays extracted from this image revealed a long lifetime component of 489 ps (77% contribution by pre-exponential amplitude) at 2.57 eV. This lifetime component was noted to be much longer than the corresponding component noted in the vicinity of the 0-0 transition at 2.64 eV (157 ps, 26%).
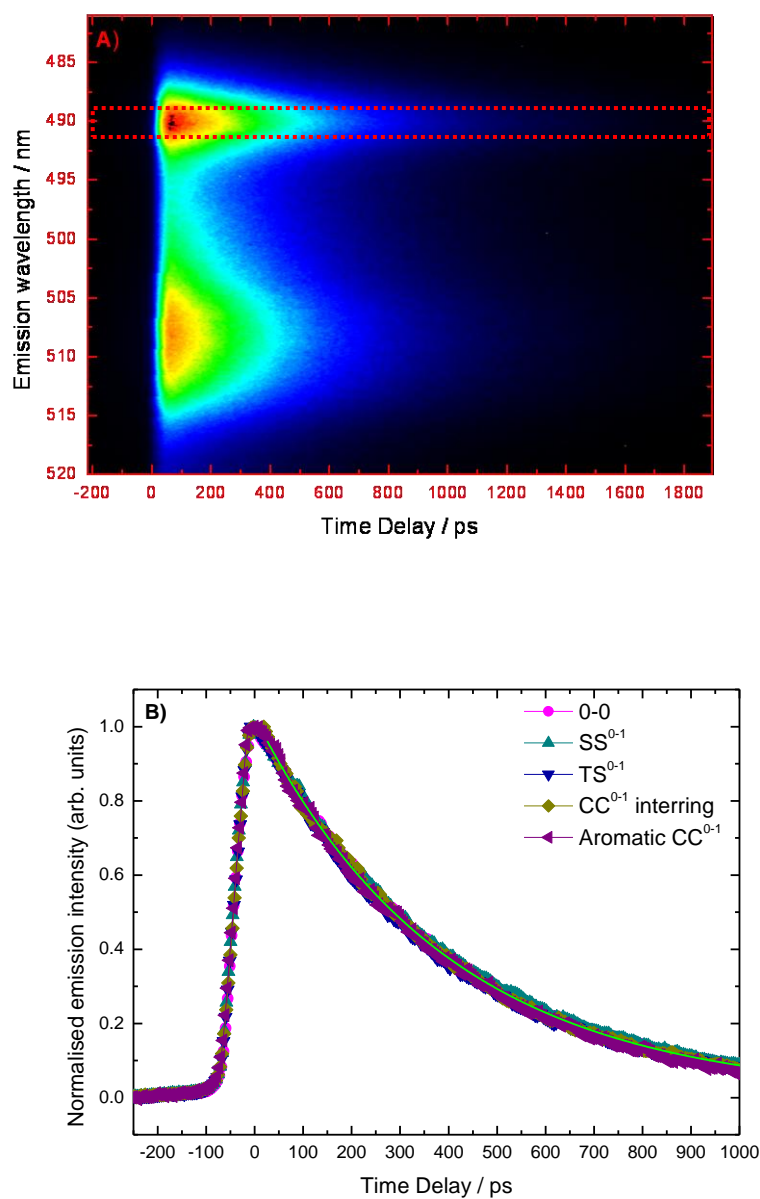
Figure 4.9: Time-resolved fluorescence data (2.92 eV excitation) of a dilute MeLPPP solution at 295 K: A) streak camera image, including sample boxed region used to measure single energy dynamics and B) selected single-wavelength decays at vibrational mode positions. The result of a global analysis performed to measure the fluorescence lifetime (green line) is also shown.
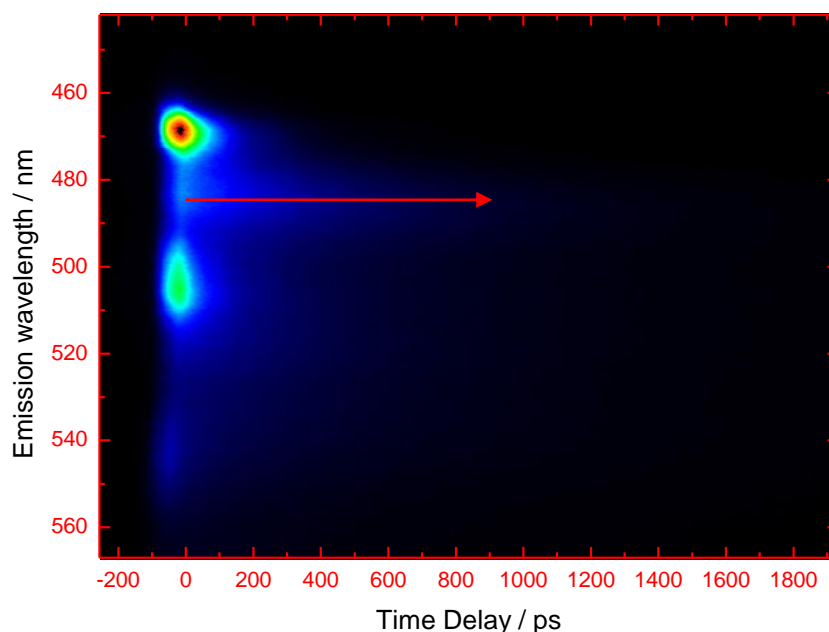
Figure 4.10: Streak camera image (2.92 eV excitation) of a MeLPPP film at 100 K. At this temperature the fluorescence lifetime can be directly observed to change with energy, with a prominent long-lifetime state at ~2.57 eV (485 nm) highlighted in the data.

The observation of energy-dependent fluorescence dynamics is a well documented property of performing measurements in film, in which interchain exciton migration can occur. As described in section 2.6, exciton migration typically occurs through exciton energy transfer from high to low energy chromophores. These different chromophore populations by their nature emit at different energies and therefore the population of these sites can be quantified as a function of time by measuring the fluorescence dynamics at different energies. As on average an exciton will transfer off of these high energy chromophores to move to a lower energy state, exciton migration at high emission energies will appear as a significant decay term in the fluorescence dynamics. The amplitude of such a component is reduced however by moving the emission energy to lower energies, corresponding to chromophores low down in the polymer DOS, as the probability of off-chromophore energy transfer is reduced.

Exciton migration has been well-documented to occur on timescales of the order of 10 ps, [12, 18, 80, 161] and therefore any changes to the fluorescence dynamics as a result of exciton migration can only involve time constants of that order. The observation of a substantial increase to a lifetime component of the order of several hundreds of picoseconds cannot be a consequence of exciton migration and requires another explanation.

To gain more information about the nature of the long lifetime component at 2.56 eV, the fluorescence dynamics at this energy were recorded as a function of temperature and compared against the corresponding dynamics measured at the approximate position of the 0-0 transition. Before performing such measurements however, it was first necessary to choose the correct emission energies at each temperature for both the 0-0 transition and the new peak feature. The shift of the fluorescence spectrum with temperature, as measured by using the zero-delay of the streak camera images, is shown in Fig 4.11. Whereas a red-shift of the fluorescence spectrum occurs with decreasing temperature, as confirmed in section 4.3.3, no shift is observed for the small peak feature at 2.57 eV. Single-energy fluorescence dynamics selected from the image were chosen to take these observations into account; while the dynamics of the small peak feature were recorded at 2.56 eV at all temperatures, the spectral window for which the 0-0 fluorescence dynamics was measured was changed according to the red-shift of the fluorescence spectrum with temperature.
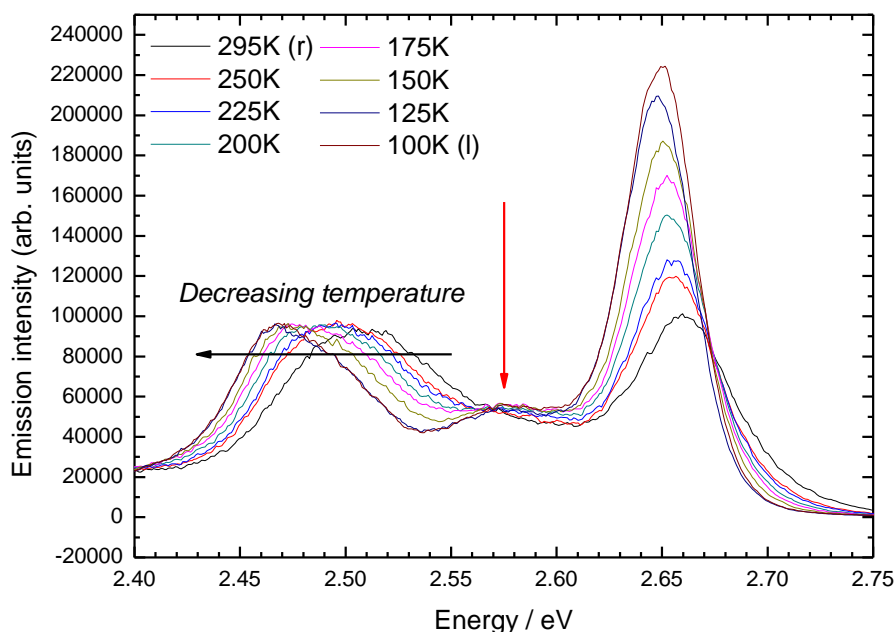
Figure 4.11: Fluorescence spectrum of the MeLPPP film at different temperatures, as recorded by selecting the zero-delay of the corresponding streak camera images. A small peak feature at ~2.57 eV is highlighted. In contrast to the general red-shift of the fluorescence spectrum with decreasing temperature, the peak feature is observed to remain at ~2.57 eV for all temperatures. Note that self-absorption is observed to heavily affect the amplitude of the 0-0 and SS transitions at ~2.65 eV.

The dynamics of the 0-0 transition at different temperatures were measured using a bi-exponential global fit, with one lifetime component linked between datasets to reflect a temperature independent fluorescence lifetime; the second lifetime component and all amplitudes were left as free parameters. This analysis yielded lifetime components of ~40 and 147 ps, with the former of these components presented as an average of the different values obtained; the results of this fitting process when applied to data recorded at 100 K are shown in Fig 4.12. The ~40 ps component is consistent with previously reported values of exciton migration in conjugated polymers,[12, 18, 83, 162] although similar lifetime components have also been associated with conformational relaxation processes in other systems.[30] MeLPPP is

however widely considered to be a rigid-rod system in which such relaxation processes are prohibited, and it is therefore more likely that the 40 ps component is associated with migration.
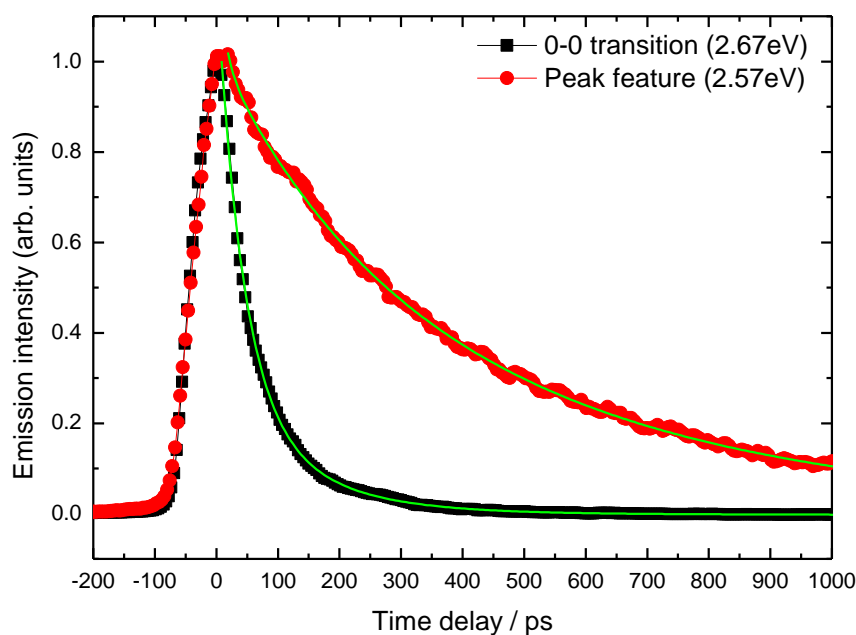
Figure 4.12: Normalised fluorescence dynamics of a MeLPPP film at 100 K at selected emission energies. A long-lived component is observed at 2.57 eV (red circles) and is concurrent with the appearance of a small peak in the fluorescence spectrum (see Figs. 4.10 and 4.11). The lifetime of this state (416 ps) is much greater than the lifetime as measured at the position of the 0-0 transition (2.67 eV, black squares). The results of multi-exponential global fitting (performed across all temperatures measured) to the data have been included (green lines).

The 147 ps component is assigned as the fluorescence lifetime of MeLPPP in film. Inspection of the literature describing similar measurements of the fluorescence lifetime of MeLPPP in film reveal a large number of different reported values, most typically of the order of ~200 ps,[80, 163] although values as short as 80 ps[104] and as long as 500 ps[18] have been reported. Repeat experiments in which the fluorescence lifetime of MeLPPP in film was measured also

yielded different results, with values varying from 113 to 200 ps obtained using the streak camera. No work in the literature has considered in detail the fundamental reason behind the variation in the fluorescence lifetime of MeLPPP with different experiments, although in the work of Hildner *et al.* it was briefly proposed that behaviour could be attributed to the varying effectiveness of intra-DOS relaxation processes.[18]

Following on from the analysis of the fluorescence dynamics of the 0-0 transition, global analysis of the fluorescence dynamics at 2.56 eV at different temperatures was performed. On the basis that the fluorescent dynamics at this energy would contain a contribution from the polymer fluorescence lifetime, one decay component was fixed to 147 ps, as obtained above; the second component was linked across all temperatures. This process yielded a longer lifetime of 416 ps. The results of this fitting process when applied to fluorescence dynamic data taken at 100 K are also shown in Fig 4.12.

4.4   Discussion

4.4.1   SSF and Raman spectroscopy

In the SSF data shown in Fig. 4.1B, the emergence of well resolved, sharp peaks that shift in energy exactly with the excitation line at excitation energies equal to and below 2.661 eV is ascribed to a transition from SSF to Raman emission. The origin of this crossover can be understood by considering the position of the excitation line within the absorption spectrum. At 2.756 eV excitation occurs within the low-energy edge of the absorption spectrum at 13 K (see inset Fig. 4.3), fulfilling the required conditions for SSF spectroscopy. By decreasing the energy to 2.661 eV and low energies, excitation becomes non-resonant below the edge of the absorption spectrum, resulting in Raman emission in the place of SSF.

Instances of the transition between fluorescence and SSF to Raman spectroscopy have not been clearly identified in the literature.[152] The transition to Raman emission when exciting off-resonance must be considered in the interpretation of fluorescence data at the risk of forming incorrect conclusions. For example, in SSF one aims to excite localised excitations in the bottom of the DOS. This is achieved by tracking the red-shift of the fluorescence with decreasing excitation energy. When the fluorescence no longer shifts, excitation of the localised states has been achieved. If however a crossover to Raman emission occurs the fluorescence peak positions will continue without end to shift with a fixed separation with respect to the excitation source, preventing identification of the correct excitation energy for SSF. This would lead to complications for example in the vibronic analysis of fluorescence spectra; Raman emission will shift the peak positions away from their true energetic positions and thus change the effective vibronic energies measured.

4.4.2 Temperature dependent fluorescence vibronic analysis

Using experimental results obtained from Raman and SSF spectroscopy, in addition to the results of theoretical calculations performed by Karabunarliev *et al.*,[69] a simple model was established to fit the fluorescence data obtained from MeLPPP in film at different temperatures. The success of this model was dependent on the introduction of two 'new' contributions that could not be identified in either the Raman or SSF data. The first of these peaks, a vibronic contribution at ~2.43 eV, was determined to be an overtone mode combining C-C$^{0-1}$ interring mode and the SS$^{0-1}$ mode. This conclusion was on the basis that the temperature dependence of that mode amplitude closely followed the temperature dependence of the SS$^{0-1}$ mode. It should be noted that the position of this mode is also in good agreement with the energy of a C=C stretch mode, as identified in theoretical work.[69] This possibility was rejected however as no C=C mode could be identified in either the Raman (as measured elsewhere[72, 151, 153, 154]) or SSF data.

The justification of a second contribution, consisting of a peak at ~2.51 eV, is beyond the limits of this study. Theoretical investigations of the vibrational modes in conjugated polymers have often proved unable to fit to experimental data in similar low intensity regions of fluorescence.[71]   In some polymers these low intensity regions have been justified by the presence of a large number of closely spaced rotational modes of the polymer backbone;[69] in a ladder-type conjugated polymer however, such as MeLPPP, examples of such rotational modes are prohibited by bridging between adjacent phenyl groups along the polymer backbone. As such a complete theoretical description of the vibrational modes in MeLPPP continues to be of interest to the research community.[164]

The results of the fitting process were able to confirm primary contributions in the fluorescence spectrum of MeLPPP from an aromatic CC stretch mode, a CC interring stretch mode, a TS mode and a SS mode at 50 K; agreement to results obtained from theoretical, Raman and SSF studies could however only be accomplished on the basis that the 0-0 transition lie off of the largest peak in the spectrum. A progression of modes in the fluorescence spectrum corresponding to transitions originating from thermally excited vibrational levels of the SS mode in the excited-state was observed at higher temperatures. The existence of such a progression can be readily justified by considering that vibrational energy of the SS mode (26 meV) is comparable with the thermal energy available at room temperature (~20 meV). Subsequently one would expect these modes to be thermally populated (according to simple Boltzmann statistics) even after thermalisation according to Kasha's rule[40] has occurred, with the potential for multiple orders of the mode to be excited at room temperature, albeit with a substantially reduced probability for higher mode orders.

The existence of these so-called hot vibrational modes in the excited state can be used to explain several features of the temperature dependence of the mode amplitudes shown in Fig. 4.6. Given that the total number of excitons in the excited state is approximately fixed (for

the same excitation density), population of the thermally excited levels occurs at the expense of the number of excitons in the zero-phonon level; this can be observed as a decrease in the amplitude of the 0-0 transition upon increasing the temperature from 125 to 295 K. The decrease in amplitude also affects the temperature dependence of some of the modes that are also dependent on the population of the zero-phonon level in the excited state; over the same temperature range a small decrease in intensity is also observed for the SS^{0-1} and overtone modes (Fig. 4.6B) in addition to a large decrease in intensity of the aromatic CC^{0-1} stretch mode (data not included here).

In contrast to these findings the temperature dependence of the CC^{0-1} interring stretch mode is observed to behave in the opposite manner, with an increase in intensity observed between 125 and 295 K. This behaviour is attributed to the presence of emissive transitions to different vibrational levels in the ground state originating not only from the zero-phonon level of the excited state, but also from thermally populated hot levels also in the excited state. Transitions from these thermally excited levels occur to all other vibrational levels in the ground state, resulting in a progression of modes offset by an integer number of quanta of the SS mode. As a consequence, some transitions beginning from the zero-phonon level overlap with some transitions originating from the hot levels in the excited state; for example, a transition beginning from the first thermally excited SS mode in the excited state to the first aromatic CC mode in the ground state will overlap with the CC^{0-1} interring stretch transition. This results in the actual temperature dependence of the modes differing from their projected behaviour, as the temperature dependence of a particular peak is determined by contributions from both the zero-phonon and hot vibrational levels in the excited state, with the relative ratio of the two mediated by the degree of thermal population of the hot fluorescence levels. This is the reason for the observed net increase in amplitude of the CC^{0-1} interring stretch mode with temperature between 125 and 175K observed in Fig. 4.6C; as the temperature is increased, there is an

effective increase to the peak amplitude due to an increasing contribution from the first hot aromatic CC stretch transition at those peak energies. It should be noted that contributions from higher-order hot levels, e.g. those from the second and third thermally excited SS levels, are not expected to have as significant an influence due to the smaller population of excitons in those levels.

Following the same line of reasoning as outlined above, one would also perhaps expect to see a similar influence of hot fluorescence on the temperature dependence of other vibronic modes in the spectrum. For example, the 0-0 transition would also be expected to contain an additional contribution from the degenerate transition originating from the first thermally excited level of the SS mode in the excited state to the first excited level of the SS mode in the ground state (effectively the SS^{1-1} transition); no such contribution however is readily observed. It is possible in this circumstance that the amplitude of the SS^{1-1} transition is much weaker than the 0-0 transition and therefore the influence of hot fluorescence at this energy is not easily observed, however this is speculation. The amplitude of the hot fluorescence transitions will be dependent on the overlap integrals of the relevant vibrational wavefunctions involved and as such a detailed understanding can only be achieved by calculating these integrals, which is beyond the course of this experimental study.

It is clear from the discussion above that the SS mode has a significant influence on both the form and temperature dependence of the fluorescence spectrum of MeLPPP. The nature of electron-phonon coupling to such low energy modes has however recently been challenged by Hildner *et al.*.[155] In this work single-molecule spectroscopy was performed on MeLPPP in a variety of solid-state matrices and it was demonstrated that a low energy mode of ~20 meV, corresponding to the SS^{0-1} mode identified previously, was frozen out at low temperatures. In these studies this low energy mode was attributed to weak coupling of the polymer to low-frequency vibrations of the surrounding solvent matrix.

The results of my study are not sufficient to provide further clear evidence for or against the model outlined in Ref. [155]. If they are however to remain consistent with that framework, then the results of this study provide further information into the nature of the coupling between solvent and matrix. For example, the results of temperature dependent measurements would suggest that the solvent coupling is not only responsible for a single transition peak in the fluorescence spectrum, but an entirely new series of transitions. Thermal population of such a mode must occur with increasing temperature, with multiple replicas of the mode excited at high temperatures, resulting in the appearance of the hot SS^{1-0}, SS^{2-0}, SS^{3-0} and SS^{4-0} transitions identified at 275 K. Furthermore this solvent mode, including its excited state replicas, must also be able to couple to each vibrational mode individually, in order to explain the temperature dependence of the CC^{0-1} interring stretch mode shown in Fig. 4.6C.

The concept of hot fluorescence can be used to successfully explain the temperature dependence of the mode amplitudes between 150 and 275 K. For temperatures equal to and less than 150 K however a critical change in behaviour is observed. This is clearly demonstrated in the temperature dependence of the zero-phonon transition, which suddenly decreases between 125 and 50K. Furthermore it is clear that this decrease in intensity is matched at the same time by the sudden increase in intensity of the SS^{0-1} transition occurring at ~137 K and the change in the temperature dependence of the hot SS^{1-0} transition at ~150 K. The HR parameter for the SS mode, as calculated using Eq. 4.2, is shown in Fig. 4.13. Whereas between 275 and 137 K the HR parameter remains approximately constant, between 125 and 75 K a dramatic increase is observed with decreasing temperature. Given that the vibrational energy of the SS mode was observed to remain approximately constant with temperature (~24 meV), the change in the HR parameter shown in Fig. 4.13 can be considered to be reflective of a change in the value of ΔQ with temperature.
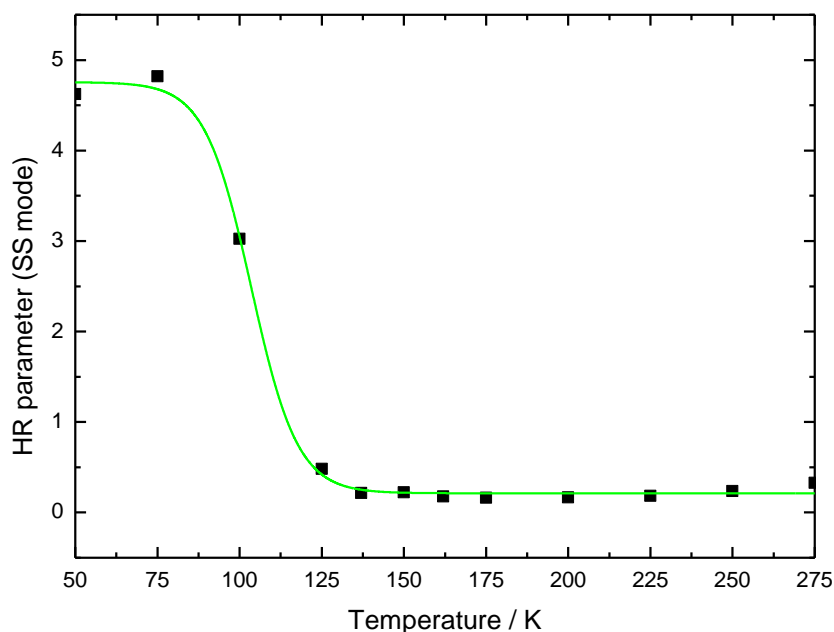
Figure 4.13: The temperature dependence of the HR parameter for the SS vibrational mode in MeLPPP, calculated using Eq. 4.2. The HR parameter is observed to remain approximately constant between 275 and 137 K. At a critical temperature of ~125 K a dramatic increase is observed to occur which is attributed to a change in conformation of the polymer. Lines have been drawn as a guide to the eye.

It is proposed that the change in behaviour at ~125 K is the result of a change in conformation of the polymer chain at that temperature. It also follows that the similar critical points observed in the temperature dependence of the various modes amplitudes shown in Fig. 4.6, and by extension the temperature dependence of the PLQY shown in Fig. 4.7, are also a consequence of this change in conformation.

It is clear that below ~125 K any change in the polymer conformation must dominate over any temperature dependence of the vibrational modes, as evidenced by the fact that the 0-0 transition amplitude is observed to decrease from 125 to 50 K; if the temperature dependence of

this mode was solely governed by the thermal population of hot vibronic levels, then one would expect to observe an increase in amplitude of 0-0 transition with decreasing temperature.

According to the FC principle, the absorption and emission spectra of a conjugated polymer should form the mirror images of one another. It is therefore not unreasonable to suggest that the influence of temperature on the fluorescence spectrum of MeLPPP as discussed above would also extend to the temperature dependence of the absorption spectrum. Due to increased inhomogeneous broadening, a detailed analysis of the vibronic modes in the absorption spectrum of MeLPPP, similar to that performed for the fluorescence spectrum, is not possible. A more qualitative measure can be developed by considering the temperature dependence of the absorption peak feature at 2.72eV shown in the inset of Fig. 4.3.

The width of the peak at 2.72 eV, obtained by fitting a single broad Gaussian peak to the absorption data between 2.68 and 2.76 eV, is plotted as a function of temperature in Fig. 4.14; an example of the basic fitting procedure is also included in the inset of Fig. 4.14. As can be seen, between 295 and 150 K a near-linear decrease in the peak width is observed with decreasing temperature. At 150 K however a prominent change in behaviour is recorded, with the peak width then remaining approximately constant between 150 and 10 K. The fact that this critical point occurs at the same temperature as that noted in the peak amplitudes of the modes in the fluorescence spectrum would suggest that the same structural change that influences the fluorescence spectrum of MeLPPP with temperature also influences the temperature dependence of the absorption spectrum. It is however important to note that, regarding the temperature dependence of the absorption spectrum, it is not possible to determine whether this change influences the inhomogeneous broadening or the amplitude of the vibrational modes that contribute to the spectrum: for example, as the single peak that was used to fit the absorption data averages over several different modes, the change in the peak

width may be due to a decrease in the amplitude of the low energy modes in the spectrum with decreasing temperature.
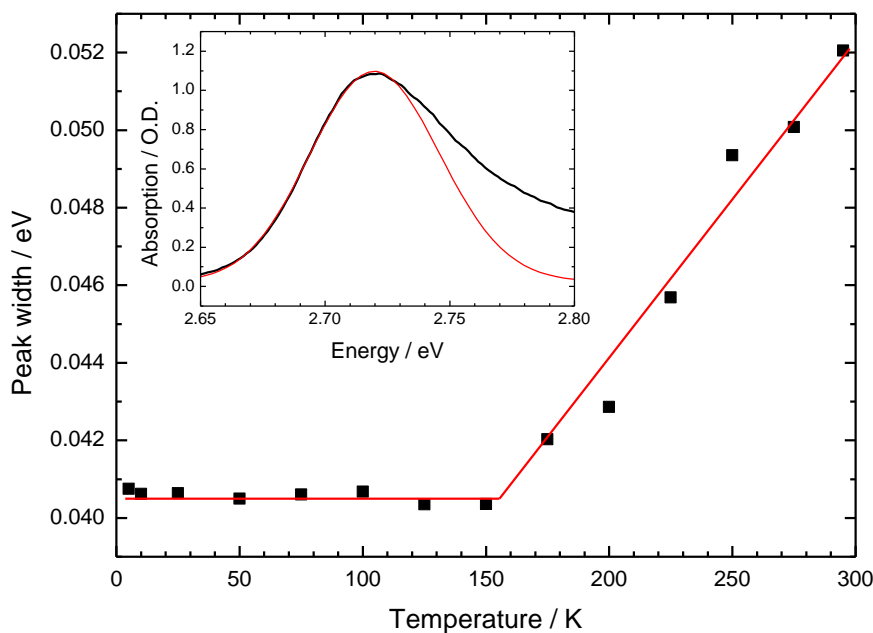
Figure 4.14: Width of absorption peak feature at 2.72 eV at different temperatures, as obtained by fitting a single Gaussian peak to the data in that vicinity. As was noted in the temperature dependence of vibronic features in the fluorescence spectrum, a prominent change in behaviour is noted at 150 K. Inset: example of the basic fitting procedure, as applied to the absorption data at 295 K.

It is interesting to note that the changes in behaviour observed at ~125-150 K are concurrent with a decrease in the amplitude of the first thermally excited replica of the skeletal stretch mode to low levels, as recorded in Fig. 4.6. It is therefore not unreasonable to propose that the conformation of the polymer chain is related to and perhaps stabilised by the thermal occupation of the hot low energy vibrations. Upon freezing out these modes at low temperatures the chain can no longer support one particular conformation and instead is forced

to revert into a different molecular geometry, corresponding to a different ΔQ, resulting in the observed change in the mode amplitudes. A similar concept has been used to describe the influence of temperature in determining the average conjugation length of a polymer chain, in which thermally populated low energy rotational modes are able to generate breaks in the conjugation along the backbone.[157, 159] In these studies however the changes in the structure of MeLPPP are observed to occur at a particular temperature and are instead mediated by a low energy stretching mode. Regardless of its physical origin, the observation of a change in the conformation of MeLPPP with temperature is a new and important result which contradicts the idea that the polymer backbone exists in a completely inflexible rigid-rod structure.[140, 141]

As this study is limited to investigations of an experimental nature, the conclusions drawn above regarding temperature-dependent structural changes in MeLPPP requires further support from both theoretical and structural studies. This work does however clearly demonstrate that a previously unreported change in the vibrational coupling in MeLPPP is occurring at a critical temperature of ~125 K. X-Ray diffraction studies have been proposed that may provide further information into this feature by monitoring the interchain order in MeLPPP films, which in turn may be partly determined by the chain conformation. Such studies will however only be available in the late-spring of 2011, after the submission date of this thesis.

4.4.3 Polarised fluorescence studies

The observation of a polarised response, as quantified by the ratio expressed in Eq. 4.3, in the fluorescence spectrum of stretched films of MeLPPP is an important finding. If there were no anisotropic response from the sample, then one would expect the ratio of emission parallel and perpendicular to the excitation source to be equal to one and independent of energy. Furthermore, a systematic anisotropic response, such as one introduced by stretching the film along a single direction, would not be expected to produce the degree of variation observed in

the ratio measured with emission energy. The observation of clear peak features in the ratio at the position of the vibrational modes, even when no such features can be observed in the fluorescence spectra from which the ratio is derived (see Fig. 4.8A), strongly suggests that the polarised response of the films observed in these plots is fundamentally related to the vibrational modes of the polymer. It should be noted that the interpretation of the absolute values of the polarised ratio recorded in Fig. 4.8 is non-trivial. Unlike the fluorescence anisotropy of an isotropic system, which can be related to the angle between the absorption and emission dipole moments of a chromophore (see section 3.9.1), the ratio measured in these experiments can only be taken as a qualitative measure of the degree of polarisation.

The observation of a fundamental relationship between the polarisation of fluorescence in MeLPPP and the vibrational modes of the polymer is highly significant. As discussed in section 4.1, under the Born-Oppenheimer approximation it is not possible for the electron-phonon coupling of a molecule to influence the orientation of the electronic dipole moment of that system and therefore by extension the polarisation of fluorescence. The results of Fig. 4.8 therefore demonstrate that the Born-Oppenheimer approximation cannot completely describe the properties of electron-phonon coupling in MeLPPP and that a new approach is required. Of most interest in this context are the concepts developed by Spano *et al.,*[144-149] which were briefly discussed in section 4.1. As part of his work Spano considered systems in which the interchain interactions between polymer chains were comparable to the intramolecular interactions. In such situations an excitation of a polymer chain, including any electron-phonon coupling to the vibrational modes of that chain, would also be coupled to a similar excitation of an adjacent polymer chain and under such circumstances emission would occur from both one and two-particle states corresponding to completely symmetric modes.

One key property of the models developed by Spano was that the electron-phonon coupling in a conjugated polymer would have a large influence on the fluorescence polarisation from such a

system, with the magnitude of this effect determined by both the size of the molecular aggregates considered[144] and the degree of order in those systems.[145] It is therefore possible that the relationship between the electron phonon coupling and fluorescence polarisation in MeLPPP recorded in the study detailed in this chapter is indicative of moderate interchain interactions between adjacent polymer chains in film. Such a conclusion if confirmed could be considered surprising; MeLPPP is an example of a conjugated polymer in which large side-groups have been added to the polymer chain to aid solubility.[140, 141] These side-groups could pose a limit on how close such polymer chains could pack together in film, with the interchain separation in MeLPPP estimated in one study to be 14 Å.[80] This value is much greater than the interchain spacing in the conjugated polymers and aggregates studied by Spano (3-6 Å).[145, 149]

In order to confirm the role of interchain interactions in determining the polarisation of fluorescence observed in Fig. 4.8, further experimental and theoretical studies are required. Such work could be contained within the X-Ray diffraction studies proposed in section 4.4.2 to investigate the structure properties of MeLPPP with temperature. In chapter 6 of this thesis experimental evidence is presented from femtosecond pump-probe measurements which demonstrate the formation of interchain exciton states in MeLPPP. Such states can only be formed via interchain interactions in the solid-state, which corroborates with the origin of the polarised fluorescence in MeLPPP proposed above.

4.4.4 Time-resolved fluorescence spectroscopy

As demonstrated in Fig. 4.12, the fluorescence lifetime of MeLPPP in solution was found to be independent of energy and therefore by extension independent of the vibrational mode through which emission occurs. Such a finding is in agreement with the well-established theory of Strickler and Berg.[165] In general terms such a theory states that, when considering the rate of decay of a single population, the population fluorescence dynamics must be treated as a whole,

with only one decay rate assigned to it. This single rate would implicitly involve an average over the oscillator strength of all possible vibronic transitions.

Picosecond fluorescence studies performed in film demonstrate several differences to the corresponding results obtained in solution. Most of these differences can be attributed to exciton migration occurring in the film, which results in an energy-dependent decay term measured to be ~40 ps. More importantly however the longest lifetime component recorded in the fluorescence dynamics was observed to vary significantly with emission energy, increasing from 147 ps at 2.67 eV to 416 ps at 2.56 eV. It should be noted the fluorescence lifetime of MeLPPP was measured to undergo a similar magnitude of increase between 2.67 and 2.63 eV in low-temperature picosecond fluorescence studies performed by Hildner *et al.*.[18]

The spectral region in which this long-lived lifetime component is observed (see Fig. 4.10) is found to overlap with the spectral region of the TS^{0-1} transition identified in section 4.3.3 above. It is therefore important to consider whether this increase in lifetime is associated with the underlying vibrational mode in this spectral region, or is instead due to another cause. There are several pieces of evidence in favour of ruling out the contribution of a vibrational mode. The first is that if the lifetime component was an inherent property of the vibronic mode, then a similar change in the fluorescence lifetime in energy would have been noted in solution as well; as clearly demonstrated in Fig. 4.9 no such difference was measured. The second piece of evidence arises from considering the fluorescence spectrum of the MeLPPP film as a function of temperature. The zero-delay spectrum of the film is shown as a function of temperature in Fig 4.11. As can be seen, while the majority of the spectrum of MeLPPP shows a red-shift with decreasing temperature, as noted previously, the peak feature at ~2.57 eV appears to remain spectrally stationary. If this peak and the associated long-lifetime component were associated with the TS mode, then a spectral shift of this peak in concordance with the remainder of the fluorescence spectrum would have been observed. The observation

of no spectral shift of this peak with temperature instead suggests the presence of a new underlying state in the film with a different fluorescence lifetime.

As be seen in Figs. 4.3 and 4.4, the peak attributed to this new state was not observed in steady-state fluorescence measurements which were also made in film. A summary of the fluorescence spectra of different MeLPPP films collected over the course of this study and others, prepared from the same base solution of MeLPPP, is given in Fig. 4.15. The amplitude of a peak feature at ~2.57 eV is found to vary between different samples. On the basis that all films were prepared from the same polymer solution, this variation is attributed to the introduction of a defect state in films of MeLPPP as a consequence of external effects.

In order to develop a better picture of the spectrum of this defect state, the fluorescence spectra at zero delay and 1000 ps delay, as recorded using the streak camera, were compared. This was made on the basis that, after 1000 ps, nearly all singlet excitons on the polymer would have recombined and thus any remaining contribution to the fluorescence would arise as a result of the long-lived defect state. This is shown in the inset of Fig. 4.15. The spectrum at later times not only contains a well-resolved peak centred at ~2.57 eV, but also has a very broad tail that extends down to the edge of the streak camera image at 2.25 eV. Such an example of a broad emission spectrum in a conjugated polymer system is characteristic of a defect state.[166, 167]
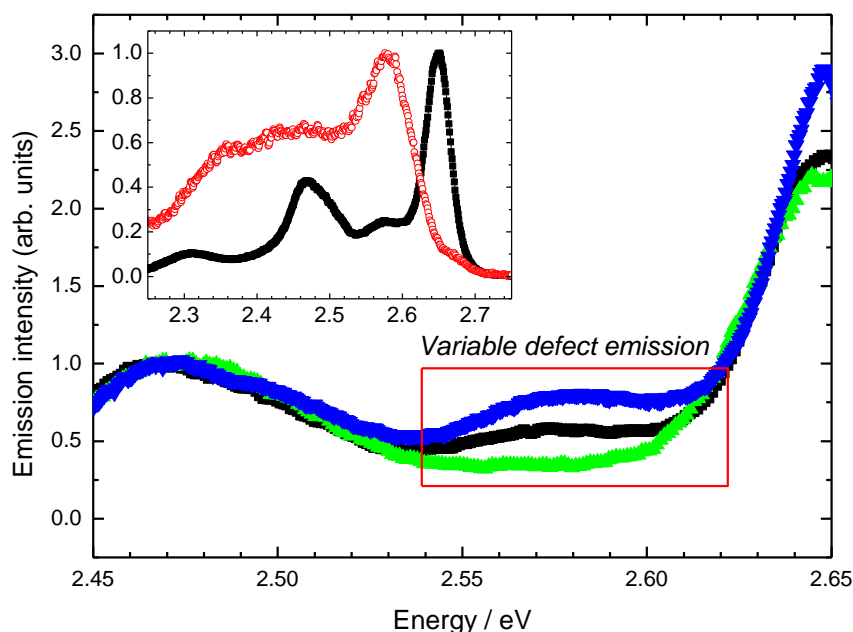
Figure 4.15: Fluorescence spectra of three different MeLPPP films at 100 K, 2.92 eV excitation, as measured by recording the zero-delay of the corresponding streak camera images. A broad peak feature at ~2.57 eV is recorded with variable intensity, indicating the presence of an underlying defect state. Note that to facilitate comparison of the defect emission in different films, the spectra have been normalised to their emission intensity at 2.47 eV. Inset: comparison of the normalised fluorescence spectra of a MeLPPP film (100 K) containing a defect state, recorded at zero (black squares) and 1000 ps (red circles). In addition to a well-resolved peak at 2.57 eV, the broad emission spectrum of the defect is found to extend down to 2.25 eV.

Comparison of the fluorescence dynamics of the polymer (2.67 eV) and defect (2.57 eV) at early times reveals no obvious build-in lifetime of the defect population that matches any component in the polymer decay; both signals are instead observed to rise to their maximum at the zero-delay time. Such a finding would indicate that any energy transfer between the two moieties occurs on a timescales smaller than ~23 ps, the time resolution of the streak camera for these experiments.

The potential role of a defect state in determining the excited-state dynamics in films of MeLPPP has to date not been widely considered and must be taken into account in the interpretation of time-resolved studies. For example, the observation of a ~500 ps lifetime component in picosecond studies performed by Hildner *et al.*[18] at 2.63 eV can now be clearly attributed to the defect state identified in these studies, as opposed to an increase in the fluorescence lifetime of the polymer with emission energy as was concluded therein. Recent work has been performed by List *et al.* in which the role of photophysical defects in a number of different conjugated polymers, including MeLPPP, was considered.[168] This work identified the potential formation of keto-type defects in MeLPPP, in which photo-oxidation of one of the alkyl side-groups results in the formation of a C=O moiety on the backbone. The results of these studies however are yet to be published and as such no detailed comparison can currently be made to the defect identified in these studies.

To best develop a more complete understanding of this photophysical defect, two courses of action are proposed: the first is to perform a more thorough investigation of the intensity of the defect in the fluorescence spectrum of MeLPPP as a function of film preparation conditions. For example, such a study could consider how the intensity of defect emission is affected by factors such as the amount of time a spun film is exposed to oxygen and light, in addition to the properties of film degradation under different intensities of laser excitation. A second study could also be performed to consider the rate of energy transfer between polymer and defect by operating at higher time-resolutions. Such measurements could be performed either using a different time-range on the streak camera, or by employing other experimental techniques such as time-correlated single-photon counting, or femtosecond pump-probe spectroscopy, depending on the minimum temporal resolution required.

4.5   Conclusions

A comprehensive experimental study of electron-phonon coupling in the ladder-type conjugated polymer MeLPPP has been performed using steady state, polarised and picosecond fluorescence spectroscopy. Results obtained using Raman and SSF spectroscopy have been used to identify the principal vibrational modes of the polymer, with the results obtained in good agreement with theoretical quantum chemical predictions of molecular chain dynamics for the related ladder-type oligomer $OLPPP_5$. SSF studies performed at 13 K also reveal a crossover from SSF to Raman emission at low excitation energies, with the potential impact of this crossover on the interpretation of SSF studies considered.

Using a multi-gaussian fitting procedure, the temperature dependence of key vibrational modes in the fluorescence spectrum of MeLPPP has been investigated, with results demonstrating the thermal population of low energy stretching modes of the polymer backbone in the excited state after thermalisation. The thermal population of these low energy modes has a significant influence on the temperature dependence of the other vibrational modes of the polymer, with a new set of transitions originating from these excited levels also appearing in the fluorescence spectrum at higher temperatures.

Significantly, below a critical temperature of ~150 K a transfer of oscillator strength between the 0-0 transition and the SS^{0-1} mode occurs and it has been proposed that such a change is indicative of a change in the polymer chain conformation at this temperature. Furthermore, as this transfer in oscillator strength was observed to be concurrent with a decrease in intensity of the thermally populated levels in the excited state, it is proposed that the low energy vibrations of the chain play a role in stabilizing the polymer conformation in the excited state: freezing these modes out at low temperatures forces the polymer chain to adopt a new conformation.

Having established the position and nature of the vibrational modes which make up the fluorescence spectra of MeLPPP, an investigation into more specific points concerning the fundamental nature of electron-phonon coupling in the polymer has been considered. Polarised measurements performed on stretched films of MeLPPP demonstrate a fundamental relationship between the vibrational mode of the polymer through which fluorescence occurs and the corresponding fluorescence polarisation. This observation is highly significant as it is not consistent with the theoretical framework outlined by the commonly accepted Born-Oppenheimer principle. In this context the theoretical approach of Spano was considered, with the observation of a relationship between the electron-phonon coupling and the fluorescence polarisation attributed to strong interchain interactions in MeLPPP in the solid-state.

Picosecond fluorescence spectroscopy has been used to address the issue of whether the electron-phonon coupling in a conjugated polymer has an influence on the fluorescence lifetime. The fluorescence lifetime of MeLPPP in solution is independent of energy and therefore by extension independent of both the type and order of the vibrational mode through which fluorescence occurs, in agreement with well-established theories. More complex dynamic behaviour was recorded in MeLPPP in film. Whereas the signature of exciton migration can be isolated as a ~40 ps decay component at certain emission energies, in agreement with previous results, the longest lifetime component of the fluorescence decay also changes with excitation energy, increasing from 147 ps to 416 ps over a spectral range of ~0.1 eV which is concurrent with the presence of a small peak in the fluorescence spectrum. Rather than being attributed to one of the primary vibrational modes of the polymer, the difference in lifetime is instead attributed to a significant contribution from a broad, underlying photophysical defect in films of MeLPPP, with repeat measurements performed for different films demonstrating varying degrees of defect concentration. The role of such a defect in

determining the excited-state dynamics of MeLPPP has not been widely considered and could

impact the interpretation of fluorescence lifetime studies in MeLPPP if not properly considered.

Chapter 5   High photoluminescence quantum yield due to intramolecular energy transfer in the Super Yellow conjugated copolymer

Sections of this work have been submitted for publication:

5.1   Introduction

Conjugated copolymers have been established as excellent model systems in which to investigate intramolecular energy transfer processes such as intrachain exciton energy transfer[20] and fluorescence quenching.[166] A great deal of interest has also arisen in the application of conjugated copolymers as the active layer in various optoelectronic devices, such as organic light emitting diodes (OLEDs)[16, 169, 170] and polymer solar cells;[171-174] by using a single copolymer with different monomer subunits, as compared to multiple polymers, a greater deal of control over key parameters such as morphology and device efficiency is made possible.

The phenyl substituted poly(para-phenylene vinylene) (PPV) copolymer Super Yellow[175] (SY) has been successfully applied as the active component in various OLED devices. This is in no small part due to an outstanding range of material characteristics, including a high photoluminescence quantum yield (PLQY), long shelf and operational lifetime and performance at elevated temperatures.[176-180] To date the properties of SY have only been considered within device architecture. Studies by Najafov *et al.* have shown that the primary

photoexcitation of SY is an intramolecular exciton with binding energy of 0.6 eV,[181] although such studies primarily focussed on the dissociation of such excitons under external electric fields. Many questions still remain however concerning the fundamental photophysical properties of this material.

This chapter relates the findings of an investigation into the photophysical properties of SY, performed with the aims of providing an insight in the properties of the excited-states in the material and addressing the molecular origin of the relatively high PLQY of the copolymer. This work was carried out in collaboration with Dr Luis Cury from the Universidade Federal de Minas Gerais, who was resident in Durham University as a Visiting Fellow.

The findings of this investigation are separated into two sections. This first section (5.3) reviews the results of basic steady-state spectroscopic investigations of SY performed by Dr Cury. This section is to be distinguished apart from the remainder of the chapter as I was not actively involved with the recording of these measurements; they are included on the basis that I was involved with the analysis and interpretation of the results, which are related to and correlate to a certain extent with the findings of chapter 4 of this thesis. The second section (5.4) of this chapter focuses on the results of picosecond fluorescence studies that were recorded and analysed exclusively by myself.

In summary, the photophysical properties of the conjugated copolymer SY have been studied using steady-state and picosecond fluorescence spectroscopy. Analysis of the steady-state fluorescence at different temperatures is used to estimate the average conjugation length of SY in spin-coated solid thin films. Results from picosecond fluorescence studies reveal matching exponential behaviour characteristic of exciton energy transfer on a 10 ps timescale from high energy copolymer subunits to low energy subunits. The PLQY of SY is measured and it is

proposed that its relatively high value is directly related to the intramolecular energy transfer and subsequent trapping of excitons on low energy copolymer sites.

5.2 Experiment

5.2.1 Materials

Thin films and solutions of SY were prepared from a base solution of the copolymer in p-xylene (Romil, 3 mg·ml^{-1}). In order to get the polymer to dissolve the solution was heated at 80 ^{0}C for 30 minutes before being left to stir for 24 hours. Significant gelation of the solution was observed at room temperature, corresponding to a 2% level of tolane-bisbenyl (TBB) defects along the copolymer backbone, as according to Ref. [175]. Thin films were fabricated by spin-coating the re-heated base solution on to glass substrates at 2000 rpm, before leaving the substrates on a hot-plate for a further 30 minutes to remove the p-xylene. Solution samples were prepared by diluting the base solution down to a concentration of ~0.001 mg·ml^{-1} in order to reduce the intensity of emission and prevent saturation of the detection equipment.

5.2.2 Spectroscopic measurements

Temperature dependent steady-state fluorescence measurements were performed using a Jobin-Yvon Horiba Fluorlog-3 fluorimeter, with thin film samples mounted in a displex He cryostat under a dynamic vacuum of 10^{-5} mbar. Absorption spectroscopy was performed using a Schimadzu UV3600 spectrophotometer. Thin film PLQY measurements were performed using a PTFE coated integrating sphere (Lab Sphere) and a Jobin-Yvon Horiba Fluoromax-3 fluorimeter.[131] Solution PLQY measurements were performed using the comparative method[132] where 9,10-diphenyl anthracene solution in cyclohexane (Aldrich) was used as a reference.

Picosecond time-resolved fluorescence studies were performed using a Hamamatsu C5860 streak camera coupled to a monochromator (SpectraPro-2300i). Pulses (2 ps, 76 MHz) generated from a Coherent Mira 900 Ti:Sapphire picosecond laser, coupled to a second-harmonic generator, were used to produce a vertically polarized excitation source at 2.79 eV. A time resolution of <23 ps and a spectral resolution of 0.02eV was achieved with this setup, with fluorescence decays at individual energies obtained by averaging over a 0.02eV wide boxed section of the camera image.

5.3   Collaborative work

5.3.1 Results

The PLQY (φ) of SY thin films was determined using the method outlined by de Mello *et al.* (see section 3.8.3),[130, 131] with a value of $\varphi_{SY} = (17\pm1)$% obtained at an excitation energy of 3.09eV. This value is higher than the PLQY of (2-methoxy-5-(2₀-ethyl)-hexyloxy-p-phenylenevinylene) (MEH-PPV) recorded using the same experimental technique: $\varphi_{MEH-PPV} = (10\pm1)\%$.[130]

The PLQY of SY in solution was recorded using the standard comparative method.[132] As outlined in section 5.2, 9,10-diphenyl anthracene solution in cyclohexane was used as a reference, with $\eta_{anthracene}$ (refractive index) = 1.434 and $\varphi_{anthracene} = 74\%$. Straight line plots of the integrated emission versus sample concentration for both the SY and anthracene solutions are shown in Fig. 5.1; the excitation energies of the SY and anthracene were 2.76 and 3.34eV respectively. From the gradients determined from the straight line fits shown in Fig. 5.1 and using $\eta_{SY} = 1.542$, the PLQY of SY in solution is determined to be $\varphi_{SY} = (69\pm3)\%$.
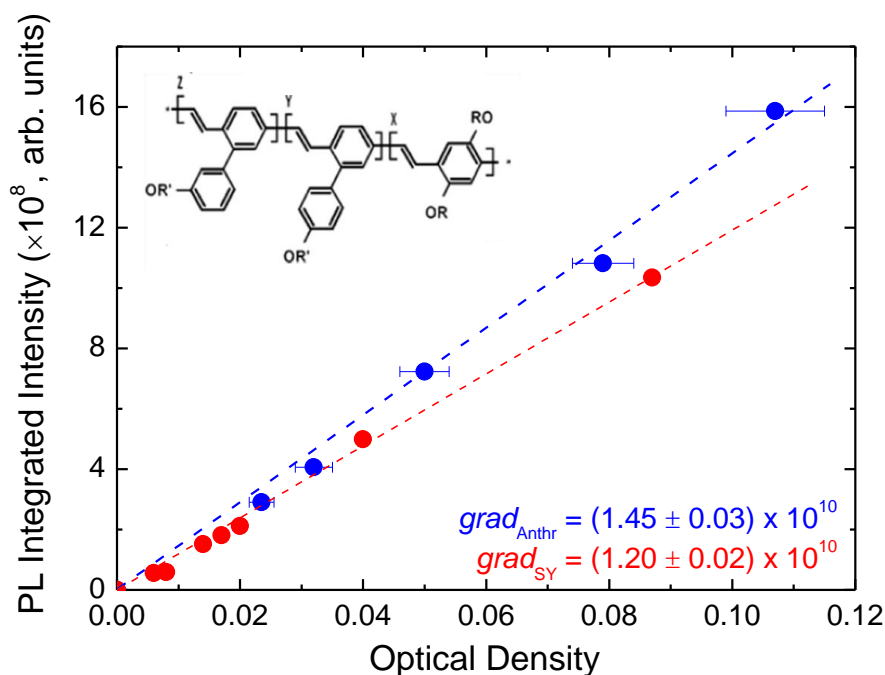
Figure 5.1: Plots of integrated emission versus the absorption intensity at excitation for the Super Yellow copolymer (red) and Anthracene (blue) (recorded by Dr Luiz Cury during his visitor's fellowship at the Department of Physics, Durham University). Best line fits to the data (dotted lines) have been included. Inset: the chemical structure of SY, highlighting the three PPV-based subunits (X, Y and Z) which make up the copolymer.

The steady-state absorption and fluorescence spectra (at different temperatures) of SY are shown in Fig. 5.2. Broad vibronic features, consistent with a large degree of spectral broadening imposed by the torsional modes of the PPV backbone, are observed in the fluorescence spectra, with individual peaks becoming more resolved at lower temperatures. Raman spectroscopy of various PPV derivatives has identified the primary vibrational modes of the PPV backbone to be a C=C stretch mode with a vibronic energy of 201 meV and a C-C stretch mode at 197 meV.[157, 182] Upon inspection it can be seen that the position of the 0-1 transition of these two modes will significantly overlap in the region of the second peak observed in the fluorescence spectra centred at approximately 2.07 eV. The first peak at

~2.25 eV is therefore assigned to the zero-phonon transition of SY and the following peaks to

the 0-1 and 0-2 replicas of the overlapping C=C and C-C stretch modes. It should be noted that

other prominent peaks identified in the Raman spectra, such as overtones of the C-H stretch

mode with vibronic energies of 160 and 162 meV, cannot be resolved in the fluorescence

spectrum at any temperature and shall not be considered further.
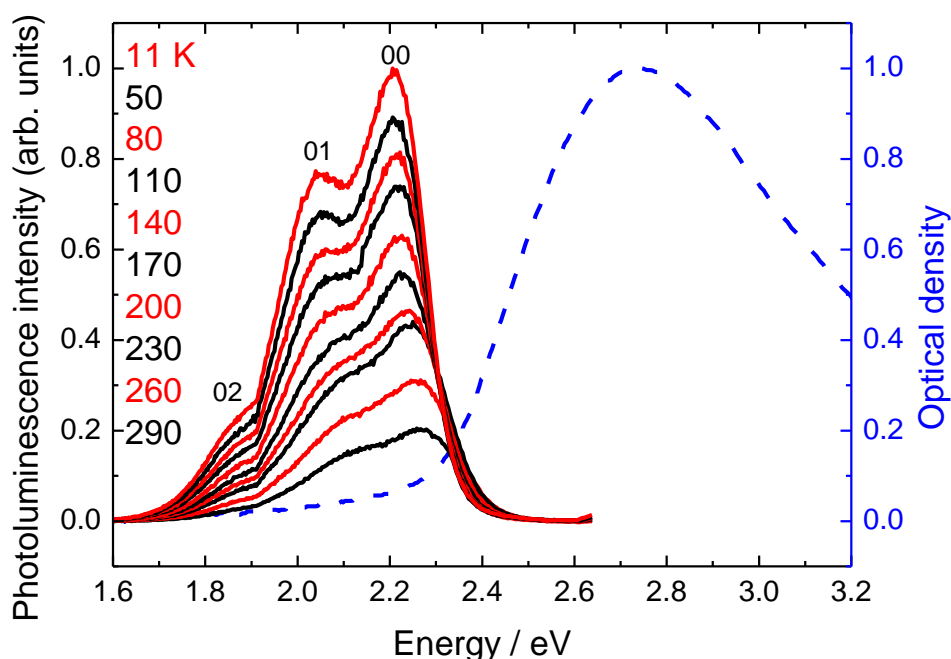
Figure 5.2: Absorption and temperature dependent fluorescence spectra (2.76 eV excitation) of Super Yellow in the solid state (recorded by Dr Luiz Cury during his visitor's fellowship at the Department of Physics, Durham University).

The temperature dependence of the fluorescence spectrum shows several trends. A general

increase in emission intensity is observed with decreasing temperature and is attributed to a

decrease in the rate of migration of excitons to defect sites which subsequently improves the

PLQY.[20, 156] A decrease in the rate of migration is also responsible for the increasing red-shift

of the fluorescence that occurs with decreasing temperature.[18, 32] By comparing the relative

intensity of the 0-0 and 0-1 peaks at 295 and 11 K it is also clear that the Huang-Rhys (HR) parameter also changes with temperature. A similar phenomenon was noted for the behaviour of the skeletal stretch mode in MeLPPP, as discussed in chapter 4. As concluded therein, this behaviour is representative of a change in the conformation of the polymer backbone with temperature.

5.3.2 Discussion

To develop a more quantitative analysis of temperature dependence of the HR parameter, each fluorescence spectrum shown in Fig. 5.2 was fitted with three Gaussian peaks; one for each of the 0-0, 0-1 and 0-2 transitions. The amplitudes extracted from the fitting processes were then used to calculate the HR parameter (S) as according to Eq. 5.1:

$$S = \frac{I_{0-1}}{I_{0-0}} \tag{5.1}$$

In Fig. 5.3 below the HR factor has been plotted as a function of temperature. As discussed above, the 0-1 peak in the fluorescence spectrum contains contributions from both the C=C and C-C stretch modes. Due to the large degree of inhomogeneous broadening in SY these modes cannot be individually resolved; the amplitude of this peak, and therefore the HR parameter, should be taken as a representative measure of both modes combined together.

The HR parameter can be quantitatively related to the change in polymer configuration in conformational space ($\Delta \boldsymbol{Q}$) as according to Eq. 5.2:

$$S = \frac{\omega |\Delta \boldsymbol{Q}|^2}{2\hbar} \tag{5.2}$$

In the work of Salaneck *et al.* it was proposed that the thermal occupation of low energy torsional modes of a polymer backbone would have a direct effect on the average conjugation length along the chain.[183] At high temperatures where many such modes would be active, breaks in the conjugation could be achieved through the rotation of adjacent chain segments; this phenomenon can be expressed below in Eq. 5.3:

$$n(T) = n_0 \exp\left(\frac{\varepsilon}{k_B T}\right) \tag{5.3}$$

In Eq. 5.3 n_0 is the average conjugation length at high temperatures and ϵ is a characteristic energy associated with the torsional modes of the backbone. This expression can be used to develop an empirical formulation for the temperature dependence of the HR parameter:[157]

$$S(T) = A + \frac{B}{n_0 \exp\left(\frac{\epsilon}{k_B T}\right) + 1} \tag{5.4}$$

In Eq. 5.4 above *A* is the HR parameter in the low temperature limit and *B* is a parameter related to the strength of the electron-phonon coupling associated with the vibrational mode in question. This expression was used to produce a numerical fit to the data shown in Fig. 5.3: as can be seen good agreement between model and experiment is found. The average conjugation length $n_0 = (7\pm1)$ measured is relatively short as compared to the PPV derivative poly[2,5-bis (2₀-ethyl-hexyl)1,4-phenylenevinylene] (BEH-PPV) $(n_0=13)$[157] and stretch oriented PPV films $(n_0=20)$.[184] The conformational energy $\epsilon=(35\pm2)$ meV is also larger than BEH-PPV $(\epsilon=28\text{meV})$,[157] which is in agreement with the smaller value of n_0 found. Although SY has a large chain regularity, as observed by gelation occurring at room temperature, thermal activation of torsional modes and the presence of TBB[175] and carbonyl[185] defects in the PPV

units, which force the polymer chain to twist in their presence, could also give rise to the small

conjugated length observed.

$$S(T) = A + B/(n_0 e^{\varepsilon/kT} + 1)$$

$A = 0.935 \pm 0.005$

$B = 6.9 \pm 0.3$

$\varepsilon = (0.035 \pm 0.002)$ eV

$n_0 = 7 \pm 1$
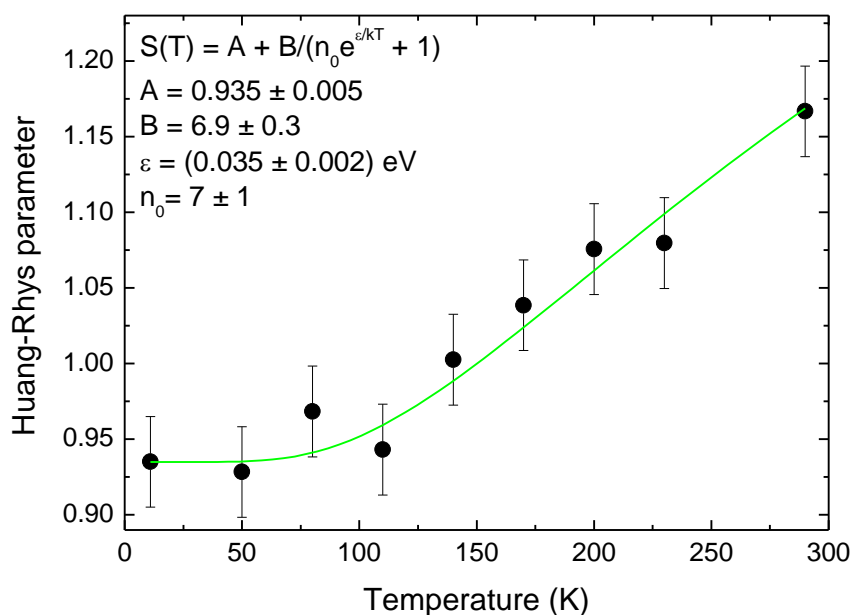
Figure 5.3: Temperature dependence of the HR parameter. The numerical fit to the data has been included (green line).

5.4   Independent work

5.4.1 Results

The streak camera data of the dilute SY solution recorded at 295 K is shown in Fig. 5.4A;

normalized single energy fluorescence decay dynamics, extracted from the streak camera image

by averaging over a 0.02 eV boxed region around the centre energies indicated, are shown in

Fig. 5.4B. As can be seen the fluorescence dynamics depend on the energy of the detection

window and feature multi-exponential behaviour. In order to analyse the data fully a multi-exponential fit was applied.

At long times (>100 ps) a single decay lifetime is found which takes a value of (649±9) ps at energies above 2.79eV and (694±5) ps below 2.79 eV. At early times (<100 ps, as highlighted in the inset of Fig. 5.4B), a single lifetime component is found which takes the form of a decay at energies above 2.79 eV and a build-in at energies below 2.79 eV. At 2.57 eV a decay of (27±3) ps is measured and found to be in good agreement with the lifetime of the build-in observed at 2.42 eV, measured to be (26±1) ps.
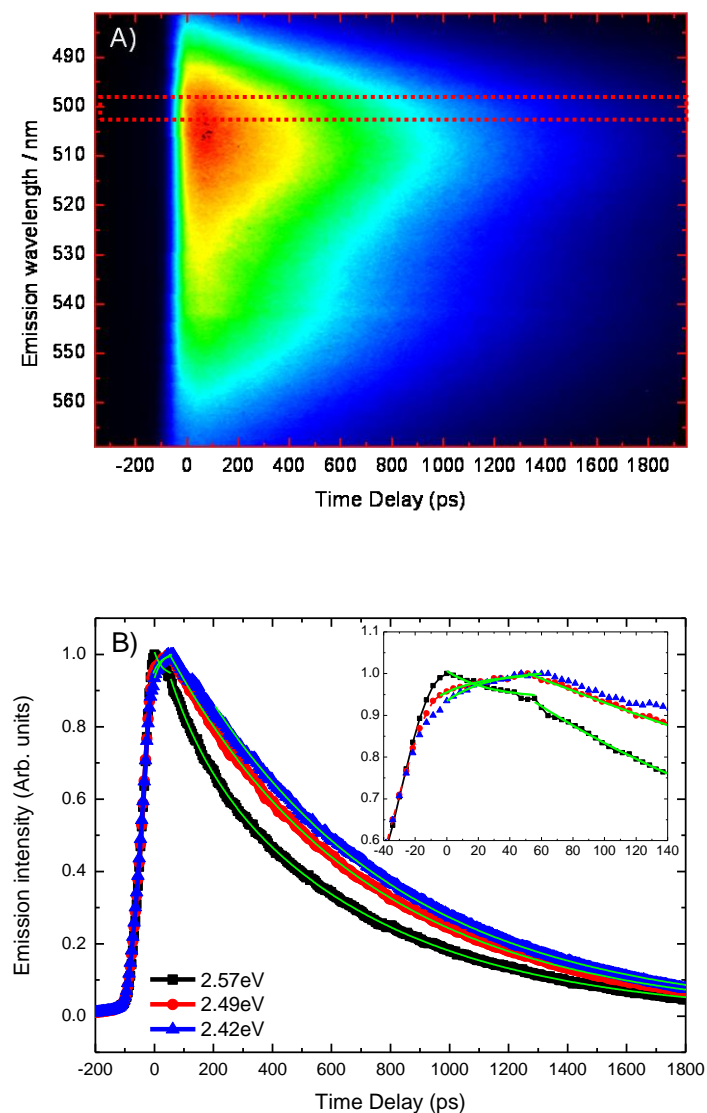
Figure 5.4: A) The streak camera image (including a sample boxed region of selected data) and B) corresponding fluorescence decays at marked excitation energies of dilute Super Yellow solution at 295 K for excitation at 2.76 eV. Inset: behaviour of the fluorescence decays at early times, highlighting a matching build-in and decay at energies of 2.42 and 2.57 eV. The results from a multi-exponential fitting process have been included (green lines).

5.4.2 Discussion

The energy dependence of the short lifetime component recorded in the fluorescence decay data is characteristic of exciton energy transfer (EET) from high energy chromophores to low energy chromophores. Furthermore, the lifetime of the energy transfer is consistent with values published for intrachain EET in other PPV derivatives.[12, 83, 162] This process is similar to that of spectral diffusion caused by energy transfer from short to long conformational subunits.[18] In this case however, the long lifetime component, which is assigned as the fluorescence lifetime, is also observed to vary with emission energy. This would suggest that the absorbing and emitting species are chemically distinct, as a single chemical species can only possess one fluorescence lifetime independent of chromophore length.[165] The energy transfer is thus assigned to occur between two of the three different monomer subunits (see inset Fig. 5.1) that make up the copolymer, with the direction of energy transfer such that excitons are transferred to the lowest in energy of the copolymer subunits. It should be acknowledged that further energy transfer from short to long conformational units may occur when possible once excitons have transferred to the lowest in energy of the three subunits; this process however cannot be detected sufficiently in solution. This is attributed to the increased interchain separation in dilute solution restricting the number of longer conformational units an exciton can access.

It should be noted that similar behaviour has been noted by Di Paolo *et al.* in the fluorescence dynamics of PPV trimers, where a short ~20 ps lifetime component was measured in addition to a longer but fixed (with respect to emission energy) fluorescence lifetime.[30] In these systems exciton migration is not possible and Di Paolo instead attributed the shorter lifetime component to conformational relaxation processes. As discussed in section 5.3.2 above the torsional modes of the SY backbone are active at room temperature and as such it is fully expected that such conformational relaxation processes mediated by these modes will also be present at room temperature. Unlike the studies of Ref. [30] however, in which all fluorescence time

components were found to be constant and only the sign of the pre-exponential component of the ~20 ps time constant change with emission energy, in the experimental studies detailed in this chapter the longer time constant, identified as the fluorescence lifetime, was also found to change with emission energy. This has already been identified above as the signature of two distinct chemical species contributing towards the fluorescence spectrum and as such a description based on energy transfer between these two units is favoured. It should be acknowledged however that conformational relaxation processes could be fundamentally linked to intrachain EET; such relaxation processes may be responsible for briefly restoring broken links in the electronic conjugation along a polymer backbone, allowing for an exciton to move further along the chain. As such it becomes impossible to distinguish between conformational relaxation and intrachain EET in systems possessing torsional degrees of freedom.

As discussed previously, the PLQY of SY is much higher than other PPV derivatives, making it an excellent candidate for use as the active layer in optoelectronic devices such as OLEDs. Using results from both steady-state and time-resolved spectroscopy it is now possible to relate this high yield in terms of the fundamental properties of the photoexcitations of the copolymer.

One of the key processes that determines the PLQY of any light emitting polymer is the quenching of excitons at non-emissive defect sites.[166] Slowing the rate of migration prevents excitons from reaching these sites and thus increases the quantum yield. This is the origin of the temperature dependence of the fluorescence spectra shown in Fig. 5.2, whereby reducing the temperature to 11 K results in a uniform ×5 increase in fluorescence intensity. From these results it is possible to infer the existence of non-emissive defects in SY, although it is not possible to confirm whether these defects are the TBB moieties described previously or another chemical species. Despite the presence of these defects however SY still possesses a high PLQY; indeed it has already been discussed above that SY has a higher PLQY than MEH-PPV, in which these defects are expected to be present in a smaller number (as reflected by the longer

conjugation length observed). Therefore there must be another process remaining at room temperature in SY to prevent excitons from reaching quenching sites.

It is proposed that after photogeneration in SY excitons become trapped on lower energy copolymer subunits as a result of intramolecular EET. EET off of these low energy sites occurs with a reduced probability as there are only a small number of available sites to hop to which are lower in energy. As a consequence an exciton must on average undergo a thermally activated uphill jump in energy in order to transfer off of the low energy sites. The intramolecular relaxation process therefore contributes towards the relatively high PLQY of the SY copolymer in solution by essentially trapping excitons on low energy segments which subsequently restricts migration to the aforementioned non-emissive defect sites. It should be noted that while intrachain EET cannot be as accurately measured in the solid-state, in which interchain EET and migration dominates the temporal response of the fluorescence and masks the intramolecular exciton subunit transfer, it is presumed that these low energy subunits will play an identical role in improving the PLQY, although such processes will be more efficient and occur on a timescale of less than 10 ps.[19, 80, 186]

5.6   Conclusions

Steady-state and picosecond fluorescence spectroscopy has been used to investigate the photophysical properties of the PPV copolymer SY. Analysis of the steady-state fluorescence at different temperatures enabled an estimate of the conformational energy ϵ and average conjugation length n_0 in spin-coated solid thin films to be made. The relatively high conformational energy $\epsilon = (35 \pm 2)$ meV and low average conjugation length $n_0 = (7 \pm 1)$ measured, as compared to other PPV derivatives, corroborate the presence of defects along the SY backbone.

Analysis of picosecond fluorescence decay data revealed the presence of two primary emission bands in the fluorescence spectrum, assigned as fluorescence from two of the monomer subunits of the copolymer. Numerical analysis of fluorescence decays recorded at emission energies corresponding to these bands revealed matching multi-exponential behaviour characteristic of intramolecular EET, with the energy transfer occurring from the high energy band to the low energy band with a lifetime of ~26 ps. The PLQY of SY was measured in film and solution and it was proposed that its relatively high value, as compared to other PPV derivatives, is related to the trapping of excitons on low energy subunits as a result of intramolecular EET.

Chapter 6 Interchain exciton formation in a ladder-type conjugated polymer

6.1 Introduction

Pump-probe spectroscopy is a powerful experimental method which can be used to measure the population dynamics of a wide variety of different excited states in conjugated polymers, such as intrachain singlet excitons,[50, 163, 187] interchain (Wannier) excitons (IEXs),[188, 189] free and geminate pair polarons[48, 49] and triplet excitons.[117, 118]

The theory of pump-probe spectroscopy was outlined in detail in section 3.6.1; for clarity, some of the key concepts covered in that section are briefly recapped here. In pump-probe spectroscopy, one typically measures the normalised differential transition ($\Delta T/T$), which quantifies the interaction of a pulse of light (designated 'probe') with a sample following the photoexcitation of that sample by an initial pulse ('pump'). There are three possible pump-probe interactions in a conjugated polymer. When the probe pulse is absorbed by an excited state generated by the pump, the process is referred to as photoinduced absorption (PA, $\Delta T/T < 0$). Stimulated emission (SE, $\Delta T/T > 0$) is possible following the interaction of the probe pulse with the S_1 singlet excitons generated by the pump. Finally, photobleaching (PB, $\Delta T/T > 0$) can be generated if both the pump and probe pulses interact with the ground-state, with the line-shape of the PB band identical to that of the (ground-state) absorption spectrum of the polymer.

By measuring the build-in and decay of the PA, SE and PB bands of a conjugated polymer in a series of measurements it is possible to build up a comprehensive picture of the excited-state dynamics in that system. This chapter outlines the details of a study in which an unknown high energy PA band in the ladder-type conjugated polymer methyl-substituted

189

poly(para-phenylene) (MeLPPP) was investigated using femtosecond pump-probe spectroscopy. This work originated from efforts made to measure the intersystem crossing yield of MeLPPP at low temperatures following the method of King *et al.*.[118] By measuring the PB decay of a conjugated polymer at both early and long delay times, it is possible to measure the relative contribution to the PB recovery of the singlet and triplet exciton populations respectively and therefore measure the intersystem crossing yield of the polymer. During the course of such an experiment, a transition in time between PB and PA was recorded in the transient transmission dynamics at a fixed probe wavelength, indicating that the PB band of MeLPPP overlapped with an unknown high energy PA band. The study of this PA band, which has not been identified in the literature to date, forms the subject of this chapter.

In summary, an unknown high energy PA band found to overlap with the PB band in the ladder-type conjugated polymer MeLPPP has been identified and characterised using femtosecond pump-probe spectroscopy. Before investigating the properties of the PB band, a review of the singlet exciton dynamics in MeLPPP is performed to provide a foundation for the analysis of the unknown PA. The results of repeat measurements performed in different films and in solution are used to demonstrate a dependence of the magnitude of the PA on the local sample morphology that is probed. Polarised measurements are then employed to measure the orientation of the excited-state transition dipole moment of the PA with respect to that of the intrachain singlet exciton population. On the collective basis of these results the PA is attributed to the formation of IEX states. The observation of IEX formation in MeLPPP using femtosecond pump-probe spectroscopy corroborates with the observation of polarised steady-state fluorescence from vibrational modes in stretched films of MeLPPP, as discussed in chapter 4 of this thesis, confirming that interchain interactions can be substantial in localised regions of MeLPPP in the solid-state.

6.2   Experiment

6.2.1   Materials

Unaligned solid thin films of the polymer MeLPPP (chain length of ~60 repeat units; polydispersity index = 1.3) were deposited by spin casting at 1500 rpm for 45 seconds from a toluene (Romil) solution (10 mg·ml^{-1}) onto sapphire substrates. Dilute solutions of MeLPPP in toluene (2×10^{-3} mg·ml^{-1}) were also prepared. The average interchain separation in these solutions is ~3 µm, which is large enough to consider any interchain interactions negligible.[120]

6.2.2   Spectroscopic measurements

Ultrafast spectroscopic measurements were made using a conventional femtosecond non co-linear pump-probe setup. 180 fs, 4 µJ, pulses of 100 kHz repetition rate at 780 nm were generated using a Coherent Mira900-f Ti:Sapphire femtosecond oscillator in conjunction with a Coherent RegA 9000 laser amplifier. The output of this system was fed into a Coherent 9400-OPA, which was used to generate pump and probe pulses in various combinations. For measurements of the transient transmission dynamics at a single wavelength the ultraviolet (UV, 390 nm) output was used to pump, with the signal beam (SB, 445-710 nm) used to probe. For measurements of the transient transmission spectrum the SB output was used to pump, with the white-light supercontinuum (WLSC, 450-870 nm) output used to probe. The variable delay between pump and probe pulses was controlled by means of a motorised linear translation stage. A variable $\lambda/4$ waveplate was introduced to the pump path and used to control the relative orientation of the pump polarisation with respect to the probe. Unless specified otherwise, the pump was oriented at ~55^0 (magic angle) with respect to the probe to ensure the transient data obtained was independent of polarisation.

Thin film samples were mounted in a closed-cycle Cryomech helium pulse tube cryostat under

a dynamic vacuum of $<10^{-5}$ mbar, allowing access to temperatures down to 10 K. Solution samples were mounted in a custom-built sample holder. After passing through a sample, spectral components in the probe were isolated using a monochromator (Bentham M300) incorporating visible and ultraviolet diffraction gratings, with the relative transmission change $\Delta T/T$ of the probe beam measured using a silicon photodetector and lock-in amplifier referenced to the mechanically chopped pump beam. For situations when the probe intensity was too weak to be adequately detected by the lock-in amplifier, the monochromator was removed and the probe beam sent to the photodetector directly. The spectral resolution of the detected signal was determined by the type of probe beam. For single-wavelength measurements in which the SB was acting as probe, the spectral width of the SB was the limiting factor and was measured to be ~10 nm using an USB4000 Ocean Optics spectrometer. For measurements in which the WLSC was used as probe, the spectral resolution was governed by the width of the entrance and exit slits on the monochromator; in order to obtain sufficient probe intensity at wavelengths down to 500 nm, the exit slit of the monochromator was fully opened, resulting in a spectral resolution of ~15 nm.

It should be noted that the pump-probe experiments detailed in this study were performed over the course of several years. Over that time period the OPA output performance was noted to drop due to the deterioration of the beta-barium borate crystal. The most measurable consequence of this was that the SB output intensity in the deep-blue spectral band, particularly at 445 nm, was found to be much lower for experiments performed in later years. This can be observed in the data presented in this chapter as a variation in the signal to noise ratio of measurements performed at a probe wavelength of 445 nm. For the last experiments performed on MeLPPP films in which the effect of polarisation was considered, the deterioration in the 445 nm intensity was significant enough to enforce the change to the detection optics detailed above.

Steady-state temperature-dependent absorption spectra were recorded using a USB4000 Ocean Optics spectrometer, with a broadband xenon lamp used to excite. Temperature dependent fluorescence spectra were recorded using a Jobin-Yvon Fluorolog-3. In both cases samples were mounted in a closed-cycle Cryomech helium pulse tube cryostat. Streak camera measurements used to determine the singlet exciton decay dynamics were performed as described in chapter 4.

6.3 Results

6.3.1 Steady-state and transient transmission spectra

The steady-state absorption spectrum of MeLPPP in the solid state at 295 K is shown in Fig. 6.1A. Four peak features corresponding to the 0-3, 0-2, 0-1 and 0-0 vibrational transitions of a carbon-carbon stretch mode are noted at 375, 400, 425 and 455 nm respectively and can be distinguished apart as a consequence of the relatively small inhomogeneous broadening in MeLPPP.[140, 141] The absorption spectrum of MeLPPP at different temperatures is shown in the inset of Fig. 6.1A. A general red-shift of the spectrum (~8 nm between 295 and 10 K) and a simultaneous small decrease in the inhomogeneous broadening are recorded with decreasing temperature. As per the discussion of chapter 4, the former change is attributed to a change in conformation of the polymer backbone with temperature;[158] the latter change is attributed to the thermal depopulation of low energy skeletal stretch modes at lower temperatures.

The steady-state fluorescence spectrum of MeLPPP is also shown in Fig. 6.1A. Four well-resolved peak features that form the mirror image of the absorption spectrum can be observed at 460, 490, 530 and 565 nm and are again attributed to the 0-0, 0-1, 0-2 and 0-3 vibrational transitions of a carbon-carbon stretch mode. The small Stokes shift measured

(~10 nm) is characteristic of a ladder-type conjugated polymer[39] and results in a moderate overlap between absorption and fluorescence between 450 and 460 nm.
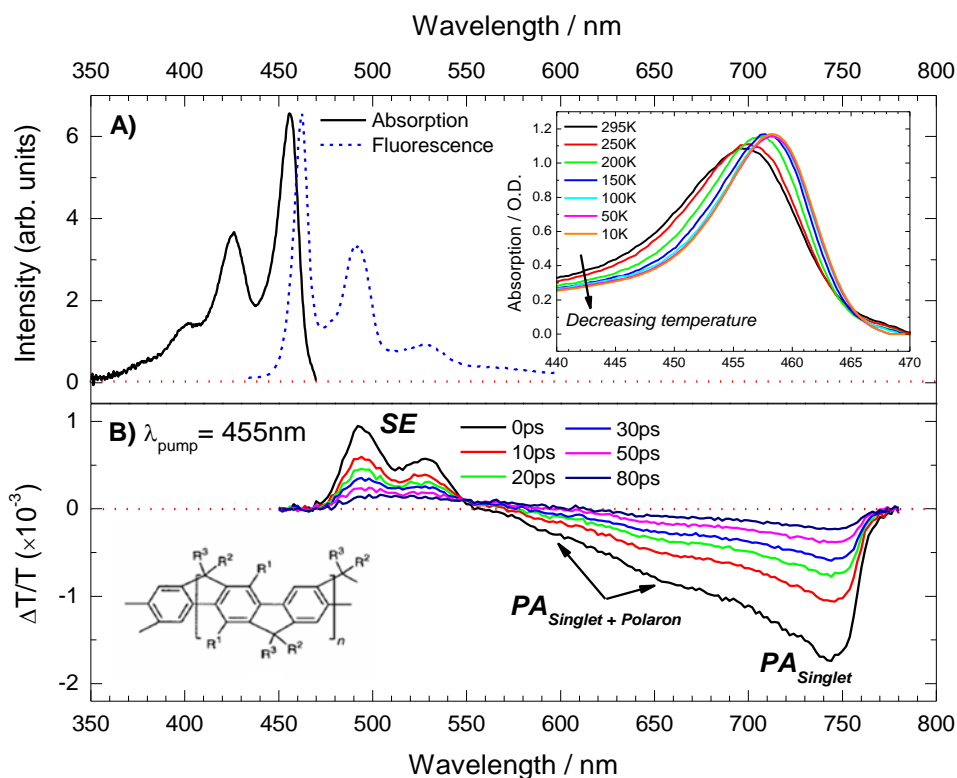
Figure 6.1: A) Re-scaled steady-state absorption (solid black line) and fluorescence (425 nm excitation, dashed blue line) spectra of a MeLPPP film at 295 K. Inset: the steady-state absorption spectrum at different temperatures. Between 440 and 455 nm a decrease in absorption is observed with decreasing temperature. B) The transient transmission spectrum of a MeLPPP film recorded at different pump-probe delay times, 455 nm excitation (3 μJcm⁻²) at 295 K. In addition to the expected SE and PA of intrachain singlet excitons, two small peaks at ~590 and 650 nm can be resolved and correspond to the overlap of two polaron PA transitions. Note that saturation of the detector by residual fundamental light from the laser amplifier (780 nm) in the probe results in a rapid drop in $\Delta T/T$ at ~760 nm. Inset: the chemical structure of MeLPPP; R^1 = Alkyl group, R^2 = Aryl group and R^3 = -CH$_3$.

The transient transmission spectrum of MeLPPP in film at 295 K for excitation at 455 nm (incident pump fluence: 3 μJcm⁻²) is shown in Fig. 6.1B for a range of pump-probe delay times.

Two positive peaks at 490 and 530 nm clearly overlap with two of the peaks in the fluorescence spectrum and are hence assigned to SE of the singlet excitons of the polymer. A broad negative feature is also recorded from 550 down to 770 nm. This band is noted to have identical decay dynamics as the SE band, as evidenced by excellent agreement between the single-wavelength transient transmission dynamics of the PA band at 750 nm and the SE band at 492 nm, which is demonstrated in Fig. 6.2. This PA band is therefore attributed to the PA of intrachain singlet excitons, corresponding to the excited-state absorption transition $S_1 \rightarrow S_N$, in agreement with the results of previous studies.[45, 46, 187, 190]
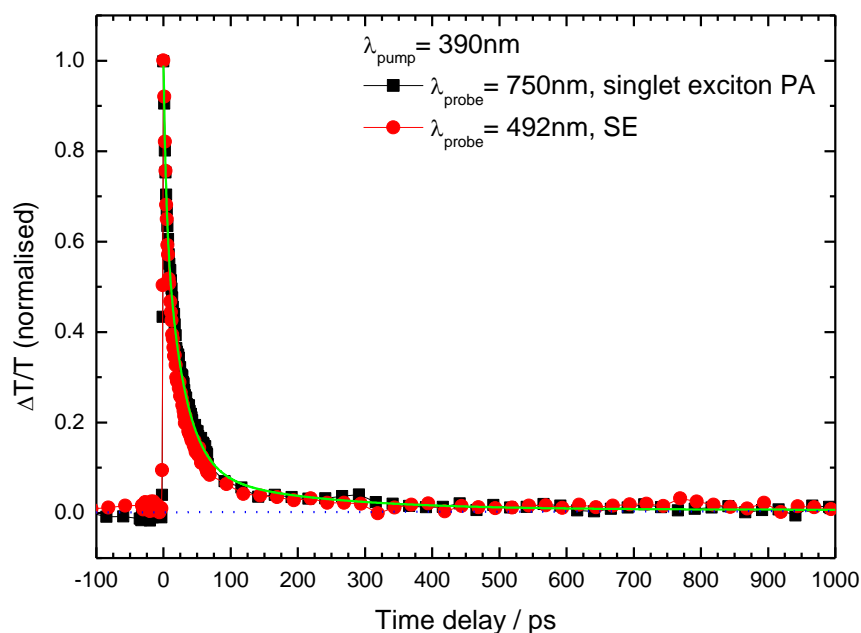
Figure 6.2: Normalised single-wavelength decay kinetics of the SE band (λ_{probe} = 494 nm, red circles) in MeLPPP, compared against that of the PA band (λ_{probe} = 750 nm, black squares) for excitation at 390 nm (3 μJcm^{-2}). Both sets of dynamics are noted to be approximately identical, with time constants of (3.9±0.3), (27±2) and (180±40) ps recorded using a multi-exponential fit (green line) for the PA data.

In addition to a decay in magnitude with time, a red-shift of the SE band is observed to occur over a time-period of the order of 10 ps, as evidenced by a change in wavelength of the SE-PA crossover (where $\Delta T/T = 0$) from 560 to 615 nm within 80 ps. This behaviour is consistent with the properties of exciton migration in conjugated polymers, which has been measured to occur on timescales between 10 and 100 ps.[12, 18, 83, 162]

The broad PA of the singlet excitons is also observed to overlap with two weaker PA bands at 590 and 650 nm, which are highlighted in Fig. 6.1B. These bands were noted to increase substantially in size upon increasing the pump fluence to 60 µJcm[-2]. At such high pump fluences bi-excitonic effects such as singlet-singlet annihilation (SSA) are expected to be prominent and have been well documented to lead to the formation of polarons via an intermediate excited singlet state.[52, 88, 90-92] The doublet of PA peaks at 590 and 650 nm is therefore assigned to the PA of two polaron transitions: $D_0 \rightarrow D_m$ and $D_0 \rightarrow D_N$, which is also in agreement with the results of previous studies.[46, 47, 64, 191]

It should be noted that various experimental factors are observed to complicate the form of the differential transmission spectrum. The SE from the fluorescence peak at 460 nm and the complete PB band, which overlaps exactly with the ground-state absorption spectrum of the polymer, are not observed as the WLSC probe used to obtain the spectra did not have sufficient intensity to be detected at wavelengths shorter than 500 nm. In addition a sudden decrease in the signal intensity to zero is observed at 760 nm and is due to the saturation of the photodetector by residual 780 nm light from the laser amplifier in the probe beam.

6.3.2 Singlet exciton dynamics

Before proceeding to investigate the properties of the PB band, a detailed study of the dynamics of the singlet exciton PA band at 750 nm was performed, with the results of this study used as a point of reference when considering the PB dynamics.

To provide a quantitative analysis of the singlet exciton dynamics, a multi-exponential decay fit was applied to the single-wavelength transient PA data at 750 nm; the result of this process is shown in Fig. 6.2. Three decay components of (3.9±0.3) ps (31% contribution by amplitude), (27±2) ps (58%) and (180±40) ps (9%) are obtained from the fit; the build-in of the PA was observed to occur within the time resolution of the system (~500fs). The physical origin of each of the decay components are now discussed in turn.

The longest lifetime component was noted to be generally reproducible across a large number of different films measured, with the values obtained ranging from (80±30) ps up to (180±40) ps. All of these lifetime components are of the same order of magnitude as the fluorescence lifetime of MeLPPP in film, as identified in streak camera studies presented in chapter 4. As discussed therein a range of fluorescence lifetimes was also obtained using the streak camera on different films, with values varying from ~110 to 200 ps. Given the similarity to these values to that measured in Fig. 6.2, the longest decay component in the singlet exciton PA is assigned to be the fluorescence lifetime of MeLPPP.

The second lifetime component of 27 ps is of the same order of magnitude as the reported timescales for exciton migration, as discussed above.[12, 18, 83, 162] In chapter 4 exciton migration was identified as a ~40ps decay component in the fluorescence dynamics of MeLPPP in film, as measured using a streak camera. The signature of exciton migration was also identified in transient transmission spectrum of MeLPPP in section 6.3.1 above as a red-shift in the SE band

over a time period of the order of 10 ps. In single-wavelength transient measurements exciton migration is expected to appear as a decay component. A single probe wavelength will interact only with a subset of the total distribution of chromophores in the polymer density of states (DOS); only those sites on which the exciton has the correct energy to interact with the probe will be measured. If a mechanism exists which can move an exciton off of that subset of sites, such as exciton migration, a loss in the single-wavelength transient measurements at that probe wavelength will be recorded. Given the similarity of this component to those assigned in other studies and the observation of a red-shift of the SE band recorded in these measurements to occur over a similar time period, the 27 ps component recorded in the singlet PA is assigned to the effect of exciton migration.

Unlike the first two components discussed above, the shortest decay component noted in the singlet PA was found to vary significantly in amplitude with the incident pump fluence. The results of a series of experiments in which the singlet exciton PA at 750 nm was monitored as a function of incident pump fluence is shown in Fig. 6.3. As can be seen a short decay component is observed to build in and become more prominent as the pump fluence is increased. To provide a more quantitative analysis of this behaviour a global multi-exponential fit was applied to the data, with the longest lifetime component fixed across all datasets to represent the fluorescence lifetime of the polymer; the results of this process are also included in Fig. 6.3, with the variation of the shortest lifetime component with fluence presented in Table 6.1.
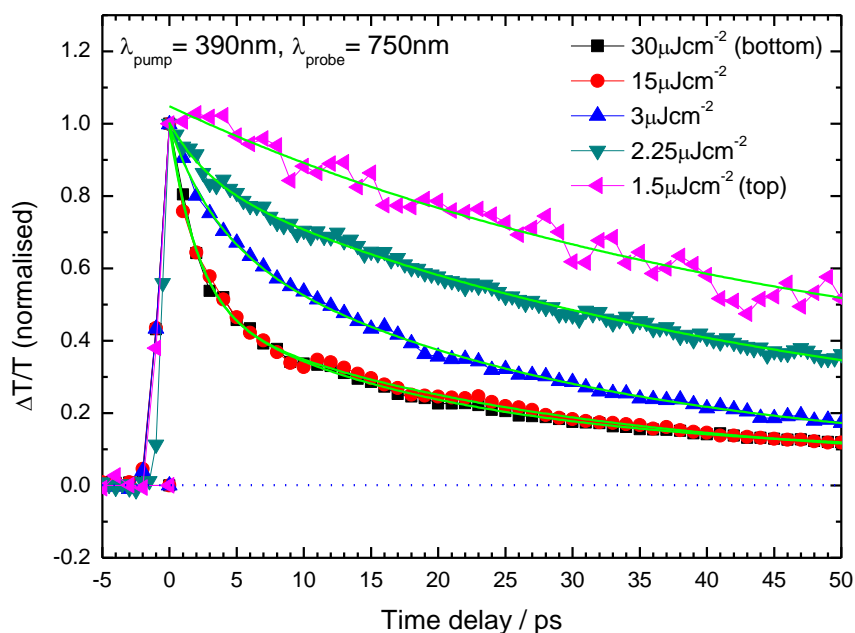
Figure 6.3: Normalised single-wavelength decay kinetics of the singlet exciton PA (λ_{pump}= 390 nm, λ_{probe}= 750 nm) for a range of incident pump fluences. A short component is observed to build in amplitude as the fluence is increased and is assigned to the effect of SSA.

A clear trend emerges from the data presented in Table 6.1. At large pump fluences the overall PA decay is dominated by a ~2 ps decay term. Upon decreasing the pump fluence from 30 to 2.25 μJcm^{-2} there is a substantial decrease in the relative contribution of the short component, to the extent that at 1.5 μJcm^{-2} the short component is no longer detected.

This behaviour shown in Fig. 6.3 and Table 6.1 is characteristic of a loss of a fraction of the singlet exciton population due to SSA. As discussed in section 2.6.6, during SSA two singlet excitons come sufficiently close to one another as to be able to exchange energy, with one exciton giving all of its energy to the other. This results in the formation of an excited singlet state.[52, 88, 90-92] As part of this mechanism one exciton is lost to the ground state and SSA therefore acts to quench the singlet population. At high excitation densities the excitons are

photogenerated close to one another and thus have a large probability to meet and interact within their lifetime; decreasing the excitation density reduces this probability and thus, as observed in Table 6.1, the relative contribution of SSA to the overall decay dynamics.[79, 88] The critical incident fluence at which SSA is first observed in these experiments (2.25 μJcm^{-2}) is of the same order of magnitude as that recorded in other conjugated polymers (0.7-1.0 μJcm^{-2} in regio-regular polythiophene,[117, 192] ~1.0 μJcm^{-2} in polyfluorene[88]). On the evidence presented above the ~2 ps component noted in the decay of the singlet exciton PA is therefore attributed to SSA.

Incident pump fluence / μJcm^{-2}	Singlet PA pre-exponential amplitude 1 (% by amplitude)	Singlet PA time constant 1 / ps
30	49±3	2.0±0.2
15	51±2	2.2±0.2
3	28±3	3.4±0.6
2.25	15±2	2.9±0.6
1.5	0	-

Table 6.1: Variation of the singlet exciton PA (λ_{pump}= 390 nm, λ_{probe}= 750 nm) as a function of incident pump fluence, as obtained using global multi-exponential fitting.

6.3.3 Photobleaching dynamics

The PB band of MeLPPP was investigated in a piecewise manner by recording the transient transmission dynamics at a discrete number of probe wavelengths. Unlike the SE and singlet exciton PA bands discussed above in sections 6.3.1 and 6.3.2, the PB recovery of MeLPPP in

film demonstrates non-trivial behaviour which cannot be immediately explained. The results of a series of measurements in which the probe wavelength was varied across the 0-0 feature of the absorption band at 295 K are shown in Fig. 6.4A. It should be noted that in these experiments a moderately high pump fluence of 15 μJcm^{-2} was used because measurements performed at 445 nm were subject to very small signal to noise ratios. In order for this data recorded to be analysed with any degree of accuracy, a high pump fluence was required.

At 295 K in all cases a PB signal is observed to build-in within the time resolution of the system (~500 fs). This is in agreement with the build-in of the singlet exciton population, as recorded at 750 nm and discussed in section 6.3.2 above. A fast decay component is observed to become quicker with decreasing probe wavelength. At a probe wavelength of 460 nm the decay on short time periods is characterised by a (5.3±0.1) ps (75% contribution by amplitude) time constant, whereas at 445 nm a (0.7±0.3) ps (76%) time constant is obtained.

Interestingly, for all probe wavelengths measured no component corresponding to the fluorescence lifetime can be identified. For example, at 460 nm the remaining contribution to the PB decay is provided by a (26±2) ps (25%) component, which is in good agreement with the component assigned as exciton migration in the analysis of the singlet exciton PA. No contribution corresponding to the fluorescence lifetime of the singlet excitons, which was identified as a ~180 ps decay component in the analysis of the singlet exciton PA, is recorded. This is a surprising result as the singlet excitons are the primary photoexcitations in MeLPPP and therefore some contribution from the recombination of these states is expected to be observed in the PB recovery.
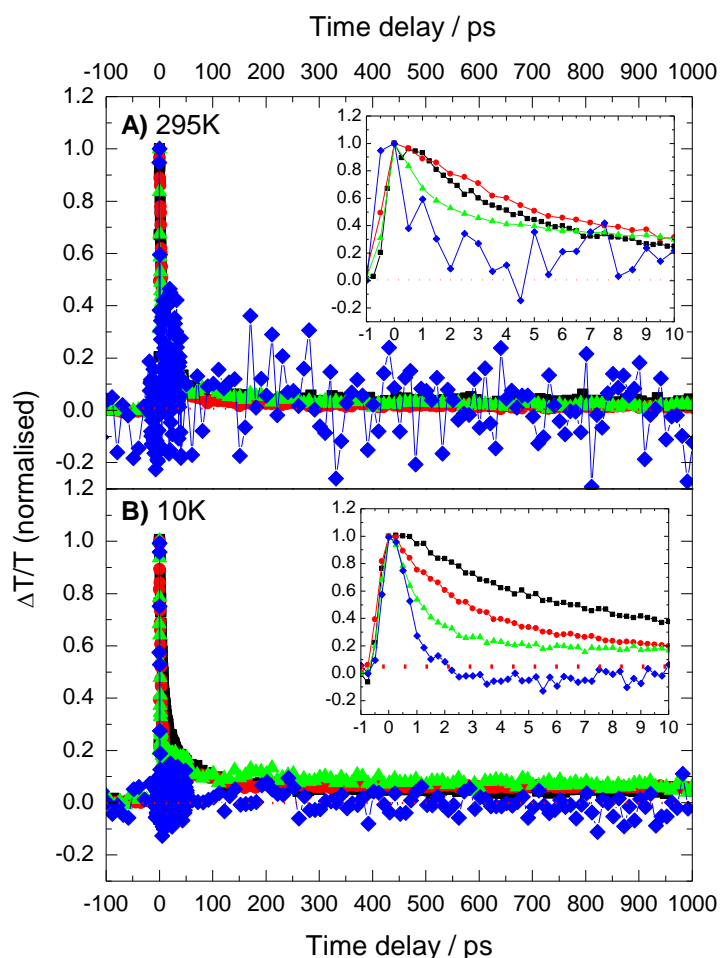
Figure 6.4: Normalised transient transmission dynamics of MeLPPP in film, for excitation at 390 nm (15 μJcm^{-2}) and probe wavelengths across the PB band of the polymer at 465 (black squares), 460 (red circles), 450 (green triangles) and 445 nm (blue triangles). A) For measurements at 295 K, an increasing fast component is noted with decreasing probe wavelength. Inset: close-up of the behaviour at early times. B) At 10 K an increasing fast component is also observed with decreasing wavelength and is much more prominent than at 295 K. At 445 nm a crossover from PB to PA is observed to occur after ~2 ps. Inset: close-up of behaviour at early times, highlighting the PB-PA crossover at 445 nm.

Exciton migration can appear as a decay term in the PB recovery on the same physical basis as to how it appears in the singlet exciton PA dynamics. The primary influence of exciton

migration in the PB recovery is to change the population of the excitons that interact with the probe pulse. As the probe pulse used in these experiments has a finite spectral width it can only interact with a narrow distribution of chromophores DOS and therefore only measure the PB recovery of a discrete number of chromophores. The migration of any excitons off of those chromophores will thus be considered as a loss of excited states (equivalent to a recovery of the ground state) as seen by the probe pulse and therefore measured as a decay component. Likewise, should an exciton migrate on to a member of that distribution of chromophores, a rise time will be noted in the PB recovery.

It is possible to perform a detailed study of the properties of exciton migration in a conjugated polymer by measuring the PB recovery as a function of probe wavelength; the migration of excitons from high to low energy chromophores can be measured as a decay in the PB recovery at short probe wavelengths and a matching build-in at long probe wavelengths (this matter is discussed in more detail in section 6.3.4).[120] In film dispersive exciton migration occurs on a <1 ps timescale,[20, 32] whereas non-dispersive exciton migration occurs with a lifetime of 10-100 ps.[20, 32, 86] The ~25 ps component assigned as the effect of exciton migration above is consistent with this latter process. It then becomes pertinent to ask whether the short decay component of the order of 1ps noted above in the PB recovery is associated with the effect of dispersive exciton migration, or is due to something else. This point will be addressed in a later section.

The PB dynamics of MeLPPP in film were also measured at 10 K for the same probe wavelengths measured at 295 K; these results are shown in Fig. 6.4B. As at 295 K, PB is recorded at the zero-delay time which is again attributed to the photogeneration of singlet excitons within the time resolution of the system. A fast decay component in the PB recovery is noted to become quicker with decreasing probe wavelength. This component is shorter than that of the corresponding PB recovery at 295 K; for example, for a probe wavelength of 460 nm

at 10 K the decay dynamics at short times is characterised by a (2.4±0.1) ps component, as
compared to (5.3±0.1) ps measured at 295 K. The most significant difference however between
the PB decay dynamics at 10 K as compared to 295 K is that for a probe wavelength of 445 nm
a crossover between PB ($\Delta T/T > 0$) and PA ($\Delta T/T < 0$) is observed to occur after ~2 ps, with
the PA then decaying to zero within 50 ps.

The form of the transient signal observed at 445 nm can only be explained by the presence of
an underlying high energy PA band that overlaps with the PB band. Indeed, the form of the
transient signals observed between 465 and 445 nm can be understood as different relative
degrees of superposition of PB with this underlying PA. For measurements between 465 and
450 nm the relative contribution of overlapping PA is not sufficiently large as to generate a
crossover in the measured signals from PB to PA, but can act to effectively quench the PB at
early times, resulting in the variation in the fast decay component discussed above. At 445 nm
however the magnitude of the PA after 2 ps is larger than the PB response, leading to a
crossover from PB to PA.

It is clear from Fig. 6.4B that the underlying PA takes a finite amount of time to build in, as
evidenced by the fact that at 445 nm at 10 K a crossover between PB and PA is only recorded
after ~2 ps. This observation indicates that the PA transition does not originate from the singlet
exciton population and thus cannot be a high energy variant of the S_1-S_N PA transition
discussed in section 6.3.2. If the PA was associated with the singlet exciton population, a
negative signal would be recorded at the zero delay time at a probe wavelength of 445 nm, with
no positive signal subsequently detected.

The existence of an underlying PA transition calls into question the effect of dispersive exciton
migration on the PB dynamics, which as discussed above would be expected to appear as a fast
decay term at probe wavelengths on the blue edge of the 0-0 transition in the PB band. On the

basis of the results obtained at 10 K it is now possible to rule out exciton migration as the primary effect which gives rise to the variation in the fast decay component noted with decreasing wavelength. It is clear upon comparing the data in Figs. 6.4A and 6.4B that for a fixed probe wavelength the decay rate of the PB is quicker at 10 K. This is however inconsistent with the properties of exciton migration, which has been established to decrease in rate with decreasing temperature.[20, 32, 193] Given the similarity of the evolution of the short decay component with probe wavelength at both 295 and 10 K, it is more likely that the behaviour at *both* temperatures is due to the increased overlap of an underlying PA with the PB, which acts to effectively quench the PB dynamics at early times, rather than the effect of exciton migration. It is however not possible, particularly at 295 K, to completely rule out some effect from dispersive exciton migration on the PB dynamics at early times.

Although no PB-PA crossover is observed for the data recorded at 295 K, the existence of overlap between the PB and an underlying PA can also be confirmed by returning to the analysis of the PB decay dynamics at 460 nm, in which no component corresponding to the fluorescence lifetime can be observed. This observation can now be attributed to a conflict between the overlapping dynamics of the PB band with an underlying PA which distorts the *measured* PB dynamics from the 'true' PB dynamics.

Wavelength and temperature dependence of the PB-PA overlap

At this point it becomes pertinent to consider whether the variation in the ratio between PB and PA with both probe wavelength and temperature arise as a result of a corresponding change in the PB, a change in the underlying PA, or a combination of both.

The behaviour of the PB-PA ratio is considered as a function of temperature first. As demonstrated in the inset of Fig. 6.1A, the absorption spectrum of MeLPPP in film is shown to

vary with temperature, with a small red-shift and narrowing of the peak features occurring with decreasing temperature. These changes are also expected to manifest in the PB band, which must follow the ground-state absorption of the polymer. As a consequence, for wavelengths shorter than 455 nm a decrease in the magnitude of the PB is expected to occur when cooling from 295 K down to 10 K. This could contribute to the relative increase in the magnitude of the PA with respect to the PB that occurs at 10K. An inspection of the inset of Fig. 6.1 reveals that at 460 nm the magnitude of the absorption, and thus in turn the magnitude of the PB at 460 nm, increases with decreasing temperature. The transient dynamics recorded at 460 nm however instead indicates an *increase* in the relative magnitude of the PA with respect to the PB at this wavelength, as characterised by the decrease in the short decay component from (5.3±0.1) ps to (2.4±0.1) ps at that wavelength. It is therefore possible to conclude that at 460 nm the increase in the magnitude of the underlying PA with respect to the PB band with decreasing temperature is not primarily due to the temperature dependence of the PB band (or equivalently the ground-state absorption) and is instead due to an increase in the magnitude of the underlying PA with decreasing temperature.

There are two important points to consider when considering how the PB-PA ratio varies as a function of probe wavelength. The first of these is the effect of exciton migration and has been discussed and subsequently eliminated as a major contributor to the observed PB dynamics above. The second point of consideration is the spectral line-shape of the PB band, which as discussed above follows the absorption spectrum of the polymer. Following on from this, it is clear that the PB at 445 nm should be much weaker than at 460 nm for all temperatures. This could contribute to the observed change in the PA-PB ratio observed with decreasing wavelength. For example at 460 nm the PB is large and thus the ratio of PA to PB is small. At 445 nm however the PB is much weaker and thus the PA-PB ratio is much larger, to the extent that the PA becomes comparable in magnitude to the PB and crossover from PB to PA can be

observed. This effect is also compounded by an overlap of the PB band with the SE band of MeLPPP, which arises as a result of the small Stokes shift between the absorption and fluorescence spectra. Returning to Fig. 6.1A, it is clear that there is a significant overlap between absorption and fluorescence for wavelengths longer than 450 nm. As a consequence, in addition to a contribution from PB at those wavelengths, there will also be a similar, positive contribution from SE ($\Delta T/T > 0$), thus increasing the total positive signal at those wavelengths and therefore reducing the ratio of the underlying PA with respect to the 'measured' PB.

Lifetime considerations

It should be noted that the lifetime of the underlying PA cannot be measured from the data presented in Fig. 6.4. In order to accurately measure the dynamics of the underlying PA, it is first necessary to isolate the PA from any overlapping contribution from the PB band. This process could theoretically be achieved by subtracting the true PB recovery at each wavelength from the transient transmission dynamics recorded in Fig. 6.4. This however presents a dilemma, as the data recorded in Fig. 6.4 demonstrates that it is impossible to measure the true PB recovery without picking up some contribution from the underlying PA. In summary, given the overlap of the PB with the PA, it is not possible with the data presented in this study to accurately extract the true PA dynamics in the polarisation independent data.

6.3.4 Variation with local morphology

In order to confirm the validity of the underlying PA feature noted to overlap with the PB band of MeLPPP in film, a series of repeat measurements were made for different films prepared in an identical manner as for those investigated in section 6.3.3 above. A selection of some of the results obtained at 10 K for a probe wavelength of 450 nm from two different films is shown in

Fig. 6.5. Note that repeat measurements performed on different regions of the same sample have also been included in this comparison.
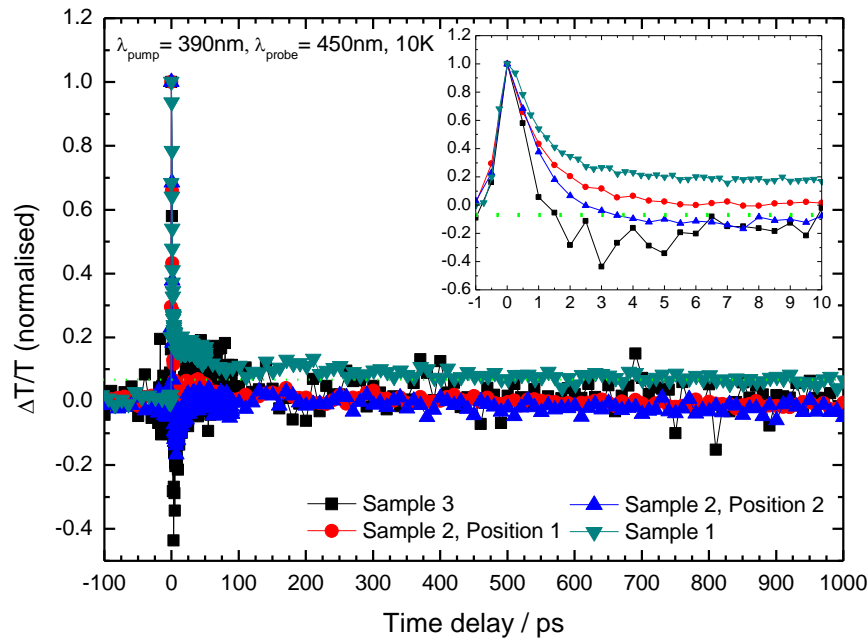
Figure 6.5: Normalised transient transmission dynamics at 10 K, measured at 450 nm (λ_{pump} = 390 nm, 15 μJcm^{-2}) repeated for a series of different MeLPPP films and different sample positions as indicated. A clear variation in the dynamics at early times is observed, with the measured ratio of PB with respect to the underlying PA changing between measurements. The variation is attributed to a dependence of the ratio on the local sample morphology. Inset: close up of the behaviour at early times, in which the variation at early times between repeat measurements is clear, with a crossover from PB to PA recorded in two cases to occur within 1-3 ps.

The transient transmission dynamics obtained across multiple repeat measurements for both different films and even different regions of the same film vary significantly at early times. Indeed, for two of the measurements performed (see sample 3 and sample 2, position 2) a PB-PA crossover is observed between 1 and 3 ps. Following on from the discussion of the behaviour observed in Fig. 6.4, the variation of the dynamics at early times in different films

and sample positions is attributed to a variation in the PB-PA ratio for each measurement. Given that throughout the repeat measurements the experimental conditions were kept constant, the variation in the PB-PA ratio observed can only be attributed to a change in the local sample morphology in which the pump-probe interaction is made.

To investigate the role of the local sample morphology further, the results obtained in film were compared with the results of similar measurements of the PB dynamics made in dilute solution. A selection of these measurements for a series of probe wavelengths across the PB band of MeLPPP in solution at 295K is shown in Fig. 6.6.

In contrast to that measured in film, no ultrafast quenching of the PB dynamics can be observed in solution. For example, it is clear upon comparing the data obtained at 440 nm in solution and 445 nm in film that there is no quenching of the PB in solution due to the presence of an underlying PA. It has instead been proposed that the PB dynamics in solution are instead dominated by the effect of intrachain exciton migration, with a decay of 4.2 ps noted at 440 nm matched by an identical 4.2 ps build-in at longer probe wavelengths of 450 and 460 nm.[120] Note that any contribution from any interchain processes, such as interchain exciton migration, is eliminated by performing measurements in dilute solution.

Unlike the PB dynamics measured in film at 295K, the PB dynamics in solution performed under similar pump and probe conditions can be completely explained by intrachain exciton migration; no contribution from an underlying PA state can be observed. It is therefore possible to conclude that the underlying PA feature in MeLPPP previously recorded is a consequence of interchain interactions that occur in the solid state.
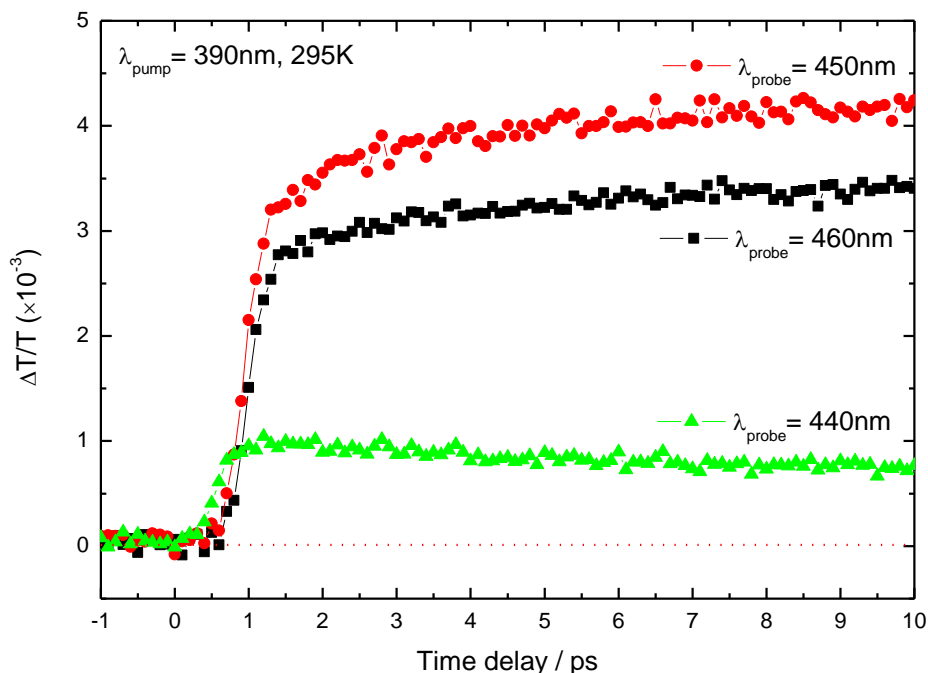
Figure 6.6: PB dynamics of MeLPPP in solution at a series of different probe wavelengths at 295 K (λ_{pump}= 390 nm, pump fluence unspecified). A decay component of 4.2 ps at 440 nm (green triangles) is matched by an identical build-in component at longer wavelengths (450 nm and 460 nm, red circles and black squares respectively) and has been attributed to the effect of intrachain exciton migration in solution. No rapid quenching of the PB by an underlying PA state can be observed at any of the wavelengths measured, in contrast to that observed in film (recorded by Dr Simon King of the Organic Electroactive Materials Group, Department of Physics, Durham University; figure taken and adapted from Ref. [120] and used with the permission of the author).

6.3.5 Polarisation dependence

In addition to polarisation independent studies performed under magic angle conditions, the PB dynamics at 10 K for a probe wavelength of 445 nm were also investigated as a function of pump and probe polarisation; these results are shown in Fig. 6.7. When the PB dynamics are measured with the pump and probe parallel polarisations aligned parallel to one another ($\Delta T/T_{\parallel}$) only PB is measured, with the decay dynamics principally characterised by a (1.1 ± 0.1) ps component. Significantly however, when the pump and probe polarisations are

aligned to be perpendicular ($\Delta T/T_\perp$), only a PA signal is measured, with the dynamics of this PA characterised by a (1.0±0.1) ps build-in component and a (36±6) ps decay component.

The decay lifetime of $\Delta T/T_\parallel$ and the build-in lifetime of $\Delta T/T_\perp$ are in excellent agreement with one another. Furthermore, as can be seen in the inset of Fig. 6.7, the build-in of $\Delta T/T_\perp$ only begins when the decay of $\Delta T/T_\parallel$ occurs. This confirms that there is a transfer of the excitation population measured in $\Delta T/T_\parallel$ (corresponding to PB only) to $\Delta T/T_\perp$ (corresponding to PA only), with the transfer characterised by a 1 ps component.
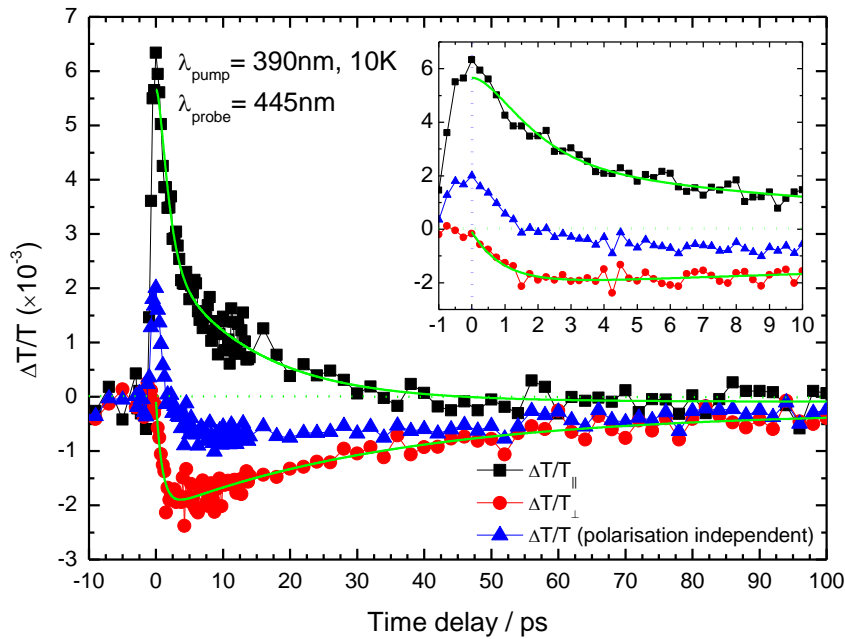
Figure 6.7: Polarisation dependent transient transmission dynamics, measured for a probe wavelength of 445 nm at 10 K (λ_{pump}= 390 nm, 15 μJcm^{-2}). When the pump and probe polarisations are set parallel ($\Delta T/T_\parallel$, black squares) only PB is measured. When the pump and probe are perpendicular however ($\Delta T/T_\perp$, red circles) only PA is measured. The polarisation independent PB dynamics, as produced by combining $\Delta T/T_\parallel$ and $\Delta T/T_\perp$ according to Eq. 6.1, has also been included (blue triangles). Inset: close up of dynamics, highlighting a (1.1±0.1) ps decay in $\Delta T/T_\parallel$ that matches a (1.0±0.1) ps build-in in $\Delta T/T_\perp$.

The polarised PB dynamics can be combined together as to produce a polarisation independent result as according to Eq. 6.1 below (also see section 3.9.3):

$$\Delta T / T(polarisation\ independent) = \frac{1}{3}[\Delta T / T_{\parallel} + 2 \cdot \Delta T / T_{\perp}] \qquad (6.1)$$

The polarisation independent dynamics are also included in Fig. 6.7. These dynamics show a clear similarity to the polarisation independent dynamics presented in Fig. 6.4 under the same experimental conditions, with a PB-PA crossover noted at a delay time of 1 ps. The fact that the measured PB-PA ratio is different in each case is attributed to the role of local sample morphology, as discussed in section 6.3.4 above.

Before proceeding further, it is important to clarify the physical meaning of $\Delta T / T_{\parallel}$ and $\Delta T / T_{\perp}$. When the pump pulse interacts with a sample, only those chromophores that have a transition dipole moment with a non-vanishing projection on to the pump polarisation can be excited. This results in the excitation of a finite number of chromophores, which is referred to as photoselection. This principle equally applies to the interaction of any excited states with the probe pulse. As a consequence, when the pump and probe polarisations are parallel, the probe pulse is only able to interact with those states with a dipole moment largely parallel to that of the photoexcitation population in the short time limit, i.e. the singlet exciton population. Likewise when the pump and probe are perpendicular, the probe pulse is only able to interact with those states that possess transition dipole moments largely perpendicular to that of the initial photoexcitations. Therefore in order to measure a net signal for $\Delta T / T_{\perp}$ a physical mechanism must exist that rotates the orientation of the transition dipole moments of the initial photoexcitations.

It is now clear from the polarisation dependent and independent dynamics measured in Fig. 6.7 that the underlying PA transition found to overlap with the PB as discussed previously in the

context of Figs. 6.4 and 6.5 can be attributed to the PA of a state with a dipole moment perpendicular to that of the initial intrachain singlet exciton population.

6.4   Discussion

The results presented in section 6.3.3, in which the PB dynamics of MeLPPP in film are considered as a function of probe wavelength and sample temperature, clearly demonstrate the presence of a high energy PA that overlaps with the PB band of the polymer. This PA has not been previously identified in the literature, primarily due to the lack of detailed ultrafast studies of the PB band in MeLPPP. Using the results obtained from ultrafast polarised transient measurements of the PB band and supported by a detailed study of the excited-state dynamics in MeLPPP, it is now possible to identify the origin of this PA.

The polarised data presented in section 6.3.5 (see Fig. 6.7) above confirms that the PA in question is associated with a transition dipole moment that is perpendicular to that of the primary photoexcitations of MeLPPP; namely the initial intrachain singlet exciton population. These states are generated on a femtosecond timescale,[58] as confirmed by a build-in of the singlet exciton PA and PB transient signals within the time resolution of the experimental system used, and have been demonstrated in previous studies to be delocalised largely parallel to the polymer backbone on which they exist.[87, 150] After photogeneration there are several possible mechanisms which can rotate the transition dipole moment of these states. The simplest of these is for the polymer chain on which excitations are generated to undergo conformational relaxation and rotate.[31, 87, 125] MeLPPP has however been established to form a rigid, rod-like backbone structure in which rotation of the backbone is prohibited.[87, 140, 141] As a consequence, any contribution to a rotation of the transition dipole moment in the excited state from conformational relaxation can be ruled out.

Exciton migration in film also contributes as a mechanism in which the transition dipole moment of an excited state can be changed. In an unaligned, isotropic film there is a random distribution of chain orientations and therefore a random distribution of transition dipole moments. As an exciton moves away from the chromophore on which it was photogenerated there is a high probability for the chromophore on which it ends up on to have a different orientation to that form which it originated.[32, 133, 134] Consequently over time the transition dipole moment of an exciton population will evolve on average to be different from that it began with. Exciton migration cannot however be responsible for the appearance of the PA observed to overlap with the PB in MeLPPP, as it only affects the energies of the singlet exciton population and does not directly result in the generation of a new state or PA transition. Furthermore the role of singlet excitons being responsible for the PA has been discussed above and subsequently eliminated on the basis that the underlying PA state is formed 1 ps *after* the singlet exciton population has been photogenerated.

Polarised spectroscopy has been applied by King *et al.* to study the orientation of singlet and triplet excitons in the conjugated polymer polyfluorene.[194] As part of this work it was demonstrated that the transition dipole moment associated with the triplet state is perpendicular to that of the singlet state. The underlying PA identified in this study cannot however be attributed to the formation of triplet excitons for several reasons. Due to the planar backbone structure of the polymer, the rate of intersystem crossing in MeLPPP is very small and not compatible with a 1 ps rise in the underlying PA as measured in section 6.3.5.[195-197] Furthermore, the lifetime of triplet excitons in MeLPPP has been measured to be 170 μs,[191] which is several orders of magnitude greater than the lifetime of the underlying PA, which was measured above to be (36 ± 6) ps.

The final process considered in the context of this chapter which can rotate the polarisation of an excited-state in a conjugated polymer is for there to be a sufficient degree of interchain

interaction such that an exciton becomes delocalised over two adjacent chains, resulting in the formation of an IEX state in which the electron of the exciton lies on one chain, with the hole lying on the other. This concept is considered in more detail below. Following the interaction of the polymer with the polarised pump pulse, only intrachain singlet excitons are generated. Polarisation studies of the steady-state absorption and fluorescence spectra in MeLPPP have demonstrated that the absorption transition dipole of these excitons is approximately parallel to the polymer backbone.[87] An IEX state by definition is delocalised over two adjacent chains and therefore has a transition dipole moment with a different orientation to that of the intrachain excitons. As a consequence, the delocalisation of an intrachain exciton to form an IEX state will result in the rotation of the excited-state transition dipole moment.

Based on the evidence presented above, the high energy PA in films of MeLPPP is assigned to the PA of IEXs generated in regions of the polymer film where the distance between polymer chains is suitable to support such a state. At the zero-delay time, the interaction of the pump pulse with the sample generates intrachain singlet excitons. In some regions of the polymer these excitons are able to become delocalised over two chains, forming an IEX state, with this process occurring with a time constant of 1 ps. This timescale can be measured as a matching build-in and decay between the parallel and perpendicular pump-probe polarisations of the dynamics measured at 445 nm; a fraction of the intrachain singlet exciton population that is probed by $\Delta T/T_\parallel$ is lost to form IEXs, which is represented by a matching 1 ps component in the decay of $\Delta T/T_\parallel$ and the build-in in $\Delta T/T_\perp$, the latter of which selectively probes the IEX population. Furthermore it is also important to note that no IEX states are formed at the zero-delay time with the interaction of the pump pulse; IEX formation requires an intrachain singlet exciton population to be generated first.

Attributing the unidentified PA to IEX formation is consistent with the finding of section 6.3.4 that the PA could only be measured in the solid-state and not in dilute solution. In the case of

the latter, any interchain interactions can be considered to be negligible and as a consequence interchain exciton formation is prohibited. The variation observed for the magnitude of the PA with the local sample morphology in film is also consistent with PA to IEX states. In order to be able to support the required interchain interactions for the formation of an IEX, the polymer chains in film must be packed together sufficiently closely and in a relatively ordered manner. Such behaviour has been considered at length in other systems; for example, the role of sample morphology on the formation of IEX states has been comprehensively investigated in regio-regular and regio-random polythiophenes.[189, 198-200]

Regio-regular polythiophenes have been demonstrated to self-organise into a two-dimensional lamellar structure, mediated by the interpenetration of the side-groups of adjacent polymer chains.[199] In these ordered regions the interchain separation has been measured to be as small as 3.8 Å[201, 202] and as such regio-regular polythiophenes demonstrate significantly enhanced yields of IEX formation as compared to their regio-random counterparts,[117, 189] which lack the aforementioned ability to self-organise into an ordered structure. Even within the class of regio-regular polythiophenes, the yield of IEX formation can be noted to vary significantly between polymers and is sensitive to the degree of regio-regularity.[99, 117]

Returning to the films of MeLPPP under study, the variation in the magnitude of the IEX population with sample and sample position can be understood to arise as a result of a variation in the local polymer order. In the films under investigation in this study it is possible that the local interchain order is larger in some regions than others and may also vary between films. Studies on films of regio-regular polythiophenes have demonstrated a similar variance in the degree of order within one film, with both ordered and disordered regions contributing to the observed excited-state dynamics.[106, 117, 189] This matter is also considered in chapter 7 of this thesis.

The interchain separation in films of MeLPPP has been estimated in the literature to be ~1.4 nm.[80] This increased interchain separation in MeLPPP could explain why the magnitude of the IEX PA is much smaller to that of regio-regular polythiophenes, in which the interchain separation is over three times smaller. This larger separation is attributed to the presence of bulky side groups added to the polymer backbone to aid solubility, which make it difficult for adjacent polymer chains to pack tightly together as is the case in region-regular polythiophenes. Simultaneously however the observation of IEX formation in MeLPPP implies that the interchain separation in films of MeLPPP is not too large as to completely prevent IEX formation.

MeLPPP possess a relatively small degree of inhomogeneous broadening for a conjugated polymer, which has been attributed to a high degree of intrachain order inferred by double-bridging between adjacent phenyl groups along the polymer backbone.[140, 141] It is not known for certain however whether MeLPPP can also possess a high degree of interchain order which may also contribute to the low degree of inhomogeneous broadening and simultaneously the formation of IEX states. It has been recorded that the inhomogeneous broadening in regio-regular polythiophenes, in which the interchain order is high, has been measured to be smaller than that of the corresponding regio-random derivatives in which the interchain order is much smaller.[189, 203] The question of interchain order in MeLPPP can only be sufficiently addressed by performing a detailed structural study of MeLPPP in film using an appropriate method, such as X-Ray diffraction. As mentioned in chapter 4 of this thesis, such studies have been proposed and are planned to be completed in the spring of 2011.

The existence of strong interchain interactions in regions of MeLPPP films corroborates with the findings of chapter 4 of this thesis, which considered the properties of electron-phonon coupling in the same polymer using a variety of steady-state and time-resolved fluorescence spectroscopic techniques. In that work a fundamental relationship between the vibrational

mode through which fluorescence occurs and the corresponding fluorescence polarisation was observed, indicating a failure of the Born-Oppenheimer approximation in describing the properties of electron-phonon coupling in the system. This failure was tentatively attributed to the role of moderate interchain interactions in MeLPPP and the subsequent effect of these interactions on the properties of the electron-phonon coupling, as according to theories outlined in the work of Spano *et al.*.[144-149] When presented this evidence was considered to be not entirely sufficient to conclusively prove the existence of strong interchain interactions in MeLPPP. The work of this chapter in which IEX formation has been proven through direct measurement agrees with and supports the findings of chapter 4.

The energy of the IEX PA in MeLPPP is very high and is one of the only instances to this author's knowledge in which the PA of an excited-state in a conjugated polymer overlaps with the ground state absorption spectrum of that polymer. It should be noted that previous studies which have investigated the formation of IEX states in conjugated polymers have demonstrated an overlap of the IEX PA with the SE of the polymer, confirming that in general for conjugated polymers the IEX PA is a relatively high energy transition. In the work of Rothberg *et al.* the PA of 'spatially indirect' excitons in poly[2-methoxy-5-(2'-ethyl- hexyloxy)-1,4-phenylene vinylene] was reported at an energy of 560 nm and was also recorded to overlap with the SE of that polymer.[188] It should be noted in those studies a crossover from SE to PA, similar to the crossover between PB and PA noted in this study, was found to occur as a function of *excitation* wavelength. In addition, in the work of Cerullo *et al.* in MeLPPP an additional PA band at 471 nm was observed to build in at very high excitation densities and was attributed to the formation of IEX states.[204] It should be noted that in those studies the incident pump fluence used was of the order of 1 mJcm^{-2}, which is several orders of magnitude larger than that used in the experimental work detailed in this chapter.

It is clear from the discussion above that there is a large amount of evidence in favour of assigning the high energy PA investigated in these studies to the absorption of IEX states. At first glance however the temperature dependence of the IEX formation appears to be inconsistent with this. The formation of IEX states in a conjugated polymer is expected to be a thermally activated process.[15, 21] If an IEX state formed is more delocalised than the initial intrachain singlet state from which it originates, the decrease in the binding energy between initial and final states must be compensated for. In the absence of an electric field, thermal energy can be used, increasing the probability of the required jump to occur and therefore increasing the rate of IEX formation.

As discussed above, the data presented in Fig. 6.4 confirms that the magnitude of the IEX PA is larger at 10 K than at 295 K. This corresponds to ~20 meV loss of thermal energy. This energy is negligible as compared to the amount of excess energy used to excite the polymer; for excitation at 390 nm as compared to the absorption maximum at ~455 nm, this corresponds to ~470 meV of excess energy. As a consequence, although the loss in thermal energy can be considered a negligible effect on the rate of IEX formation, the origin of the increase in the IEX formation is still surprising. On the basis that the excess energy for IEX formation remains approximately the same at both 295 and 10 K, the increased rate of IEX formation can instead only be attributed to a change in the local morphology of MeLPPP at low temperatures. As discussed previously, such a statement can only be formally concluded on the basis of detailed structural studies performed at different temperatures. It is however interesting to note that in chapter 4 of this thesis, the results of temperature dependent fluorescence studies were used to argue that MeLPPP in film undergoes some degree of conformational or structural change at temperatures below ~150 K. This conformational change could give rise to the observed increased yield of IEX formation by allowing the polymer chains to pack more closely to one

another. Such a point however is speculative and requires further experimental work to be performed before any firm conclusions can be drawn.

6.5   Conclusions

In summary, femtosecond pump-probe spectroscopy has been successfully used to identify and characterise an unknown high energy PA band in solid thin films of the ladder-type conjugated polymer MeLPPP. Following transient studies, performed as a function of probe wavelength, temperature and polarisation, this PA has been assigned to that of IEX states.

The IEX PA builds in with a time period of 1ps which is assigned to the time required for an intrachain singlet exciton to become delocalised over adjacent polymer chains. No IEX formation was observed to occur with the interaction of the pump pulse, confirming that the intrachain singlet exciton population is required as a precursor for IEX formation. The magnitude of the IEX PA is sensitive to the local polymer morphology, which is in good agreement with the reported properties of IEX formation in other conjugated polymers.

IEX formation in MeLPPP is more efficient at lower temperatures than at higher temperatures, implying that in this polymer it is easier for an intrachain singlet exciton to become delocalised over adjacent polymer chains at low temperatures. This result could be a consequence of the structural change noted to occur in MeLPPP with temperature as was recorded in chapter 4. As was concluded therein however, such a result can only be confirmed by performing a detailed structural analysis of the polymer with temperature, using a method such as X-Ray diffraction.

The energy of the IEX PA in these studies is one of the only instances in which PA transition of a conjugated polymer is high enough in energy as to overlap with the ground-state absorption. Furthermore the results of these studies strongly corroborate with the findings of chapter 4 of this thesis, in which a failure of the Born-Oppenheimer approximation in describing the

properties of electron-phonon coupling in MeLPPP was attributed to the presence of strong interchain interactions in films of the polymer. Despite the addition of bulky side groups added to the polymer backbone to aid solubility, adjacent polymer chains in MeLPPP in the solid state are able to stack close enough to one another in localised regions to support the formation of IEX states.

Chapter 7   Dynamics of delocalised polaron generation in a regio-regular polythiophene/PCBM blend

7.1 Introduction

7.1.1 The photophysics of regio-regular and regio-random polythiophenes

Understanding the photophysics of charge generation in a blend of a conjugated polymer with an electron acceptor such as [6,6]-phenyl-C_{61}-butyric acid methyl ester (PCBM) is currently the subject of a widespread research effort. The overall aim of this work is to apply an understanding of the fundamental process of charge generation at a molecular level to the development of more efficient organic solar cells. As part of this research effort, many ideas and models, sometimes conflicting, have been introduced in the literature over a relatively short period of time. At present there is no truly universally accepted model of charge generation in an organic solar cell.

Regio-regular polythiophene derivatives, such as regio-regular poly(3-hexylthiophene) (RR-P3HT) and regio-regular poly(dodecylthiophene-2,5-diyl) (P3DDT) have emerged as promising candidates for use in an organic solar cell, demonstrating power-conversion efficiencies approaching 5% in bulk-heterojunction devices based on PCBM.[205, 206]   The relatively high efficiency of these devices has been attributed in part to the ability of regio-regular polythiophenes to self-organise into a two-dimensional lamellar structure, in a process mediated by the interpenetration of the side-groups of adjacent polymer chains.[199, 207, 208] In this ordered structure, a schematic of which is shown in Fig. 7.1, the distance between adjacent planes of polymer chains is very small and as such regio-regular polythiophenes

demonstrate high charge mobilities and strong interchain interactions for a conjugated polymer. X-Ray diffraction studies have determined the interplanar spacing in RR-P3HT and P3DDT to be 3.8 Å,[201, 202, 208] although accurate structural modelling of such data suggests that this value should be doubled to 7.6 Å take into account the effect of side-group rotation that occurs when the polymer chains are brought together in close proximity.[207]
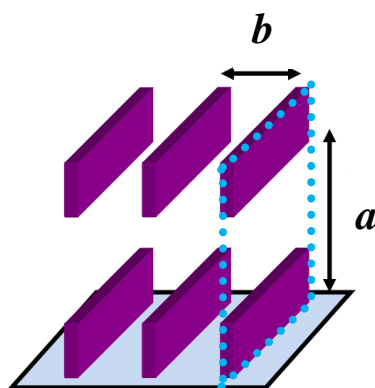
Figure 7.1: Lamellar structure of a regio-regular polythiophene. The interpenetration of adjacent polymer chains (purple blocks), results in the formation of 2D sheets of polymer (blue dotted line) stacked perpendicular to the substrate direction. In the figure *a* is the interchain spacing and *b* the interplanar spacing, which has been measured to be 7.6Å in P3DDT.[207] Figure adapted for use from Ref. [199].

One of the primary consequences of the strong interchain interactions in a regio-regular polythiophene is that the electron and hole of an intrachain singlet exciton can be readily delocalised over adjacent polymer chains to form an interchain singlet exciton state.[146, 189, 198-200, 209] The properties of interchain interactions in RR-P3HT have been thoroughly investigated. In the work of Brown *et al.*, the formation of interchain excitons in RR-P3HT was delineated by modelling the contribution of vibronic modes in the absorption and fluorescence spectra of the polymer. As part of this work, interchain exciton absorption was identified as the lowest energy peak in the absorption spectrum, confirming that in RR-P3HT the interchain exciton state is lower in energy than the corresponding intrachain state.

Brown's work was built upon by the results of quantum-chemical simulations performed by Spano *et al.*, in which it was demonstrated that the spectroscopic properties of RR-P3HT could be explained using a model in which emission was made solely from aggregate states of polymer. The key aspect of this model, which was discussed in chapter 4, is that the interactions between adjacent polymer chains in the aggregate states are comparable in strength to the electron-phonon coupling of a single chain.[145, 146, 210]

Another consequence of the strong interchain interactions in a regio-regular polythiophene is that the photoluminescence quantum yield (PLQY) of such a polymer is much lower than the corresponding regio-random derivative; the PLQY of RR-P3HT has been measured to be <0.5%, as compared to 8% in region-random poly(3-hexylthiophene) (RRa-P3HT).[189, 211] The reason for this has been attributed to the role of interchain interactions in splitting the first excited state ($1B_u$) of the polymer into two energy levels, with the lower level attaining A_g symmetry. Emission from this level is forbidden under the selection rules[211] (see section 2.4.1) and consequently the decay of the singlet exciton state in RR-P3HT is primarily non-radiative; radiative transitions can however become weakly allowed in the presence of any intermolecular disorder.

In a regio-regular polythiophene it is possible for the electron and hole of an exciton to move sufficiently apart from one other as to result in the formation of a geminate polaron-pair (GPP). GPP formation at the expense of the singlet exciton population is a process mediated by excitation energy[117] and can be explained using the model of hot exciton dissociation, as developed by Arkhipov *et al.*[15, 21] In this model the brief increase in local chain temperature that arises as a result of the thermalisation of excess excitation energy leads to an increased probability for the electron and hole of an exciton to overcome their respective coulomb interaction, leading to the formation of a GPP. The strong interchain interactions in a

regio-regular polythiophene allow this process to happen at lower excess energies than that required in the corresponding regio-random derivative.[117, 189]

There are two primary decay pathways associated with the GPP state. The first is for the electron and hole of the GPP to recombine.[189] This process occurs only between the electron and hole of a single GPP, as opposed to the electron and hole of different GPPs, and is thus referred to as geminate recombination. Geminate recombination can be distinguished apart from bi-molecular recombination on the basis that the rate of the former is independent of excitation density, while the latter is not.

The second decay pathway of the GPP state is for the electron and hole to move further apart such that no correlations of any kind remain between the two, leading to the formation of a pair of free polarons (c.f. the discussion of section 2.3.3 concerning polaron formation from excited singlet exciton states).[189, 192] This is particularly significant in the context of an organic solar cell: in a regio-regular polythiophene, charge generation following photoexcitation can occur independently of any interaction with the electron acceptor. This was demonstrated in the work of Piris *et. al.* in which the internal quantum yield of free polaron generation in pristine RR-P3HT was measured to be 15%; this value was recorded to increase to 50% at early times following the introduction PCBM into the system.[192]

7.1.2 Charge generation in an organic solar cell blend

The basic physical principle behind efficient charge generation in an organic photovoltaic system is the introduction of an electron acceptor, such as PCBM, into the polymer host to facilitate the dissociation of excitons. This mechanism is widely understood to involve the formation of a charge-transfer (CT) state at the polymer/acceptor interface, which occurs as a result of electron transfer from singlet excitons in the excited host to the acceptor material (see

section 2.7.2).[93, 94, 104, 107, 171, 212, 213]   Recent work has developed the role of the CT state in charge generation further by confirming charge generation through the direct excitation of a ground-state CT complex, indicating that CT states can be formed independently of the photoexcitation of singlet excitons.[97, 108]

The importance of the CT state in determining the dynamics of free carrier generation and the total charge yield of a polymer/acceptor blend is still the subject of debate. One commonly accepted concept is that the dynamics of charge generation are determined by the dissociation of the CT state[99] which occurs through a manifold of tightly packed charge-separated states.[8, 93, 100, 214] Recent investigations have revealed that the fate of the CT state is determined by the polymer chain conformation. In the work of Hallermann *et al.*, a marked decrease in the intensity of CT emission due to charge recombination across the polymer/acceptor interface was recorded in RR-P3HT, as compared to the corresponding regio-random derivative RRa-P3HT where relatively strong CT emission was observed.[109] These findings have been developed further as part of time-resolved studies of charge generation and recombination in RR-P3HT and RRa-P3HT by Guo *et al.*.[106, 117, 215] A key conclusion of this work was that whereas in RR-P3HT/PCBM blends the CT dissociation yield is close to 100%, in RRa-P3HT/PCBM blends, despite an equally efficient electron transfer to PCBM, geminate recombination of the CT state is responsible for a massive loss (~70%) of potential charges within 800 ps.

Another key aspect of Guo's work concerned the role of morphology in determining the dynamics of polaron formation in RR-P3HT/PCBM blend films. Guo was able to demonstrate two different mechanisms by which polarons could be formed in such a system: i) the instantaneous (<100 fs) formation of polarons generated in interfacial regions of polymer and acceptor, and ii) delayed polaron formation, where singlet exciton migration from bulk domains of polymer is the rate limiting process for charge formation.
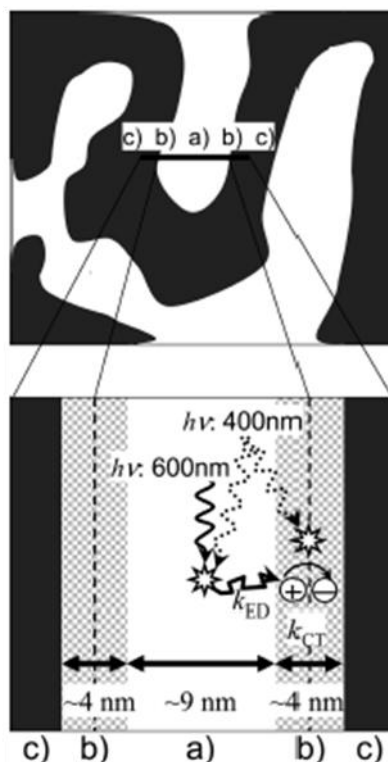
Figure 7.2: Pathways towards charge generation in RR-P3HT/PCBM blend films, as determined by Guo *et al.*.[106] In a bulk-heterojunction blend, polymer and acceptor form a bi-continuous network of overlapping phases. Ordered domains of pure polymer (a) are formed away from domains of pure acceptor (c). The key conclusion of Guo's work was to infer the existence of an intermediate disordered region (b) in which the order of the polymer is disturbed by the presence of the PCBM. Low incident photon energies selectively excite ordered regions of polymer, with charge generation proceeding through the migration to and subsequent dissociation of excitons in interfacial regions. High incident photon energies can simultaneously excite both ordered and disordered regions, leading to the formation of charges on two timescales; one occurring on a femtosecond timescale, the latter determined by the properties of exciton migration/diffusion. Figure adapted for use from Ref. [106].

The relative contribution of the two mechanisms outlined above was shown to be a function of excitation energy. Whereas at low excitation energies singlet excitons are generated solely in the bulk domains, which are characterised by a high degree of interchain order and a low energy absorption, excitation at high energies can simultaneously excite both the bulk and interfacial regions of polymer. In the interfacial regions the natural ordered structure of the

polymer chains is disturbed by the presence of the PCBM molecules, resulting in a disordered structure with higher energy absorption. These different regions and the related processes by which charges are formed are illustrated in Fig. 7.2.

In an effort to try and establish a firm conceptual footing on which to proceed concerning the photophysics of charge generation in an organic photovoltaic system, a study of the photoexcitation dynamics in bulk-heterojunction blends of regio-regular P3DDT with the electron acceptor PCBM was performed using femtosecond pump-probe spectroscopy. Even during the relatively short course of this study new ideas were introduced in the literature, primarily the work of Guo *et al.* referenced above. The work described in this chapter aims to build upon the ideas of Guo in order to develop an understanding of the various processes leading up to the generation of charges. In particular, focus is placed on the generation of charges in ordered domains of polymer, which was not fully addressed by Guo.

In summary, charge generation in ordered regions of polymer in P3DDT/PCBM (1:1 wt%) blends has been characterised by measuring the dynamics of photoinduced absorption bands corresponding to delocalised polaron states, as identified in recent studies by Guo *et al.*.[106, 215] Pathways towards charge generation are identified by correlating the build-in dynamics of the aforementioned polaron band with the decay of the singlet exciton and GPP PA bands of the polymer. The results of measurements performed as a function of excitation energy are used to determine the relative contribution of these states towards charge generation in ordered regions of the blend. The results of this study demonstrate that, following excitation at high incident photo energies, the dissociation of GPP states, rather than the migration of singlet exciton from the bulk to PCBM interfaces, is the primary mechanism by which charges are formed in ordered regions. This is significant, as the geminate recombination of the GPP state then constitutes a fundamental and significant loss mechanism of potential charges. This study also demonstrates that femtosecond pump-probe spectroscopy can be used to gain a significant

amount of information concerning the dynamics of charge generation in an organic solar cell blend and sets a foundation for future research as part of a wider project in this rapidly developing field.

7.2   Experiment

7.2.1 Materials

Solid thin films of P3DDT (M_W = 39770, polydispersity index = 1.48, >98% head-to-tail regio-regularity, Plextronics), P3DDT doped with PCBM (>99%, Sigma-Aldrich) in a 1:1 weight ratio and pristine PCBM were deposited by spin casting at 1500 rpm for 45 seconds onto sapphire substrates from toluene (Romil) solutions of concentration 10 mg.ml^{-1}. The chemical structure of P3DDT is given in Fig. 7.3; the chemical structure of P3HT is also included for reference.

A) Poly(dodecylthiophene-2,5-diyl) (P3DDT)   **B) Poly(3-hexylthiophene) (P3HT)**
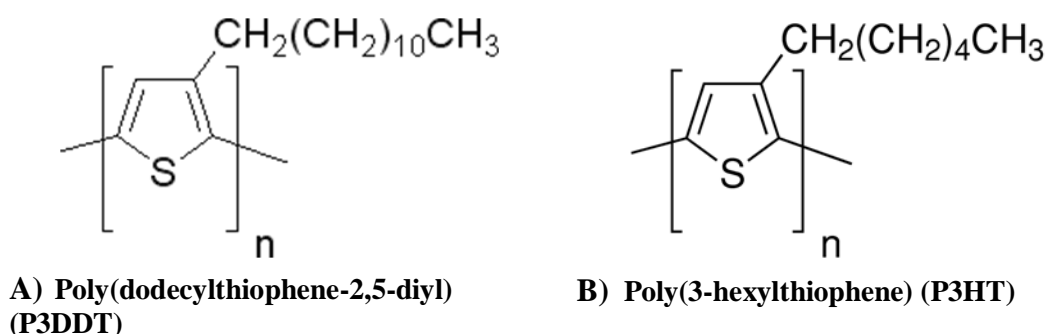
Figure 7.3: Chemical structures of A) P3DDT and B) P3HT. Note that in this study, the (head-to-tail) regio-regular variant of P3DDT was used.

7.2.2 Spectroscopic measurements

Ultrafast spectroscopic measurements were made using a conventional femtosecond non-colinear pump-probe setup, as described in chapter 6. A single-wavelength output

(450-710, 390 nm) was used to pump, with both a white-light supercontinuum (WLSC, 450-870 nm) and a single-wavelength near-infrared (NIR) idler output (800-1200 nm) used to probe. For all experiments the polarisation of both pulses were orientated at 55^0 (magic angle) to each other using a variable $\lambda/4$-waveplate. Detection of the probe beam was performed using a silicon photodiode in the visible and a liquid-nitrogen cooled indium gallium arsenide detector in the NIR. All measurements were performed at 295 K.

It should be noted that due to the fixed relationship between the wavelength of the signal beam and idler outputs of the OPA (see section 3.5), it was not possible to perform a study of the NIR PA bands in the pristine and blend films using excitation into the main polymer absorption band at 550nm, as would be preferred; in such cases it was instead necessary to provide excitation using the 390 nm output. The consequences of this are discussed in a later section.

Steady-state absorption spectra were obtained using a Schimadzu UV-3600 spectrophotometer. Fluorescence spectra were recorded using a custom-built setup. Samples were mounted in a closed-cycle He cryostat under a dynamic vacuum of 10^{-4} mbar and excited using an electronically modulated 355 nm diode laser. Photoluminescence was collected in a right-angle geometry with respect to excitation and measured using a silicon photodiode and a lock-in amplifier referenced to the modulation frequency of the excitation. Time-correlated single-photon counting (TCSPC) measurements used to determine the fluorescence lifetime of P3DDT were performed as described elsewhere.[20]

7.3 Results and discussion

7.3.1 Exciton dissociation and charge generation in P3DDT/PCBM (1:1 wt %) blend films

Absorption and fluorescence spectra of P3DDT and P3DDT/PCBM films

The steady-state absorption and fluorescence spectra of solid thin films of pristine P3DDT, pristine PCBM and P3DDT/PCBM (1:1 wt%) blends are shown in Fig 7.4A. The absorption spectrum of P3DDT is in excellent agreement with previous results,[203] with three overlapping peak features recorded at 525, 560 and 605 nm. The lowest energy peak in the absorption spectrum at 605 nm has been attributed to the absorption of singlet interchain exciton states in the polymer,[209] although this was redeveloped by Guo to be specifically assigned to the absorption of ordered regions of polymer (see the discussion of section 7.1.1 and Fig. 7.2).[106, 117] Similarly the peak at 560 nm has been attributed to the absorption of intrachain singlet excitons, or equivalently, as assigned by Guo, to the absorption of disordered regions of polymer.[106, 117, 209] The fact that the absorption of ordered regions occurs with a lower probability than disordered regions can be attributed to the interchain character of the singlet excitons in ordered regions. Upon doping the polymer with PCBM a blue-shift of ~10 nm with respect to the pristine films is observed and is consistent with a decrease in the average conjugation length of the polymer chains in the presence of the PCBM molecules.[103, 205, 216]
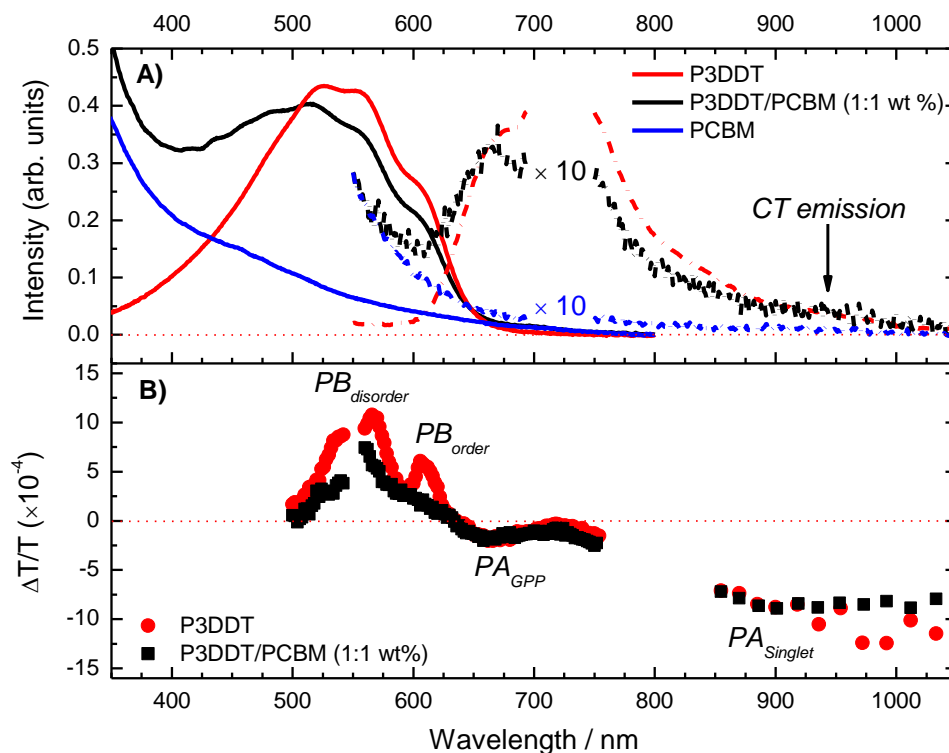
Figure 7.4: A) Re-scaled steady-state absorption (solid lines) and fluorescence (355 nm excitation, dash-dot lines) spectra of thin films of pristine P3DDT (red), P3DDT/PCBM (1:1 wt %) (black) and PCBM (blue). A weak peak in the fluorescence spectrum of the blend film attributed to CT emission is highlighted. Note that data has been rejected around 710 nm due to saturation from the second-harmonic of the excitation source. B) Femtosecond transient transmission spectra of pristine P3DDT (red circles) and P3DDT/PCBM (1:1 wt %) blend (black squares) at the zero pump-probe delay time. Each spectrum was recorded in two steps; between 500 and 750 nm a WLSC probe was used in conjunction with 550 nm excitation (incident pump fluence: 3 µJcm^{-2}); between 850 and 1050 nm a single wavelength probe was used in conjunction with 390 nm excitation (15 µJcm^{-2}). Note that the incident pump fluence was adjusted between measurements to maintain the same excitation density in the polymer. Data has been rejected in the region around 780 nm due to saturation from the fundamental of the laser amplifier.

The fluorescence spectra of the pristine and blend films are also compared in Fig. 7.4A. As expected a large reduction in fluorescence intensity is observed upon doping the polymer, which is attributed to the quenching of singlet excitons due to electron transfer between the polymer and PCBM moieties. A very weak peak can just be detected in the fluorescence

spectrum of the blend film at ~950 nm. In the work of Hallermann *et al.* the contribution of CT emission in the fluorescence spectra of RR-P3HT/PCBM was measured and attributed to a very weak peak on the low energy shoulder of the fluorescence spectrum at 1033 nm.[109] As per the analysis of that study, the peak in the P3DDT/PCBM (1:1 wt %) spectrum is attributed to low intensity CT emission.

Pristine P3DDT: transient transmission spectra and dynamics

The transient transmission spectrum of pristine P3DDT at the zero pump-probe delay time is shown in Fig 7.4B. This data was recorded in two steps: between 500 and 750 nm the WLSC was used to probe in conjunction with 550 nm excitation; between 850 and 1050 nm the single wavelength output was used to probe in conjunction with 390 nm excitation. In order to maintain the same excitation density the incident pump fluence was adjusted according to the absorption spectrum of the polymer.

The transient transmission spectrum of P3DDT is in excellent agreement with other regio-regular polythiophene derivatives[99, 106, 189, 192] and as such the various PA bands are classified in accordance with the established results of previous studies. The region of positive differential transmission in pristine P3DDT which overlaps with the absorption of the polymer is assigned as photobleaching (PB), with clearly resolved peaks identified at 525, 560 and 605 nm. As per the discussion of the absorption spectrum above, the peak at 605 nm is attributed to the PB of ordered regions of polymer, with the peak at 560 nm attributed to the absorption of disordered regions.[106, 117] It should be noted that the PB band at wavelengths shorter than 525 nm is not observed in Fig. 7.4B, as the intensity in the WLSC in that spectral region was not sufficient to be detected.

No stimulated emission can be observed in the transient transmission spectrum of the pristine polymer between 600 and 800 nm. This is attributed to the low PLQY of the polymer as a result of the interchain character of the singlet excitons.[189] In the place of the stimulated emission, a small photoinduced absorption (PA) band centred at 660 nm is observed. In previous studies this band has been attributed to the PA of GPP states in the polymer.[117, 189] To confirm this, single-wavelength transient transmission dynamics at 660 nm were measured as a function of incident pump fluence from 7.5 µJcm^{-2} up to 45 µJcm^{-2}; this data is shown in Fig. 7.5. In accordance with previous results,[117, 189] an intensity-independent ultrafast decay component of (0.9±0.1) ps is recorded at early times using multi-exponential global fitting and is characteristic of the geminate recombination of the GPP state.
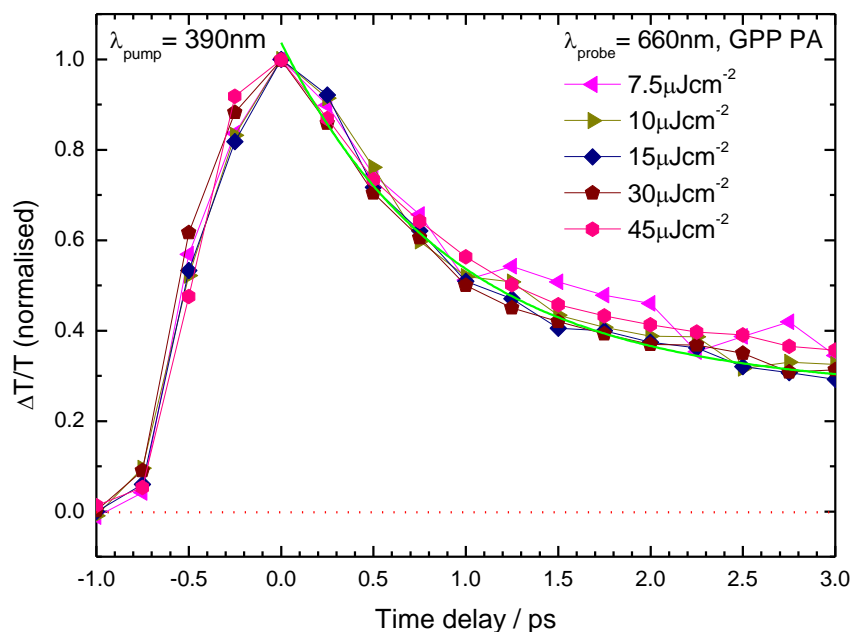
Figure 7.5: Normalised transient PA dynamics of the GPP band in pristine P3DDT, recorded as a function of incident pump fluence (λ_{pump}= 390 nm, λ_{probe}= 660 nm). For all decay dynamics a constant ultrafast decay component (0.9 ps as measured using global multi-exponential fitting, green line) was measured and is indicative of geminate-pair recombination.

The broad PA band extending into the NIR for wavelengths greater than 750 nm has been attributed in the literature to the PA of singlet exciton states.[117, 189, 192] The single-wavelength transient transmission dynamics of this band at a probe wavelength of 1200 nm are shown in Fig. 7.6. Before proceeding to analyse the decay dynamics of this band, the weak fluorescence decay of the singlet excitons in pristine P3DDT was measured using TCSPC. These studies were performed exclusively by Dr. Konstantinos Bourdakos of the Organic Electroactive Materials Group, Durham University, with decay components of (30 ± 1) ps (36% by pre-exponential amplitude), (206 ± 1) ps (55%) and (613 ± 5) ps (9%) obtained following a multi-exponential analysis. The longest lifetime component of 613 ps is attributed to the fluorescence lifetime of P3DDT in film and is in excellent agreement with reported values of the fluorescence lifetime in RR-P3HT (600-660 ps).[192, 217] The fact that this lifetime is relatively long compared to other conjugated polymers (see chapter 4, in which the fluorescence lifetime of ladder-type methyl-substituted poly(para-phenylene) was determined to be ~200 ps) can be attributed to the fact that the fluorescence transition in P3DDT is partially forbidden. The majority of the decay is dominated by a 206 ps component, which has been attributed to the non-radiative decay of the singlet excitons.[192]

The decay components obtained using TCSPC were used to provide a foundation for analysis of the decay of the singlet exciton PA. Initial attempts to analyse the data incorporated 206 and 613 ps lifetime components as fixed parameters in a multi-exponential fitting process; in such cases however the amplitude of the 613 ps component was measured to be small enough as to be considered negligible. Subsequent fitting processes instead incorporated the 206 ps component alone as a fixed parameter; the results of this process are shown in Fig. 7.6, with decay components of (1.9 ± 0.4) ps (44%) and (22 ± 3) ps (48%) obtained. Previous studies in which the excitation dynamics of RR-P3HT were monitored as a function of incident pump fluence (for excitation at 400 nm) have identified a 2 ps time component above a critical

incident fluence of ~1 μJcm^{-2} to be characteristic of singlet-singlet annihilation (SSA).[117, 192] A similar critical fluence of 1 μJcm^{-2} for the onset of SSA has also been recorded in polyfluorene.[88] Recent studies of SSA in RR-P3HT have also been performed which have demonstrated a critical excitation density of 1×10^{12} photons/cm^2 for the onset of SSA.[217] The reported values from the literature are smaller than the pump fluence used in the experiments detailed in this chapter (15 μJcm^{-2}, 3×10^{12} photons·cm^{-2}). The 2 ps component observed in the decay of the singlet PA in the pristine films is therefore assigned to the effect of SSA. Note that no component corresponding to SSA can be identified in the TCSPC data, as the incident pump fluence used in those experiments was several orders of magnitude smaller than for pump-probe measurements.

The absence of any identifiable component corresponding to the fluorescence lifetime in the singlet exciton PA can be attributed to the forbidden nature of the radiative recombination of these states in P3DDT; in pump-probe experiments the weak contribution from the fluorescence lifetime in the singlet exciton PA is much smaller in comparison to the contribution of SSA and subsequently cannot be detected.

The decay component of 22 ps is assigned to the effect of exciton migration, which has been well documented to occur on such timescales[12, 18, 20, 83] and is the same order of magnitude as the 30 ps component identified in the fluorescence decay using TCSPC. Note that in chapter 6 exciton migration in methyl-substituted ladder-type poly(para-phenylene) was identified as a ~25 ps decay component in the singlet exciton PA of that polymer.
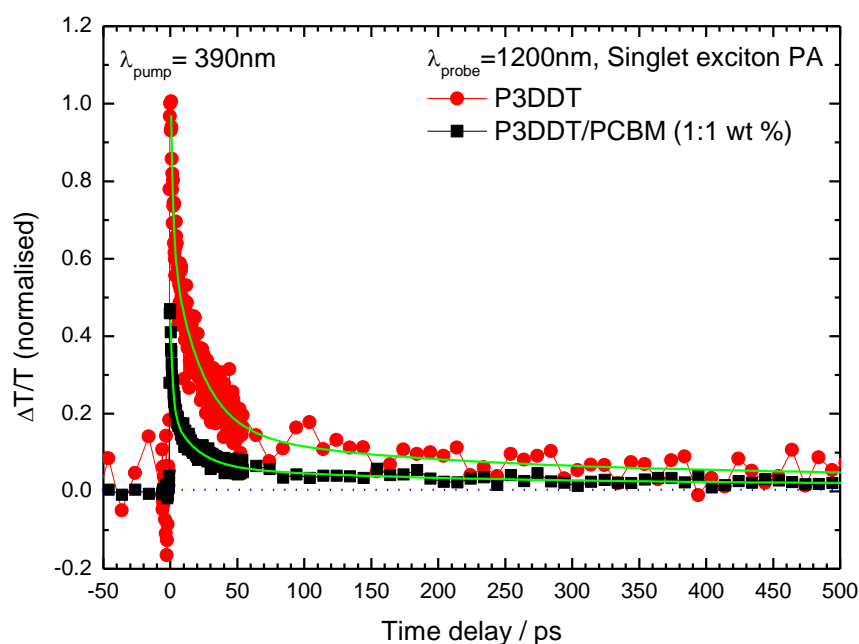
Figure 7.6: Transient PA dynamics of the singlet exciton PA band in pristine P3DDT (red circles) and P3DDT/PCBM (1:1 wt %) blend films (black squares), recorded at 1200 nm (λ_{pump}= 390 nm, 15 μJcm^{-2}). Quenching of the singlet excitons is recorded in the blend film at the zero delay time and is attributed to the occurrence of electron transfer from the polymer to the PCBM. The results of a multi-exponential fit have been included (green lines).

P3DDT/PCBM: transient transmission spectra and dynamics

The transient transmission spectrum of the blend film is compared against that of the pristine film in Fig. 7.4B. Upon doping a blue-shift and reduction in intensity of the PB band is observed and follows the corresponding change of the absorption spectrum. PA bands similar to that identified in the pristine film corresponding to singlet excitons and GPPs are identified at 1000 and 660 nm respectively. A reduction in intensity of the singlet PA band at the zero-delay time is observed. This is attributed to the quenching of singlet excitons at the polymer/acceptor interfaces within the pulse-limited minimum time resolution of the experimental system (~500 fs). The quenching is simultaneously accompanied by a non-

uniform increase in intensity in the PA between 630 and 750 nm, confirming the presence of a new overlapping PA band due to the addition of the PCBM.

At this point in this study it is important to highlight that the enforced decision to excite at 390 nm for measurements in the NIR (see section 7.2.2) has important consequences for the photophysical processes that occur in the blend film. It is clear from Fig. 7.4A that excitation at 390 nm will be made primarily into the PCBM molecules in the blend. Therefore under these excitation conditions most of the excited-states generated in the blend film will be singlet exciton states in the PCBM molecules, with a smaller fraction of singlet excitons being generated in the polymer. Electron transfer following excitation of PCBM molecules in a RR-P3HT/PCBM blend system has been observed to occur within 250 fs, leading to the formation of charges in both the polymer and PCBM.[103] Therefore excitation at 390 nm in the blend film will generate pathways towards charge generation originating from both the polymer and PCBM, complicating any analysis of the polaron PA bands under such conditions.

On the basis that excitation at 390 nm would not influence the properties of the polymer singlet excitons generated in the blend film, the transient transmission dynamics of the singlet exciton PA at 1200 nm was measured; this data is compared against the corresponding PA dynamics of the pristine film at the same probe wavelength in Fig. 7.6. As expected, the singlet exciton PA of the blend film is quenched with respect to the pristine film at the zero-delay time. Multi-exponential analysis of the data was performed as for the pristine film, with a decay component of 206 ps included in the fitting routine as a fixed parameter. From this decay components of (1.9 ± 0.1) ps (54%) and (19 ± 2) ps (32%) are obtained and match within error the decay components of the singlet PA obtained in the pristine film. As per the discussion of the pristine film above, these decay components are assigned to the effects of SSA and exciton migration respectively.

The observation of similar lifetime components attributed to SSA and exciton migration in both the pristine and blend films confirms that these processes are largely unaffected by the presence of the PCBM molecules in the blend films. In results to be presented and discussed below, SSA is confirmed in both the bulk regions of polymer and the disordered regions close to the PCBM interfaces, and therefore does indeed occur independently of the PCBM concentration. The decay component of the singlet PA attributed to exciton migration cannot however be assigned to excitons generated in the disordered interfacial regions of polymer, as it has been established in previous work that the polymer-acceptor distance in these regions is short enough to result in the generation of polarons within 100 fs;[106] exciton migration in these disordered regions is therefore not required as a precursor to charge formation. The 19 ps component assigned as exciton migration above can therefore only be associated with singlet excitons generated in the bulk regions of polymer.

In an ideal study of the photophysics of charge generation in the P3DDT/PCBM blend, an analysis of the localised polaron (LP) PA band identified by Guo at a probe wavelength 1000 nm[106, 215] is highly desirable. According to Guo, LP states are generated in disordered regions of polymer and are subsequently characterised by low charge mobility and a low rate of bi-molecular recombination. Given that an investigation of this band could only be made following excitation of the PCBM, a direct investigation of the LP PA band is not considered in this study. An indirect investigation of the LP dynamics can however be made by measuring the recovery of the PB band at 560 nm, which corresponds to ground-state recovery in the disordered interfacial regions of polymer.[106, 117] This data is shown in Fig. 7.7. It should be noted that such a measurement of the LP dynamics is not ideal, as it is not possible to isolate the build-in dynamics of this state by measuring the PB recovery.
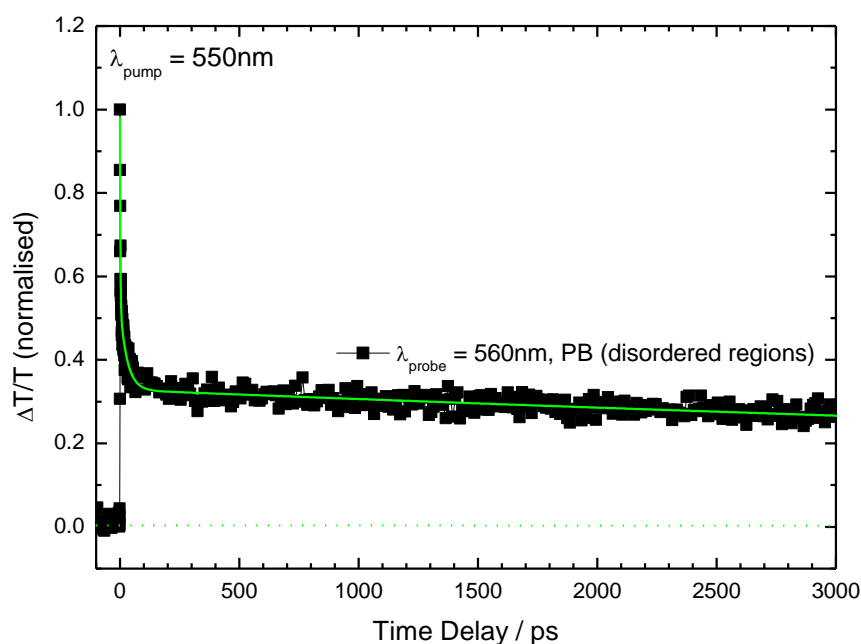
Figure 7.7: Transient transmission dynamics of the PB band at 560 nm in a P3DDT/PCBM (1:1 wt %) blend, corresponding to the ground-state recovery of disordered regions of polymer, (λ_{pump}= 550 nm, 3 μJcm^{-2}). The PB recovery is characterised primarily by a (1.7±0.1) ps component at early times and a (14.9±0.9) ns component at longer times. The former component is assigned to the effect of SSA in disordered regions of the blend; the latter is assigned to the lifetime of LP states.

The PB recovery in disordered regions is characterised by decay components on different timescales. At early times the recovery is governed by a (1.7±0.1) ps decay component, which is equal to within error the decay component in the singlet exciton PA assigned to the effect of SSA. SSA is expected to appear as a decay term in the PB recovery as in such a process one exciton is lost to the ground state (see sections 2.6.6 and 6.3.2 for more details). The observation of a 1.7 ps component in the PB recovery of disordered regions of polymer is therefore attributed to the SSA of singlet excitons generated in those regions.

The PB recovery at long times is characterised by a (14.9±0.9) ns decay component, which is much longer than the fluorescence lifetime of the singlet exciton population. This component is however of the correct order of magnitude to be associated with the decay of a polaron state, which has been measured in the literature to occur over timescales ranging between ~800 ps and 1 μs.[47, 104] In light of this fact and on the basis of previous observations, the ~15 ns decay component is assigned to the decay of the LP states in disordered regions of polymer.

To investigate the dynamics of the new PA band observed in the blend film between 630 and 750 nm, single wavelength transient transmission dynamics were measured at 715 nm where both the singlet and GPP PA bands were noted to be at a minimum in the pristine film. This data is shown in Fig. 7.8. Build-in components of (2.4±0.6) ps and (13±1) ps are recorded at short times, with a (1400±40) ps decay noted at longer times. A rise in signal corresponding to ~60% of the maximum PA is also recorded at the zero-delay time.

The long lifetime decay component is again of the correct order of magnitude to be associated with the bi-molecular recombination of a polaron state.[47, 104] A comparison between the dynamics of this state at 715 nm and that of the LP state analysed above can be used to confirm that the former, which has the shorter decay lifetime of the two, is more susceptible to bi-molecular recombination and therefore is the more mobile polaron state. In light of this observation and in accordance with previous results[106, 215] the PA band at 715 nm is assigned to delocalised polaron (DP) states generated in ordered regions of the blend in which the charge mobility is high.

The build-in of the DP PA at the zero-delay time demonstrates the formation of DP states within the time resolution of the experimental system. Such behaviour is indicative of the quenching of singlet excitons photogenerated within close proximity to a PCBM moiety and corroborates with the quenching of the singlet PA band observed in the zero-delay transient

transmission spectrum of the blend film shown in Fig. 7.4B. It should be noted that electron transfer between polymer and PCBM acceptor sites has been reported to occur with a lifetime as short as 50 fs[107] and would therefore with the equipment used in this study appear to occur instantaneously.
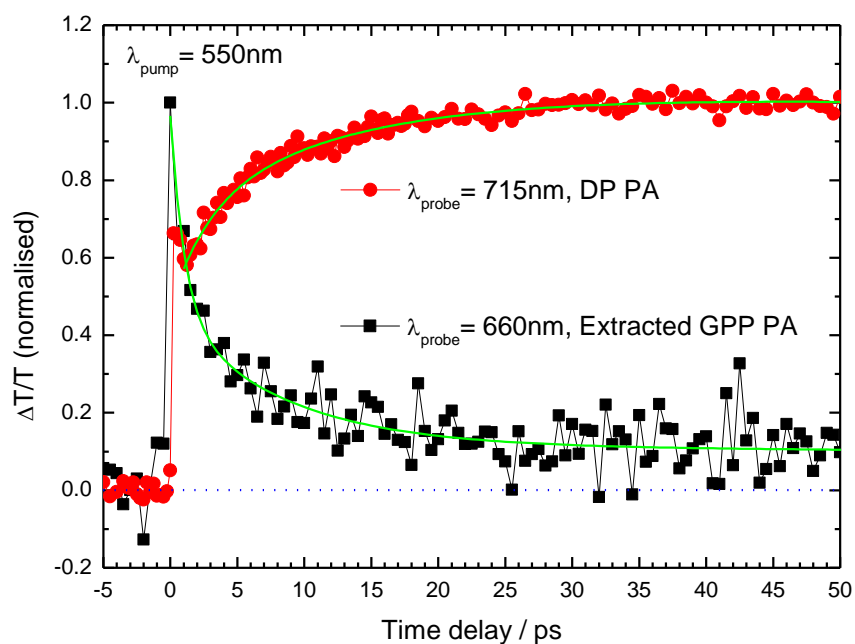
Figure 7.8: Normalised transient PA dynamics of the GPP states extracted at 660 nm (black squares) and DP states at 715 nm (red circles) for a P3DDT/PCBM (1:1 wt %) film (λ_{pump}= 550 nm, 3 µJcm^{-2}). A matching 9 ps build-in and decay is observed in the dynamics of the DP and GPP PA bands and is attributed to the formation of polarons as a consequence of GPP dissociation.

The ~2 ps component measured in the build-in of the DP PA is in excellent agreement with the component assigned to the effect of SSA in the decay of the singlet exciton PA. During SSA, an exchange of energy between two singlet excitons that collide on a single chromophore leads to the generation of polaron states via a high energy delocalised singlet intermediate (S_N),[52, 88, 90-92] as according to Eq. 7.1 below:

$$S_1 + S_1 \rightarrow S_0 + S_N \;\; with \;\; S_N \rightarrow (1 - \eta)(S_1 + Q) + \eta(P3DDT^+ + P3DDT^-) \qquad (7.1)$$

In Eq. 7.1 $P3DDT^+$ and $P3DDT^-$ are the polymer cations and anions respectively, with η the probability of the dissociation of the S_N state and $(1 - \eta)$ the corresponding probability of the S_N state undergoing thermalisation and returning to the S_1 level. On the basis that the dissociation of the S_N state to polarons occurs on a femtosecond timescale,[46] one would therefore expect with the onset of SSA to observe a build-in of polaron states with the same lifetime component as that of the relevant decay component of the singlet exciton dynamics (measured to be 2 ps above). The 2 ps build-in of the DP PA is therefore assigned to the generation of polarons in ordered regions of the blend as a consequence of SSA. Note that this observation, combined with the assignment of SSA in the PB recovery of disordered regions of polymer (see Fig. 7.7), confirms that singlet excitons can interact and annihilate in both ordered and disordered regions of polymer in the blend.

The 13 ps build-in of the DP PA has no matching analogue in the decay dynamics of the singlet excitons at 1200 nm; singlet exciton migration cannot therefore be the determining factor in the non-instantaneous generation of DP states under these excitation conditions. In light of this it was pertinent to consider any correlation between the decay of the GPP PA band at 660 nm with the build-in of the DP PA. A direct analysis of the GPP PA could not be performed however due to significant overlap with the DP PA band. This overlap could be identified by the presence of a long-lived decay component, similar to that observed at 715 nm, in the single-wavelength dynamics at 660 nm. Therefore in order to isolate the GPP PA, the dynamics at 715 nm were subtracted from the PA at 660 nm on the basis that at long times the total dynamic response was completely determined by the DP population. The validity of this process was confirmed by measuring the GPP dynamics in the pristine film at the same wavelength, in which it was found that only a negligible fraction of IEX states remained after

1.5 ns. The transient transmission dynamics of the GPP PA extracted as a result of this process are shown in Fig. 7.8 and compared against the build-in of the DP PA.

The decay of the GPP PA band has lifetime components of (1.2 ± 0.4) ps (54%) and (10 ± 3) ps (31%), in addition to a small long-lived component. The ~1 ps component is in excellent agreement with that recorded at the same probe wavelength in the pristine film and is assigned as the geminate recombination of the GPP states. The contribution of geminate recombination to the total decay dynamics in the blend film (54%) is noted to be only slightly smaller than that obtained in the pristine film (67%), confirming that geminate recombination of the GPP states in the blend is largely unaffected by the presence of the PCBM molecules. This confirms that, as expected, GPP formation occurs primarily in the ordered bulk domains of polymer and away from the disordered interfacial regions of polymer and PCBM.

The 10 ps decay of the GPP PA correlates with the 10ps build-in of the DP PA and is indicative of a direct relationship between these states. The 10 ps decay of the GPP PA is therefore attributed to the time required for a GPP state to dissociate and form free polarons in ordered domains of polymer.

Contribution of triplet excitons in P3DDT

Before proceeding further the potential role of triplet excitons in influencing the dynamics in both the pristine and blend films is considered and subsequently eliminated. First of all, it has been well documented that triplet formation in regio-regular polythiophenes is hindered by the strong interchain interactions that are characteristic of these polymers.[117, 189] This was checked by measuring the PB recovery of the pristine film at 566 nm (data not included here). The triplet exciton lifetime of a conjugated polymer is typically of the order of 1 ms[93, 218] and thus, for the experimental setup used here, can only be observed as a moderate background in the dynamics of the PB recovery; no such component was observed.

Secondly it is possible to rule out the potential role of intersystem crossing within the CT manifold[93, 197] (see section 2.7.2) as a precursor to triplet formation by measuring the CT emission from the blend. As discussed above in context of Fig. 7.4A, a very weak emission peak attributed to CT emission was detected on the low energy shoulder of the fluorescence of the blend film at ~950 nm. This is lower in energy than the reported triplet energy level for P3HT (750 nm),[197] which is expected to be comparable to the corresponding value in P3DDT given the similarity between the chemical structure of P3HT and P3DDT. As a consequence CT intersystem crossing to the triplet manifold in P3DDT is energetically prohibited. It should be noted that the experimental facilities required to measure the triplet energy of P3DDT directly were not available during the course of this study.

7.3.2 Excitation energy dependence of delocalised polaron generation

In section 7.3.1 above it was demonstrated that, for excitation at 550 nm, the dynamics of DP generation in ordered regions of polymer in a P3DDT/PCBM (1:1 wt%) blend film on a picosecond timescale are principally determined by the dissociation of GPP states. The

absence of any lifetime component characteristic of the migration of singlet excitons in the build-in of the DP PA is initially surprising. It has already been shown that singlet excitons exist in the ordered regions of the blend and are able to contribute to the generation of DP states through SSA. It then becomes pertinent to ask why these singlet excitons are not apparently able to migrate to and dissociate at the interfaces between polymer and acceptor to form DP states.

To investigate this point further, the DP PA at 715 nm was measured at different excitation (pump) wavelengths; this data is shown in Fig. 7.9. These experiments were performed on the basis that, as expressed in section 7.1.1, the formation of GPP states is governed by the degree of excess excitation energy used in the photoexcitation of the singlet population.[21, 117] By performing measurements at low excitation energies, at which the singlet excitons are generated with no excess energy, one would expect to prevent GPP formation in the polymer and thus freeze out any contribution from the dissociation of GPP states towards the generation of DP states. This in turn would make it possible to resolve any additional contribution to the DP PA build-in, potentially such as that from the migration and subsequent dissociation into polarons of singlet excitons in interfacial regions.

Following a multi-exponential analysis of the data shown in Fig. 7.9, two build-in components are obtained at each excitation wavelength in addition to one decay component. At all excitation wavelengths a build-in component of ~2 ps was obtained and attributed to the generation of DP states as a consequence of SSA, as discussed in section 7.3.1. The second build-in component was noted to vary in both amplitude and time as a function of excitation wavelength; this behaviour is summarised in Table 7.1. In addition, it can be seen directly from Fig. 7.9 that the magnitude of the DP PA at the zero-delay time decreases to zero upon increasing the excitation wavelength from 550 to 600 nm.
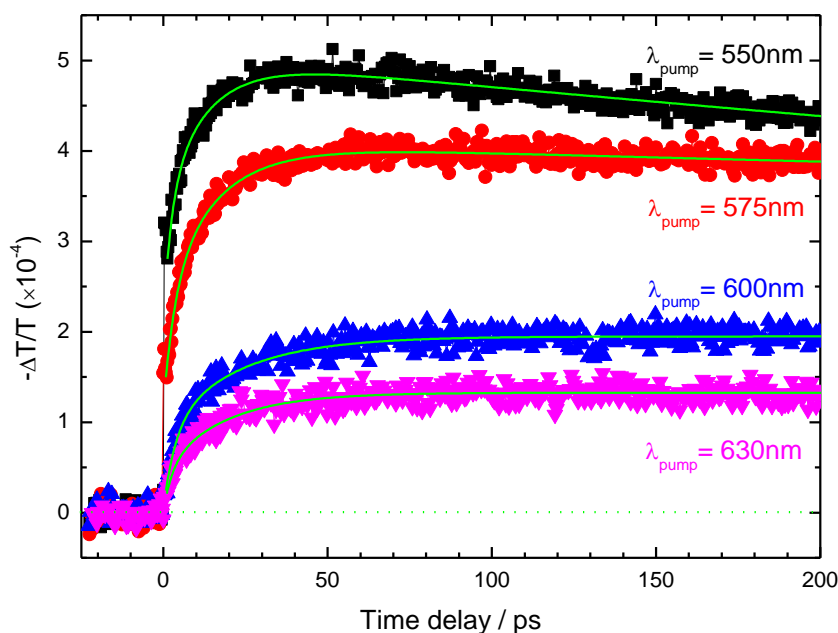
Figure 7.9: Comparison of DP PA build-in dynamics measured at a probe wavelength of 715 nm, for different excitation wavelengths (as marked). An incident pump fluence of 3 μJcm^{-2} was used for excitation at 550 nm; for other excitation wavelengths the incident fluence was adjusted to maintain the same absorbed excitation density. In addition to a reduction in the number of DP states generated at the zero-delay time, an increase in the build-in lifetime of DP states is also observed with decreasing excitation energy.

The variation in magnitude of the DP PA at the zero-delay time with excitation wavelength can be attributed to the nature of the polymer morphology into which excitation is made. For excitation at 550 nm, excitons are generated in both the disordered regions of polymer close to the polymer/acceptor interfaces and the ordered bulk regions of polymer, with those excitons generated in ordered regions created with excess energy. The excitons generated in the disordered interfacial regions undergo electron transfer to PCBM molecules within 100 fs, resulting in the formation of LP states on the same timescale. A fraction of these states must move into the bulk to form DP states on a femtosecond timescale, in order to result in the build-in of DP states measured in this study to occur within the time resolution of the experimental

system (~500 fs). If all LP states returned to the bulk with 100% efficiency, then it would not be possible to observe the build-in of LP states on a femtosecond timescale, which contradicts with the observation of LP formation within 250 fs in a RR-P3HT/PCBM blend in a previous study.[106] From this it is possible to infer that there must be a non-unity probability for a LP state to move into the bulk and form a DP state, leading to a branching ratio between the formation of DP and LP states following exciton dissociation in interfacial regions.

Excitation wavelength / nm	DP Pre-exponential amplitude 2 / x10^{-4}	DP time constant 2 (build in) / ps
550	1.7±0.2	13±1
575	1.7±0.2	15±1
600	1.03±0.08	23±2
630	0.84±0.08	19±2

Table 7.1: DP PA build-in (probe wavelength: 715 nm) lifetimes and pre-exponential components for different excitation wavelengths, obtained using multi-exponential fitting.

Increasing the excitation wavelength to 600 nm and longer moves the excitation line entirely into the ordered bulk regions of polymer, with no excitons generated in the disordered interfacial regions. Under such conditions excitons are not generated sufficiently close to a PCBM molecule as to immediately undergo electron transfer to the PCBM molecules, and therefore cannot dissociate to form polarons on a femtosecond timescale.

The time constant of the non-instantaneous DP build-in is now considered. As can be seen in Table 7.1, this value increases from 13 ps at 550 nm to ~20 ps at 600 nm. This latter value obtained at low excitation energies is in excellent agreement with the decay constant of ~20 ps

assigned as the effect of exciton migration in the singlet PA dynamics at 1200 nm in the blend. Therefore, rather than interpreting the variation in the build-in lifetime measured as an increase in lifetime of a single component, this behaviour is instead attributed to a turnover in the relative contributions of GPP dissociation and exciton dissociation, following singlet migration to interfacial regions, towards the generation of DP states in ordered regions of the blend. This point is considered in more detail below.

As discussed above, excitation at 550 nm results in the generation of excitons in ordered regions of the blend with excess energy. This excess energy can be used by an exciton to generate a GPP state with a high probability. Therefore at high energies, a fraction of the singlet excitons which are photogenerated are rapidly converted into GPP states, which then dissociate in the bulk regions of polymer to form DP states. As a consequence at high excitation energies, the build-in of the DP PA is dominated by the dissociation of the GPP states, which is characterised by a 10 ps lifetime component.

Upon reducing the excitation energy from 550 to 600 nm, excitons in the bulk are generated with less excess energy and subsequently GPP formation in the bulk at the expense of the singlet exciton population is prohibited; as a consequence no 10 ps component is observed in the build-in of the DP PA. Under these circumstances DP formation instead occurs as a result of the dissociation of excitons that must first migrate from the bulk to the interfacial regions of polymer and acceptor. The rate limiting step in this process is the migration of excitons, which is characterised by a 20 ps lifetime component. This behaviour is in excellent agreement with measurements of the transient transmission spectra of pristine RR-P3HT recorded elsewhere, in which the GPP PA band at 660 nm was found to decrease to negligible levels upon increasing the excitation wavelength from 400 to 600 nm.[117]

The observation of an intermediate lifetime of 15 ps at 575 nm demonstrates that while at this wavelength the majority of DP states are generated from the dissociation of GPP states, a measurable contribution also arises simultaneously from the migration of singlet excitons, resulting in a build-in lifetime between the two limits of ~10 and ~20 ps. It is expected that the relative contributions of GPP dissociation and exciton migration towards DP formation could be determined by fitting an additional decay component to the DP dynamics in an effort to resolve the effect of each process individually. For the data presented in Fig. 7.9 however the signal-to-noise ratio was not sufficiently high enough to allow for such an analysis; only an average lifetime component was measured.

In addition to a change in the build-in lifetime, the decay lifetime of the DP PA is noted to increase at longer excitation wavelengths. This increase in lifetime is concurrent with a decrease in the maximum value of the DP PA, or equivalently the maximum number of DP states that are formed. This observation confirms that the relatively short polaron lifetime associated with the DP state can be attributed to bi-molecular recombination; reducing the degree of bi-molecular recombination by decreasing the number of DP states in the polymer results in an increase to the DP lifetime.

The behaviour of the pre-exponential amplitude component associated with the build-in of the DP PA is now considered. From Table 7.1 a general decrease in amplitude is observed to occur with increasing excitation wavelength. Between 500 and 600 nm this decrease is concurrent with the aforementioned decrease of the GPP contribution with excitation wavelength. It is therefore not unreasonable to suggest that the decrease in the pre-exponential amplitude over this range of wavelengths is merely reflective of removing the contribution of GPP dissociation towards the generation of DP states in ordered regions of the blend. Developing this idea further, it is clear that the dissociation of GPP states make a significant contribution towards the total number of DP states formed in ordered bulk regions of the blend; the yield of DP states

formed when exciton migration and dissociation is the primary mechanism of DP formation (at 600 nm) is almost 50% of that when GPP dissociation is the primary mechanism (at 550 nm).

One possible explanation for the difference in the DP yields described above is that a number of the singlet excitons which migrate to the interfacial regions and dissociate to form charges do not return to the bulk within 200 ps, which was the maximum delay time measured in Fig. 7.9. The dissociation of singlet excitons as a consequence of electron transfer to the PCBM moieties occurs in the disordered regions of polymer that exist at the PCBM interfaces. As discussed above in context of polaron formation at the zero-delay time, this will result in a branching ratio following dissociation between the formation of LP and DP states. This would explain the observation above that the DP yield from exciton migration appears low in comparison to that from GPP dissociation; some of the polarons that are formed following exciton migration to interfacial regions are LP states which do not return to the bulk to be measured as DP states. This is opposed to the case of GPP dissociation, which occurs entirely within the bulk and therefore results solely in the formation of DP states.

The existence of a branching ratio between LP and DP states following the migration and subsequent dissociation of excitons in interfacial regions is in agreement with the observation of exciton migration as a precursor to the formation of *LP* states, as evidenced by a correlation between the build-in and decay dynamics of the LP and singlet exciton PA bands recorded in previous work.[106]

Another factor which is expected to contribute to the low yield of DP states obtained when singlet exciton dissociation is the primary mechanism of DP formation, and compared to that when GPP dissociation is the primary mechanism, is the number of polarons created in each dissociation event. The dissociation of a GPP occurs entirely within the bulk polymer and results in the formation of both a polymer anion and cation:

$$GPP \xrightarrow{dissociation} P3DDT^+ + P3DDT^- \qquad (7.2)$$

This is however not the case for the dissociation of a singlet exciton at a PCBM interface, which occurs as a consequence of electron transfer from the polymer to the acceptor, resulting in the formation of a PCBM anion and a polymer cation:

$$S_1 \xrightarrow{dissociation} P3DDT^+ + PCBM^- \qquad (7.3)$$

Therefore, in a single dissociation event, GPP dissociation is expected to produce twice as many polymer polarons as compared to exciton dissociation at a PCBM interface. This is significant, as the DP PA at 715 nm selectively probes the population of polarons in ordered regions of *polymer*; the PA of the PCBM anion has been reported to overlap with the LP PA at ~1000 nm in RR-P3HT/PCBM blends.[192]

The low yield of DP states formed as a consequence of exciton migration, as compared to GPP dissociation, can be used to answer the question posed at the beginning of this section, concerning why no component associated with migration was observed in the DP build-in dynamics at 550 nm excitation. At 550 nm excitation a population of singlet excitons must still remain following GPP formation, as confirmed by the fact that both SSA is observed to occur at that wavelength and that exciton migration in the bulk was identified as a decay component in the singlet exciton PA (see Fig. 7.6) for excitation at 390 nm. As the yield of DP states formed as a consequence of GPP dissociation is much greater than that formed following the migration and subsequent dissociation of singlet excitons at PCBM interfaces, the DP build-in at 550 nm is dominated by the dissociation dynamics of the GPP population and masks any contribution from the migration and subsequent dissociation of singlet excitons.

It is clear that in order to resolve the contribution of singlet exciton migration towards the formation of polarons, a study of the LP build-in dynamics would prove highly beneficial, as GPP formation is expected to be heavily hindered if not restricted completely in disordered regions,[189] leaving exciton migration as the only active mechanism by which LP states are formed on a picosecond timescale. As noted above however, the build-in dynamics of the LP PA was not considered in this study, as this band could only be measured using 390 nm excitation. Under such conditions it would not be possible to resolve any contribution towards LP formation from the migration of singlet excitons in both the polymer and PCBM to the interfacial regions. In order to address this issue, improvements have been recently proposed to the femtosecond pump-probe system used in these experiments. This work will primarily focus on improving the spectral range of the WLSC output from the OPA, such that the WLSC can be used as a probe in the NIR. This will remove the need to use the idler output of the OPA as a probe source and thus in turn the restriction on the choice of excitation wavelength.

To further investigate the role of exciton migration as a precursor to polaron generation, a study in which the singlet, LP and DP PA dynamics are measured as a function of the doping ratio is proposed. The doping ratio of a blend film is expected to have a significant influence on the time required for an exciton generated in the bulk to migrate to and reach an interface with a PCBM molecule; at large doping ratios the average distance between polymer and acceptor domains will be smaller than at low doping ratios and thus under such conditions an exciton will reach a PCBM interface in a shorter period of time. In addition to varying the doping ratio, a study of the properties of exciton migration at different excess exciton energies is also proposed. As demonstrated above, excitons in the bulk ordered regions of polymer are generated with excess energy. Although it has been established that the excess energy is used as part of GPP formation, it would be of interest to establish whether the excess energy could also be used in part to change the properties of exciton migration. As the work detailed in this

chapter was a preliminary study of the properties of charge generation in a regio-regular polythiophene/PCBM blend, building up as complete a picture as possible of the pathways contributing towards charge generation in such a system was preferred at the expense of a detailed study of more specific aspects, such as the properties of exciton migration. A study of the properties of exciton migration is thus proposed for further investigation following the submission date of this thesis.

7.3.3 Model for delocalised polaron generation

The results and discussion of the previous section are used here to present a simple model which summarises the various pathways leading up to DP formation in a P3DDT/PCBM blend; a schematic of this model is given in Fig. 7.10. Understanding the properties of the DP state is of particular interest when considering the operation of a solar cell device based on a regio-regular polythiophene. As determined in previous work and confirmed in this study, it is the DP state which is the more mobile of the two polaron populations generated in a regio-regular polythiophene/PCBM blend.[106, 215] DP states are therefore expected to reach the electrodes of a solar cell device with a higher probability than LP states, and thus in turn are expected to form a significant contribution to the total photocurrent of such a device.[215]
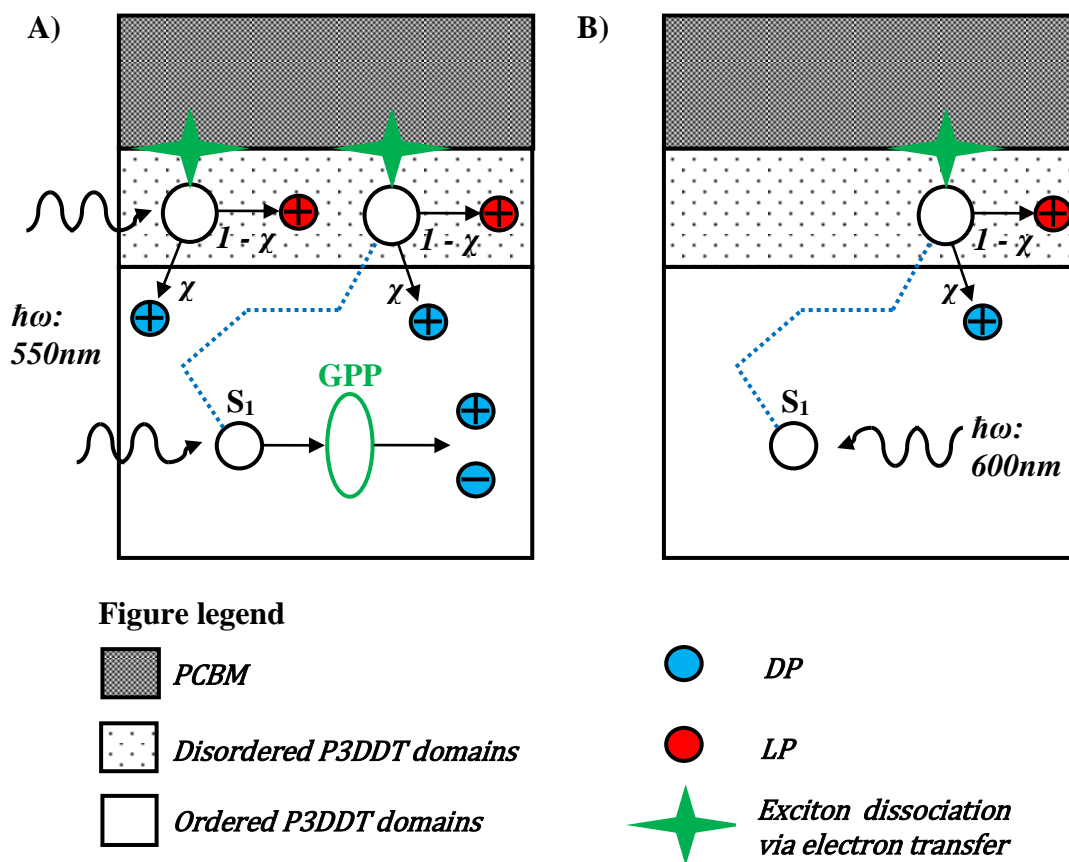
Figure 7.10: Schematic summarising the key mechanisms of DP generation in P3DDT/PCBM bulk-heterojunction blend, proposed as a results of the work herein, for excitation at A) high (>2.07 eV) and B) low energies (≤2.07 eV). A): For excitation at high energies charge generation proceeds in both ordered and disordered domains of polymer. In both regions polaron pair generation is possible through SSA (not indicated in figure). In disordered regions, charges are generated as a consequence of exciton dissociation at the interface between polymer and acceptor; either an exciton is generated directly at the interface, leading to immediate electron transfer, or must first migrate there (blue dotted lines). A fraction (χ) of the polarons generated as a consequence of exciton dissociation in disordered regions move back into ordered regions to form DP states; the remaining fraction (1-χ) of those that do not remain as LP states. In ordered regions, a fraction of the singlet population form GPP states in a process mediated by excitation energy. These GPP states can either recombine geminately or dissociate, with the latter process generating DP pairs. B): For excitation at low energies excitons are generated solely within the bulk, with DP formation possible due to SSA. GPP formation does not occur at low excitation energies and therefore additional DP formation can only occur as a result of the migration and subsequent dissociation of excitons at the polymer/acceptor interfaces.

The foundation for this model is that charge generation occurs in both the ordered regions of polymer in the bulk, characterised by the PA of DP states, and the disordered regions of polymer that form in close proximity to the PCBM interfaces, characterised by the PA of LP states; this was determined in the work of Guo *et al.* and confirmed in the excitation energy dependent measurements presented in Fig. 7.9.[106, 117, 215] Whereas excitation at high energies (>2.07 eV, Fig. 7.10A) can excite both ordered and disordered regions of polymer, excitation at low energies (≤2.07, Fig. 7.10B) selectively excites ordered regions of polymer. Charge generation in each case proceeds according to different mechanisms characterised by different timescales; these are summarised below.

High energy excitation

At high energy excitation (>2.07 eV) singlet excitons are instantaneously generated in ordered bulk regions of polymer and in disordered regions. In disordered regions these excitons are sufficiently close to a PCBM molecules as to undergo electron transfer within 50 fs. A fraction of the LP states that are formed as a result of this process are able to rapidly transfer to the ordered regions of polymer on a femtosecond timescale, resulting in the build-in of the DP states within the time resolution of the experimental system used here (~500 fs). The results of this chapter also confirm that those singlet excitons that are not immediately quenched in disordered regions can undergo SSA on a 2 ps timescale, which will also contribute to the formation of LP states.

In ordered regions of the blend at high excitation energies, strong interchain interactions coupled with excess excitation energy result in the formation GPP states at the expense of some of the singlet exciton population. This process occurs rapidly, as evidenced by a rise in the GPP PA within the time resolution of the experimental system used (see Fig. 7.7). These GPP states can dissociate to form DP states, resulting in a build-in of the DP PA characterised by a

~10 ps component. The singlet excitons that do not form GPP states undergo SSA, resulting in an additional build-in of DP states characterised by a 2 ps component. It is presumed that any singlet excitons that remain are able to migrate to the interfaces between polymer and acceptor to result in the formation of LP states. Only a fraction of these LP states that are formed return to the bulk to form DP states, making DP generation as a result of singlet exciton migration and dissociation less efficient than GPP dissociation, with the latter subsequently dominating the DP build-in dynamics.

Low energy excitation

At low excitation energies (≤2.07 eV) singlet excitons are not generated in the disordered regions of polymer at the PCBM interfaces and consequently no build-in of DP states is observed to occur on a femtosecond timescale following excitation. Singlet excitons are instead generated in the ordered bulk regions of polymer, but are no longer generated with any excess energy. This greatly reduces the probability for a singlet exciton to delocalise into a GPP state. As at high energy excitation, SSA occurs in the bulk, resulting in the build-in of DP states on a 2 ps timescale. The remaining singlet excitons migrate to the interfacial regions of polymer and acceptor, resulting in the formation of LP states. As discussed above in the context of high energy excitation, a fraction of the LP states formed as a result of this process are able to move rapidly back into the ordered regions of polymer, resulting in the formation of DP states. The rate limiting step as part of this process is the migration of singlet excitons to the interfaces and is characterised by a ~20 ps decay component in the singlet exciton PA and a matching ~20 ps build-in component in the DP PA.

The role of the GPP state towards delocalised polaron formation

There are two key consequences of the contribution of GPP states towards the formation of DP states in ordered regions of polymer in a regio-regular polythiophene/PCBM blend. The first is that excitation at low energies prevents GPP formation and therefore removes a channel by which DP states can be formed. Given the relative inefficiency of the migration to and subsequent dissociation of singlet excitons in interfacial regions as a replacement mechanism by which DP states can be generated, the total yield of DP states formed at low excitation energies is smaller than at high excitation energies. Taking into account the fact that excitation at low energies also removes an additional channel by which DP states can be generated, namely those formed as a consequence of the instantaneous quenching of excitons photogenerated in interfacial regions, the results of this study demonstrate a 73% reduction in the total number of DP states (as quantified by a 73% reduction in the maximum of the DP PA) at 630 nm excitation as compared to 550 nm excitation.

The second key consequence concerns the fundamental properties of the GPP state itself. As demonstrated in Fig. 7.7, geminate recombination of the GPP state acts to quench approximately 50% of the initial GPP population within 1 ps. Given that it has been demonstrated in section 7.3.2 that, at high excitation energies, GPP dissociation contributes towards ~40% of the total number of DP states formed, geminate recombination acts as a significant loss mechanism of potential DP states.

7.4   Conclusions

In summary, femtosecond pump-probe spectroscopy has been used to provide insight into the photophysics of DP generation in blends of the regio-regular polythiophene P3DDT doped with the electron acceptor PCBM. The DP state has been established to play an important role in

determining the photovoltaic response of an organic solar cell device based on a regio-regular polythiophene/PCBM blend and as such understanding the properties of the DP state is a matter of great interest.

By measuring and correlating the dynamics of the DP PA band at 715 nm in the blend with the PA decay of other key states, a simple model for DP generation in blend films has been developed. DP formation in ordered regions of a P3DDT/PCBM blend is strongly dependent on the choice of excitation energy and occurs through various mechanisms that occur on different timescales. At high excitation energies, excitons are generated in both ordered bulk regions of polymer and disordered regions of polymer that form in close proximity to the PCBM interfaces. The excess energy of the excitons generated in ordered regions of the blend results in the formation of GPP states at the expense of the singlet population. DP formation is then characterised by three primary contributions; the ultrafast quenching of singlet excitons generated directly at PCBM interfaces within 500 fs, SSA occurring within 2 ps and the dissociation of GPP states within 10 ps. Decreasing the excitation energy selectively excites the bulk ordered regions of polymer, with no excess energy available in the bulk to generate GPP states. DP formation then proceeds through SSA occurring within 2 ps and the migration to and subsequent dissociation of excitons in the interfacial regions between polymer and acceptor within 20 ps.

The yield of DP states formed at high energy excitation, when GPP dissociation is the dominant mechanism by which DP states are formed on a picosecond timescale, is greater than the corresponding yield of DP states formed at low excitation energies when singlet exciton migration and dissociation is the dominant mechanism. This is attributed to the regions of the blend in which both processes occur. GPP dissociation occurs entirely within the bulk of the polymer and results in the formation of only DP states; in the latter process the electron-transfer interaction which results in the formation of polarons occurs in the disordered regions of

polymer. The polarons generated in disordered regions have only a finite probability to return to the bulk, resulting in a branching ratio between the formation of DP and LP states following exciton dissociation.

The results of this study demonstrate that activating the contribution of GPP dissociation towards DP generation at high excitation energies increases the total number of DP states that can be formed in a regio-regular polythiophene/PCBM blend. Furthermore at such excitation energies GPP dissociation is responsible for a significant portion of the total number of DP states that are generated, contributing to ~40% of the DP states formed at 550 nm excitation. In this context the geminate recombination of the GPP state within 1 ps is crucial, as it accounts for a loss of ~50% of the initial GPP population before GPP dissociation can occur. This constitutes an inherent loss mechanism of potential DP states in a regio-regular polythiophene/PCBM blend.

The study presented in this chapter was a preliminary investigation into the properties of charge generation in a typical organic photovoltaic system. As of January 2011 this work will extend into a much larger research project with the same aim and it is hoped that many of the key issues that have arisen in this preliminary study, both experimental and conceptual in nature, can be addressed and built upon as part of that project. The present work does however demonstrate the power of femtosecond pump-probe spectroscopy in building up a comprehensive description of the fundamental photophysical processes in an organic photovoltaic system. As such the application of this method should be considered key in any future experimental work.

Chapter 8   Conclusions

The research contained within this thesis, in which time-resolved laser spectroscopy has been applied to the study of a variety of conjugated polymers, has advanced the understanding of the photophysical properties of the excited states in these systems.

The properties of exciton-phonon coupling in the ladder-type conjugated polymer methyl-substituted poly(para-phenylene) (MeLPPP) were investigated using steady-state and picosecond fluorescence spectroscopy. In MeLPPP the amplitudes of the key vibrational modes of the polymer vary as a function of temperature. This phenomenon is largely governed by the thermal population of low energy stretching modes of the polymer backbone, which occurs in the excited-state long after the thermalisation of excess energy. In addition to this effect the temperature dependence of the mode amplitudes also demonstrates that MeLPPP undergoes some form of structural change at temperatures equal to and below 150K which has not been considered in the literature to date. This change manifests as a redistribution of intensity between different modes and has a significant effect on the temperature dependence of the fluorescence spectrum of the polymer.

It is proposed that the aforementioned structural changes in MeLPPP with temperature are related to the thermal population of the low energy stretch modes of the chain. This is made on the basis that a structural change is observed following a significant decrease in the population of the low energy modes. The thermal population of these modes can be thought to stabilise the chain structure at high temperatures; upon removing these modes at low temperatures the polymer chain is forced to adopt a new structure. In order to fully confirm these findings, temperature dependent structural studies based on X-Ray diffraction have been proposed.

Polarised measurements performed on stretched films of MeLPPP demonstrate a fundamental relationship between the electron-phonon coupling and the fluorescence polarisation. This observation is highly significant as it is not consistent with the theoretical framework outlined by the commonly accepted Born-Oppenheimer principle. In this context the theoretical approach of Spano *et al.* was considered and it is proposed that the relationship between the electron-phonon coupling and the fluorescence polarisation can be attributed to strong interchain interactions in MeLPPP in the solid-state.

Having built up a thorough understanding of the nature of electron-phonon coupling in the fluorescence spectrum of MeLPPP, it was confirmed using picosecond fluorescence spectroscopy that the fluorescence lifetime of the polymer was independent of both the type and order of the vibrational mode through which decay occurred, in good agreement with well-established theories. An apparent deviation from such behaviour in MeLPPP can arise as the result of the contribution from a previously unidentified defect state that overlaps significantly with the fluorescence spectrum of the polymer. The existence of a defect state in MeLPPP demonstrates that the conclusions of some previous studies, in which an increase in the fluorescence lifetime of the polymer from 200 to 500 ps was observed and attributed to the effectiveness of intra-DOS relaxation processes, are incorrect.

The excited-state dynamics in MeLPPP was also investigated using femtosecond pump-probe spectroscopy. Results obtained in film demonstrate that MeLPPP can support an interchain exciton (IEX) state, in which the electron and hole of an exciton become delocalised over two adjacent polymer chains. IEX formation in MeLPPP does not occur instantaneously, but instead requires a population of intrachain singlet excitons to be generated first. A small number of these excitons can then become delocalised over adjacent chains on an ultrafast timescale, assuming that in the vicinity of those excitons the polymer chains are packed

sufficiently close to one another to support the required degree of interchain interaction for the formation of an IEX state.

The observation of some degree of IEX formation in MeLPPP corroborates with the results of polarised fluorescence spectroscopy performed on the same polymer, in which a failure of the Born-Oppenheimer approximation in describing the properties of electron-phonon coupling was also attributed to the presence of strong interchain interactions in film. This finding also demonstrates that, in spite of the presence of bulky side-groups along the backbone of MeLPPP, it is still possible for adjacent chains of MeLPPP in the solid-state to pack close enough to one another as to facilitate IEX formation.

The photoinduced absorption (PA) transition of the IEX state is high in energy and overlaps with the photobleaching band of the polymer. This is one of the few instances in a conjugated polymer where a PA transition is high enough in energy to do so. This observation also confirms that, in order to ensure a complete and comprehensive study of the excited-state dynamics in a conjugated polymer, a dynamical investigation of the properties of the photobleaching band is required, in addition to the remainder of the transient absorption spectrum as is more typically performed.

Results obtained at different temperatures confirm that IEX formation in MeLPPP is more efficient at lower temperatures than at higher temperatures. Assuming that the other relevant excitation conditions are fixed, this observation implies that it is easier for an intrachain singlet exciton to become delocalised over adjacent polymer chains at low temperatures. This can be potentially attributed to the aforementioned structural properties of MeLPPP with temperature, as was investigated using steady-state fluorescence spectroscopy. This result can only be properly confirmed using a suitable structural probe, such as X-Ray diffraction, to perform a detailed structural analysis of MeLPPP as a function of temperature.

The excited-state dynamics in the conjugated copolymer Super Yellow were investigated using picosecond time-resolved fluorescence spectroscopy. In solutions of Super Yellow, singlet excitons undergo intramolecular energy transfer between different monomeric subunits that make up the copolymer, with the energy transfer occurring from high energy subunits to low energy subunits. This effect of funnelling the singlet exciton population on to low energy subunits is proposed to be behind the relatively high photoluminescence quantum yield of the polymer; the singlet exciton population becomes essentially trapped on these low energy subunits and thus has a smaller probability of reaching a non-emissive quenching site.

The properties of electron-phonon coupling in Super Yellow were also investigated. In a similar manner to MeLPPP, the thermal population of low energy vibrations corresponding to the torsional modes of the copolymer backbone have a significant influence on both the intensity of the vibrational modes and the conjugation length of Super Yellow. The action of these torsional modes is however hindered by conformational defects, whose presence reduces the average conjugation length of the system.

Finally, the dynamics of delocalised polaron (DP) generation in blends of the regio-regular substituted polythiophene poly(3-dodecylthiophene-2,5-diyl) (P3DDT) doped with [6,6]-phenyl-C_{61}-butyric acid methyl ester (PCBM) was investigated using femtosecond pump-probe spectroscopy. DP formation in ordered regions of a P3DDT/PCBM blend is strongly dependent on the choice of excitation energy and occurs through various mechanisms that occur on different timescales.

At high excitation energies, excitons are generated in both ordered and disordered regions of the blend, with a number of excitons in ordered regions forming geminate polaron pair (GPP) states, as a consequence of strong interchain interactions. Under such circumstances, the dissociation of the GPP state provides a significant contribution to the total number of DP states

generated and occurs within 10 ps. Decreasing the excitation energy eliminates this channel, with the migration and subsequent dissociation of singlet excitons to the PCBM interfaces that occurs within 20 ps becoming the rate-limiting step towards DP generation.

The dynamics and yield of DP formation is dependent on the excitation energy and the various pathways of charge generation open at that energy. By eliminating both the contributions of DP formation from GPP dissociation and the instantaneous quenching of excitons generated close to the PCBM interfaces by exciting at low excitation energies, a substantial decrease (~70%) in the total number of DP states is recorded.

The dissociation of GPP states formed in ordered regions of polymer in a regio-regular polythiophene/PCBM provides a significant contribution towards the total number of DP states formed at high excitation energies. Crucially however, geminate recombination of the GPP state within 1 ps accounts for a loss of ~50% of the initial GPP population before GPP dissociation can occur. This constitutes an inherent loss mechanism of potential DP states in a regio-regular polythiophene/PCBM blend and must be taken into account when considering the efficiency of an organic solar cell device based on such a system.

In summary, this thesis demonstrates that time-resolved laser spectroscopy on picosecond and femtosecond timescales is a powerful tool which can be used to gain a significant amount of information concerning the properties and dynamics of the excited states in conjugated polymers. Such materials exhibit rich dynamics on ultrafast timescales and as such the application of such experimental methods will continue to be vital in developing a complete understanding of not only the fundamental photophysical properties of conjugated polymers, but also in turn some of the various factors which determine the efficiency of optoelectronic devices based on these materials.

References

1. *The Nobel Prize in Chemistry 2000*, Nobelprize.org, 3 Jan 2011, http://nobelprize.org/nobel_prizes/chemistry/laureates/2000/

2. J. H. Burroughes, D. D. C. Bradley, A. R. Brown, R. N. Marks, K. Mackay, R. H. Friend, P. L. Burns, and A. B. Holmes, Nature **347**, 539 (1990).

3. *Lumiotec to start shipping OLED Lighting panels next month*, oled-info.com, Jan 3 2011, http://www.oled-info.com/lumiotec-start-shipping-oled-lighting-panels-next-month

4. *OLED TV*, Oled-info.com, 3 Jan 2011, http://www.oled-info.com/oled-tv

5. *LGChem white OLED panels photos*, Oled-info.com, Jan 3 2011, http://www.oled-info.com/lg-chem-white-oled-panels-photos

6. L. Yongye, X. Zheng, X. Jiangbin, T. Szu-Ting, W. Yue, L. Gang, R. Claire, and Y. Luping, Advanced Materials **22**, 135 (2010).

7. D. Voss, Nature **407**, 442 (2000).

8. C. Brabec, V. Dyakonov, J. Parisi, and N. S. Sariciftci, *Organic Photovoltaics: Concepts and Realization* (Springer, Verlag Berlin Heidelberg, 2003).

9. *Pictures of the future spring 2005: organic solar cells*, Siemens.org, Jan 3 2011, http://www.siemens.com/innovation/en/publikationen/publications_pof/pof_spring_2005/organic_solar_cells.htm

10. W. P. Su, J. R. Schrieffer, and A. J. Heeger, Physical Review Letters **42**, 1698 (1979).

11. H. Bässler, M. Gailberger, R. F. Mahrt, J. M. Oberski, and G. Weiser, Synthetic Metals **49**, 341 (1992).

12. T. E. Dykstra, E. Hennebicq, D. Beljonne, J. Gierschner, G. Claudio, E. R. Bittner, J. Knoester, and G. D. Scholes, Journal of Physical Chemistry B **113**, 656 (2009).

13. P. A. Bobbert, Nature Materials **9**, 288 (2010).

14. S. Karabunarliev, M. Baumgarten, E. R. Bittner, and K. Mullen, Journal of Chemical Physics **113**, 11372 (2000).

15. V. I. Arkhipov and H. Bassler, Physica Status Solidi a - Applied Research **201**, 1152 (2004).

16. K. T. Kamtekar, H. L. Vaughan, B. P. Lyons, A. P. Monkman, S. U. Pandya, and M. R. Bryce, Macromolecules **43**, 4481 (2010).

17. S. A. Jenekhe, Nature Materials **7**, 354 (2008).

18. R. Hildner, U. Lemmer, U. Scherf, and J. Kohler, Chemical Physics Letters **429**, 103 (2006).

19. M. H. Chang, M. J. Frampton, H. L. Anderson, and L. M. Herz, Physical Review Letters **98**, 027402 (2007).

20. F. B. Dias, K. T. Kamtekar, T. Cazati, G. Williams, M. R. Bryce, and A. P. Monkman, ChemPhysChem **10**, 2096 (2009).

21. V. I. Arkhipov, E. V. Emelianova, and H. Bassler, Physical Review Letters **82**, 1321 (1999).

22. G. Lanzani, G. Cerullo, C. Brabec, and N. S. Sariciftci, Physical Review Letters **90**, 047402 (2003).

23. C. Rulliere ed., *Femtosecond Laser Pulses: Principles and Experiments* (Springer, New York, 2005).

24. G. Lanzani, G. Cerullo, D. Polli, A. Gambetta, M. Zavelani-Rossi, and C. Gadermaier, Physica Status Solidi a-Applied Research **201**, 1116 (2004).

25. T. Blythe and D. Bloor, *The electrical properties of conjugated polymers* (Cambridge University Press, London, 2005).

26   J. Keeler and P. Wothers, *Why chemical reactions happen* (Oxford University Press, Oxford, 2003).

27   F. M. B. Dias, *Organic Semiconductor Materials*, Durham University, 2007).

28   R. H. Petrucci and W. S. Harwood, *General Chemistry* (Prentice-Hall, New Jersey, 1997).

29   A. S. Davydov, *Theory of molecular excitons* (McGraw-Hill, New York, 1962).

30   R. E. Di Paolo, J. S. de Melo, J. Pina, H. D. Burrows, J. Morgado, and A. L. Maçanita, Chemphyschem **8**, 2657 (2007).

31   F. B. Dias, A. L. Macanita, J. S. de Melo, H. D. Burrows, R. Guntner, U. Scherf, and A. P. Monkman, Journal of Chemical Physics **118**, 7119 (2003).

32   I. G. Scheblykin, A. Yartsev, T. Pullerits, V. Gulbinas, and V. Sundström, Journal of Physical Chemistry B **111**, 6303 (2007).

33   D. Hertel and H. Bassler, Chemphyschem **9**, 666 (2008).

34   J. Brandrup, E. H. Immergut, and E. A. Grulke, *Polymer Handbook* (John Wiley and Sons, New York, 1999).

35   C. Kittel, *Introduction to solid state physics* (John Wiley and Sons, New York, 2005).

36   K. Pichler et al., Journal of Physics: Condensed Matter **5**, 7155 (1993).

37   A. J. Heeger, S. Kivelson, J. R. Schrieffer, and W. P. Su, Reviews of Modern Physics **60**, 781 (1988).

38   S. Tretiak, A. Saxena, R. L. Martin, and A. R. Bishop, Physical Review Letters **89**, 097402 (2002).

39   G. Heimel, M. Daghofer, J. Gierschner, E. J. W. List, A. C. Grimsdale, K. Mullen, D. Beljonne, J.-L. Bredas, and E. Zojer, The Journal of Chemical Physics **122**, 054501 (2005).

40   M. Pope and C. E. Swenberg, *Electronic processes in organic crystals and polymers* (Oxford University Press, New York, 1999).

41   A. P. Monkman, H. D. Burrows, L. J. Hartwell, L. E. Horsburgh, I. Hamblett, and S. Navaratnam, Physical Review Letters **86**, 1358 (2001).

42   V. I. Arkhipov, E. V. Emelianova, P. Heremans, and H. Bassler, Physical Review B **72** (2005).

43   D. Hertel, H. Bassler, U. Scherf, and H. H. Horhold, Journal of Chemical Physics **110**, 9214 (1999).

44   I. Fishchuk, V. I. Arkhipov, A. Kadashchuk, P. Heremans, and H. Bassler, Physical Review B **76** (2007).

45   V. Gulbinas, Y. Zaushitsyn, V. Sundström, D. Hertel, H. Bassler, and A. Yartsev, Physical Review Letters **89**, 107401 (2002).

46   C. Gadermaier, G. Cerullo, G. Sansone, G. Leising, U. Scherf, and G. Lanzani, Physical Review Letters **89**, 117402 (2002).

47   V. Gulbinas, D. Hertel, A. Yartsev, and V. Sundström, Physical Review B **76** (2007).

48   V. Gulbinas, Y. Zaushitsyn, H. Bassler, A. Yartsev, and V. Sundström, Physical Review B **70** (2004).

49   C. Silva, et al., Physical Review B **64** (2001).

50   S. V. Frolov, Z. Bao, M. Wohlgenannt, and Z. V. Vardeny, Physical Review Letters **85**, 2196 (2000).

51   C. Gadermaier, G. Cerullo, G. Sansone, U. Scherf, and G. Lanzani, Synthetic Metals **137**, 1457 (2003).

52   A. Kohler, D. A. dos Santos, D. Beljonne, Z. Shuai, J. L. Bredas, A. B. Holmes, A. Kraus, K. Mullen, and R. H. Friend, Nature **392**, 903 (1998).

53   A. Kadashchuk, et al., Physical Review Letters **93** (2004).

54   C. W. Tang and S. A. VanSlyke, Applied Physics Letters **51**, 913 (1987).

55   R. H. Friend, et al., Nature **397**, 121 (1999).

56   G. Yu, J. Gao, J. C. Hummelen, F. Wudl, and A. J. Heeger, Science **270**, 1789 (1995).

57   N. Tessler, G. J. Denton, and R. H. Friend, Nature **382**, 695 (1996).

58   J. R. Lakowicz, *Principles of fluorescence spectroscopy* (Kluwer Academic / Plenum Publishers, New York, 1999).

59   M. Tong, C. X. Sheng, and Z. V. Vardeny, Physical Review B **75** (2007).

60   W. W. Parson, *Modern Optical Spectroscopy* (Springer, Heidelberg, 2009).

61   A. Corney, *Atomic and Laser Spectroscopy* (Clarendon, Oxford, 2006).

62   T. Virgili, D. Marinotto, C. Manzoni, G. Cerullo, and G. Lanzani, Physical Review Letters **94** (2005).

63   X. P. Zhang, Y. J. Xia, R. H. Friend, and C. Silva, Physical Review B **73** (2006).

64   C. X. Sheng, M. Tong, S. Singh, and Z. V. Vardeny, Physical Review B **75** (2007).

65   S. Gasiorowicz, *Quantum Physics* (Wiley, New York, 2003).

66   H. Yersin ed., *Highly Efficient OLEDs with Phosphorescent Materials* (Wiley-VCH, Weinheim, 2008).

67   C. Rothe and A. P. Monkman, Physical Review B **68** (2003).

68   J. J. Sakuari, *Modern Quantum Mechanics* (Addison Wesley, 1994).

69   S. Karabunarliev, E. R. Bittner, and M. Baumgarten, Journal of Chemical Physics **114**, 5863 (2001).

70   J. Gierschner, H. G. Mack, H. J. Egelhaaf, S. Schweizer, B. Doser, and D. Oelkrug, Synthetic Metals **138**, 311 (2003).

71   J. Gierschner, H.-G. Mack, L. Luer, and D. Oelkrug, The Journal of Chemical Physics **116**, 8596 (2002).

72   L. Cuff, M. Kertesz, U. Scherf, and K. Mullen, Synthetic Metals **69**, 683 (1995).

73   H. Bassler and B. Schweitzer, Accounts of Chemical Research **32**, 173 (1999).

74   F. B. Dias, A. L. Macanita, J. S. de Melo, H. D. Burrows, R. Guntner, U. Scherf, and A. P. Monkman, The Journal of Chemical Physics **118**, 7119 (2003).

75   G. R. Hayes, I. D. W. Samuel, and R. T. Phillips, Physical Review B **52**, 11569 (1995).

76   R. Kersting, U. Lemmer, R. F. Mahrt, K. Leo, H. Kurz, H. Bässler, and E. O. Göbel, Physical Review Letters **70**, 3820 (1993).

77   B. P. Lyons and A. P. Monkman, Physical Review B **71**, 235201 (2005).

78   T. Forster, Discussions of the Faraday Society **27**, 7 (1959).

79   P. E. Shaw, A. Ruseckas, J. Peet, G. C. Bazan, and I. D. W. Samuel, Adv. Funct. Mater. **20**, 155 (2010).

80   V. Gulbinas, I. Mineviciute, D. Hertel, R. Wellander, A. Yartsev, and V. Sundström, Journal of Chemical Physics **127** (2007).

81   D. L. Dexter, The Journal of Chemical Physics **21**, 836 (1953).

82   N. J. Turro, *Modern Molecular Photochemistry* (The Benjamin/Cummings Publishing Company, Menlo Park, 1978).

83   E. E. Nesterov, Z. Zhu, and T. M. Swager, Journal of the American Chemical Society **127**, 10083 (2005).

84   M. Rubinstein and R. H. Colby, *Polymer physics* (Oxford University Press, Oxford, 2003).

85   B. Movaghar, M. Grünewald, B. Ries, H. Bassler, and D. Würtz, Physical Review B **33**, 5545 (1986).

86   E. W. Snedden, L. A. Cury, K. N. Bourdakos, and A. P. Monkman, Chemical Physics Letters **490**, 76 (2010).

87   H. L. Vaughan, A. P. Monkman, L. O. Palsson, B. S. Nehls, T. Farrell, and U. Scherf, Journal of Chemical Physics **128** (2008).

88   S. M. King, D. Dai, C. Rothe, and A. P. Monkman, Physical Review B **76**, 085204 (2007).

89   B. Kraabel and D. W. McBranch, Chemical Physics Letters **330**, 403 (2000).

90   C. Silva, M. A. Stevens, D. M. Russell, S. Setayesh, K. Müllen, and R. H. Friend, Synthetic Metals **116**, 9 (2001).

91   M. A. Stevens, C. Silva, D. M. Russell, and R. H. Friend, Physical Review B **63** (2001).

92   Q. H. Xu, D. Moses, and A. J. Heeger, Physical Review B **68** (2003).

93   B. C. Thompson and J. M. J. Frechet, Angewandte Chemie-International Edition **47**, 58 (2008).

94   J.-L. Bredas, J. E. Norton, J. Cornil, and V. Coropceanu, Accounts of Chemical Research **42**, 1691 (2009).

95   C. Deibel and V. Dyakonov, Reports on Progress in Physics **73**, 096401 (2010).

96   M. A. Green, K. Emery, Y. Hishikawa, and W. Warta, Progress in Photovoltaics: Research and Applications **16**, 61 (2008).

97   T. Drori, C. X. Sheng, A. Ndobe, S. Singh, J. Holt, and Z. V. Vardeny, Physical Review Letters **101** (2008).

98   C. Deibel, Physica Status Solidi (a) **206**, 2731 (2009).

99   I.-W. Hwang, D. Moses, and A. J. Heeger, The Journal of Physical Chemistry C **112**, 4350 (2008).

100 T. M. Clarke, A. M. Ballantyne, J. Nelson, D. D. C. Bradley, and J. R. Durrant, Adv. Funct. Mater. **18**, 4029 (2008).

101 C. Deibel, T. Strobel, and V. Dyakonov, Adv Mater **22**, 4097 (2010).

102 P. E. Keivanidis, T. M. Clarke, S. Lilliu, T. Agostinelli, J. E. Macdonald, J. R. Durrant, D. D. C. Bradley, and J. Nelson, The Journal of Physical Chemistry Letters **1**, 734 (2010).

103 S. Cook, R. Katoh, and A. Furube, The Journal of Physical Chemistry C **113**, 2547 (2009).

104 J. G. Muller, J. M. Lupton, J. Feldmann, U. Lemmer, M. C. Scharber, N. S. Sariciftci, C. J. Brabec, and U. Scherf, Physical Review B **72**, 195208 (2005).

105 J. M. Lupton and J. Klein, Chemical Physics Letters **363**, 204 (2002).

106 J. Guo, H. Ohkita, H. Benten, and S. Ito, Journal of the American Chemical Society **132**, 6154 (2010).

107 C. J. Brabec, G. Zerza, G. Cerullo, S. De Silvestri, S. Luzzati, J. C. Hummelen, and S. Sariciftci, Chemical Physics Letters **340**, 232 (2001).

108 J. Holt, S. Singh, T. Drori, Y. Zheng, and Z. V. Vardeny, Physical Review B **79** (2009).

109 M. Hallermann, I. Kriegel, E. D. Como, J. M. Berger, E. v. Hauff, and J. Feldmann, Adv. Funct. Mater. **19**, 3662 (2009).

110 C. L. Lee, I. W. Hwang, C. C. Byeon, B. H. Kim, and N. C. Greenham, Adv. Funct. Mater. **20**, 2945 (2010).

111 Y. Li, R. Mastria, K. Li, A. Fiore, Y. Wang, R. Cingolani, L. Manna, and G. Gigli, Applied Physics Letters **95**, 043101 (2009).

112 J. S. Moon, J. K. Lee, S. Cho, J. Byun, and A. J. Heeger, Nano Letters **9**, 230 (2008).

113 Coherent, *Operator's Manual: The Coherent Mira Model 900-F Laser* (Coherent laser group, Santa Clara, 1997).

114 J.-C. Diels, *Ultrashort Laser Pulse Phenomena* (Academic Press, Inc., San Diego, 1995).

115 Coherent, *Operator's Manual: RegA Model 9000 Laser* (Coherent laser group, Santa Clara, 1997).

116 Coherent, *Operator's Manual: The Coherent Model 9400 Optical Parametric Amplifier* (Coherent laser group, Santa Clara, 1997).

117 J. Guo, H. Ohkita, H. Benten, and S. Ito, Journal of the American Chemical Society **131**, 16869 (2009).

118 S. M. King, C. Rothe, D. Dai, and A. P. Monkman, Journal of Chemical Physics **124,** 234903 (2006).

119 *IMS Series: Motorised Translation Stages*, Newport, 3 Jan 2011, http://www.newport.com/images/webdocuments-en/images/14410.pdf

120   S. King, *Ultrafast processes and excited state dynamics in conjugated polymers*, Durham University, 2008.

121   Hamamatsu, *Hamamatsu Streak Camera C5680: Instruction manual* (Hamamatsu, 2003).

122   S. I. Hintschich, *Picosecond studies of excited states in conjugated polymers*, Durham University, 2007.

123   Shimadzu, *Shimadzu UV-VIS-NIR Spectrophotometer UV-3600: Operation manual* (Shimadzu, 2004).

124   Jobin-Yvon, *Fluorolog-3: Operation manual* (Jobin-Yvon-Horiba, 2002).

125   H. L. Vaughan, F. M. B. Dias, and A. P. Monkman, Journal of Chemical Physics **122** (2005).

126   S. T. Hoffmann, E. Scheler, J.-M. Koenen, M. Forster, U. Scherf, P. Strohriegl, H. Bässler, and A. Köhler, Physical Review B **81**, 165208 (2010).

127   N. T. Harrison, D. R. Baigent, I. D. W. Samuel, R. H. Friend, A. C. Grimsdale, S. C. Moratti, and A. B. Holmes, Physical Review B **53**, 15815 (1996).

128   J. G. Grasselli, M. K. Snavely, and B. J. Bulkin, *Chemical applications of Raman spectroscopy* (John Wiley and Sons, Inc., New York, 1981).

129   C. N. Banwell, *Fundamentals of molecular spectroscopy* (McGraw-Hill, Maidenhead, 1983).

130   J. C. de Mello, H. F. Wittmann, and R. H. Friend, Advanced Materials **9**, 230 (1997).

131   L. O. Pålsson and A. P. Monkman, Advanced Materials **14**, 757 (2002).

132   A. T. R. Williams, S. A. Winfield, and J. N. Miller, Analyst **108**, 1067 (1983).

133   A. Ruseckas, P. Wood, I. D. W. Samuel, G. R. Webster, W. J. Mitchell, P. L. Burn, and V. Sundström, Physical Review B **72**, 115214 (2005).

134   N. P. Wells, B. W. Boudouris, M. A. Hillmyer, and D. A. Blank, The Journal of Physical Chemistry C **111**, 15404 (2007).

135   K. M. Gaab and C. J. Bardeen, The Journal of Physical Chemistry B **108**, 4619 (2004).

136   S. Westenhoff, W. J. D. Beenken, R. H. Friend, N. C. Greenham, A. Yartsev, and V. Sundström, Physical Review Letters **97**, 166804 (2006).

137   A. W. Grice, D. D. C. Bradley, M. T. Bernius, M. Inbasekaran, W. W. Wu, and E. P. Woo, Applied Physics Letters **73**, 629 (1998).

138   G. Grem, G. Leditzky, B. Ullrich, and G. Leising, Advanced Materials **4**, 36 (1992).

139   C. Kallinger, et al., Advanced Materials **10**, 920 (1998).

140   U. Scherf and K. Müllen, Die Makromolekulare Chemie, Rapid Communications **12**, 489 (1991).

141   U. Scherf, Journal of Materials Chemistry **9**, 1853 (1999).

142   G. Heimel, M. Daghofer, J. Gierschner, E. J. W. List, A. C. Grimsdale, K. Mullen, D. Beljonne, J. L. Bredas, and E. Zojer, Journal of Chemical Physics **122** (2005).

143   S. Karabunarliev and E. R. Bittner, Journal of Chemical Physics **118**, 4291 (2003).

144   F. C. Spano, The Journal of Chemical Physics **118**, 981 (2003).

145   F. C. Spano, The Journal of Chemical Physics **122**, 234701 (2005).

146   J. Clark, C. Silva, R. H. Friend, and F. C. Spano, Physical Review Letters **98**, 4 (2007).

147   F. C. Spano, S. C. J. Meskers, E. Hennebicq, and D. Beljonne, Journal of the American Chemical Society **129**, 7044 (2007).

148   F. C. Spano, L. Silvestri, P. Spearman, L. Raimondo, and S. Tavazzi, The Journal of Chemical Physics **127**, 184703 (2007).

149   F. C. Spano, The Journal of Chemical Physics **116**, 5877 (2002).

150   H. L. Vaughan, *Steady-state and ultrafast depolarisation in rigid-rod conjugated polymers*, Durham University, 2009.

151   D. Somitsch, F. P. Wenzl, J. Kreith, M. Pressl, R. Kaindl, U. Scherf, G. Leising, and P. Knoll, Synthetic Metals **138**, 39 (2003).

152   B. Schweitzer, G. Wegmann, D. Hertel, R. F. Mahrt, H. Bässler, F. Uckert, U. Scherf, and K. Müllen, Physical Review B **59**, 4112 (1999).

153   D. Somitsch, F. P. Wenzl, E. J. W. List, P. Wilhelm, U. Scherf, G. Leising, and P. Knoll, Macromolecular Symposia **181**, 383 (2002).

154   D. Somitsch, F. P. Wenzl, U. Scherf, G. Leising, and P. Knoll, Macromolecular Symposia **181**, 389 (2002).

155   R. Hildner, L. Winterling, U. Lemmer, U. Scherf, and J. Köhler, Chemphyschem **10**, 2524 (2009).

156   O. V. Mikhnenko, F. Cordella, A. B. Sieval, J. C. Hummelen, P. W. M. Blom, and M. A. Loi, Journal of Physical Chemistry B **112**, 11601 (2008).

157   F. A. C. Oliveira, L. A. Cury, A. Righi, R. L. Moreira, P. S. S. Guimaraes, F. M. Matinaga, M. A. Pimenta, and R. A. Nogueira, The Journal of Chemical Physics **119**, 9777 (2003).

158   E. J. W. List, C. Creely, G. Leising, N. Schulte, A. D. Schlüter, U. Scherf, K. Müllen, and W. Graupner, Chemical Physics Letters **325**, 132 (2000).

159   S. Guha, J. D. Rice, Y. T. Yau, C. M. Martin, M. Chandrasekhar, H. R. Chandrasekhar, R. Guentner, P. S. de Freitas, and U. Scherf, Physical Review B **67** (2003).

160   P. Bojarski, A. Kaminska, L. Kulak, and M. Sadownik, Chemical Physics Letters **375**, 547 (2003).

161   G. Cerullo, M. Nisoli, S. Stagira, S. De Silvestri, G. Lanzani, W. Graupner, E. List, and G. Leising, Chemical Physics Letters **288**, 561 (1998).

162   K. Kanemoto, Y. Imanaka, I. Akai, M. Sugisaki, H. Hashimoto, and T. Karasawa, Journal of Physical Chemistry B **111**, 12389 (2007).

163   W. Graupner, G. Leising, G. Lanzani, M. Nisoli, S. Desilvestri, and U. Scherf, Chemical Physics Letters **246**, 95 (1995).

164   J. Gierschner, Personal communication at OP 2009: The 8th international conference on optical probes of conjugated polymers and organic nanostructures, on the subject of modelling electron-phonon coupling in ladder-type conjugated polymers, (Beijing, China, 2009)

165   S. J. Strickler and R. A. Berg, Journal of Chemical Physics **37**, 814 (1962).

166   S. I. Hintschich, C. Rothe, S. Sinha, A. P. Monkman, P. S. de Freitas, and U. Scherf, Journal of Chemical Physics **119**, 12017 (2003).

167   E. J. W. List, M. Gaal, R. Guentner, P. S. de Freitas, and U. Scherf, Synthetic Metals **139**, 759 (2003).

168   E. J. W. List, in *OP 2009: The 8th international conference on optical probes of conjugated polymers and organic nanostructures* (Beijing, China, 2009).

169   F. I. Wu, P. I. Shih, Y. H. Tseng, C. F. Shu, Y. L. Tung, and Y. Chi, Journal of Materials Chemistry **17**, 167 (2007).

170   M.-J. Park, J. Kwak, J. Lee, I. H. Jung, H. Kong, C. Lee, D.-H. Hwang, and H.-K. Shim, Macromolecules **43**, 1379 (2010).

171   Y. Zhou, K. Tvingstedt, F. Zhang, C. Du, W.-X. Ni, M. R. Andersson, and O. Inganäs, Adv. Funct. Mater. **19**, 3293 (2009).

172   R. Kroon, M. Lenes, J. C. Hummelen, P. W. M. Blom, and B. De Boer, Polym. Rev. **48**, 531 (2008).

173   D. Veldman, et al., Journal of the American Chemical Society **130**, 7721 (2008).

174   O. Inganas, F. L. Zhang, K. Tvingstedt, L. M. Andersson, S. Hellstrom, and M. R. Andersson, Advanced Materials **22**, 100 (2010).

175   H. Becker, H. Spreitzer, W. Kreuder, E. Kluge, H. Schenk, I. Parker, and Y. Cao, Advanced Materials **12**, 42 (2000).

176   X. Gong, D. Moses, A. J. Heeger, S. Liu, and A. K. Y. Jen, Applied Physics Letters **83**, 183 (2003).

177 E. B. Namdas, P. Ledochowitsch, J. D. Yuen, D. Moses, and A. J. Heeger, Applied Physics Letters **92**, 183304 (2008).

178 S.-R. Tseng, H.-F. Meng, K.-C. Lee, and S.-F. Horng, Applied Physics Letters **93**, 153308 (2008).

179 L. Edman, M. A. Summers, S. K. Buratto, and A. J. Heeger, Physical Review B **70**, 115212 (2004).

180 J. Cabanillas-Gonzalez, S. Yeates, and D. D. C. Bradley, Synthetic Metals **139**, 637 (2003).

181 H. Najafov, I. Biaggio, T.-K. Chuang, and M. K. Hatalis, Physical Review B **73**, 125202 (2006).

182 H. S. Woo, S. C. Graham, D. A. Halliday, D. D. C. Bradley, R. H. Friend, P. L. Burn, and A. B. Holmes, Physical Review B **46**, 7379 (1992).

183 W. R. Salaneck, O. Inganas, B. Themans, J. O. Nilsson, B. Sjogren, J. E. Osterholm, J.- L. Bredas, and S. Svensson, The Journal of Chemical Physics **89**, 4613 (1988).

184 S. Heun et al., Journal of Physics: Condensed Matter **5**, 247 (1993).

185 F. Papadimitrakopoulos, M. Yan, L. J. Rothberg, H. E. Katz, E. A. Chandross, and M. E. Galvin, Molecular Crystals and Liquid Crystals Science and Technology. Section A. Molecular Crystals and Liquid Crystals **256**, 663 (1994).

186 B. J. Schwartz, T.-Q. Nguyen, J. Wu, and S. H. Tolbert, Synthetic Metals **116**, 35 (2001).

187 W. Graupner, G. Leising, G. Lanzani, M. Nisoli, S. DeSilvestri, and U. Scherf, Physical Review Letters **76**, 847 (1996).

188 M. Yan, L. J. Rothberg, F. Papadimitrakopoulos, M. E. Galvin, and T. M. Miller, Physical Review Letters **72**, 1104 (1994).

189 X. M. Jiang, R. Österbacka, O. Korovyanko, C. P. An, B. Horovitz, R. A. J. Janssen, and Z. V. Vardeny, Adv. Funct. Mater. **12**, 587 (2002).

190 M. G. Harrison, G. Urbasch, R. F. Mahrt, H. Giessen, H. Bassler, and U. Scherf, Chemical Physics Letters **313**, 755 (1999).

191 A. P. Monkman, H. D. Burrows, I. Hamblett, S. Navaratnam, U. Scherf, and C. Schmitt, Chemical Physics Letters **327**, 111 (2000).

192 J. Piris, T. E. Dykstra, A. A. Bakulin, P. H. M. van Loosdrecht, W. Knulst, M. T. Trinh, J. M. Schins, and L. D. A. Siebbeles, Journal of Physical Chemistry C **113**, 14500 (2009).

193 E. J. W. List, C. Creely, G. Leising, N. Schulte, A. D. Schluter, U. Scherf, K. Mullen, and W. Graupner, Organic Light-Emitting Materials and Devices IV **4105**, 419 (2000).

194 S. M. King, H. L. Vaughan, and A. P. Monkman, Chemical Physics Letters **440**, 268 (2007).

195 S. A. Bagnich, H. Bässler, and D. Neher, Journal of Luminescence **112**, 377 (2005).

196 S. M. King, R. Matheson, F. B. Dias, and A. P. Monkman, Journal of Physical Chemistry B **112**, 8010 (2008).

197 H. D. Burrows, J. S. de Melo, C. Serpa, L. G. Arnaut, A. P. Monkman, I. Hamblett, and S. Navaratnam, The Journal of Chemical Physics **115**, 9601 (2001).

198 R. Österbacka, C. P. An, X. M. Jiang, and Z. V. Vardeny, Science **287**, 839 (2000).

199 H. Sirringhaus et al., Nature **401**, 685 (1999).

200 F. Feller and A. P. Monkman, Physical Review B **61**, 13560 (2000).

201 T.-A. Chen, X. Wu, and R. D. Rieke, Journal of the American Chemical Society **117**, 233 (1995).

202 T. J. Prosa, M. J. Winokur, and R. D. McCullough, Macromolecules **29**, 3654 (1996).

203 B. K. Kuila and A. K. Nandi, Journal of Applied Polymer Science **111**, 155 (2009).

204 G. Cerullo, S. Stagira, M. Nisoli, S. De Silvestri, G. Lanzani, G. Kranzelbinder, W. Graupner, and G. Leising, Physical Review B **57**, 12806 (1998).

205   J. Y. Kim, K. Lee, N. E. Coates, D. Moses, T.-Q. Nguyen, M. Dante, and A. J. Heeger, Science **317**, 222 (2007).

206   Y. Kim, et al., Nat Mater **5**, 197 (2006).

207   T. J. Prosa, M. J. Winokur, J. Moulton, P. Smith, and A. J. Heeger, Macromolecules **25**, 4364 (1992).

208   J. Wang, Polymer Degradation and Stability **89**, 15 (2005).

209   P. J. Brown, D. S. Thomas, A. Köhler, J. S. Wilson, J.-S. Kim, C. M. Ramsdale, H. Sirringhaus, and R. H. Friend, Physical Review B **67**, 064203 (2003).

210   F. C. Spano, J. Clark, C. Silva, and R. H. Friend, The Journal of Chemical Physics **130**, 074904 (2009).

211   O. J. Korovyanko, Ouml, R. sterbacka, X. M. Jiang, Z. V. Vardeny, and R. A. J. Janssen, Physical Review B **64**, 235122 (2001).

212   J. J. Benson-Smith, L. Goris, K. Vandewal, K. Haenen, J. V. Manca, D. Vanderzande, D. D. C. Bradley, and J. Nelson, Adv. Funct. Mater. **17**, 451 (2007).

213   K. Tvingstedt, K. Vandewal, A. Gadisa, F. Zhang, J. Manca, and O. Inganäs, Journal of the American Chemical Society **131**, 11819 (2009).

214   P. Peumans and S. R. Forrest, Chemical Physics Letters **398**, 27 (2004).

215   J. M. Guo, H. Ohkita, S. Yokoya, H. Benten, and S. Ito, Journal of the American Chemical Society **132**, 9631 (2010).

216   X. Ai, M. C. Beard, K. P. Knutsen, S. E. Shaheen, G. Rumbles, and R. J. Ellingson, The Journal of Physical Chemistry B **110**, 25462 (2006).

217   S. Cook, L. Y. Han, A. Furube, and R. Katoh, Journal of Physical Chemistry C **114**, 10962 (2010).

218   C. Rothe, S. I. Hintschich, A. P. Monkman, M. Svensson, and R. M. Anderson, The Journal of Chemical Physics **116**, 10503 (2002).